UNIVERSITÀ
DEGLI STUDI
DI PADOVA

INSTITUTO
SUPERIOR
TÉCNICO

UNIVERSITÀ DEGLI STUDI DI PADOVA
CENTRO INTERDIPARTIMENTALE *"Centro Ricerche Fusione"*
UNIVERSIDADE TECNICA DE LISBOA

JOINT RESEARCH DOCTORATE IN FUSION SCIENCE AND ENGINEERING
CYCLE XXIV

PH.D. THESIS

FIRST WALL CONDITIONING AND PLASMA EDGE STUDIES IN RFP AND TOKAMAK DEVICES

Coordinator:
Ch.mo Prof. Piero MARTIN
Supervisors:
Ch.mo Prof. Leonardo GIUDICOTTI
Dr. Paolo INNOCENTE

Doctoral Student:
Stefano MUNARETTO

Contents

Abstract

In the stars hydrogen nuclei are continuously transformed into helium atoms releasing huge amounts of energy. The aim of the research on controlled thermonuclear fusion is to reproduce on earth what happens in the stars, in order to provide sustainable energy supply for the new generations.

The research began in the 1950s, when several "fusion machines" were established in nearly every industrialized nation. In 1968 in the Soviet Union researchers, using a strong toroidal magnetic field in the so-called tokamak device (the Russian acronym for ***to****roidal'naya* ***ka****mera s* ***ma****gnitnymi* ***k****atushkami that means toroidal chamber with magnetic field), were able to achieve for the first time promising temperature levels and plasma confinement times, two of the main criteria to achieve fusion. Following this result, in the early 1980s a generation of large tokamak experiments were built: the Join European Torus (JET) in Europe, the Doublet III in US and the Japan Torus (JT-60) in Japan. A series of good results obtained in those experiments led to project and then to start building the next step fusion experiment, ITER, as a result of an international collaboration. The aim of this machine is to demonstrate the scientific feasibility of fusion. This should be last step before the first demonstrative fusion reactor power plant, called DEMO.*

One of the major issues in the design and construction of a nuclear fusion reactor based on a magnetically confined plasma is the interaction of the hot plasma with the first wall material components of such a device. On one hand plasma can be contaminated by impurities or the wall can absorb an unsafe quantity of radiative tritium. On the other particle bombardment and the high energy flux on the wall could alterate the first wall material structures. Many present or planed experiments are devoted to address this point: for example the present experiments at JET which study the effect on plasma of an ITER like wall or the planed International Fusion Materials Irradiation

Facility (IFMIF) device which will study the effect of fusion neutron radiation on materials.

The work I carried out during my PhD and presented in this thesis is inserted in this field of research. It was mainly focused on the study of the plasma edge and its interaction with the first wall, both by an experimental and by a theoretical point of view. Most of my work has been carried out at Consorzio RFX, where it is in operation the largest Reversed Field Pinch device, RFX-mod. The Reversed Field Pinch (shortly called RFP) is one of the three main magnetic configurations tested to confine a plasma, the other two are the tokamak and the stellarator. In particular all the experimental part has been done on RFX-mod, where I worked on several experimental devices in order to perform the coating with a thin layer of lithium of the plasma facing components made of graphite and to study the effectiveness of different fuelling techniques. The theoretical part was devoted to learn how to use transport codes to describe the edge plasma physics and to apply them to the modelling of tokamak Scrape-Off Layer, in case of limiter as well divertor configurations.

Since the study of the plasma edge developed during these three years was done by experimental and theoretical points of view, it was found convenient to organize this manuscript in two main parts, the experimental one in chapters 3, 4 and 5 and the theoretical one in chapters 6, 7 and 8.

Chapter 1 *contains an introduction to the nuclear fusion. The physical principles involved and the three experiments I worked on (RFX-mod, FTU and JET) will be briefly presented. There is also a brief description of ITER, the next step fusion experiment.*

Chapter 2 *provides an overview of the physics concerning the edge and the interactions between plasma and solid materials.*

Chapter 3 *presents the work carried out to provide RFX-mod with a room temperature pellet injector to perform wall conditioning by mean of Li pellets and to perform impurities transport studies. Together with the injector are also presented the diagnostics and the techniques used to measure the ablation rate and the trajectory of the pellet when is lunched inside the plasma. In the second part of the chapter is described the ablation code used to evaluate the required pellet parameters, depending on the aim of its injection.*

Chapter 4 *is dedicated to describe the RFX-mod lithization. In the first part are described the experimental campaigns performed to optimize the wall conditioning technique, while in the second part discusses the effects of lithization on the plasma behavior. Particular attention was paid to the evidence also on RFX-mod of the three effects that are clearly noted in most of the devices where the lithization was applied: electron density profile peaking, particle/energy confinement time improvement and impurity reductions.*

Chapter 5 *presents a different aspect of the density control. On RFX-mod two different refueling techniques used: the hydrogen pellet injection and the gas puffing. These two techniques are described and compared in terms of efficiency and plasma perturbation. Here are also described the main parts of the cryogenic pellet injector I had to deal with and some test I did to ensure its optimization to perform the H pellet injection required for refuelling studies and routine RFX-mod operation.*

Chapter 6 *deals with the simulation of JET edge by mean of the EDGE2D transport code. Here it is presented a study of the validity range of the code, a comparison of the simulation results with the prediction of a 0-dimensional model and the study of different divertor regimes that can be achieved as a function of the electron core plasma density and temperature.*

Chapter 7 *provides a description of the multifluid transport code B2 and the kinetic neutrals code EIRENE that have been used to model the FTU plasma edge. Here are briefly introduced the Braginskii equations to describe the plasma edge transport and their reduced set solved by B2. Then the implementation of several magnetic equilibrium and plasma features are discussed.*

Chapter 8 *presents the work carried out to prepare the simulations in order to model FTU edge. Here are described the first simulations performed, their comparison with the experimental results and also the solutions adopted to fit the data.*

Chapter 9 *concludes the thesis with the discussion of the most important results achieved and the discussion of future developments.*

Abstract

Nel nucleo delle stelle l'idrogeno viene continuamente trasformato in elio rilasciando grandi quatità di energia. La ricerca sulla fusione termonucleare controllata ha l'obiettivo di riprodurre sulla terra quanto avviene nelle stelle, per poter produrre energia in modo sostenibile.

La ricerca iniziò negli anni '50 quando diverse "macchine da fusione" furono costruite in quasi tutti i paesi industrializzati. In Unione Sovietica nel 1968 per la prima volta dei ricercatori, usando intensi campi magnetici toroidali nei dispositivi denominati tokamak (dal russo ***to****roidal'naya* ***ka****mera s* ***ma****gnitnymi* ***k****atushkami, cioé cella toroidale con bobine magnetiche), furono in grado di ottenere plasmi caratterizzati da valori promettenti di temperatura e tempo di confinamento, due dei criteri principali per ottenere la fusione. In seguito a questi risultati negli anni '80 fu costruita una serie di dispositivi di tipo tokamak di grandi dimensioni: il Join European Torus (JET) in Europa, Doublet III negli Stati Uniti e il Japan Torous (JT-60) in Giappone. I buoni risultati ottenuti da questi esperimenti hanno portato a progettare prima, e ad iniziare a costruire poi, ITER, l'esperimento da fusione di nuova generazione frutto di una collaborazione internazionale. Scopo di questo esperimento sarà dimostrare scientificamente la fattibilità della fusione. Questo dovrebbe essere l'ultimo passo prima dell'impianto dimostrativo di produzione di energia elettrica da fusione denominato DEMO.*

Una delle difficoltà maggiori che si incontrano nella progettazione e nella realizzazione di un reattore nucleare a fusione basato su plasmi confinati magneticamente è l'interazione fra il plasma stesso e le componenti del reattore ad esso affacciate. Da una parte infatti il plasma potrebbe venir contaminato dalle impurezze rilasciate o la parete può assoribire una ecessiva e pericolosa quantità di trizio radiattivo. Dall'altra il bombardamento di particelle e gli alti flussi termici che colpiscono le componenti del reattore potrebbero alterarne la struttura.

Il lavoro da me svolto durante il dottorato e presentato in questa tesi si inserisce nell'ambito della ricerca sulla fusione nucleare. In particolare si è concentrato nello studio della regione di plasma più vicina alle superfici solide e la sua interazione con esse, sia da un punto di vista sperimentale che teorico. La maggior parte del lavoro è stato svolto presso il Consorzio RFX, dove opera RFX-mod che è l'esperimento in configurazione Reversed Field Pinch di maggiori dimensioni al mondo. Il Reversed Field Pinch (o RFP) è una delle tre principali configurazioni magnetiche utilizzate per confinare il plasma, le altre due sono la giÃă citata tokamak e quella denominata stellarator. In particolare tutta la parte sperimentale della mia tesi è stata svolta su RFX-mod, dove ho partecipato a diverse sessioni sperimentali per poter ricoprire di un sottile film di litio le componenti a contatto col plasma, che sono fatte di grafite. La parte teorica si è concentrata nello studio di codici di trasporto che descrivono il plasma di bordo e nella loro applicazione per simulare lo Scrape Off-Layer di tokamak sia in configurazione limiter che divertore.

Poiché lo studio del plasma di bordo svolto durante questi tre anni è stato fatto sia dal punto di vista sperimentale che da quello teorico, si è trovato conveninte organizzare il presente scritto in due parti principali. La parte sperimentale verrà descritta nei capitoli 3, 4 e 5 mentre quella teorica nei capitoli 6, 7 e 8.

Capitolo 1 *contiene una breve introduzione alla fusione nucleare. Verrano brevemente presentati i principi fisici e i tre esperimenti (RFX-mod, FTU, JET) su cui ho lavorato. C'è inoltre una breve descrizione di ITER, l'esperimento di nuova generazione.*

Capitolo 2 *dà una visione d'insieme della fisica coinvolta nello studio di plasmi che interagiscono con superfici solide.*

Capitolo 3 *presenta il lavoro svolto per dotare RFX-mod di un iniettore di pellet a temperatura ambiente per poter svolgere la litizzazione per mezzo di pellet di litio e per poter studiare il trasporto di impurezze. Assieme all'iniettore vengono anche presentati le diagnostiche e le tecniche utilizzate per misurare il tasso di ablazione e la traiettoria dei pellet una volta lanciati all'interno del plasma. nella seconda parte del capitolo c'è la descrione del codice di ablazione utilizzato per stabilire le caratteristiche richieste dei pellet a seconda dello scopo del loro utilizzo.*

Capitolo 4 *è dedicato alla descrizione della litizzazione di RFX-mod. Nella prima parte sono presentate le campagne sperimentali svolte per ottimizzare la tecnica di litizzazione. Nella restante parte si presentano gli effetti della litizzazione sul plasma. Particolare attenzione viene prestata alla presenza dei tre effetti chiaramente osservati nella maggior parte degli esperimenti dove era già stata svolta: il piccaggio dei profili di densità, il miglioramento del tempo di confinamento di particelle ed energia, la riduzione delle impurezze.*

Capitolo 5 *presenta un diverso aspetto del controllo di densità. Le tecniche utilizzate su RFX-mod per fornire il plasma di particelle sono l'iniezione di pellet di idrogeno e l'immissione di gas. Le due tecniche vengono descritte e comparate in termini di efficenza e perturbazione del plasma. Vengono inoltre descritte le principali componenti dell'iniettore di pellet criogenici su cui ho lavorato e alcuni test svolti per ottimizzarne l'utilizzo in funzione degli esperimenti sul rifornimento di particelle e del normale utilizzo su RFX-mod.*

Capitolo 6 *è dedicato alle simulazioni del plasma di bordo dell'esperimento JET, svolte con il codice di trasporto EDGE2D. Viene presentato uno studio del range di validità del codice, un confronto con le previsioni di un modello 0-dimensionale e lo studio dei diversi regimi che si possono ottenere nella regione del divertore al variare della densità e della temperatura nel plasma.*

Capitolo 7 *descrive B2, un codice di trasporto al bordo, e il codice di neutri EIRENE che sono stati utilizzati per simulare il plasma di bordo di FTU. Vengono introdotte brevemente le equazioni di Braginskii che descrivono il trasporto al bordo e le semplificazioni fatte nel codice per risolverle. Il capitolo si conclude con la descrizione di come si configurino vari equilibri magnetici e le condizioni al contorno del plasma.*

Capitolo 8 *presenta il lavoro svolto per preparare le simulazioni che descrivono il plasma di bordo di FTU. Vengono descritte le prime simulazioni fatte, il loro confronto con i risultati sperimentali e varie soluzioni per aumentare l'accordo tra i due.*

Capitolo 9 *conclude la tesi con la discussione dei maggiori risultati ottenuti e le prospettive future.*

Thermonuclear Fusion

Most of the energy used on earth, either directly or indirectly, comes from fusion reactions. Indeed fusion reactions occur in the hot and dense core of the sun, like in all the other stars, where light nuclei are fused to form heavier nuclei with the release of a great amount of energy. This central core is about 0.1% of the sun's total volume. The remainder of the sun is a "thermal blanket" through which the energy produced by fusion must pass by conductive, convective and radiative energy transfer processes before it reaches the surface of the sun where it is radiated into space, a small fraction of which subsequently reaches earth and makes life possible [1].

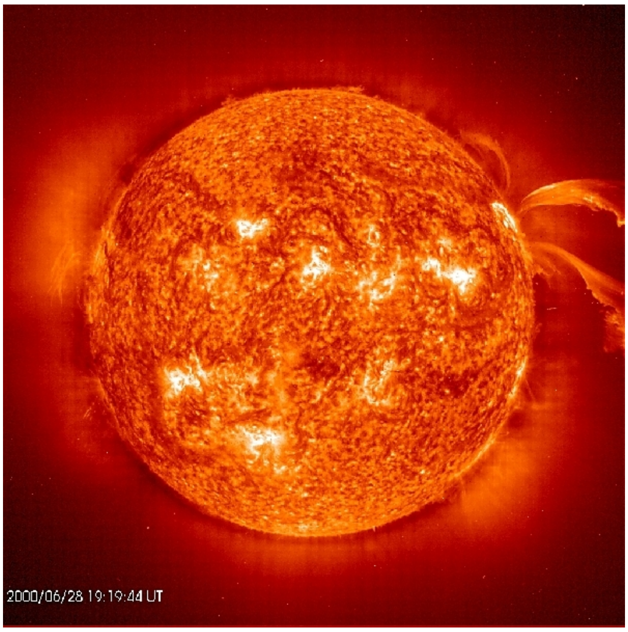

Figure 1.1: The sun activity.

Sun is composed mostly of hydrogen, with a few percent of He and heavier elements. In sun the hydrogen is "burned" into helium, which is converted into ever heavier nuclides up to iron and nickel, after which fusion reactions are not anymore exothermic.

Sun was “born” with gravity pulling together interstellar gas, composed mainly of hydrogen, to form a dense cloud of matter. As gravity pulls the atoms together, gravitational potential energy was converted into thermal energy, heating the collapsing gas cloud. At some point, the temperature and nuclide density at the center of the collapsing matter became sufficiently high that fusion reactions begin to occur (i.e., the sun *ignites*).

Fusion reactions occurring in the core of the sun are:

$$\begin{aligned} p + p &\rightarrow D + e^{+} + \nu_e \\ D + p &\rightarrow {}^{3}He + \gamma \\ {}^{3}He + {}^{3}He &\rightarrow {}^{4}He + 2p \end{aligned}$$

where p denotes a proton, D a deuteron, ${}^{3}He$ and ${}^{4}He$ are helium isotopes, γ stands for a high-energy photon, e^{+} for a positron and ν_e for an electron neutrino. The energy release is due to the difference in mass between reactants and products, according to the Einstein equation $E = mc^2$.

1.1 Fusion on Earth

The reactants can interact if they are raised to sufficient high temperature T so that their thermal motion provides the necessary kinetic energy ($E_{av} = k_B T$, where k_B is Boltzmann’s constant). Fusion reactions induced by the thermal motion of the reactants are called *thermonuclear reactions*. However, the temperatures needed are very high, typically $10 \div 300 \times 10^6\,K$. At these temperatures, the reactants exist as a plasma, a state of matter consisting of separated electrons and positively charged nuclei. The challenge to produce fusion energy in useful quantities is to confine a high temperature plasma of light elements for sufficiently long times and at sufficiently high nuclide densities to allow the fusion reactions to produce more energy than is required to produce the plasma.

The reaction with the largest cross-section (that indicates the probability of interaction between particles) at the lowest energies between the possible reactions involving hydrogen, helium and their isotopes is:

$$D + T \rightarrow {}^{4}He + n + 17.59\,MeV \tag{1.1}$$

as shown in figure 1.2.

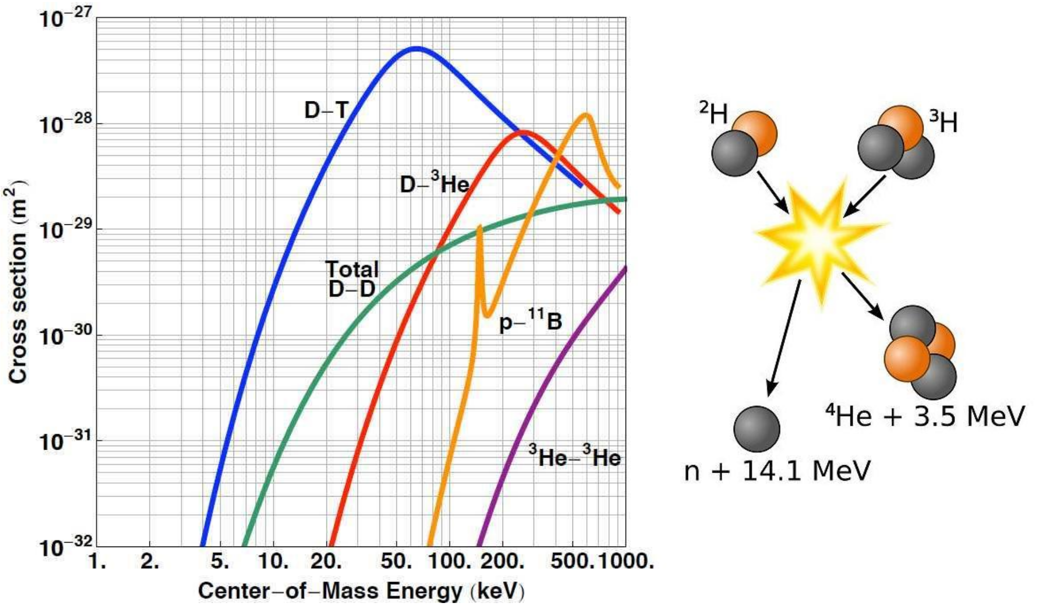

Figure 1.2: On the left the fusion cross section for couples of reactants. On the right a sketch of the D-T fusion reaction.

1.1.1 Burning Criteria

In 1957 John D. Lawson expressed the conditions of a high temperature plasma confined for sufficiently long times and at sufficiently high nuclide densities in the so-called *Lawson criterion* [2]. It is a criterion for a positive energy balance using quantities such as the thermal cycle efficiency η of power reactors.

A positive energy balance of a fusion reactor means that the energy produced by fusion reactions has to exceed that required to create and sustain the plasma itself, also accounting for the energy losses for emission of radiation, or confinement degradation. It can be written as:

$$P_b + P_t \leq \eta (P_b + P_t + P_n) \tag{1.2}$$

where P_b is the power loss due to bremsstrahlung, P_t is the heating power that should be introduced in to the plasma to reach the fusion temperature, P_n is the energy produced by the fusion reactions and η is the efficiency in converting the produced energy into input power for the reactor.

The *Lawson criterion* is the balance of equation 1.2 written in terms of confinement time, plasma density and temperature:

$$n\tau_E \geq \left(\frac{\eta}{1-\eta} \frac{W_{DT}}{4} < \sigma v >_T - b\sqrt{T} \right)^{-1} . \tag{1.3}$$

where $W_{DT} = 17.59\,MeV$ is the energy released after a single $D - T$ fusion reaction, $<\sigma v>_T$ the product of the reaction cross-section and the relative velocity of the reactants averaged over a Maxwellian velocity distribution and b is a constant depending on the effective charge Z_{eff}.

In the years the criteria has changed slightly to a more physics oriented condition. The aim is an ignited plasma where all energy losses are compensated by the α particles (${}^4_2He$ nuclei) from the fusion reactions, which transfer their energy of $3.5\,MeV$ to the plasma while slowing down. Neutrons cannot be confined and therefore leave the plasma without interactions. Their energy is that converted to electric energy. In this case the energy balance becomes

$$P_b + P_t \leq P_\alpha \tag{1.4}$$

and the Lawson criterion becomes

$$n\tau_E \geq 3T\left(\frac{W_\alpha}{4} < \sigma v >_T - b\sqrt{T}\right)^{-1} \tag{1.5}$$

the so-called *ignition criterion*. W_α is the energy of a single α particle after a fusion reaction and it is $W_\alpha = W_{DT}/5$.

This ignition curve has a minimum at about $T \simeq 20\,keV$ (where $1\,eV \simeq 11600\,K$). By isolating the temperature dependence in the RHS of equation 1.5 it is obtained the so called *triple product*:

$$n\tau_E T_i \geq 3 \cdot 10^{21}[m^{-3}keVs]. \tag{1.6}$$

Another useful parameter to quantify the efficiency of a fusion reactor is the ratio Q between the power produced by the fusion reactions and that spent to heat the plasma. It is expressed as:

$$Q = \frac{5P_\alpha}{P_H}. \tag{1.7}$$

When $Q = 1$ the fusion reactions generate an amount of energy equal to that necessary to heat the plasma, this condition is dubbed *breakeven.* When $Q = 5$ the energy of the α particles coincides with the energy of the plasma heating, hence theoretically only the 50% of the energy losses has to be compensated while neutrons carry a power equal to $4P_H$ off the plasma. When $Q \rightarrow \infty$ the plasma reaches the ignition because $P_H \rightarrow 0$. In general it is desirable that $Q \geq 10$ for a fusion reactor.

The progress on the values of the triple product reached in fusion devices since the beginning of experiments in plasma physics is shown in figure 1.3.

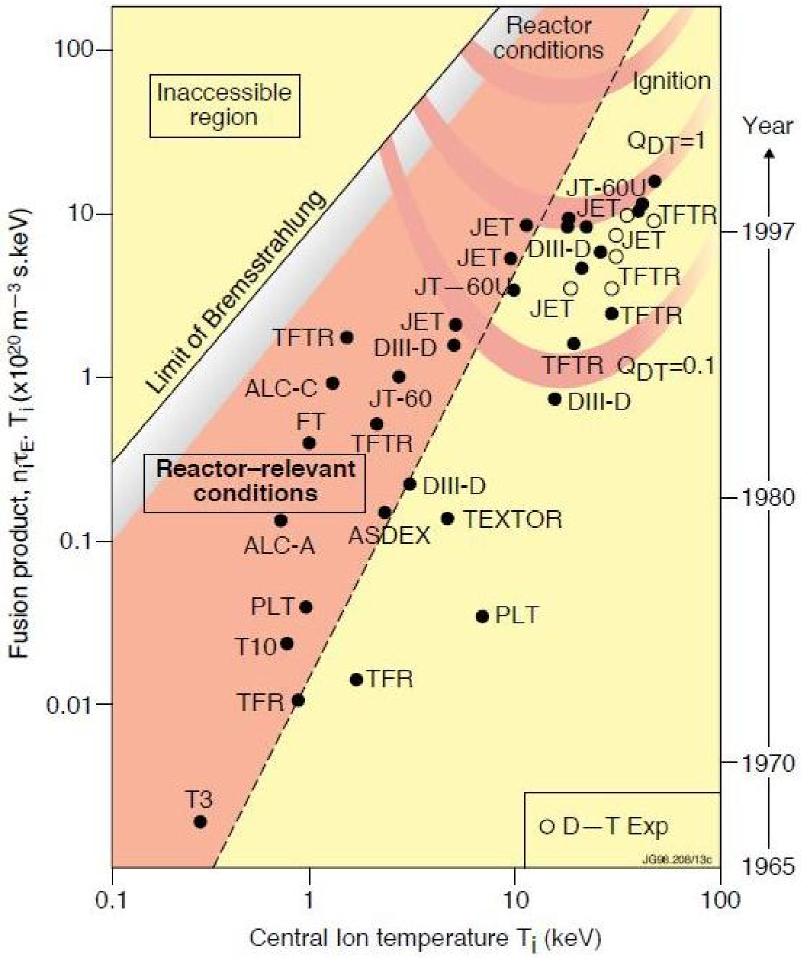

Figure 1.3: Values of the triple product obtained in experiments as function of the central ion temperature T_i.

1.2 Magnetic confinement

The triple product dictates the strategy for developing fusion power as energy producing system. To achieve temperatures of about $T \simeq 20\ keV$ and the required density and confinement time simultaneously a possible approach is the magnetic confinement, since a plasma is composed of charged particles.

Fusion research has investigated different magnetic field geometries and the toroidal one resulted to be the most effective in term of confinement. In figure 1.4 the toroidal coordinate system that will be used through this thesis are sketched.

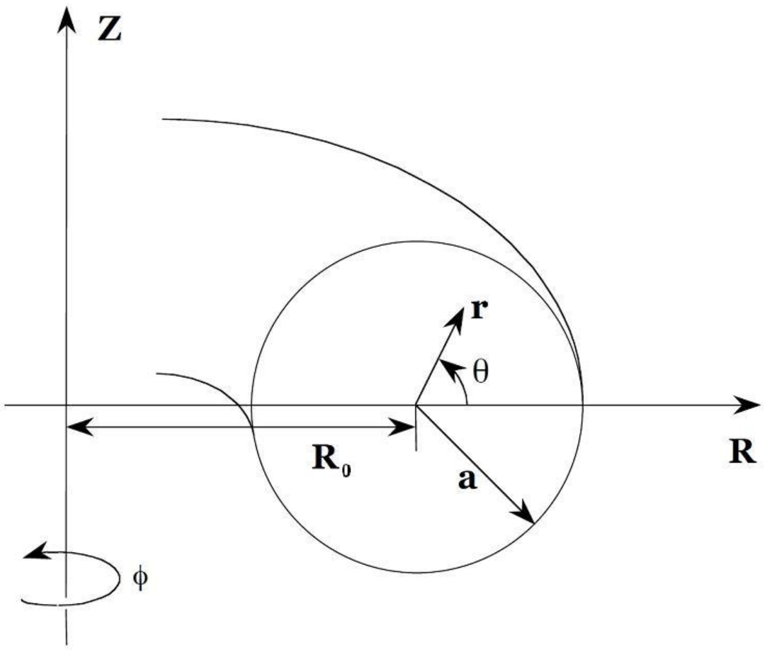

Figure 1.4: Toroidal coordinate system.

In a system with purely toroidal magnetic field, the magnetic field curvature and gradient originate a vertical drift which is in opposite directions for ions and electrons. The resulting electric field causes an outward $E \times B$ drift of the whole plasma (see figure 1.5), and therefore such a simple magnetic field configuration will be unstable.

To avoid the charge separation it is necessary to twist the magnetic field lines by additional magnetic field components. An important parameter for the study of a toroidal magnetic configuration is the *safety factor* $q(r)$. It is defined as:

$$q(r) \equiv \frac{\Delta\Phi}{2\pi} = \frac{rB_\phi(r)}{R_0 B_\theta(r)}, \tag{1.8}$$

with B_ϕ and B_θ the toroidal and poloidal components of the magnetic field respectively.

The inverse of this quantity represents the number of poloidal turns done by a helical field line per one toroidal turn. The majority of the field lines does not close upon itself and maps the whole so-called *flux surface.* Between these surfaces there are some special magnetic surfaces, called *rational surfaces*, where field lines close on themselves after n toroidal and m poloidal turns. On these surfaces the value of q corresponds to the opposite of the rational number m/n ($q = -m/n$).

Figure 1.5: Vertical drifts and associated $E \times B$ in a toroidal field.

1.2.1 The MHD theory

A large variety of plasma properties such as the magnetic equilibrium or several instabilities associated with them can be described using a fluid model called *resistive Magneto Hydro Dynamics* (MHD) [3]. A brief introduction to this theory is given in the following.

The fluid description is limited to plasmas where charge separation is negligible. The conditions for this to occur are essentially two: the length scales have to be larger than the Debye length (λ_D) while the time scales have to be longer than the inverse of the plasma frequency (ω_P). These threshold quantities are defined as follows:

$$\lambda_D = \sqrt{\frac{k_B T}{8\pi n e^2}} \qquad \omega_P = \sqrt{\frac{4\pi n e^2}{m_e}} \tag{1.9}$$

where k_B is the Boltzmann's constant, T is the plasma temperature, n is the plasma density, e is the electron charge and m_e the electron mass.

The MHD model can be developed starting from microscopic considerations [4] and by means of Maxwell's equations. In this framework the plasma dynamics is described by a set of equations obtained considering it as a mixture of two oppositely charged fluids. The resulting set of MHD equations are: the continuity equation; the motion equation; the energy equation; the generalized Ohm's equation and the induction equation. They are written respectively as:

$$\frac{\partial \rho}{\partial t} + \nabla \cdot (\rho \mathbf{v}) = 0 \tag{1.10}$$

$$\rho \left(\frac{\partial \mathbf{v}}{\partial t} + (\mathbf{v} \cdot \nabla \mathbf{v} \right) = \mathbf{j} \times \mathbf{B} - \nabla p + \frac{1}{\mu_0 \eta} \mathbf{E} \tag{1.11}$$

$$\frac{\partial \epsilon}{\partial t} + \nabla \cdot (\epsilon \mathbf{v}) = -\mathbf{p} \nabla \cdot \mathbf{v} + \eta \mu_\mathbf{0} \mathbf{j}^\mathbf{2} + \nabla \cdot (\mathbf{k_B} \nabla \mathbf{T}) \tag{1.12}$$

$$\mathbf{E} + \mathbf{v} \times \mathbf{B} - \eta \mathbf{j} = \frac{1}{ne} (\mathbf{j} \times \mathbf{B} - \nabla p) \tag{1.13}$$

$$\frac{\partial \mathbf{B}}{\partial t} = \nabla \times (\mathbf{v} \times \mathbf{B}) + \frac{\eta}{\mu_0} \nabla^2 \mathbf{B} \tag{1.14}$$

In the previous equations, ρ denotes the fluid mass density, $\mathbf{v}$ the fluid velocity field, η the fluid resistivity, p the fluid pression and ϵ the internal energy per unit mass. The RHS terms in equation 1.13 are often negligible, so in most cases the generalized Ohm's equation is substituted by the simpler Ohm's equation that reads:

$$\mathbf{E} + \mathbf{v} \times \mathbf{B} = \eta \mathbf{j} \tag{1.15}$$

1.2.2 MHD equilibrium and instability

It was seen that a magnetic surface is a surface ergodically covered by a magnetic field line as it goes around the torus. In toroidal geometry the magnetic surfaces are nested surfaces and their cross-section in a poloidal plane forms a set of smooth closed curves. The degenerate magnetic surface with the limiting zero values is called *magnetic axis* (figure 1.6).

Well defined nested magnetic surfaces are usually taken to be a requirement for adequate plasma equilibrium as described by MHD equation:

$$\mathbf{j} \times \mathbf{B} = \nabla p \tag{1.16}$$

These magnetic surfaces are constant pressure surfaces, since $\mathbf{B} \cdot \nabla p = 0$ and the current-density lines lie on these surfaces because $\mathbf{j} \cdot \nabla p = 0$.

The MHD equations moreover predict that under certain conditions a small perturbation in a fluid quantity, like the density, the fluid velocity, or the magnetic field, can grow unstable in time. These phenomena are called MHD instabilities [5]. They influence in many ways the global plasma properties, and can deteriorate the plasma confinement performances.

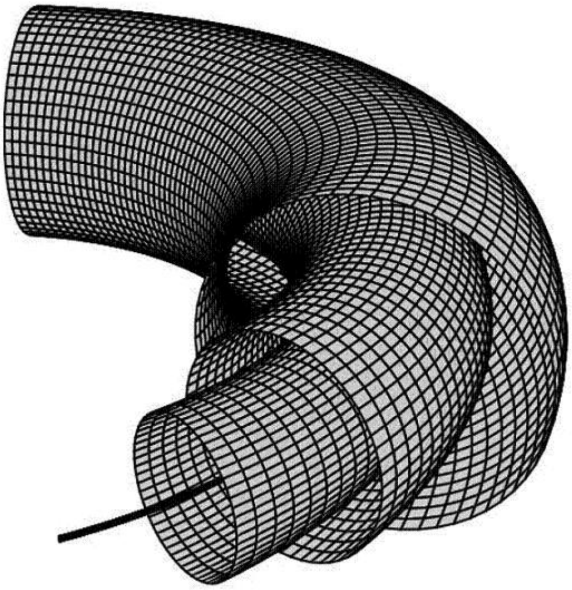

Figure 1.6: Magnetic surfaces and magnetic axis in toroidal geometry.

To analyze the influence of the instabilities it has to be considered that the equilibrium of a magnetic configuration is stable if it is a point of minimum of the potential energy. For each shift of $\tilde{\mathbf{A}}$ from equilibrium, there is an increase potential energy:

$$\delta V[\vec{\xi}(\vec{r}_0, t)] \geq 0. \tag{1.17}$$

The analysis performed in MHD approximation leads to the Suydam criterion [6] for the stability:

$$\frac{rB_z^2}{\mu_0}\left(\frac{1}{q}\frac{dq}{dr}\right)^2 + 8\frac{dp}{dr} > 0. \tag{1.18}$$

where the cylindrical geometry is assumed and μ_0 is the magnetic permeability in vacuum. A negative pressure gradient causes an instability that can be balanced only by a gradient of the safety factor sufficiently large. This equation is a necessary but not sufficient condition for stability.

The perturbation $\tilde{\mathbf{A}}$ of the quantity $\mathbf{A}$ in a toroidal plasma can also be Fourier analyzed as follows:

$$\tilde{\mathbf{A}}(r,t)=\sum_k \tilde{A}_k(r)e^{i(\mathbf{k}\cdot\mathbf{r}-\omega t)}=\sum_k \tilde{k}(r)e^{i(m\theta+n\varphi-\omega t)} \tag{1.19}$$

where $\mathbf{k} = (k_r, k_\theta, k_\varphi) = (k_r; m/r; n/R_0)$ is the wavevector in toroidal coordinates, and m and n are the poloidal and toroidal mode number, respectively. Each couple (m; n) represents a helical perturbation, or mode. The angular frequency ω is in general a complex quantity, $\omega = \omega_R + i\omega_I$, of which the real part describes the propagation velocity, while the imaginary part represents an exponential growth ($\omega_I > 0$), or damping of the perturbation amplitude ($\omega_I < 0$). A helical magnetic perturbation with wavevector k can become unstable if it fulfills the resonance condition $\mathbf{k}\cdot\mathbf{B} = 0$, where $\mathbf{B} = (0, B_\theta, B_\varphi)$ is the equilibrium magnetic field. In fact, a perturbation with $\mathbf{k}\cdot\mathbf{B} \neq 0$ would bend the mean magnetic field, and it would be thus energetically unfavored. The above resonance condition can be rewritten as follows:

$$\mathbf{k}\cdot\mathbf{B}=\frac{m}{r}B_\theta+\frac{n}{R_0}B_\varphi=0\rightarrow q(r)=-\frac{r}{R_0}\frac{B_\varphi(r)}{B_\theta(r)}=-\frac{m}{n} \tag{1.20}$$

This shows that helical instabilities can grow only at radial positions where the safety factor assumes rational values. For this reason, these positions are called rational or resonant radii.

1.2.3 Toroidal Magnetic Configurations

Several magnetic field geometries have been investigated in fusion research to seek the best conditions for plasma confinement. The toroidal configurations have given the best confinement performances up to now. Three different configurations of the magnetic field have been conceived in the '50s and are under investigation worldwide. A brief overview of the three configuration (the stellarator [7], the tokamak [8] and the reversed field pinch [9]) in order of invention is presented in the following.

STELLARATOR The stellarator was designed in 1951 by Lyman Spitzer, Jr. at Princeton. In a stellarator the twist of the field lines is created by external coils wound around the plasma torus, as shown in figure 1.7. Due to these external currents the plasma shape is not circular, but shows some indentation. These external coils have the advantage that the current can be controlled from outside, and can flow continuously, but their shape is very complex to built from the engineering point of view.

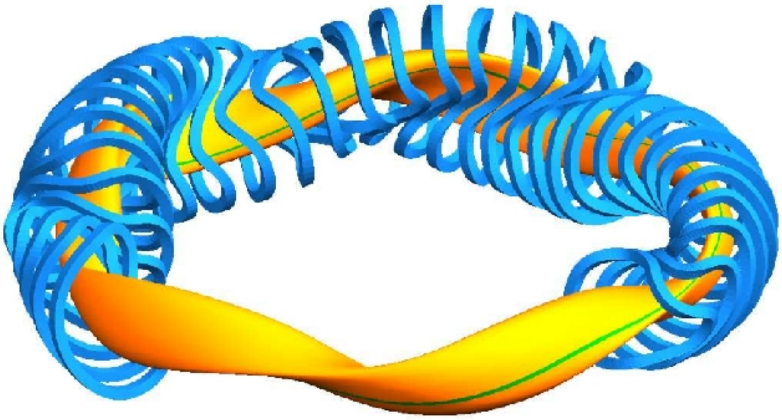

Figure 1.7: Schematic view of Wendelstein 7-X [10].

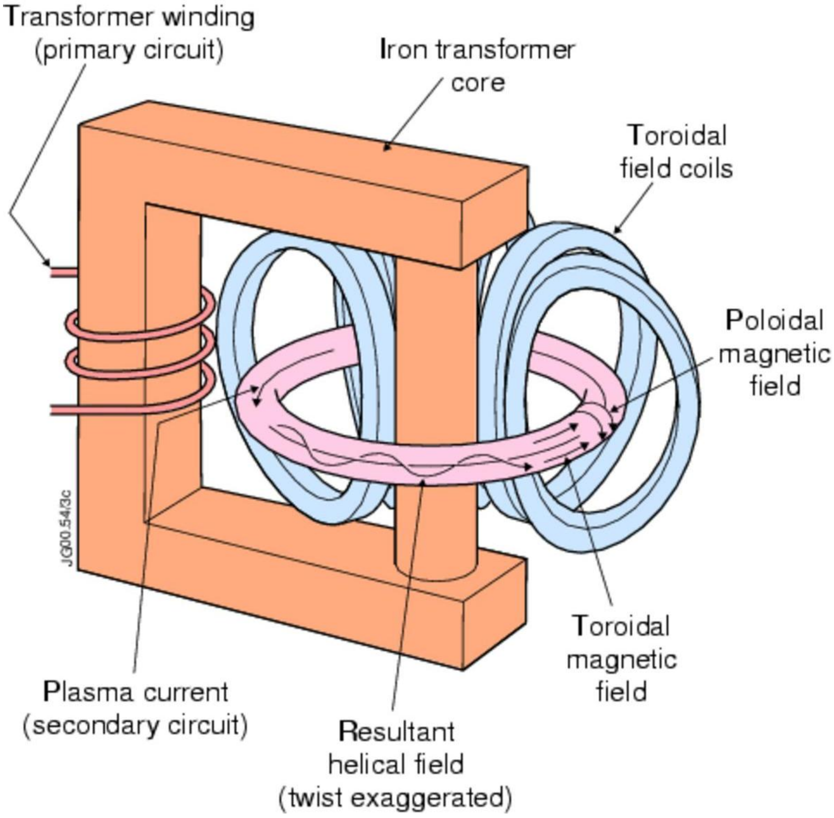

Figure 1.8: Schematic view of a Tokamak configuration.

TOKAMAK The tokamak approach was proposed by two Russian physicists, Tamm and Sakharov, in 1952 and then realized by another Russian scientist, Artsimovich [11]. The toroidal magnetic field is provided by simple magnets and the necessary twist is produced by the plasma itself, by means of an electric current in the plasma which gives rise to the poloidal component of the twisted magnetic field. The current also serves for plasma build-up and heating. This current is produced by induction, the plasma acting as the secondary winding of a transformer. It is shown in figure 1.8. Tokamak configuration is characterized by $B_\theta \ll B_\varphi$, as shown in figure 1.9, with B_φ of some Tesla. This configuration has proved to be very successful in improving the desired fusion plasma conditions and presently best experiments in terms of performance are based on the tokamak principle. Also ITER, the next step device, is based on the tokamak configuration. From the Suydam criterion in toroidal geometry derives that for the stability of this configuration a safety factor at the edge always greater than one is required (see figure 1.10). This imposes a limit on the plasma current, and consequently to the ohmic heating that originates from the obtained plasma current. It follows that the tokamak configuration needs additional heating to achieve the request plasma conditions for a fusion reactor.

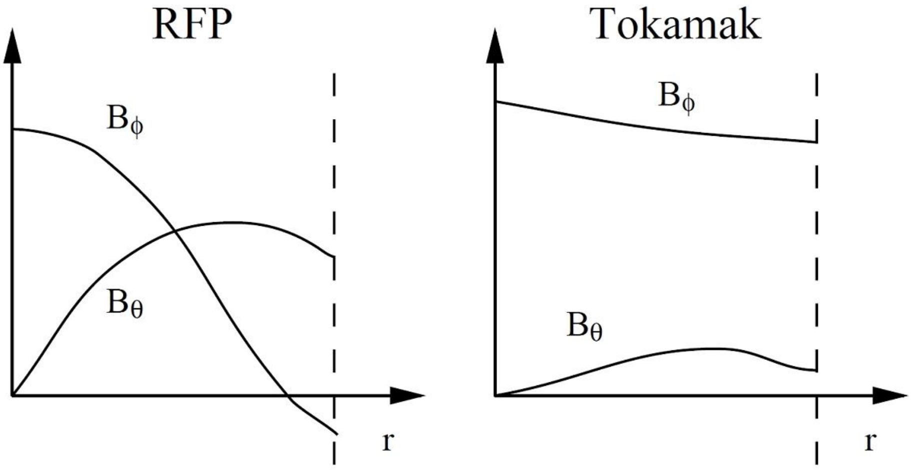

Figure 1.9: Sketch of RFP and tokamak equilibrium magnetic fields.

REVERSED FIELD PINCH (RFP) The first RFP device was ZETA, in operation from 1954 to 1968 in UK. The RFP magnetic configuration is a near minimum energy state to which the plasma spontaneously relaxes [12]. It aims to confine the plasma exploiting the same pinch effect of tokamaks. The main differences are represented by amplitude and behavior of the magnetic field components. Indeed in the RFP configuration, differently from the tokamak one, $B_\theta \approx B_\varphi$. Moreover in RFP B_φ reverses its verse at the edge, in the so called reversal region. These differences are shown in figure 1.9.

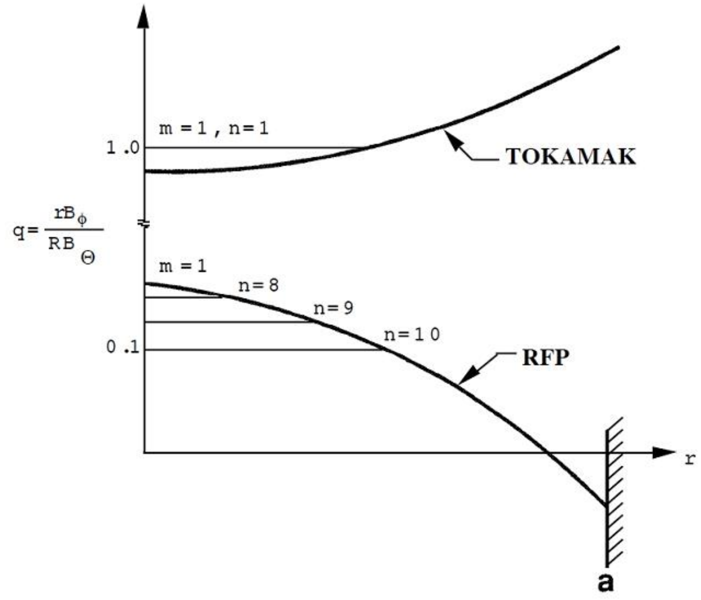

Figure 1.10: Safety factor profiles for a tokamak and a RFP. Horizontal lines indicate the $(m = 1; n)$ rational radii.

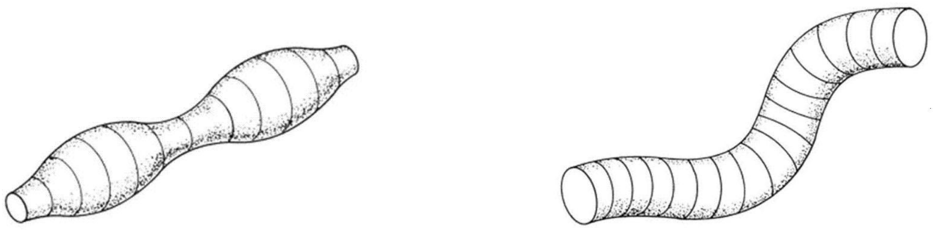

Figure 1.11: m = 0 (left) and m = 1 (right) deformations of the LCFS.

In terms of safety factor in RFP $q < 1$ all along the minor radius. RFP is therefore an intrinsically unstable configuration. Indeed a broad spectrum of $(m = 1; |n| \leq 2R_0/a)$ magnetic modes is resonant throughout the plasma radius, and several $(m = 0; n \geq 1)$ modes are resonant at the reversal radius (figure 1.10), leading to a distortion of the *Last Close Flux Surface* of the plasma. The unperturbed magnetic surfaces (figure 1.6) are shrunk and enlarged by the m = 0 modes whereas the m = 1 modes generates an helical deformation, as shown in figure 1.11.

1.3 Magnetic Fusion Devices

In this section IT will be briefly presented the three devices studied during this thesis, RFX-mod, FTU, JET, and ITER, the future of the research on magnetically confined plasmas.

1.3.1 RFX-mod

The RFX-mod (**R**eversed **F**ield e**X**periment modified) [13, 14] is a RFP device derived by a modification of RFX [15, 16], operating at Consorzio RFX in Padova. The first plasma of RFX-mod was obtained in 2004. The main features of RFX-mod (in figure 1.12) are listed in table 1.1.

RFX-mod	
Major radius	$2\,m$
Minor radius	$0.46\,m$
Plasma current	$< 2\,MA$
Toroidal magnetic field	$< 0.7\,T$
Plasma discharge duration	*up to* $0.5\,s$

Table 1.1: Main Parameters of the RFX-mod device.

Important features of RFX-mod are a set of 192 independently driven saddle coils aimed at actively controlling the local radial perturbations at the edge and a new design of the first wall tiles.

Of particular interest for this thesis is the first wall. It is composed by 2016 graphite tiles that cover completely the inner part of the vacuum vessel (see figure 1.13). The shape of the tiles was designed to improve plasma-wall interaction by reducing the heat flux peaking on leading edge. Graphite was chosen for its low atomic number Z and for its capability to withstand high power loads.

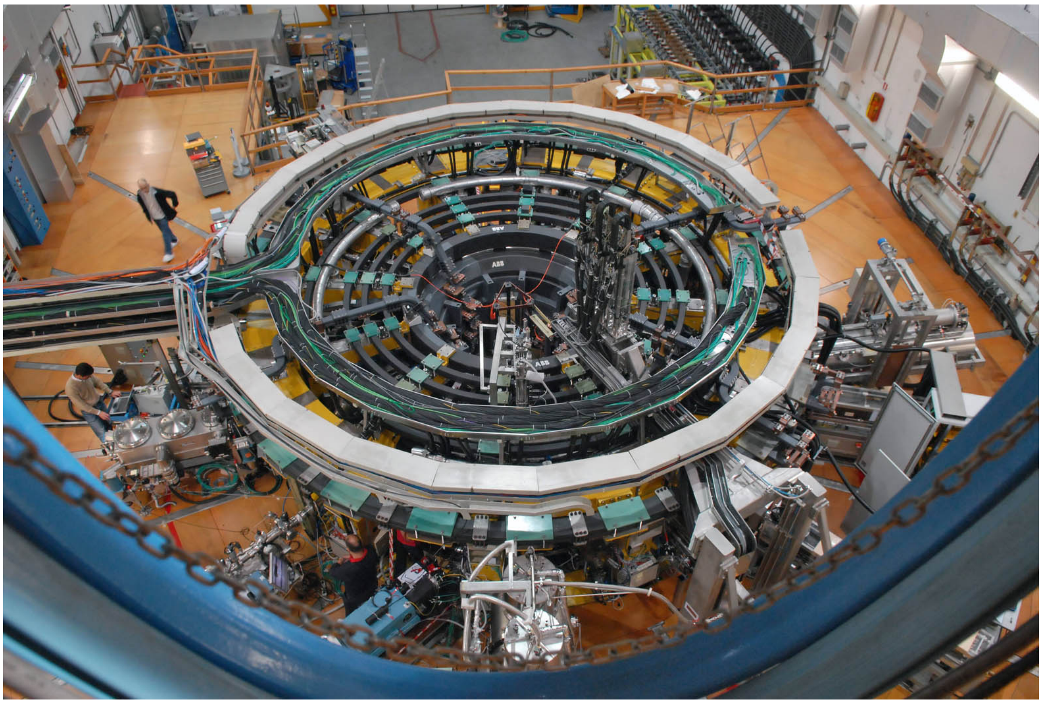

Figure 1.12: Picture of the RFX-mod experiments surrounded by plasma diagnostics.

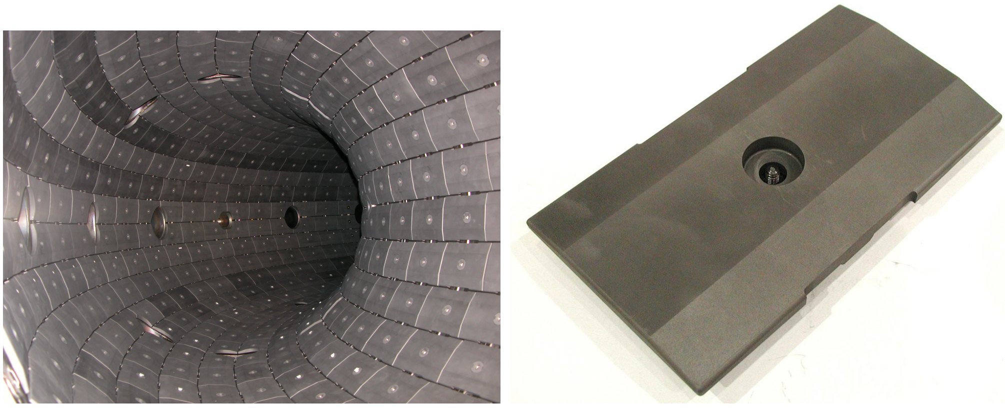

Figure 1.13: A picture of the first wall and of a tile of RFX-mod.

1.3.2 FTU

The **F**rascati **T**okamak **U**pgrade (FTU) [17] is a device situated at ENEA in Frascati. It is the upgrade of the FT experiment [18, 19]. Its main features are summarized in table 1.2, a picture of it is reported in figure 1.14.

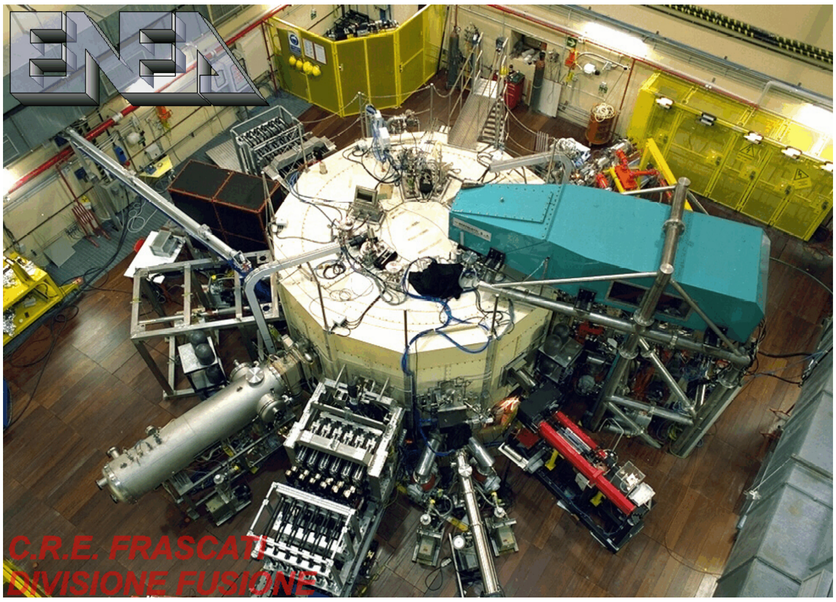

Figure 1.14: Picture of the FTU experiments (S?) surrounded by plasma diagnostics.

FTU	
Major radius	$0.935\,m$
Minor radius	$0.31\,m$
Plasma current	$< 1.6\,MA$
Toroidal magnetic field	$8\,T$
Plasma discharge duration	*up to* $1.5\,s$

Table 1.2: Main Parameters of the FTU device.

The FTU device is a medium-sized high magnetic field tokamak. The machine produces plasmas with densities at or above the level of a reactor with a plasma current flat-top of $1.5\,s$ duration. The device has the option of displacing the plasma both towards a toroidal limiter (see section 2.1), which is located on the high field side and has a relatively large plasma-wall contact area (of about $1.7\,m^2$), or towards a poloidal limiter, which has a much smaller plasma-wall contact surface (about $0.026\,m^2$).

To produce a high field, a current of about 38 kA per 1.5 s has to pass through the toroidal windings. As all the FTU windings are copper coils, their resistivity is lowered by cooling them with liquid nitrogen, at about 77 K.

In FTU are also studied new first wall materials, like liquid metals, potentially interesting for future fusion reactors. To do it, since the end of 2005 a Liquid Lithium Limiter (LLL) has been installed on FTU. In figure 1.15 are shown the first wall of FTU and the LLL.

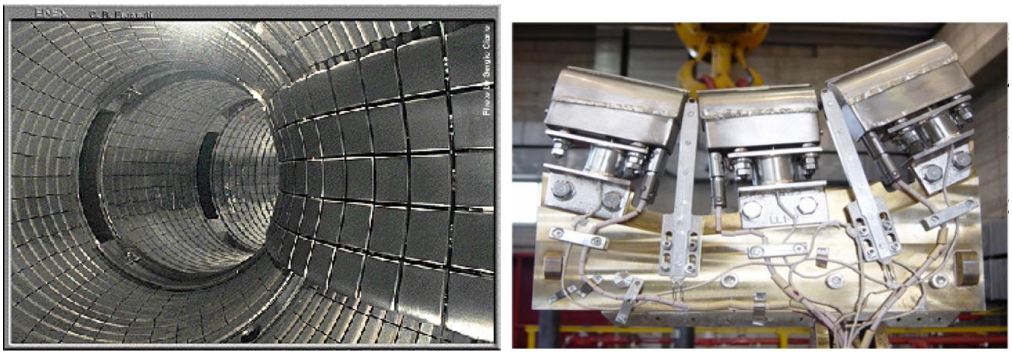

Figure 1.15: A picture of FTU first wall and of the Liquid Lithium Limiter.

1.3.3 JET

Situated in Culham, UK, the **J**oint **E**uropean **T**orus (JET) was built from 1979 to 1983 (First Plasma was achieved on 25 June 1983) [20]. The main objective of JET was to obtain and study plasmas in conditions and dimensions approaching those needed in a thermonuclear reactor. The studies were aimed at defining the parameters, the size and the working conditions of a tokamak reactor [21]. Throughout the years of JET exploitation, most of the design parameters were exceeded and after achieving all its initial objectives, JET was upgraded and modified to investigate the most promising regimes of operations and to perform comprehensive studies of heat exhaust techniques and plasma-wall interaction. JET also allows operation in Deuterium-Tritium. Its main features are summarized in table 1.3, a picture of it is shown in figure 1.16.

By virtue of its size, ITER-like geometry, large plasma current and unique capability to operate with tritium fuel and beryllium plasma facing components, JET is ideally positioned to advance the state of ITER preparations. In order to move in this direction a series of strategic upgrades are an integral part of the ongoing JET programme [22, 23].

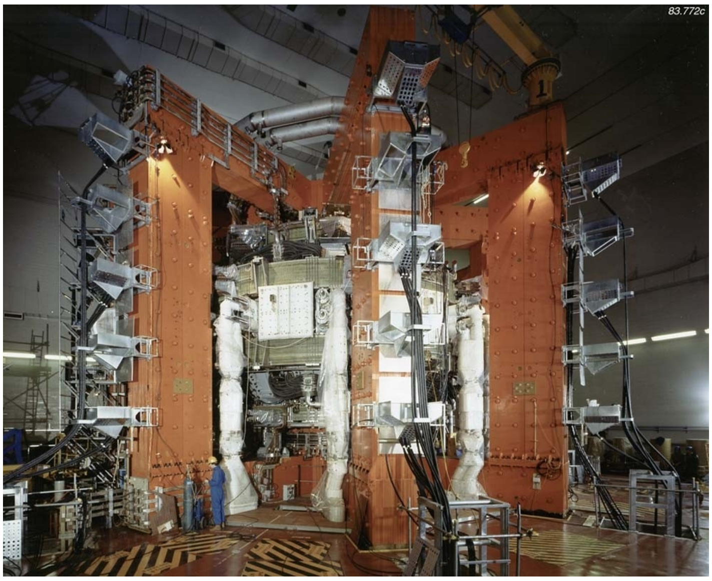

Figure 1.16: Picture of the JET experiments surrounded by plasma diagnostics.

JET	
Major radius	$2.96\,m$
Minor radius horizontal	$1.25\,m$
Minor radius vertical	$2.10\,m$
Plasma current	$6\,MA$
Toroidal magnetic field	$4\,T$
Plasma discharge duration	$up\,to\,20\,s$

Table 1.3: Main Parameters of the JET device.

Of particular interest for this thesis is the ITER-like wall (ILW) project [24, 25]. It is the principal experiment on plasma-wall interactions and plasma-compatibility with the material combination foreseen for the activated phase of ITER. In the new wall, the main elements in direct contact with the plasma are solid Be tiles, segmented to minimize eddy currents and castellated to avoid thermal stress cracking. Be-coated ($8\mu m$) Inconel is used for recessed areas of the inner wall subject to lower heat and particle fluxes and W-coated CFC tiles are used in a few areas of the first wall exposed to high power loads. W-coated carbon fiber composite (CFC) is also used for most of the divertor tiles. A picture of the first wall is given in figure 1.17. Sketch of the ITER and JET ILW first wall is given in figure 1.18.

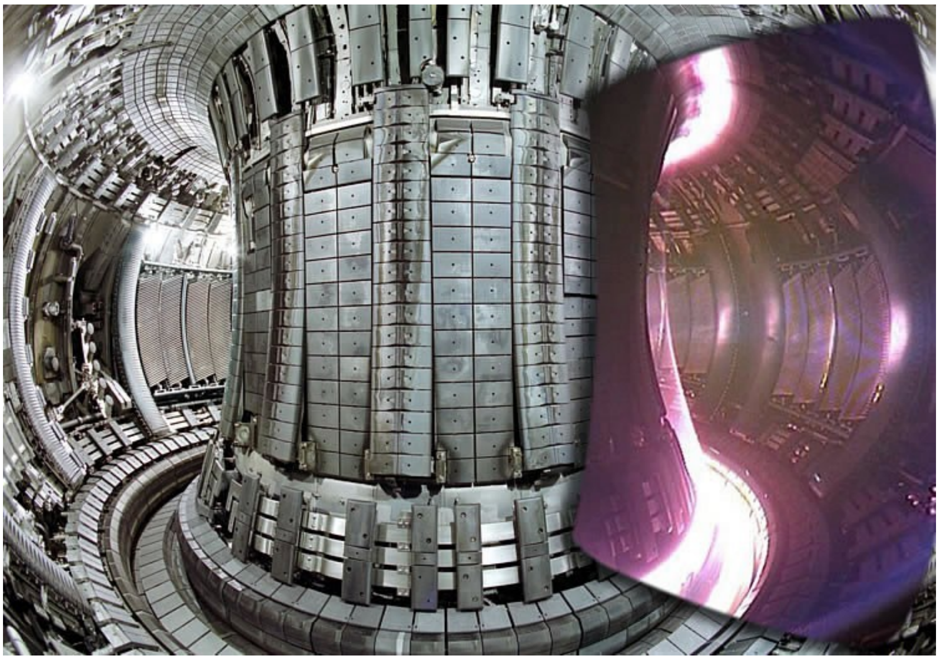

Figure 1.17: Picture of the JET first wall. On the right with plasma.

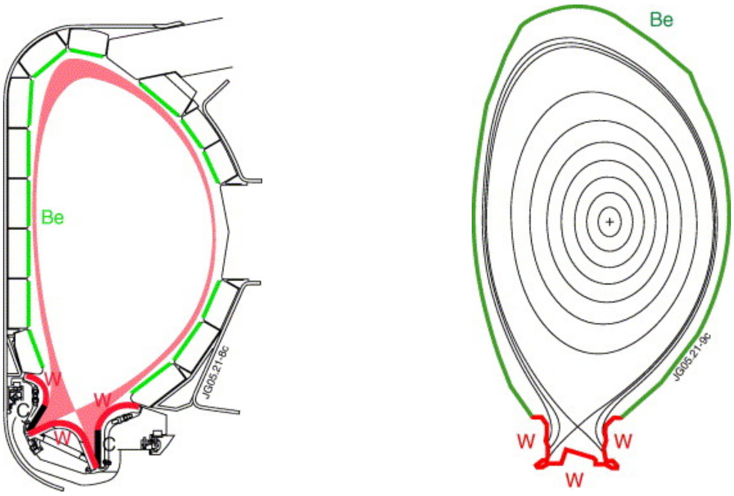

Figure 1.18: On the left the ITER primary materials choice, backup solution is an all tungsten divertor. On the right the JET configuration to test an all W divertor.

1.3.4 ITER

On November 21, 2006, the seven ITER members (European Union, Japan, Russian Federation, People's Republic of China, South Korea, India and United States of America) formally agreed to fund the project of the **I**nternational **T**hermonuclear **E**xperimental **R**eactor [26], a burning plasma experiment based on the tokamak concept.

It is designed to have $Q \geq 10$ that means to produce at least 500 MW of fusion power from 50 MW of input power, the first of all fusion experiments to produce net energy. ITER would also offer the possibility of studying several reactor relevant scientific and technological issues, which are beyond the present experimental capabilities. The main aims of ITER are:

- the fusion of 0.5 g of deuterium/tritium mixture in its approximately 840 m^3 reactor chamber;
- to achieve extended burn in inductively-driven plasmas with $Q \geq 10$. This point must be demonstrated at nominal fusion power output of about 500 MW for a range of operating scenarios and with a duration sufficient ($\simeq$ 400 s) to achieve stationary conditions;
- to demonstrate steady state operation using non-inductive current drive with a ratio of fusion power to input power for current drive of at least 5;
- the possibility of higher Q operation exploitation, if favorable confinement conditions can be achieved.

A schematic of ITER is reported in figure 1.19, whose characteristics are summarized in table 1.4.

ITER	
Fusion Power	500 MW
Power Amplification (Q)	≥ 10
Major Radius	6.2 m
Minor Radius	2 m
Machine Height	26 m
Machine Diameter	29 m
Plasma Volume	837 m^3
Maximum toroidal field	5.3 T
Plasma Current	15 MA
Pulse length	$\geq 400\,s$

Table 1.4: Main Parameters of the ITER Tokamak.

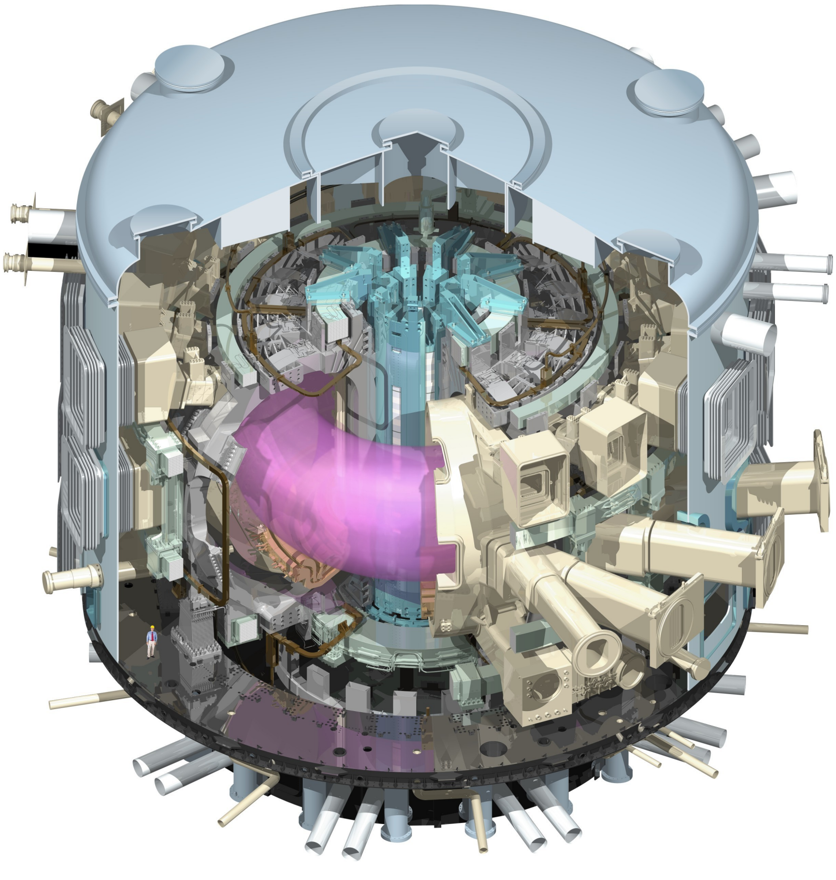

Figure 1.19: Schematic of ITER.

Edge Physics and Plasma-Wall Interaction

In magnetic fusion processes at plasma edge and plasma-wall interaction (PWI) play a crucial role for achieving a steady state burning fusion plasma. The helium-ash must be removed from the plasma and the first wall has to withstand and dissipate the α-particle heating power. Wall erosion affects its lifetime and releases impurities into the plasma, which then cause fuel dilution and energy loss due to radiation from the plasma. The wall may further act as a reservoir for the hydrogen fuel isotopes leading to an uncontrollable additional source of fuel atoms.

This chapter will provide an overview of the edge plasma physics to understand the work described in the following part of the thesis. In section 2.1 the main configuration of the edge are presented and the edge plasma region in contact with the wall, the so-called *Scrape-Off Layer*, is presented. Sections 2.2 and 2.3 will provide a description of the basic interaction process between plasma and material walls. Finally, section 2.4 will introduce the mains wall conditioning techniques.

2.1 Edge configurations

In the core region of the plasma, magnetic surfaces close on themselves. Charged particles move mainly along the magnetic field lines, due to the Lorentz force, and thus are confined on magnetic flux surfaces. This confinement is not perfect and plasma particles can diffuse by collisions and anomalous transport process toward the plasma edge. Outside the core region, the plasma particles move along open magnetic field lines and will mainly hit intersecting material boundaries. The region where the particles are "scraped" from the core plasma and directed toward the targets, is called *Scrape-Off Layer* (SOL).

In magnetically confined plasmas a nonlinear relation exists between the process occurring at the wall, the proprieties of the edge plasma and those of the main plasma. Examples of interlinked quantities are: the density and temperature profiles; the concentration and penetration depth of neutral hydrogen isotopes atoms and of plasma impurities into the SOL; the power flow in the edge and its radiated fraction [27]. This means that the SOL region gets very important in any devices since it acts as a “bridge” between the main plasma and the solid surfaces. Moreover the SOL region is directly related to the input power requirements compatible with the core confinement.

2.1.1 Limiter and Divertor SOLs

The simplest way to control the SOL region is to introduce a solid element inside the plasma, localizing the plasma surface interaction. The solid element, called *limiter*, can take several geometrical forms, such as an annulus or a portion of it in the poloidal direction (called *poloidal limiter*) or a protruding structure attached to the vessel in toroidal direction (*toroidal limiter*) or even an object inserted at a specific toroidal and poloidal position (*rail limiter*). In figure 2.1 there is a schematic representation of these three kind of limiters.

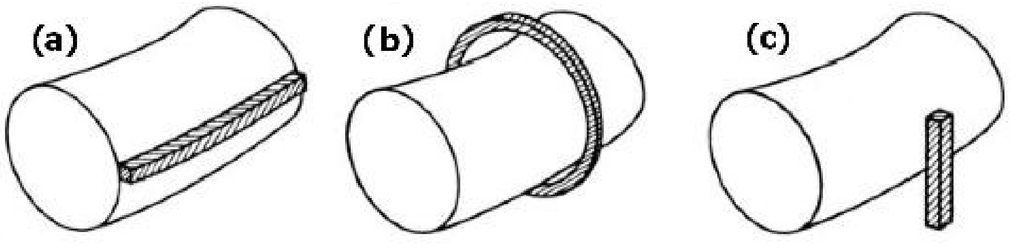

Figure 2.1: Schematic representation of different types of limiter: (a) a toroidal limiter; (b) a poloidal limiter; (c) a rail limiter.

The presence of a solid object defines clearly the Last Close Flux Surface, that is the last inner surface before the first one touching the limiter counting from inside. The LCFS therefore defines two regions, the main plasma inside and the Scrape-Off Layer outside, as it is schematically shown in figure 2.2.

The benefits coming from the presence of a limiter are mainly three: protection of the wall from plasma, localization of the plasma-surface interaction and localization of the main neutral particle source. For these reasons it is commonly made of refractory material, such as carbon,

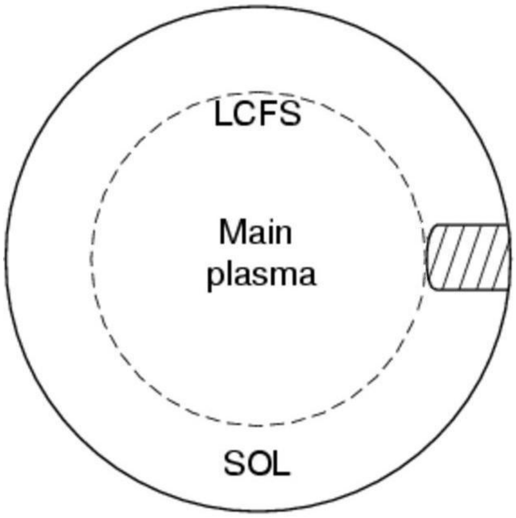

Figure 2.2: The presence of a limiter defines the LCFS, separating the main plasma from the SOL.

molybdenum or tungsten. A serious drawback of introducing a limiter is that neutral atoms sputtered from its surface are directed towards the center of the plasma, increasing the impurities content. To overcome this problem without waiving the benefits, mainly two solutions are adopted: wall conditioning and divertor configuration. The first one will be presented in section 2.4. The other solution is to move the region of the plasma-surface interaction away from the plasma core, to minimize the impurity content of the plasma by taking remote the main impurities source and by reducing the heat flux to target plates due to radiation losses. Since the approximately circular shape of the poloidal field in a limiter configuration is largely created by the plasma current I_P, an external conductor carrying a current I_D in the same direction as I_P can modify it to a figure-of-eight shape. The configuration so produced is called *poloidal divertor configuration* and it is shown in figure 2.3.

At some point between the two current centers a null in the poloidal field, and thus a magnetic *X-point*, exists. The magnetic flux surface passing through the X-point is called the magnetic *separatrix*. The location of plasma-surface interaction is achieved simply by introducing a solid surface which cuts through the flux surfaces surrounding the I_D channel. In this way it is created a region of closed flux surfaces inside the separatrix surrounding the I_P channel and containing the *main plasma*. The separatrix is therefore the Last Close Flux Surface and the field lines outside from the separatrix are open field lines directly connected to the

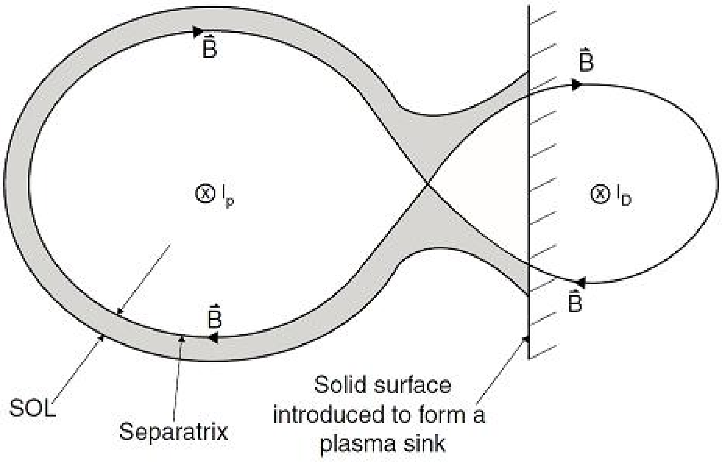

Figure 2.3: The poloidal field $\mathbf{B}_\theta^{plasma}$ created by I_{plasma} is diverted by the $\mathbf{B}_\theta^{\mathbf{coil}}$ created by a divertor coil current I_D parallel to I_{plasma}.

solid surface, called *divertor targets* creating the SOL. It is moreover created another region below the X-point and inside the separatrix at the bottom of the vessel. This region is called *private plasma.* A schematic representation is given in figure 2.4.

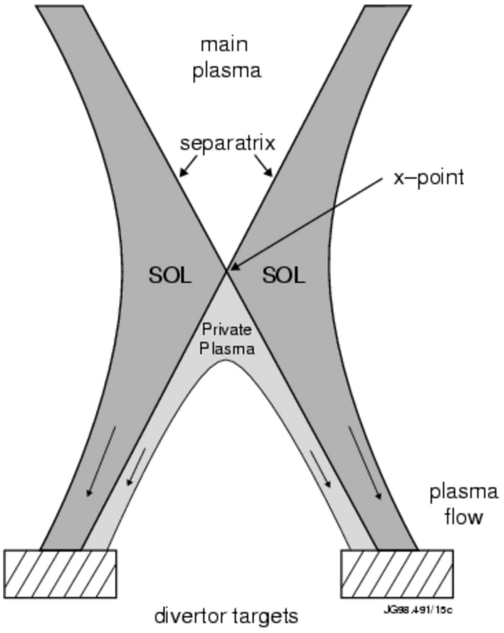

Figure 2.4: Enlargement of the plasma configuration near the divertor targets.

Studies done on divertor configurations show that this solution is very effective at screening impurities from the main plasma [28]. Moreover it has been discovered that such configuration has several other benefits, such as [29]:

- the access to regimes with low power load onto solid surfaces and low target erosion maintaining a good core plasma energy confinement
- the achievement of sufficient particle removing which is necessary for core plasma density control.

2.1.2 Main features of the Scrape-Off Layer

Solid elements which intersect the magnetic field serve as perfect plasma sink and impose a flow direct along the field lines. The flux tubes generated at each solid element are filled with plasma by perpendicular transport. This allows to reduce the transport inside the SOL to a 2-dimensional problem (see fig. 2.5):

1. flow along the field line;
2. diffusion in radial direction.

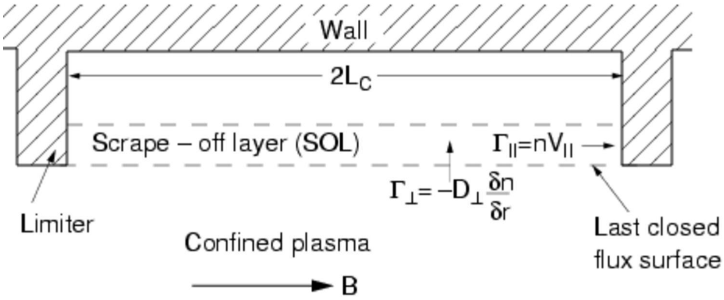

Figure 2.5: Schematic diagram of the plasma flow from the confined plasma into the SOL by cross-field diffusion and along the field in the SOL to the target.

Starting from this consideration, some features of the Scrape-Off Layer can be easily estimated, such as the thickness and the radial density variation. In steady state, if any other sources or sinks such as ionization are considered negligible in the SOL, the loss along the field from any given flux tube is balanced by the net flow across the field into the flux tube. The flux density coming from the core by cross field diffusion can be written as

$$\Gamma_{\perp} = D_{\perp} \frac{dn}{dx} \tag{2.1}$$

with $D_{\perp}$ the cross field diffusion coefficient.

Due to the plasma sink at the end of the field lines, a symmetric flow towards both ends develops. At the symmetry plane, called *stagnation plane* the parallel flow velocity $v_{\shortparallel}$ must be zero. At both the ends, considering the plasma quasi-neutrality ($n_e = n_i$), the plasma fluid velocity could not exceed the isothermal sound speed $c_s = [k(T_e + T_i)/m_i]^{1/2}$. Moreover the *Bohm criterion* [30] imposes that flow velocity at the surfaces always reaches sound speed, therefore the only possibility is that at both the ends the flow velocity is equal to the sound speed $v_{\shortparallel} = c_s$.

Scrape-Off Layer thickness

It is possible to relate the toroidal length of the flux tube, called connection length ($2L_c$), and the SOL thickness $l_{\perp}$ starting from the average transport velocities $v_{\shortparallel}$ and $v_{\perp}$.

$$\frac{v_{\perp}}{v_{\shortparallel}} \approx \frac{l_{\perp}}{L_c} \tag{2.2}$$

From the above considerations, the average velocities are:

$$\begin{cases} v_{\shortparallel} = c_s/2 \\ v_{\perp} = D_{\perp} \cdot \left(\frac{1}{n}\right) \frac{dn}{dx}, \end{cases} \tag{2.3}$$

with $dn/dx \approx n/l_{\perp}$. Therefore the SOL thickness is

$$l_{\perp} = \sqrt{\frac{2D_{\perp}L_c}{c_s}}. \tag{2.4}$$

Considering typical values, for example $D_{\perp} = 1\, m^2 s^{-1}$, $T_e = T_i = 25\, eV$ and $L = 50\, m$, the SOL thickness is $l_{\perp} \approx 4\, cm$. It means that the SOL is very thin compared to its length, and this comes from the enormous difference between $v_{\shortparallel}$ and $v_{\perp}$.

Radial density variation

Starting from the mass conservation along the flux tubes it is possible to calculate the radial variation of density inside the SOL. As already seen the loss along the field from any given flux tube is balanced by the net flow across the field into the flux tube, that means

$$\frac{d}{dx}D_{\perp}\frac{dn}{dx} = \frac{d}{dz}(nv_{\shortparallel}). \tag{2.5}$$

Considering the density constant along the flux tube and the increase of the velocity linear from zero to c_s the right hand side of 2.5 becomes $RHS = nc_s/L_c$. The density radial variation is therefore

$$n(x) = n_{LCFS}e^{-\frac{x}{\lambda}} \tag{2.6}$$

with λ the characteristic radial scale length of density, equal to

$$\lambda = \sqrt{\frac{D_{\perp}L_c}{c_s}}. \tag{2.7}$$

2.2 Recycling

In most device magnetically confined plasma have a duration at least one order of magnitude longer than the particle replacement time. This means that on average each plasma ion goes to the target and returns to the plasma many times during the discharge. A coarse idea of the process is briefly described below.

When a charged particle hit a solid surface it tends to stick to it a time long enough to recombine. Ions have a finite probability of backscattering from a solid surface and they do it usually as neutrals, picking up electrons from the surface. Electrons also stick to solid surfaces, thus a solid surface acts as an effective sink for plasma. It is not a mass sink since the particles hitting the solid surface are then released as neutrals. For solid surfaces which are insulator or electrically isolated, opposite charges build up on the surface exposed to plasma, quickly leading to surface recombination. The resulting neutral atoms generally are not strongly bound to surfaces. Then they are thermally re-emitted into the plasma where they can be re-ionized, usually by electron impact. A steady-state condition results when plasma charged pairs are impinged into the surface at the same rate as recombined neutrals re-enter the plasma. This process is called *recycling.*

A more detailed picture of the process is obtained considering that when a plasma ion or neutral arrives at a solid surface, it undergoes a series of elastic and inelastic collisions with the atoms of the solid. It may either be backscattered after one or more collisions, or slow down into the solid and be trapped. Trapped atoms can however reach again the plasma diffusing back to the surface of the solid. The ratio of incoming flux to the solid over that returning to the plasma is known as the *recycling coefficient.* The recycling coefficients can also be greater than one. It happens when the flux of particle and radiation coming from the plasma stimulate the releasing from the wall of gas which was previously adsorbed into it.

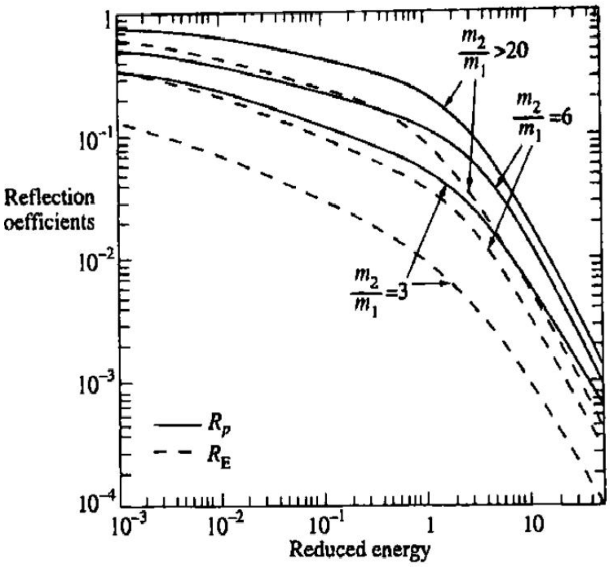

Figure 2.6: Particle and energy reflection coefficients of ions backscattered from solid surfaces as a function of reduced energy ϵ for three different ratios of the target to incident mass. The reduced energy is defined as $\epsilon = 32.5 m_2 E/[(m_1 + m_2) Z_1 Z_2 (Z_1^{2/3} + Z_2^{2/3})^{1/2}]$ where E is the energy of the incident particle [31].

The backscattering of ions incident on the surface depends on the ion energy and on the ratio of the masses of the surface atom and the incident ion. Important parameters to describe the recycling are the particle backscattering coefficient R_P and the energy reflection coefficient R_E. R_P and R_E are defined as

$$R_P = \frac{\text{number of reflected particles}}{\text{number of incident particles}} \tag{2.8}$$

$$R_E = \frac{\text{energy of reflected particles}}{\text{energy of incident particles}} \tag{2.9}$$

Values of R_P and R_E as function of reduced energy computed by Monte Carlo code simulations for a wide range of ion-target combination are plotted in figure 2.6 [8]. It shows that both particle and energy reflection coefficient increase with increasing mass ratio, as expected from momentum conservation.

Particles that are backscattered are predominantly neutral since incident ions normally pick up electrons from the solid. The average energy of the backscattered particles is determined by the ratio R_E/R_P, the mean energy being typically 30-50% of the incident energy [8]. The atoms which remain within the solid are placed either in interstitial sites or in defects in the material, such as vacancies. The behavior of the hydrogen during the diffusion depends on the heat of solution of hydrogen in the material. In the exothermic case there is a potential barrier at the surface preventing hydrogen atoms being released and therefore the hydrogen diffuses into the solid. In the endothermic case hydrogen atoms diffuse to the surface and escape from it after forming molecules by recombination.

In steady state the ion flux to the solid is balanced by the outflow. This outflow is determined by the diffusive flow towards the surface and the molecular recombination rate at the surface. In many practical cases a dynamic equilibrium is set up in which the recycled particles entering the plasma consists of $\sim 50\%$ backscattered atoms with energies lower than $5\ eV$ and $\sim 50\%$ of slow molecules with energies $\sim 0.03\ eV$. With light element wall materials the proportion of the backscattered particles as atom is lower, $\sim 30\%$ [8].

2.3 Impurity production

Particles escaping the plasma and hitting the wall will also remove neutral atoms from the wall material. Depending on the location of the surface and the plasma proprieties near the source, a certain fraction of the wall atoms will penetrate the plasma becoming ionized there. The presence of these impurities may severely degrade the plasma proprieties.

The next paragraphs will described the two main processes responsible for the plasma contamination: physical sputtering and chemical erosion.

2.3.1 Physical sputtering

The most important mechanism of impurity release is the physical sputtering since it occurs for all materials independently of the chemical nature, wall condition and wall temperature.

Physical sputtering consists in the removal of atoms from the surface of a solid as a result of impact by ions or atoms, giving rise to the presence of impurities into the plasma which cause power radiation from it. Of particular importance for impurity production is the fact that the plasma is a closed system with respect to impurity production. It means that the impurities generated by hydrogenic impact produce further impurities by physical sputtering, called self-sputtering, opening the possibility of catastrophic runaway erosion if impurities have sputtering yields (Y) exceeding unity. The sputtering yield is defined as

$$Y = \frac{\text{average number of sputtered particles}}{\text{incident ions}} \tag{2.10}$$

Physical sputtering takes place when an energetic ion or neutral atom hits a solid surface and the transferred energy from the incident particle to the lattice atom exceeds the surface binding energy. For central collisions, the fraction of the kinetic energy E_0 of an incident particle with mass m_1 which is transferred to a target atom with mass m_2 is given by $\gamma_{sp} = 4m_1m_2/(m_1 + m_2)^2$, thus the energy needed to transfer E_s to the target atom in a collision is E_s/γ_{sp}, with E_s the surface binding energy of the target solid. It is also necessary to take into account the reflection process, that is important mainly for light ions. It is done with an additional fraction of $(1 - \gamma_{sp})$. This leads to a threshold energy of

$$E_t = \frac{E_s}{\gamma_{sp}(1 - \gamma_{sp})}. \tag{2.11}$$

For most materials E_s is in the range $3.5 \div 9\ eV$, therefore for the same projectile mass the threshold energy is mainly determined by the mass of the target atoms.

Figure 2.7 shows the sputtering yields of different targets for bombardment with D atoms. Apart from the different dependence of the threshold energy from the mass of the target atoms, also the position of the maximum in Y increases with higher target masses.

2.3.2 Chemical erosion

Another erosion process occurs if the incident particles produce volatile compounds within the target material. Conversely from physical sputtering that can occur basically for all projectile-target systems, the formation of volatile molecules of the projectile with the target occurs only for some projectile-target combinations. One of the most interesting combinations relevant for a fusion device are carbon wall with hydrogen plasma or with

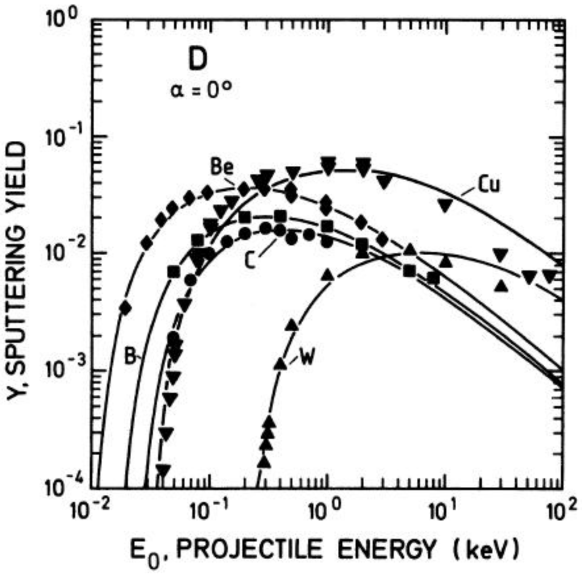

Figure 2.7: Sputtering yield Y of various target material for bombardment by D ions as function of impact energy.

oxygen as a plasma impurity. In the first case are produced methane and hydrocarbons while in the latter case carbon monoxide.

Formation of hydrocarbons by interaction of hydrogen with carbon materials (graphite) depends on a variety of parameters such as the target temperature, hydrogen impact energy and flux [32]. When hydrogen atoms of thermal energy ($E \lesssim 0.2eV$) impinge on carbon materials several kinds of hydrocarbons can be formed. The reaction rate depends on the structure of the carbon surface layer. Crystalline graphite has a reaction rate smaller than $10^{-3} eroded\, carbon/H(or D)$, but the yield increases when the surface is damaged. The highest yields (up to 10^{-1}) are obtained on amorphous carbon layers which are obtained by chemical plasma deposition [33].

The main reaction products under thermal hydrogen exposure are C_2H_x hydrocarbons, followed by the CH_3 and higher hydrocarbons. When hydrogen ions impinge on carbon, the hydrogen ions penetrate in the solid. Saturated CH_4 molecules are formed at the end of the trajectory. Molecules then diffuse through the graphite back to the surface.

When the ion that impinges with carbon materials is oxygen, it can lead to the formation of CO and CO_2. It happens with an overall yield ($CO + 2CO_2/O$) near unity. The reaction of oxygen to CO and CO_2 plays an important role in the complex processes in plasma wall interaction. It is the cause of the presence of additional carbon impurities into the plasma.

2.4 Wall conditioning

In normal vacuum conditions the first wall surface is covered by a thin layer of adsorbed gas coming from the surrounding atmosphere. The adsorbed atoms have binding energies from $0.3 \div 3\ eV$ [8]. The weakly bound species can be removed thermally.

In this way hydrogen can be adsorbed on the surface, and the typical adsorbents are impurity species such as carbon monoxide and water molecules. This gives reason to the presence of carbon and oxygen as impurities in magnetically confined plasmas. Specially during the start-up phase of a discharge, being the wall covered with adsorbed gas, the various desorption processes can lead to levels of radiation from oxygen and carbon which prevent the possibility to heat the plasma. Moreover desorption can lead to lack of density control, if the desorbed particles are the same species of the main plasma.

Plasma-wall processes described above typically occurs in a region near the surface with a thickness of few tenth of nm. The physical and chemical structure of these layers have a significant influence on the plasma-wall interaction processes and consequently on the whole plasma performance. Techniques to clean and to coat the surfaces have been therefore developed, leading to a significant improvement of plasma performance.

These techniques are usually referred to as *wall conditioning* [27]. They include:

- using a variety of plasma discharges to remove the adsorbed gas from the wall, known as *cleaning discharges*;
- covering the wall with a low Z film such as boron or carbon, known as *boronization* and *carbonization.*

The cleaning discharges can be of various types, such as glow discharges or pulsed discharges. In each case the aim is to optimize the removal of the adsorbed particles by energetic ions, neutrals or electrons. These processes are more effective than simple thermal desorption because more energy is transferred to the adsorbed species. Glow discharge cleaning (GDC) is the most widely used technique.

Although many gases have been tested for discharge cleaning, the light ions H and He have generally been used as this reduces sputtering of the substrates, which can lead to thin films of sputtered material being deposited on windows and insulators. When using hydrogen, surface cleaning is enhanced by chemical action with the formation of hydrocarbons together with H_2O and CO, that can be pumped away. In systems with mainly carbon walls, GDC in helium has been found to release oxygen, usually by forming CO. He GDC also desorbs implanted hydrogen isotopes in the wall, thus reducing recycling.

The aim to coat the walls with low Z films is to minimize the release of high Z impurities. Boronization is performed introducing into the vacuum vessel, usually at about $\sim 400^\circ\ C$, boranes such as B_2H_4 and B_2H_6. They thermally decompose and deposit a layer of boron on the wall. Boron acts as a getter and thin boron films pump both oxygen and hydrogen [8, 34, 35, 36, 37, 38]. If a lower vessel temperature is used the rate of decomposition of the gaseous boron compound is decreased. It can however be enhanced by using a glow discharge. Carbonization is similar to boronization, introducing in this case gaseous carbon compound such as methane.

An example of a wall conditioning sequence is reported in figure 2.8, where there is a scheme of a typical boronization performed on RFX-mod [38]. At the beginning the temperature of the vessel is raised up $170 \circ C$ and for 4 hours the contaminating atoms are removed from the tiles and pumped out. H_2 GDC is then performed for 30 hours to remove oxygen from the tiles, followed by 6 hours of He GDC to remove the H_2. After other 15 hours to pump out the helium, a mixture of diborane (B_2H_6) at 10% and helium at 90% is introduced for a variable time depending on the desired thickness of the deposited layer. The sequence ends with other 3 hours of He GDC to remove the H_2 coming from the diborane, other 15 hours to pump out the Helium and then the temperature is decreased again to room temperature.

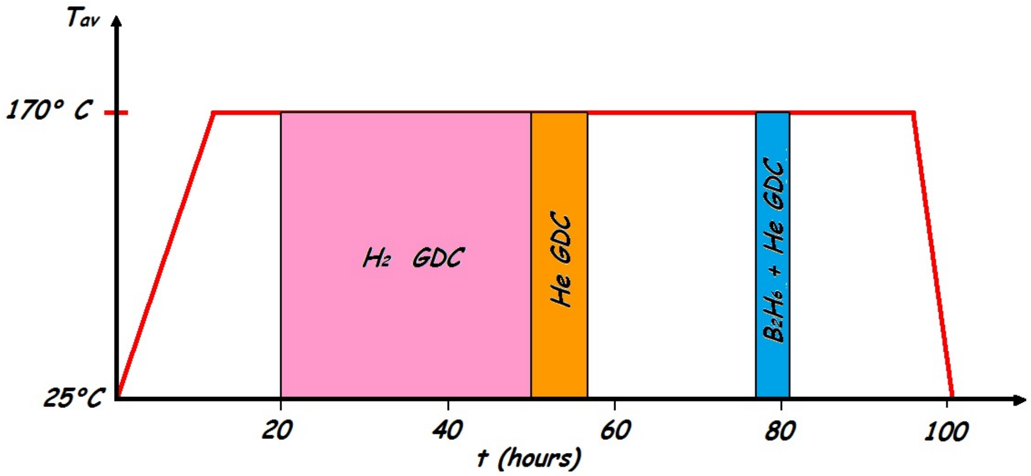

Figure 2.8: Scheme of a typical boronization performed on RFX-mod.

Room Temperature Pellet Injection in RFX-mod

In this chapter will be described the work performed to provide RFX-mod with a device that allow to inject impurities on RFX-mod and tools to control it. Impurity pellet injection has mainly two aims: transport studies and first wall conditioning. The main advantage of impurities injection by means of pellets is the possibility of performing a controlled impurity introduction with well known space and time deposition. This is useful both for transport studies, because it provides the source terms in the transport equation, and for wall conditioning, to have a good control of the thickness of the layer deposed over the graphite tiles. In figure 3.1 there is a picture of a lithium pellet injection in RFX-mod.

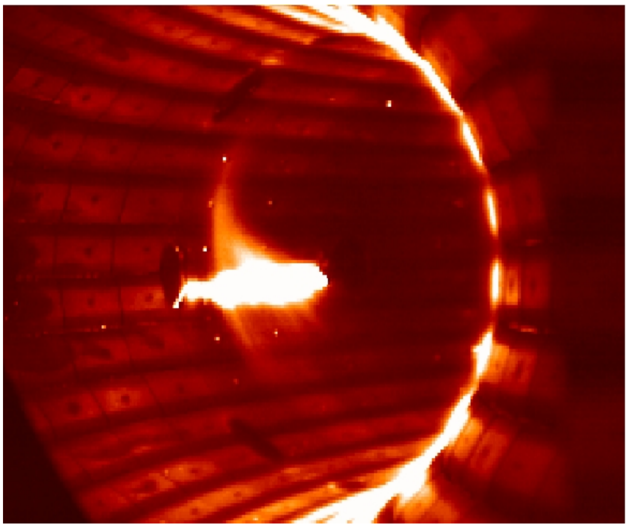

Figure 3.1: Lithium pellet injection seen by a CCD camera.

This chapter is organized as follow. In sections 3.1, 3.2 and 3.3 it is presented the work I have carried out on the optimization of the Room Temperature Pellet Injector (RTPI) [39] and on its installation on RFX-mod device. In section 3.4 the diagnostic system used to analyze the pellet penetration and deposition inside the plasma is described. In sections 3.5 and 3.6 is presented and then validated a model used to predict the pellet ablation rate in order to deposit the impurities at the right radial position in agreement with the injection purposes.

3.1 Room Temperature Pellet Injector optimization and commissioning

The RTPI allows to inject cylinders of any solid material at room temperature with length from $l \leq 0.1\,mm$ up to $l = 4.5\,mm$ and diameter from $\varnothing \leq 0.1\,mm$ to $\varnothing = 1.5\,mm$. A description of the injection technique adopted is the following. In the RFX-mod RTPI each pellet is contained in a sabot which is pneumatically accelerated along a barrel by a driver gas until it reaches a hollow bumper where it is stopped while the pellet continues in free flight with the same velocity as before the sabot-bumper impact. A scheme is shown in figure 3.2.

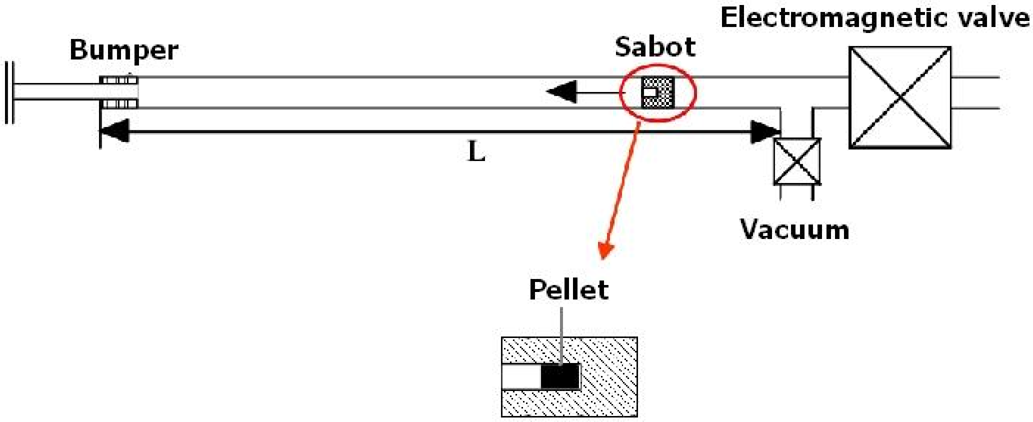

Figure 3.2: A sketch of the RTPI.

With this injection technique, the velocities are entirely determined by the sabot characteristics. Moreover, since the sabot remains in the barrel, a close tolerance between sabot and barrel diameter lets in principle only a small amount of the driver gas into the plasma. Since, as it will see in section 3.5, the required velocities are lower than the sound speed of the available driver gas, the velocity v of the sabot is simply given by

$$v = \sqrt{\frac{2pL}{\rho l}} \tag{3.1}$$

where p is the accelerating pressure, L is the length of the barrel, ρ and l are, respectively, the density and the length of the sabot.

The injector is made of three main parts: the sabot magazine, the gun and the sabot recovery system. The details of the magazine and recovery system are shown in figure 3.3.

The magazine is a vertical cylinder holding up to 25 sabots preloaded with pellets. The loader allows a full day operation because injection is limited to one pellet per discharge since sabot load and unload time is about $1\,s$ while RFX-mod pulse length is less than $0.5\,s$. Under the loader a hollow cylinder keeps the gun barrel vacuum tight. A loading mechanism based on a pneumatic transducer pulls back the cylinder and allows one sabot into a U-shaped lodging at the end of the barrel. The cylinder is then advanced to shut the barrel again and to push the sabot into the barrel. The sabot is accelerated by opening a fast electromagnetic valve which lets in the driver gas. To recover the sabot a second pneumatic transducer lifts the bumper and permits the expulsion of the sabot into a recovery box. This is obtained by a second release of driver gas at low pressure by means of the fast electromagnetic valve. To maintain the system in vacuum and to ensure a low injection of gas into the vessel the injector is pumped by means of two vacuum chambers pumped by a roots pump. The first vacuum chambers is connected to the system in the region of the gun and the second one after the bumper.

Some injector optimizations have been performed to obtain a good and reliable RTPI operation on the RFX-mod device. For example it has been necessary:

- to shield the valves from the magnetic field generated by RFX-mod;
- to cut the sabot barrel in four positions in the last $20cm$ to pump the driver gas directly from the barrel to reduce the amount of gas that reach the vacuum vessel;
- to experiment different sabot design and material in order to achieve velocities in the range $50 \div 200 m/s$, without the sabot getting stuck at the end of the barrel because of its mechanical deformation after the impact with the bumper.

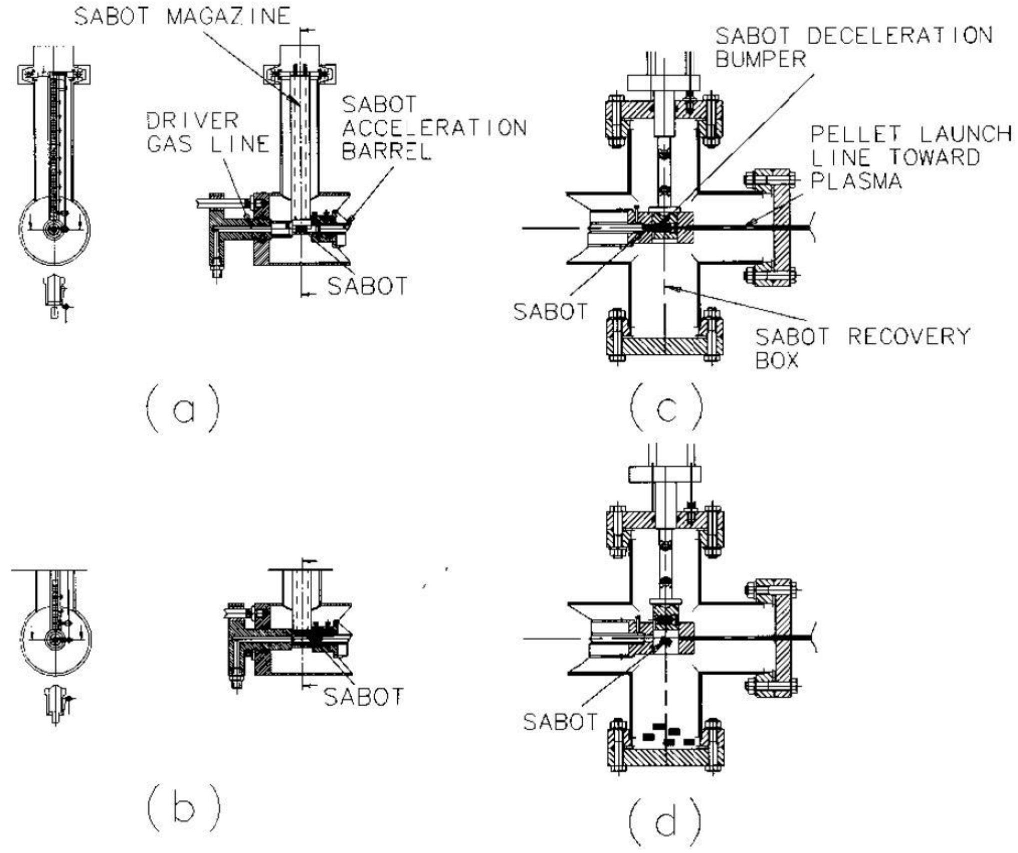

Figure 3.3: Detailed scheme of the sabot loader [(a), (b)] and of the recovery box [(c), (d)]. In (a) the cylinder is in the back position to let a new sabot in the barrel, in (b) the cylinder is in the forward position with sabot loaded and ready to be fired. In (c) the bumper is in the fire position to stop a sabot with the spring bumper, in (d) the cylinder is in the lifted position for sabot recovery.

A picture of the shape of the sabot chosen is shown in picture 3.4, where the central hole has different diameter depending on the size of pellet to be injected.

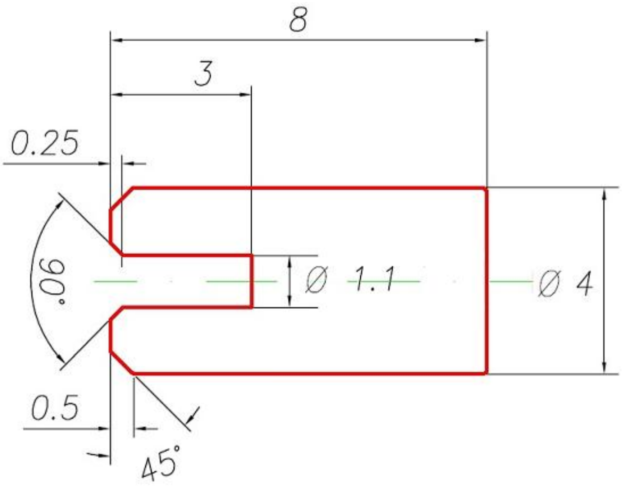

Figure 3.4: Drawing of the sabot used to accelerate the pellets.

3.2 Control system

The injector is operated by a compressed air circuit commanded by means of valves. It is shown in figure 3.5. Four valves (PV1, PV2, PV3, PV4 in the scheme) are devoted to move the loader and the recovery pneumatic transducers, two (PV5, PV6) are used to enable the presence of the driver gas in the line, two (PV8, PV9) are used to actuate the gate valves of the pumping system and one (PV7) to interface the injector with RFX-mod. There are two more valves that are needed in the driver gas system. One (PRV1) is a proportional valve used to set the launching pressure and one is the fast electromagnetic valve used to let in the driver gas. There is then a feedback system used to check the position of the movements by means of four limit switches and to check the achievement of the pre-programmed pressure by the proportional valve.

The whole control system of the injector is managed by a commercial board, the PK2120, a C-programmable controller based on the Zilog Z180 microprocessor [40]. The main features of the board required to control the injector are: a serial port to communicate with the RFX-mod central control system; ten digital outputs to control the valves; an analogical output to set the pressure of the driver gas; five digital inputs to control the state of the system; memory to record the control code.

A simple C based software has been developed on the board to remotely control the injector during the RFX-mod operations. The software has been written following three main purposes:

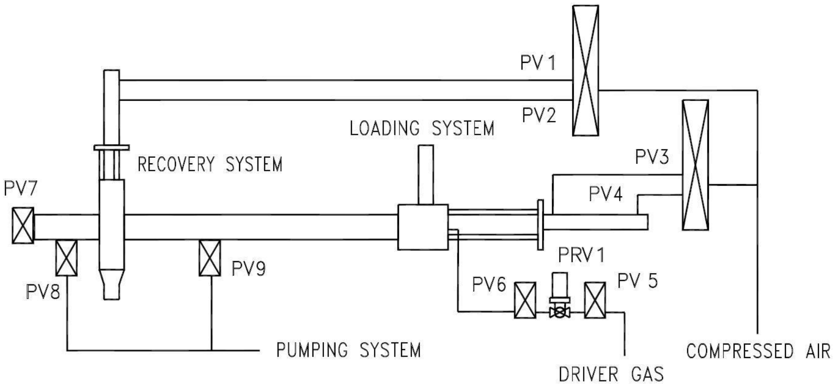

Figure 3.5: Schematic description of the compressed air circuit. PV1, PV2, PV3 and PV4 are the pneumatic valves used to move the loader and the recovery system respectively. The PV5 and PV6 are used to intercept the driver gas and to protect the proportional valve PRV1. PV7 is the valve that interfaces the injector with RFX-mod and PV8 and PV9 are the gates between the injector and the pumping system.

- to operate any mechanical part of the injector
- to be "*user friendly*" during the operations
- to avoid dangerous situations.

The first task is performed with a series of three commands, one to enable/disable each of the ten digital outputs, one to set the desired voltage to the analogical output and one to read each one of the digital input.

The second task has been implemented with a series of simple commands for the basic movements of the injector and four more complex commands to be used during the operations.

The simple commands are a short combination of opening and closing of the valves that move a single part of the injector, such as the commands *front* and *back* that move the loader piston forward and back respectively, or *up* and *down* to move the recovery piston up and down.

The four complex commands are: *enable*, *load*, *recovery*, *end*. The **enable** command opens the valves to pump the injector, set the drivergas pressure, moves the loader to be ready to load a sabot and moves up the bumper. It is used at the beginning of the operation with the injector. If everything works correctly the system reaches a "STANDBY" state. The **load** command is used to prepare a sabot on the barrel and move the bumper down. The comand can be executed only in the STANDBY state, and it brings the injector in the "READY TO FIRE" state. In this state the injector is ready to receive a trigger signal from the RFX-mod fast timing system or from the board to open the fast valve. The **recovery** command after a shot restores the initial situation by moving the bumper up, cleaning the barrel from the used sabot and bring the injector back to the STANDBY state. The last command is **end**. It is used at the end of the operation with the injector to close all the valves and to prepare the injector to be opened to refill the loader with new sabots and to empty the recovery box from used sabots.

This last command also prevents dangerous operations by checking the position of the pistons and the pressure of the drivergas. At each step the system controls if the actuators are in the right position and the drivergas is at the required pressure. If there is something wrong the system gives the “ERROR” message and the injector can be used only with the basic commands.

3.3 Lithium pellet production and storage.

Another important task to be developed has been the preparation of the lithium pellets. Based on experience gained on previous lithium pellet experiments like TFTR and Heliotron E [41, 42] care has been taken in pellet preparation to prevent contamination from impurities such as oxygen and nitrogen. Pellets are obtained by commercial lithium foils [43]. Lithium rods of the required diameter are obtained by extrusion and stored in mineral oil. Lithium handling is executed inside an inflatable glove-bag filled and continually fluxed with Helium to avoid contamination by oxygen. When new pellets are required the lithium rods are cleaned from oil, cut and inserted inside the sabots that are stored, for no more than 2 days, in an sealed box filled with Helium at a pressure of 2 *bar*. The charging of the RTPI with pellets is done in air, it requires about a couple of minutes and this is the only phase while Lithium pellets are exposed to the air, because in the RTPI they are maintained in vacuum of 10^{-7} *bar*. A first indication of the correctness of the method is obtained from the observation that pellets were gleaming at the time of insertion into the RTPI, which is a proof that lithium is not oxided. A more quantitative indication came from the measurement of the time evolution of oxygen and nitrogen line emission during pellet injection. The presence of such impurity in the lithium pellet would be detected by an increase of the intensity of their line emission, at least during the lithium pellet injection, indeed no increase of their emission has been ever observed. As example the lithization discharge #27757 is shown in figure 3.6, where there are not variations of the oxygen influx greater than the usual fluctuations.

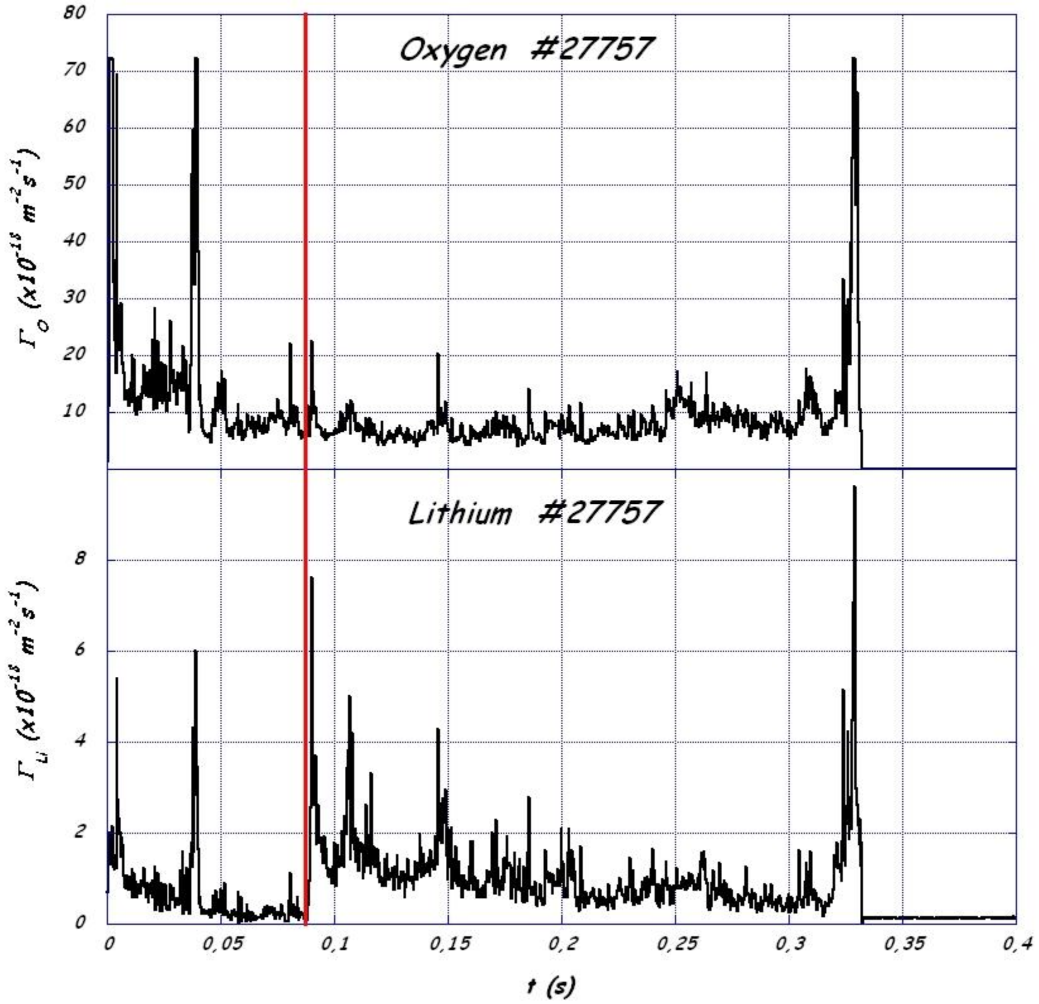

Figure 3.6: Oxygen and lithium influx during the discharge #27757 with lithium pellet injection at 90 ms.

3.4 Pellet trajectory reconstruction

Once a pellet is launched from the RTPI inside the plasma, it is important to monitor its trajectory, both to assist the optimization of the injection and for diagnostic purposes. To measure the trajectory it is exploited the radiation coming from the ablated particles surrounding the pellet, called *ablation cloud* (section 3.4.1). A system based on two absolutely calibrated two dimensional **P**osition **S**ensitive **D**etector (PSD) [44] is used to collect the emitted light (section 3.4.2), in order to have a high time resolution pellet position measurement by means of a simple data analysis (section 3.4.3).

3.4.1 Pellet ablation

As soon as the pellet enter the plasma, it is exposed to the energy fluxes carried by the plasma and it ablates at a rate depending on the energy flux available and the flux that is required to remove the particles from the pellet surface and dissociate, ionize and accelerate them [45]. In a time of the order of a microsecond the ablated particles form a cloud around the pellet, that acts as a shield from the incident particles, prolounging the lifetime of the pellet [46]. A schematic picture of what happens when the pellet is ablated is shown in picture 3.7.

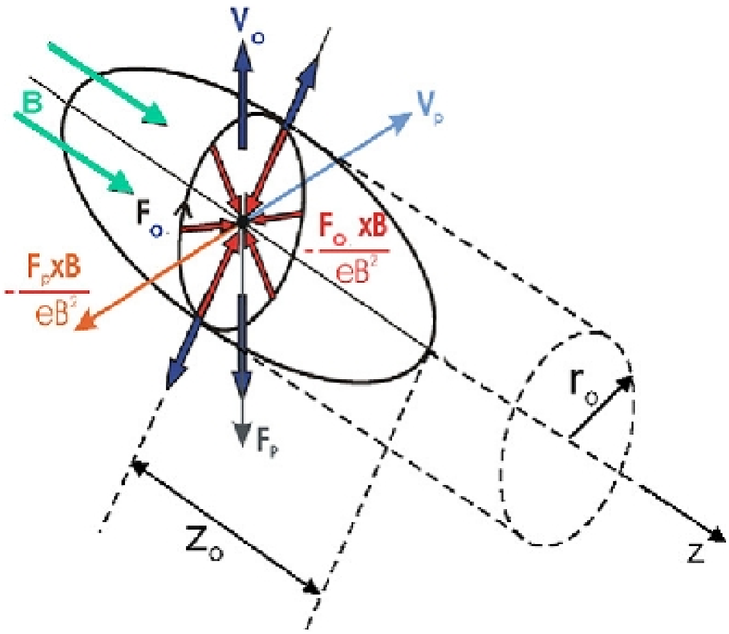

Figure 3.7: Schematic view of the cigar-shaped ablation cloud showing the different velocities and forces responsible for the full stop of the ablatant motion.

As long as the particles are neutral they follow the pellet with a velocity $\mathbf{v}_p$ and expand at a velocity $\mathbf{v}_0$. When the ablated particles are enough hot to be partially ionized, they experience the Lorentz force $\mathbf{F}_L = e \cdot (\mathbf{v}_p + \mathbf{v}_0) \times \mathbf{B}$. This stops the ablatant motion in the transverse $\mathbf{B}$ direction [47]. As a consequence the cloud expansion continues only in the magnetic field direction, resulting in the so called *cigar shaped* ablation cloud. In picture 3.8 on the left the H_{alpha} emission from neutralized Hydrogen is seen to be elongated along the magnetic field.

Moreover, due to the asymmetry of the electron and ion distribution function, there is an unbalanced pellet ablation in the two sides. This leads to a *rocket effect* that causes a pellet acceleration in the direction opposite to the side where ablation is stronger, see figure 3.8 on the right, described by

$$m_p(t)a_p(t) = \dot{g}^e(t)|v^e_{abl}| - \dot{g}^i(t)|v^i_{abl}|, \tag{3.2}$$

where m_p is the pellet mass, a_p its velocity, $\dot{g}^x$ and v^x_{abl} the erosion yield and the speed of the ablated particles, from electrons (e) and ions (i).

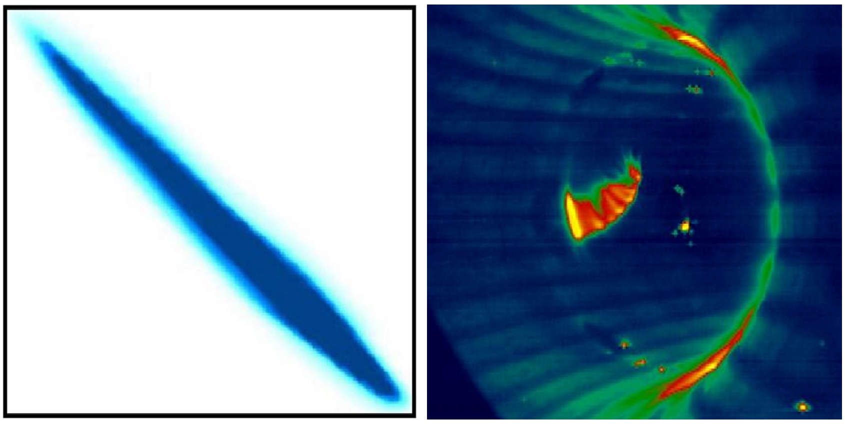

Figure 3.8: On the left a picture of the H_{alpha} emission from the ablation cloud of an Hydrogen pellet injected in the plasma, showing the cigar-shaped ablation cloud. On the right a picture of the pellet deflection due to the rocket effect.

3.4.2 The Position Sensitive Detector

The PSD is a square photodiode of $10mm^2$ with the back and front plane surface made of a resistive layer. The photoelectric current generated by the incident light can be seen as an input/output current on two electrodes placed at the sides of both photodiode surfaces (see figure 3.9). Due to the resistive surface layer, the current splits on the terminal of each surface proportionally to the distance of the light spot from the electrodes.

The spot position can be computed from the four currents by the relations:

$$x = \frac{I_{x2} - I_{x1}}{I_{x2} + I_{x1}} \frac{L}{2} \tag{3.3}$$

$$y = \frac{I_{y2} - I_{y1}}{I_{y2} + I_{y1}} \frac{L}{2}. \tag{3.4}$$

Each PSD is integrated with focusing optics (C-Mount lens with $25\,mm$ or $12mm$ focal length depending on the installation position), and amplifying

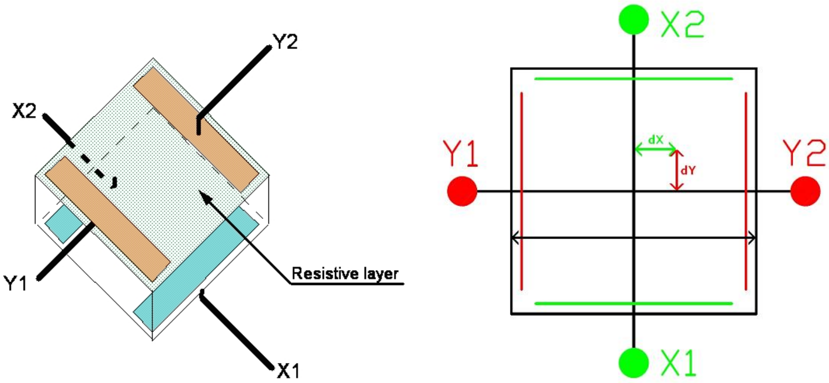

Figure 3.9: Structure of the two dimensional position sensitive detector on the left and its reference system on the right.

electronics. Two PSDs are installed at the pellet injection section, one looking at the pellet from behind, to have a measurement of the toroidal and poloidal deflections, one from the bottom, to have a measurement of the toroidal deflection and of the radial motion. The PSDs are arranged in such a way that the 3D volume defined by the intersection of the view cones of the horizontal and vertical PSD cover most of the possible pellet trajectories, as shown in figure 3.10. The device can also be used to obtain an absolute measurement of the light emitted by the pellet, after a calibration by means of an absolutely calibrated halogen lamp.

An example of the signal coming from the PSD is given in figure 3.11. The four channel are the voltage generated by the light in the four sides of the sensor illustrated in figure 3.9. The simplest way to check if the device is working properly is to look at the total current generated in the two sides of the sensor that should be the same, as shown in the plot on the right of figure 3.11.

3.4.3 Trajectory reconstruction

Starting from the measurement on the two surfaces of the PSDs it is possible to compute the three dimensional pellet trajectory inside the plasma.

On the surface of each sensor it is possible to set a reference system centered on the PSD center. In this system there is the measurement of the projection of the pellet position at each time. Therefore the projection in the three dimensional space is defined by the line passing through the point measured in the PSD and the lens focal point. Using two PSD, in theory, the pellet position is defined by the intersection of the two lines. Because of

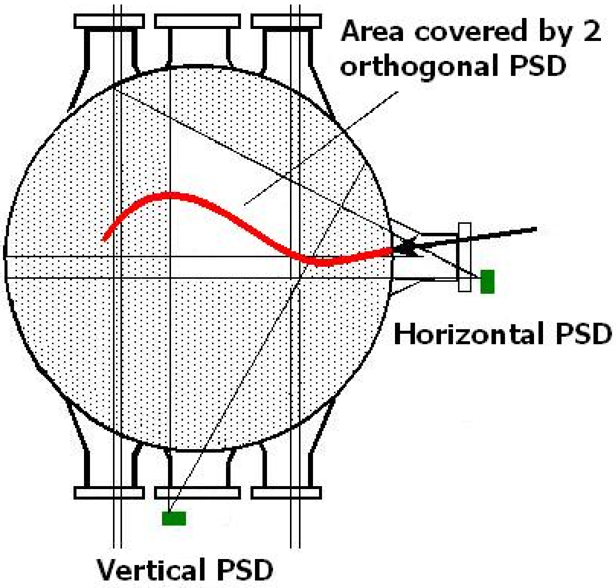

Figure 3.10: Poloidal section of RFX-mod at $\varphi = 262.5°$ in toroidal direction. It is represented an example of pellet trajectory and the system of two 2D-PSD to observe it with the view area covered.

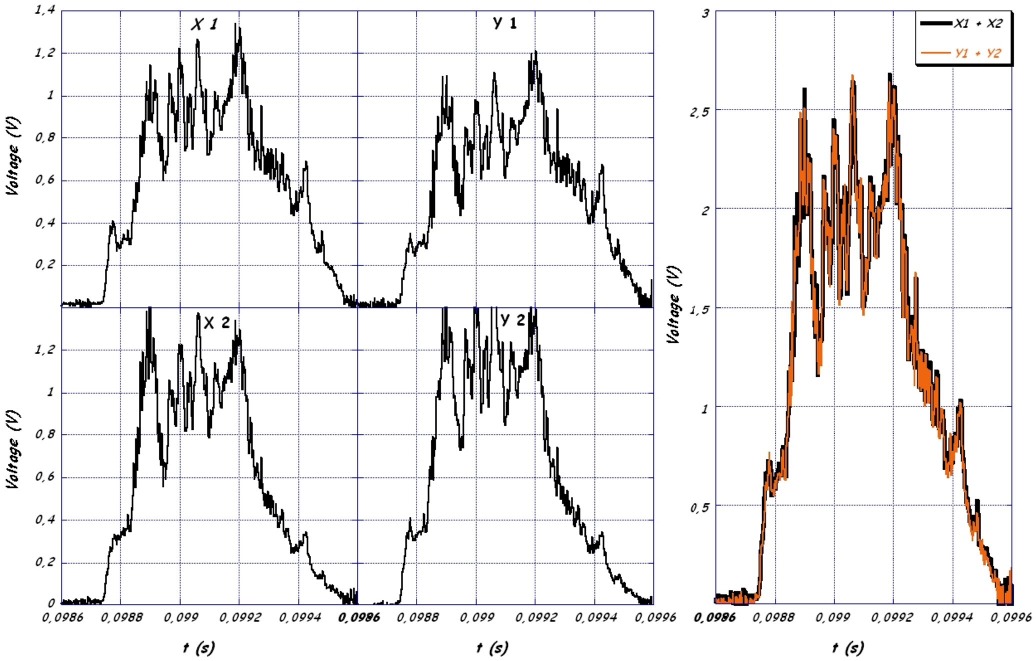

Figure 3.11: Raw signals of the four channel of a 2D-PSD during the pellet ablation.

the experimental errors the two lines usually do not intersect. To solve the problem the pellet position is assumed as the middle point of the segment perpendicular to both lines.

From mathematical point of view, the two lines that identify the pellet position projection are parametrized as a fixed point (the focal) and a versor. So the two lines are written as

$$\begin{cases} l_1 = \vec{F}_{s1} + \alpha\vec{\nu}_1 \\ l_2 = \vec{F}_{s2} + \beta\vec{\nu}_2 \end{cases} \tag{3.5}$$

where l_1 and l_2 are the two lines, $\vec{F}_{s1}$ and $\vec{F}_{s2}$ the two focal and $\vec{\nu}_1$ and $\vec{\nu}_2$ the two versors. The pellet position is the middle point of the shortest segment $\overline{HK}$ that connects the two lines. Being the shortest segment also the one perpendicular to both the lines, it is easy to find the values of α and β that identify the points H and K. Repeating the computation for each sample time in which the pellet ablation is detected by both the sensors it is possible to have a measurement of the pellet trajectory in the intersection of the two cones of view. In figure 3.12 it is given a graphical idea of the method.

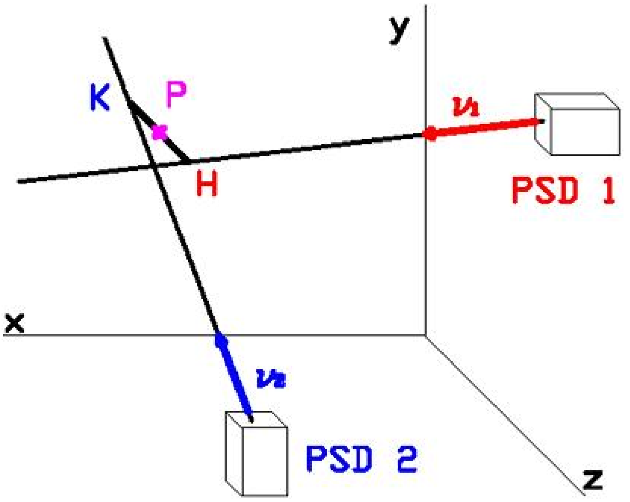

Figure 3.12: Pellet position P is calculated considering the projected position on the two 2D-PSD. Because of errors, the projections $\vec{\nu}_1$ and $\vec{\nu}_2$ do not intersect. The assumed position of the pellet is the midpoint of the segment $\overline{HK}$ perpendicular to both lines.

Trajectory reconstruction with 1 PSD

With this method the pellet trajectory can be reconstructed only where the two cones of sight intersect each other. As can be seen in figure 3.10 this is a small area with respect to the whole area of the poloidal cross section. To overcome this it is possible to assume that the pellet acceleration does not have a radial component, which means that the pellet inside the plasma mantains a constant radial velocity [44]. This is confirmed by the measurements shown in figure 3.13, where the pellet radial position measured with two PSDs is plotted as a function of time.

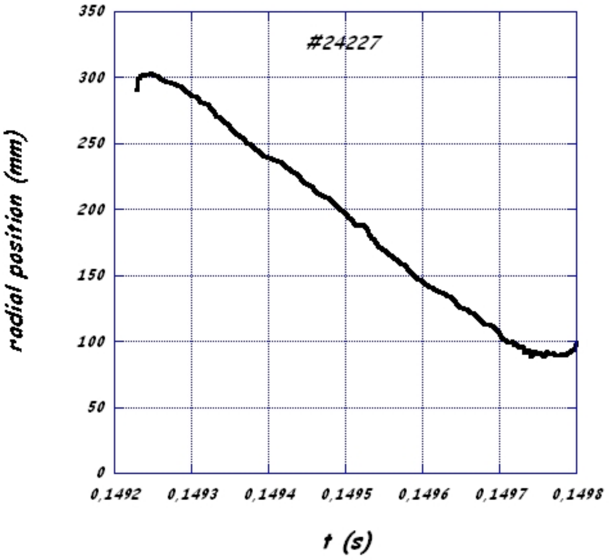

Figure 3.13: Pellet radial position as function of the time for the discharge #24227. It highlights as the pellet radial velocity is constant.

Since the radial component of the pellet distance from the RFX-mod geometrical axis decreases at a constant rate, whenever the radial component of the velocity is known it is possible to evaluate its trajectory using a single PSD that measures the poloidal and the toroidal pellet deflection. The injector is indeed equipped of two optical detectors that provide the measurement of the pellet speed, by which it is possible to evaluate the pellet radial position, while the poloidal and toroidal components are provided by the PSD looking the trajectory from behind. With this kind of reconstruction the trajectory can be computed in a wider area of the vessel with respect to that one with two PSDs. This is shown in figure 3.14, where there is a comparison between the two methods. On the left the poloidal deflection and on the right the toroidal one. In background the cones of view of the PDSs with respect to the cross sections, in green the trajectory evaluated using both the PSDs and in red the trajectory calculated using a single PSD supplemented by the radial pellet velocity. It can be seen that5 the agreement is quite good.

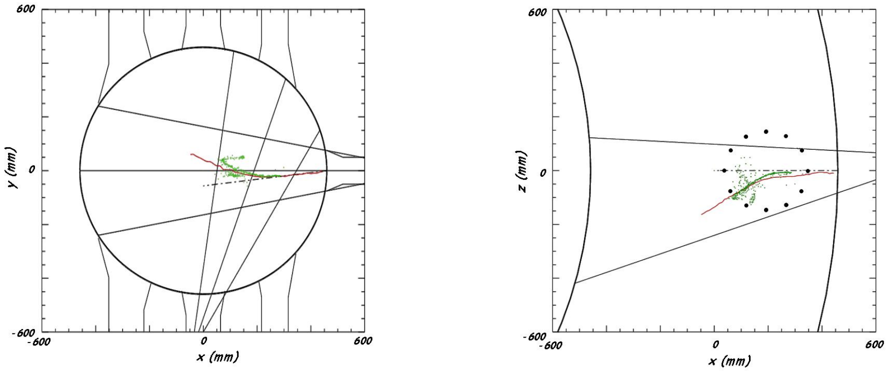

Figure 3.14: Comparison of the trajectory measured with one (red) and two (green) PSDs in discharge #24227. On the left the poloidal deflection, on the right the toroidal one.

3.5 Ablation code

An important requirement when injecting impurity pellets is their complete ablation to avoid the risk of polluting the vacuum vessel with pellet debris and to damage first wall tiles. Since pellet masses depend on the aim of the experiments, a simple model to predict the pellet ablation has been applied to compute the optimal speed. It depends on: the radial profiles of the plasma electron temperature and density; the kind of impurity injected; the pellet velocity.

The pellet ablation rate has been calculated using the model proposed by *Parks et al.* [48]. The model considers the incident heat flux, with the assumption that electrons from the background plasma stream towards the pellet along the magnetic field lines. If the pellet was not shielded by its ablation cloud, the heat flux directed from the plasma to the pellet averaged over its spherical surface would be given by $f_B \cdot q_\infty$.

The coefficient f_B accounts for the fact that the heat flux on the pellet surface is anisotropic in a magnetic field, and it is usually slightly larger than one-half [49]. The quantity q_∞ is the flux of energy crossing a plane perpendicular to the magnetic field lines asymptotically far from the pellet.

In case of Maxwellian electrons it is:

$$q_\infty = \frac{1}{4} n_e v_e (2T_e) \tag{3.6}$$

where n_e and T_e are the background electron density and temperature respectively, the product $\frac{1}{4}n_e v_e$ is the particle flux and v_e is defined as:

$$v_e = \sqrt{\frac{8T_e}{\pi m_e}}. \tag{3.7}$$

Since the pellet is shielded by the ablation cloud, the surface averaged heat flux on the pellet $< q >$ is given by

$$< q >= f_B \eta q_\infty \tag{3.8}$$

where η is the heat flux attenuation coefficient.

The same problem can be described also from a hydrodynamical point of view, where the ablation front moving into the pellet can be considered as a surface discontinuity, separating the solid and gas phases. The speed of the ablation front v_0 is also the pellet surface recession speed $v_0 = -dr_0/dt$. It is assumed that the ablation front overtakes the inward propagating heat conduction wave in a time much shorter than the total ablation time, so no incident flux is expected to heat up the interior of the pellet. To express the surface averaged heat flux on the pellet are considered: the conservation of mass, momentum and energy across the solid/gas transition layer; and the imbalance between the flux of atoms leaving the pellet surface and the flux of atoms returning from the vapor to recondense on the surface [48]. In this way it is possible to write $< q >$ as

$$< q >= n_0 v_0 (\Delta H + 2.7 T_1) \tag{3.9}$$

where n_0 and ΔH are respectively the solid density and the sublimation heat per atom of the pellet material and T_1 is the temperature of the ablated particles in the gas phase. For the isothermal transition layer assumption T_1 corresponds at the surface temperature of the pellet.

Coupling equations 3.8 and 3.9 the velocity of the receding pellet surface is

$$\dot{r}_0 = \frac{f_B \eta q_\infty}{n_0 (\Delta H + 2.7 T_1)} \tag{3.10}$$

An example of the application of the code is the computation of the optimal injection parameters in the wall conditioning case. The pellet size for wall conditioning is the maximum allowable with the sabot of the RTPI. They are cylinders with a diameter of 1.5 mm and a length of 4.5 mm, corresponding to a volume of about 8 mm^3 and a weight of 4 mg. The request for pellet speed and plasma parameters are such to provide a complete ablation of the pellet close to the plasma center. Considering as plasma parameters those of a typical medium current plasma discharge ($I_p = 1 \div 1.2 MA$, $T_e(0) = 700 eV$, $n_e(0) = 3 \times 10^{19}\, m^{-3}$) and radial profiles of the form

$$n_e(r) = n_e(0) \left[1 - \left(\frac{r}{a} \right)^{30} \right] T_e(r) = T_e(0) \left[1 - \left(\frac{r}{a} \right)^{4} \right] \tag{3.11}$$

the pellet velocity predicted for a complete ablation close to the plasma center is about $v_p \simeq 130\, m/s$. In figure 3.15 are shown the simulated ablation profiles, considering $f_B = 0.6$, $\eta = 0.6$, $T_1 = 0.35\, eV$, $n_0 = 4.64 \times 10^{28}\, m^{-3}$ and $\Delta H = 1.6\, eV/atom$. The pellet radius considered on the simulation is the equivalent radius defined as the radius of the sphere having the same volume of the pellet.

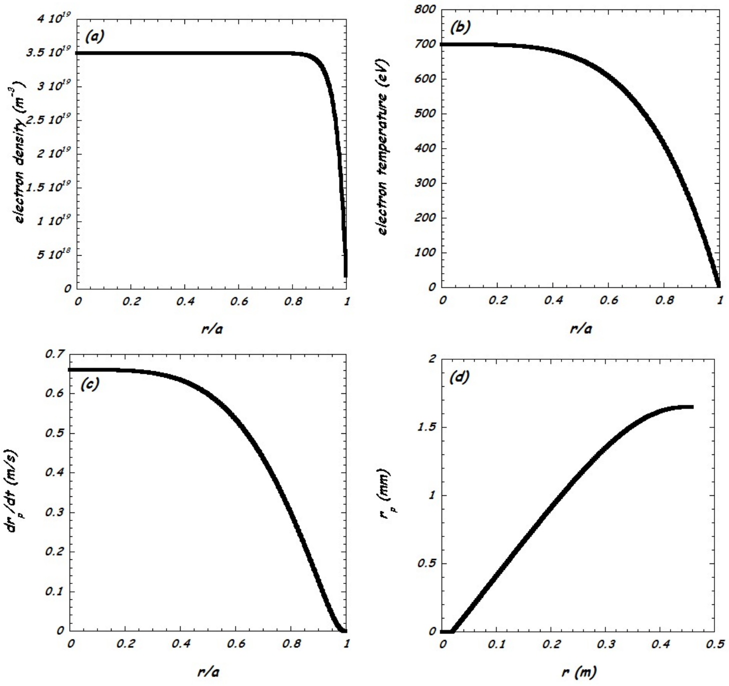

Figure 3.15: Ablation simulation of a Li pellet injected with a velocity of $v_p = 130\, m/s$. Plot (a) and (b) are respectively the electron density and temperature radial profiles of the background plasma, plot (c) the velocity of pellet ablation front and plot (d) the pellet radius as function of the distance from the torus geometrical axis.

3.6 Code validation

Measurements of pellet position performed with PSDs confirm that injected pellets with these parameters are completely ablated close to plasma center, as predicted by the code. An example of lithium pellet trajectory is given in figure 3.16 for the discharge #28005, from which it is possible to confirm the end of pellet ablation very close to the torus geometrical axis.

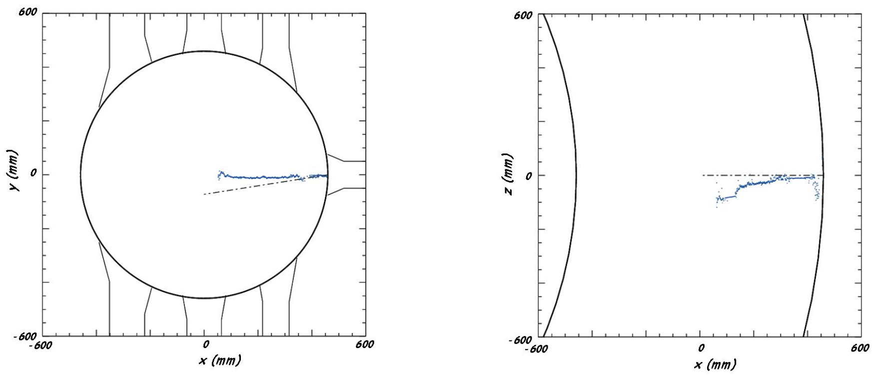

Figure 3.16: Trajectory of the lithium pellet injected in discharge #28005. On the left the poloidal deflection, on the right the toroidal one.

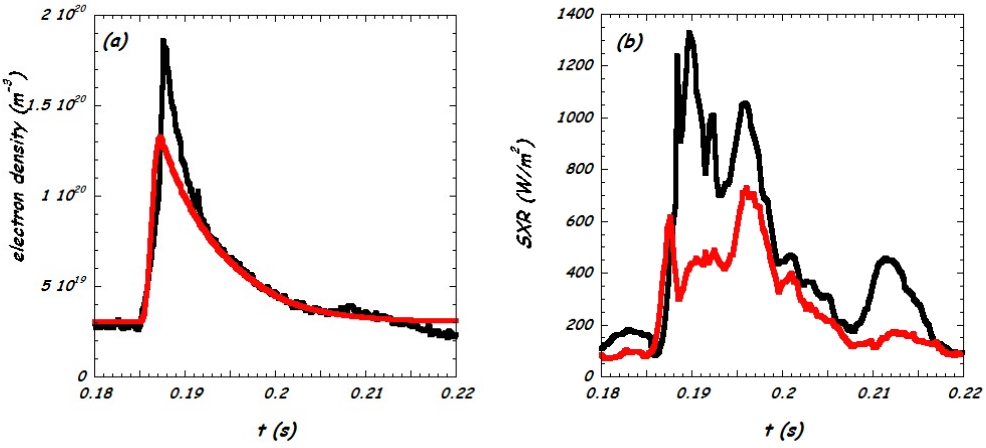

Figure 3.17: Comparison between the simulation (red) and the experimental data of discharge #28005 (black). In (a) the time evolution of the average electron density and in (b) the time evolution of the soft X-ray radiation around the injection time of the lithium pellet.

A further validation of the code comes from the first studies of impurity transport on RFX-mod, for which the results are compared also with the time evolution of the average electron density measured with the interferometer [50] (figure 3.17 (a)) and the time evolution of the soft X-ray radiation measured with the SXR tomographic diagnostic [51, 52] (figure 3.17 (b)).

In figure 3.17 it is seen that the prediction and the measurements of the time evolution of the electron density are in good agreement. The difference in the maximum value achieved can be referred to the technique used to produce the pellets described in section 3.3, that does not ensure a very accurate amount of lithium in each pellet, since it is not required for conditioning aim. The difference shown in the soft X-rays is still under investigation.

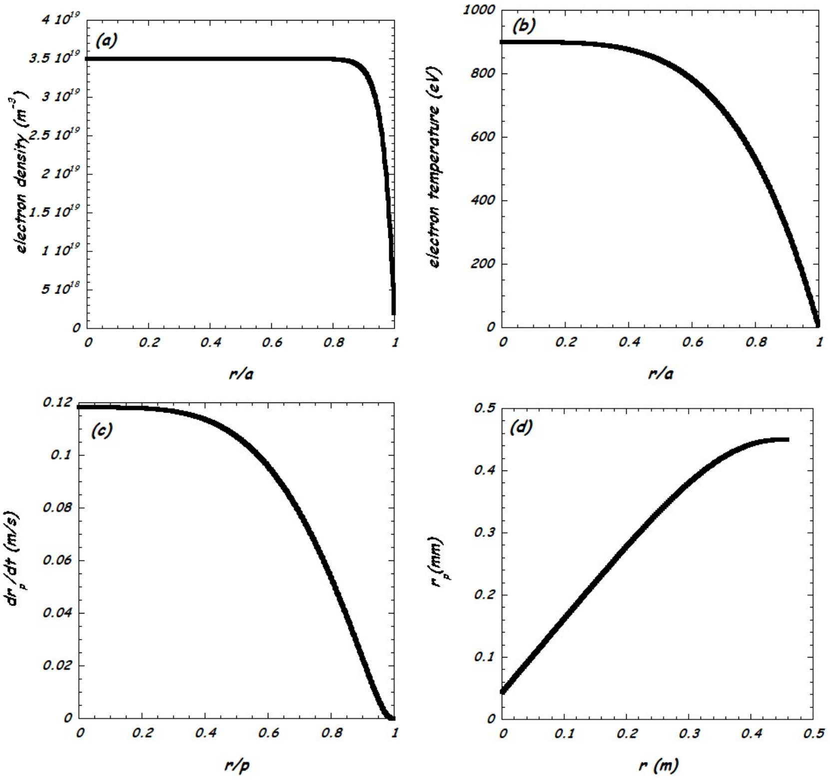

Figure 3.18: Ablation simulation of a C pellet injected of $r_p = 0.45\,mm$ with a velocity of $v_p = 100 m/s$. Plot (a) and (b) are respectively the electron density and temperature radial profiles of the background plasma, plot (c) the velocity of pellet ablation front and plot (d) the pellet radius as function of the distance from the torus geometrical axis.

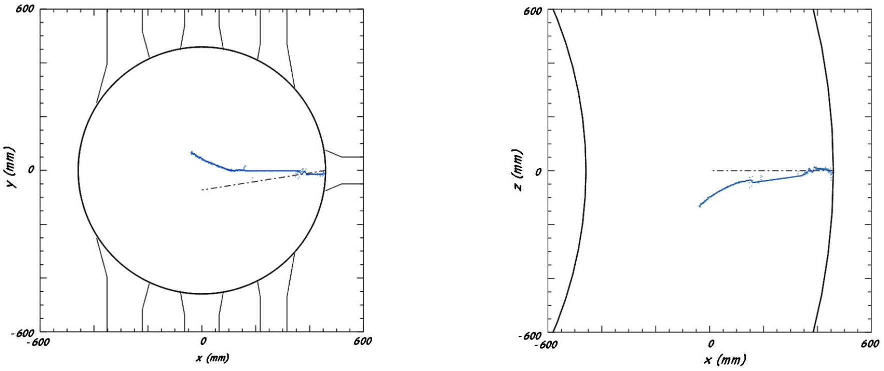

Figure 3.19: Trajectory of the graphite pellet injected in discharge #30305. On the left the poloidal deflection, on the right the toroidal one.

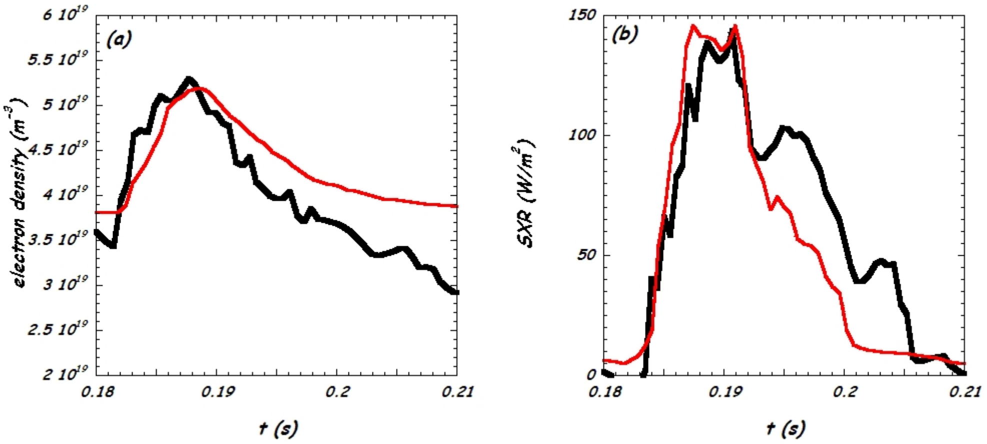

Figure 3.20: Comparison between the simulation (red) and the experimental data of discharge #30305 (black). In (a) the time evolution of the average electron density and in (b) the time evolution of the soft X-ray radiation around the injection time of the carbon pellet.

To study impurity transport on RFX-mod also carbon pellets have been injected by means of the RTPI. Since in this case the purpose of the injection is to study the impurity transport, an important feature of the pellet is that it does not perturbate the discharge, keeping the impurity concentration below 10% [39]. In figure 3.18 it is simulated the injection of a carbon pellet with an equivalent radius of $r_p = 0.45\,mm$ and a velocity of $v_p = 100\,m/s$, in a plasma with $T_e(0) = 900\,eV$, $n_e(0) = 3.5 \times 10^{19}\,m^{-3}$. The prediction also in this case is confirmed by the trajectory measured by the PSDs and shown in figure 3.19. It refers to discharge #30305, with the same $T_e(0)$ and $n_e(0)$

of the simulated one, in which a graphite pellet has been injected with a velocity $v_p \simeq 100\, ms^{-1}$.

As for the lithium pellet case, also in this case it is considered the time evolution of electron density (figure 3.20 (a)) and of soft X-ray radiation (figure 3.20 (b)). Differently from the previous case, here the electron density time evolution shows a very similar maximum value achieved and also a good agreement between the predicted and measured radiation from soft X-rays.

3.7 Conclusions

Purpose of the work described in this chapter is to provide RFX-mod with a device that allow to inject impurities on RFX-mod and tools to control it.

To do that a room temperature pellet injector designed for the old RFX experiment was optimized for RFX-mod and then installed on it. Once the injector was ready to inject impurity pellets it was also important to arrange a system able to monitor the behavior of pellets inside the plasma. The pellet trajectory is reconstructed by means of a 2D-PSD and two optical detectors. Before injecting pellets, to avoid the risk of polluting the vacuum vessel with pellet debris and to damage its tiles, a simulation of the pellet ablation was done, to have an indication of the optimum pellet mass and injection velocity.

Once that the whole system was ready several lithium and carbon pellets injection experiments have been performed confirming the proper operation of the system and the correctness of the ablation model.

RFX-mod Lithium First Wall Conditioning

In the experiments on magnetically confined plasmas first wall play a crucial role for the attainment of good plasma performance. Until now no tested first wall material proved to be able to face all the issues: low Z materials are reliable in terms of contamination but not of recycling control and gas retention, on the contrary high Z materials are not suitable to keep the Z in the plasma at low values. On tokamak [8, 34, 35] and on stellarators [36, 37] experiments, to improve the situation two solutions have been developed: wall conditioning [27] and divertor configuration [28]. The first one proved to be very effective particularly for high Z wall materials, since low Z coatings can keep to a low value the high Z impurity content, while the divertor proved to be useful for the achievement in tokamaks of the H mode improved confinement. Less effort on wall optimization has been spent for the Reversed Field Pinch (RFP) configuration; typically to decrease the device costs the RFPs use stainless steel or aluminum vacuum vessel also as first wall, sometimes adding some localized high or low Z limiters [53, 54]. Divertor solution is difficult to be implemented in the RFP configuration [55] because it implies an increase of the distance between plasma and the conductive shell, whose closeness to the plasma boundary is crucial for stability and edge error magnetic field reduction.

An example of RFP device where a greater effort was spent in wall optimization is RFX-mod. Here, following the good results obtained on Tokamak devices, were also performed lithization experimental campaigns. Aim of these campaigns was to perform the wall conditioning of RFX-mod first wall in a well controlled way. This would be done launching lithium pellets inside the plasma and letting the plasma itself to deposit a lithium layer over the carbon. Once that the whole system to inject room temperature pellets was ready it was therefore possible to perform the lithization on RFX-mod.

The beneficial effect of the lithization on plasma performance was immediately proved by the possibility to easily perform sequences of high current $I_p \geq 1.5\,MA$ discharges with a small amount of He GDCs to remove hydrogen from the wall. Moreover the lithization allowed to achieve for the first time in RFX-mod a plasma current $I_p \geq 1.9\,MA$ with an average electron density greater than $4 \times 10^{19}\,m^{-3}$ (figure 4.1).

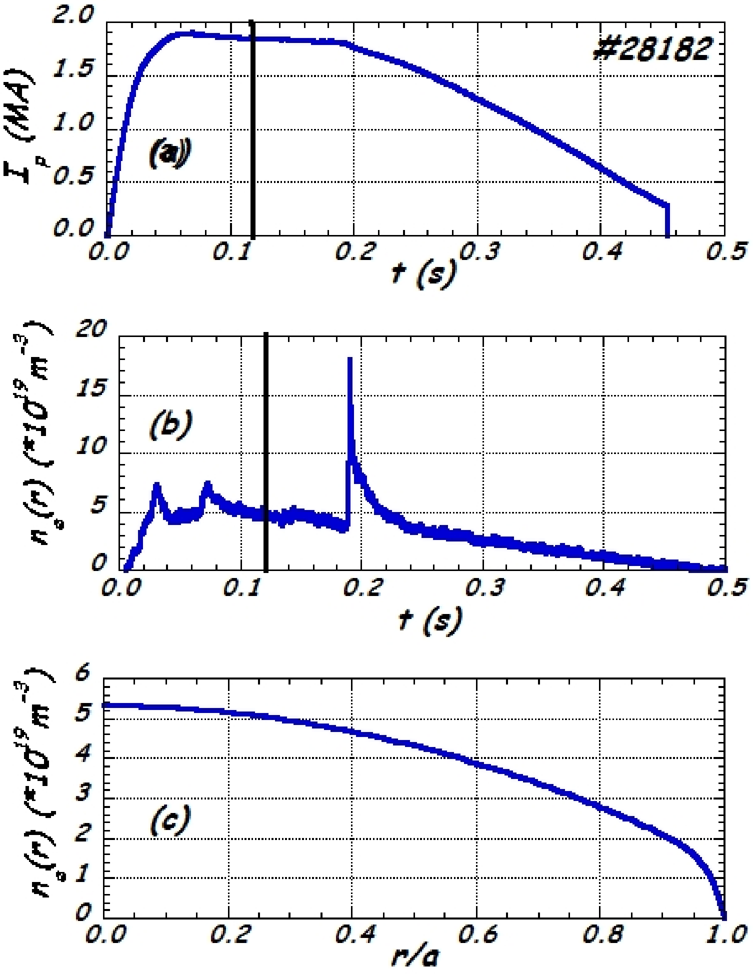

Figure 4.1: First nearly 2 MA RFX-mod plasma discharge: a) time evolution of the plasma current, b) time evolution of the electron density, c) radial profile of the electron density, with an average value of $< n_e > \approx 4 \times 10^{19}\,m^{-3}$.

In this chapter it will be presented the lithization experimental campaigns performed and the main effects of lithium wall conditioning on RFX-mod. In the first section 4.1 there is a brief overview of the wall conditioning performed on RFX-mod. In section 4.2 is described the optimization of the technique and plasma discharges used to perform the lithization. Then the first effect analyzed is the increasing of gas adsorption capacity of the first wall (4.3): after the lithization the interaction between the plasma and the first wall does not lead immediately to a loss of the density control like with a clean graphite first wall, making it easier to operate with a lithizated first wall. A particular attention was also devoted to study the reduction of the content of the two main impurities of RFX-mod, oxygen and carbon (4.4). Following the results of lithization on tokamak devices, the effects on the confinement times (4.6) and on the electron density and temperature radial profile were analyzed (4.5), with particular attention to the peaking factor and to the effects at the edge. Since the greater lithization effects have been found related to the edge, a deep analysis of the edge plasma parameters has been done, analyzing how it affects the edge transport (4.7).

4.1 Wall conditioning on RFX-mod

RFX-mod first wall is entirely covered by graphite tiles since it has been designed to operate at very high plasma current ($I_p \leq 2MA$). Graphite was chosen because it is a good solution in terms of allowed power load to the wall and impurity control. The allowed power load is very important aspect because RFX-mod can operate with ohmic input power of over 40 MW for about 0.5 s; furthermore in RFPs macroscopic deformations of the plasma due to MHD modes result in strong localized plasma wall interactions (PWI). This produces a high localized thermal power deposition, that in RFX-mod can reach values of the order of tens of MW/m^2 [56] In this framework the high sublimation temperature of graphite and the low Z of carbon help keeping low Z in the plasma. The main graphite drawback is the retained gas and consequent hydrogen recycling. Since at room temperature hydrogen desorption from graphite is very low, in the time interval between discharges hydrogen trapped during discharges is not pumped out. In a few discharges the plasma facing side of tiles becomes completely hydrogen saturated. After that graphite acts as a hydrogen reserve resulting in a hydrogen influx that depends only on the power load on the wall. The lack of influx control provides both operation and performance effects. In particular it prevents operation at a controllable density, especially at high plasma current ($I_p >$ 1.5 MA) when power load is very high.

To overcome the above limitation wall conditioning treatments between pulses and hot wall operation have been performed. Sessions of He discharges, helium Glow Discharge Cleanings (He GDCs), wall boronization [38] and wall baking are routinely used on RFX-mod, but none of them provided a conditioning valid over many discharges. Boronization coating is the most effective in controlling hydrogen influx over about 100 discharges [57] (the exact number depends on discharges characteristics: plasma current, duration, density value) but it is ineffective in modifying density profiles or significantly improving plasma performance. Boronization only slightly lowers the Z in the plasma, because it effectively reduces oxygen content, but carbon reduction is only partial and balanced by boron increases. Moreover it does not produce a significant energy confinement improvement because at low/medium density the energy loss associated to radiation is a small fraction ($\ll 10\%$) of total losses.

In the old RFX device (in operation from 1992 to 1999) it was possible to operate at a wall temperature of about $350°C$, providing in this way an empty wall at the beginning of each discharge since during the inter-discharge time interval the Hydrogen trapped in the wall was desorbed by graphite and pumped away. The hot wall operation is not any more allowed in RFX-mod because it is not compatible with its internal magnetic probes (maximum operating wall temperature is limited to $100°C$). In RFX the hot wall avoided wall saturation but introduced the problem of large density variation during the discharge often followed by a high density driven fast terminations. Indeed, in RFPs, empty graphite requires a high filling pressure to set-up the discharge and a high puffing flux to sustain the density. Because of the high quantity of injected particles the wall became filled by a huge amount of gas in the start-up phase of the discharge. Operating at $350°C$ the hydrogen is easily and suddenly released in presence of the localized plasma wall interactions (PWI). The situation is improved on RFX-mod because the feedback system of edge radial field [58] is able to strongly reduce the localized PWI.

To improve density control and plasma performance over those of boronization, the lithization technique was tested on RFX-mod, with the aim of reproducing the good results obtained on many tokamaks [59, 54, 60, 61], heliotrons [41] and stellarators [62]. Since it was the first time that lithization technique was applied in a RFP device, great care was taken to avoid irreversible problems with wall related to lithium conditioning. Indeed in RFX-mod there are three main problems related to lithization: (1) vessel windows are very close to wall radius and without shutters, which prevents using lithium evaporators because lithium coating would darken windows; (2) in RFPs the edge magnetic field is nearly poloidal and the connection length is very small, so a toroidally localized liquid lithium limiter can interact with a small toroidal angle of plasma; (3) in case of vessel venting to air lithium carbonate, forming on the surface of graphite wall, can not be removed due to the small size of vessel ports. For those reasons to gain experience on lithization technique and related problems, lithization conditioning was first tried by injecting solid lithium bullets, called *pellets*, since this technique allow to inject small and controllable amount of lithium and in case of deep pellet penetration provides an uniform toroidal deposition.

4.2 Lithium wall conditioning experiments

During the RFX-mod discharge the plasma interacts randomly with most of the graphite tiles of the first wall. To ensure that plasma interacts only with lithium it is important to ensure a uniform toroidal and poloidal deposition of it. From the pellet ablation simulations and the experiments done, it has been seen that the time needed to completely ablate the pellet (ablation time) is about $5\,ms$, while the time in which the ions coming from the pellet are confined in the plasma (deposition time) is about $20\,ms$. The long deposition time allows a uniform toroidal and poloidal lithium deposition. Indeed in RFPs devices there are large kinks perturbations due to the locking of the MHD modes that lead to a strong and localized plasma-wall interaction. This leads to a localized deposition where the plasma interact strongly with the wall. To spread toroidally the interaction in RFX-mod there is an edge radial field feedback system able to induce a rotation of the tearing modes with different phases. Using such feedback system the locking position, and therefore the position where the plasma interact strongly with the wall, changes continuously in time [58]. It follows that during the $20\,ms$ of the deposition time, the localized plasma wall interaction moves toroidally and poloidally providing a broad lithium deposition. The random rotation of the tearing modes that permits at plasma to interact with different first wall portion during the deposition time is shown in figure 4.2.

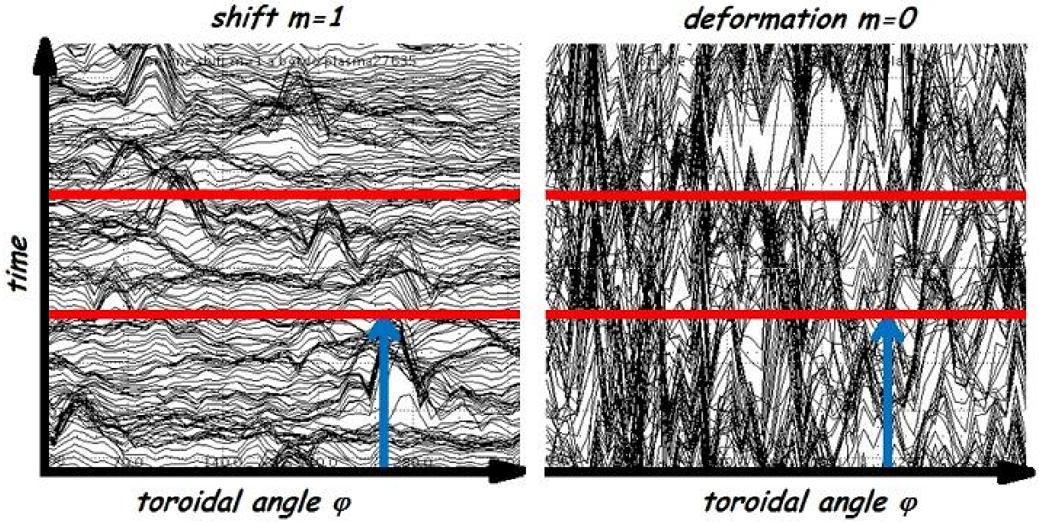

Figure 4.2: Radial displacement (a.u.) of the last closed magnetic surface due to m = 1 and m = 0 modes in shot #27635 as a function of the toroidal angle and of time (vertical direction). The red lines highlights the lithium deposition time, the arrows the toroidal position of the pellet injection.

Several experimental campaigns of lithium wall conditioning have been performed on RFX-mod. Every campaign included:

1. one or more of standard wall conditioning treatments (backing, boronization, He-GDC);
2. a sequence of medium plasma current conditioning discharges with lithium injection;
3. high plasma current discharges with or without lithium pellet injection to asses the characteristic of conditioned wall.

On each campaign about 60 conditioning discharge have been executed for a corresponding theoretical lithium thickness of about $10\,nm$ on the wall (considering all the injected lithium uniformly deposited on a smooth surface). Lithium campaigns have been performed both over clean graphite and over boronized graphite.

The first campaign has been devoted to optimize lithium conditioning discharges changing plasma target parameters and pellet injection time. To optimize target discharges, the LiI line intensity normalized by the S/XB factor [63] has been used as an indicator of lithium active on the wall. The S/XB factor denotes the ratio of the collisional ionization (S) to the excitation (X) rate coefficients, divided by the branching ratio B. The line intensity in absence of lithium sources in plasma (no pellet injection) is an approximation of lithium influx. Two LiI measurements have been used: the first one 90° toroidally from lithium injection position and the second one 180° toroidally away.

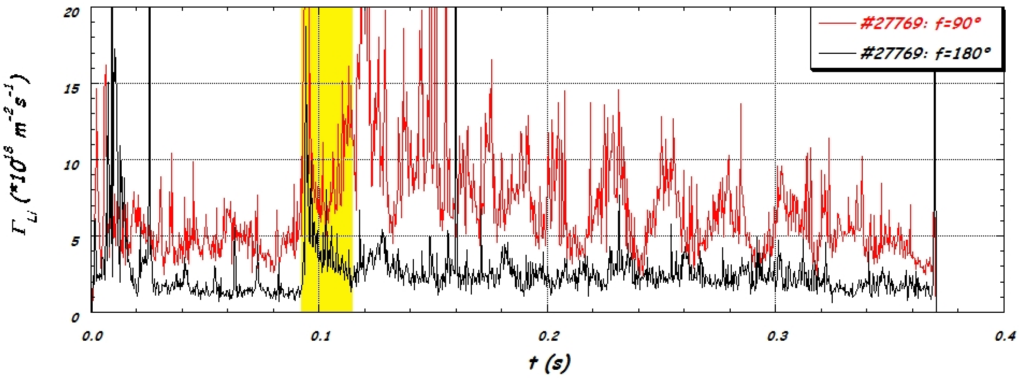

Figure 4.3: Lithium influx measured on two toroidal position: red/thin curve at 90° from injection section, black/thick curve at 180°. Yellow shaded region correspond to lithium pellet injection/deposition.

An example of the two normalized LiI intensity is shown in figure 4.3 for a discharge with pellet injection. The two measurements provide an indication of the toroidal symmetry of lithium deposition. The two measurements are not exactly equal but this can be expected due to: the different impact factor (distance from the geometrical axis) of the two lines of sight ($p/a = 0.8$ @ 90° and $p/a = 0.2$ @ 180°); the 90° line of sight is strongly affected by plasma-wall interaction because it looks directly to the wall; higher values are usually measured in RFX-mod for all influxes on external lines of sight on the low field side (like that one at 90°). Unfortunately there are not lithium sample deposition measurement available on two toroidal positions to confirm the influx measurement in terms of toroidal symmetry.

Initially Lithium pellets were injected on flat top of hydrogen plasma discharges, but with a few conditioning discharges the Li influx measured $50\,ms$ after pellet injection (to avoid LiI emission related to pellet injection) saturates to a value around $3 \times 10^{18}\,m^{-2}s^{-1}$, see Figure 4.4(a). Considering Li influx saturation as an indication of a sort of lithium "*removal*" and/or "*deactivation*" by hydrogen it has been tried to avoid these effects by injecting lithium pellets in helium discharges. Indeed with helium filling discharges a higher lithium influx has been been obtained as shown in figure 4.4(b). Furthermore, when there is no pellet injection, lithium influx decreases with about a constant rate: one half of the increasing rate

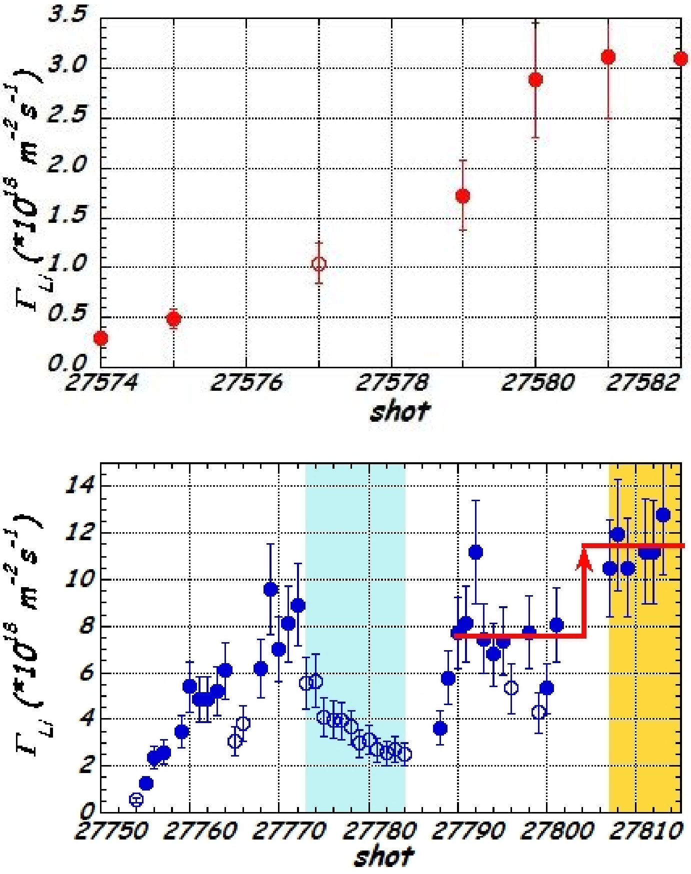

Figure 4.4: Li influx influx averaged in the $120 - 170\,ms$ time interval, measured injecting pellet on H discharges (a), He discharges (b). The error bars consider a 20% of error in calibration. Filled circles indicate discharges with Li pellet injection, empty cycles discharge without pellet injection. From pulse 27805 (yellow region) the duration of the discharges is decreased from $350\,ms$ to $250\,ms$.

observed with pellet injection (see open circles on figure 4.4 (b)). This means that on each conditioning discharge there is simultaneously lithium deposition and "*removal*"/"*deactivation*" with helium also. This suggest that reducing pulse length can reduce the deactivation phase. This was experimentally confirmed by the increased Li influx obtained by reducing the pulse duration from $350\,ms$ to $250\,ms$. This can be seen on the right side of figure 4.4 (b) where the yellow region indicates shorter helium discharges. The similar values of lithium influx measured on the first hydrogen discharges executed after helium conditioning ones confirms that moving to the discharges truly increased the amount of "*active*" lithium on the wall. This excludes the possibility that the larger lithium influx measured on helium discharges were due to the higher helium physical sputtering. A further advantage of helium discharges compared to hydrogen ones is their ability to extract hydrogen trapped on the first wall. Indeed, also after long He GDC (40 min - 2 hour), helium discharges extract a large quantity of hydrogen providing hydrogen depletion on a wall layer thicker than that provided by the He GDC. From DESOsorption diagnostic [64], which measures the total amount of gas filled-in and that extracted from the vessel, a hydrogen fraction of $20 \div 50$ % of the filled-in helium is estimated to be extracted on each helium discharge.

The described behavior is similar to that observed with lithium pellet experiments on NSTX [65]: on helium discharges the lithium influx increases with the amount of injected lithium while the hydrogen content on the wall is reduced. The presence of hydrogen on filled-in helium discharge can also explain the lithium influx decrease when no lithium pellet is injected: as for the standard hydrogen discharges the high fraction of hydrogen in the helium discharges provides lithium "*deactivation*". In RFX-mod there is not any measure to infer what the physical mechanism of such "*deactivation*" is, but it is possible to associate it to the formation of stronger Li bonds that Allain and Taylor [66, 67] have related to Li-O-H and Li-C-H formation.

Lithium "*removal*" from the vessel can be excluded by measures executed on graphite samples [68] exposed during lithium campaigns. Depth profile measurement of the present species on several samples facing the plasma was performed by SIMS (Secondary Ions Mass Spectrometry). The result of the analysis is shown in figure 4.5. Black and blue lines refers to samples exposed to plasma in the campaigns respectively before and after lithium pellets injection. Red line refers to a sample inserted during He discharges with injection of lithium pellets. Green one refers to a sample exposed during the He discharges with lithium pellet injection and the following campaign of H discharges without lithium pellet injection. Lithium signals for all the four samples are normalized to the oxygen one. The depth profile measurements show a similar amount of lithium on samples inserted during lithium pellet injection on helium plasma conditioning discharges and after high current hydrogen discharges when measured lithium influx was small (red and green lines respectively). Furthermore lithium is present and increases with the number of lithization campaigns in samples not exposed during pellet injection indicating an increasing quantity of lithium recirculating in plasma (black and blue lines) due to the lithium on the graphite wall.

The presence of lithium on a depth much higher than the thickness

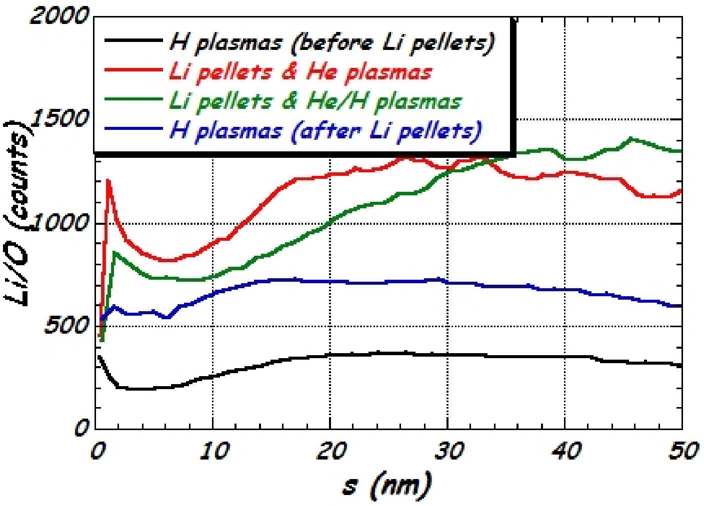

Figure 4.5: Depth profile measurement of lithium content on graphite samples: exposed to hydrogen plasma before lithization (black curve); exposed to lithization conditioning discharges only (red curve); exposed to lithization conditioning and hydrogen discharges (green curve); exposed to hydrogen discharges performed after lithization (blue curve).

corresponding to the amount of injected lithium ($\simeq 10\,nm$) is in agreement with the spontaneous diffusion of lithium into graphite forming *graphite intercalation compounds* (GICs), as presented for example *by Itou et al.* in [69].

The same deposition profiles obtained with lithization over clean graphite have been observed also in samples exposed to lithization over boronized graphite. In agreement with this observation also the effects on plasma parameters that will be discussed below are not distinguishable in the two cases.

4.3 Gas adsorption capacity and lithium saturation

Lithium wall conditioning increases wall capability to adsorb hydrogen: after lithization discharges with a similar density require a higher quantity of hydrogen. In RFX-mod, plasma density depends mainly on wall saturation level and input power; density feedback by gas puffing is difficult during discharges and density increases on a shot by shot basis. When the amount of hydrogen in the wall becomes too high, plasma current cannot be sustained and a He GDC of $20 - 40\ min$ is required to empty the wall. Gas puffing during the pulse has been tested for density control immediately after He GDC (see chapter 5), but at high current medium-high density plasmas require a high hydrogen flux that in the early current ramp-up phase of the discharge saturate the wall; then when the maximum current is reached, often very strong density increases and consequent fast discharge terminations are observed. They are the results of fast graphite degassing due to local PWIs able to increase graphite temperature over threshold for fast hydrogen release [70].

Based on RFX-mod operation method, an evaluation of wall conditioning effectiveness in term of density control can be obtained by comparing the flat-top density as a function of the total number of hydrogen particles immitted in the vacuum vessel after the last He GDCs: a higher wall adsorbing capacity provides a slower density increase. In figure 4.6 is plotted the average flat-top density for three sequences of high current discharges corresponding to three wall status (clean, lithizated and boronized graphite), not all sequences are like the three plotted, but they are representative of the three wall status. Comparing to the clean graphite case, after lithization density increase is lower for the same amount of gas, furthermore the He GDC used to recover the density control is performed after a higher quantity of wall trapped particles, when plasma density is still low (figure 4.6). Indeed with clean graphite the density can be controlled up to a total amount of about $1 - 2 \times 10^{21}$ immitted particles, instead after the lithization it can be controlled up to a total amount of about $4 - 5 \times 10^{21}$ immitted particles. Lithium absorbing effect is slightly better than that of boron, in fact the He GDC is required after about 1.5×10^{21} more immitted particles. The increased adsorbing capacity of lithium coating allows a better control of plasma density: strong gas puffing and hydrogen pellets can be used for more discharges before saturating the wall, and operation at high densities is possible without losing density control. The situation is similar to the boronization case but with the lithium adsorbing effect disappearing after a smaller number of He GDCs than in boronization case.

The loss of density control by lithization after a few discharges is similar to that found in other experiments (for example in NSTX the effect lasts for 1-2 pulses [65]), it can be related to hydrogen *"deactivation"* of lithium in the graphite (whether by the formation of Li-O-H or Li-C-H bound in graphite or LiH at the surface). Indeed, as observed on conditioning discharges, it coincides with a progressive decrease of the lithium influx on a shot to shot basis when there is no pellet injection (see figure 4.7). The total amount $\approx 4-5\times10^{21}$ of hydrogen atoms that can be adsorbed by the first wall before the

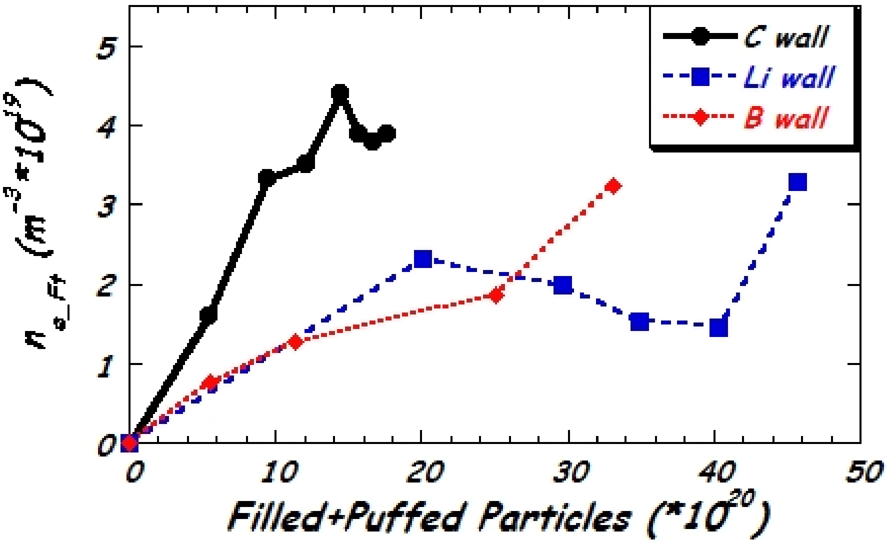

Figure 4.6: Flat-top electron density versus total filled+puffed particles for three sequences of discharges starting from He GDCs.

He GDC is needed is about a factor 10 lower than the total amount of lithium atoms injected (50 Lithium pellets corresponds to about 1.5×10^{22} atoms). This indicates that lithium loses its adsorbing capacity before reaching 1:1 ratio with hydrogen, as already observed on TFTR [59]. It is not clear the reason of this small factor, but it could be related to the deep diffusion of lithium on graphite, $\approx 10 - 100\,nm$ (see fig. 4.5), in such a way that plasma escaping hydrogen can reach only a small fraction of lithium to bound with it.

From figure 4.7 we have an indication on the He GDC (vertical lines) ability to recover a slightly higher lithium influx. It can be related to the extraction of some hydrogen bounded to lithium. Only a partial recovery is possible due to the thinner wall layer accessed by He GDC than by plasma escaping hydrogen.

In conclusion, although its beneficial effect lasts only for a short series of discharges, it is to highlight that the lithization leads to an improvement in the gas adsorption capacity with respect both to a clean graphite wall and a boronized one.

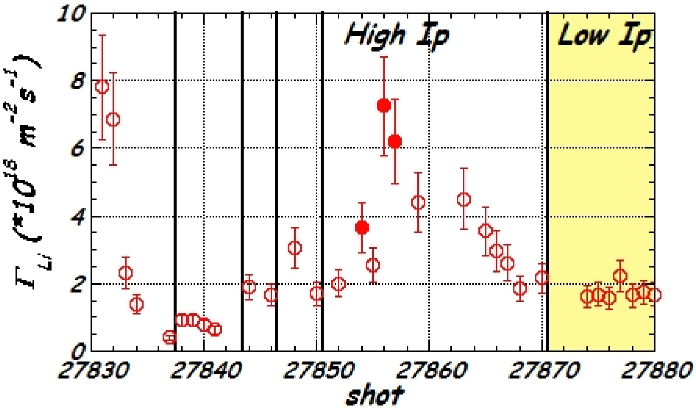

Figure 4.7: Time history of Lithium influx between 100 ms and 150 ms on different high plasma current discharges. Filled circles indicate discharges with Li pellet injection, empty cycles discharge without pellet injection, vertical lines refer to He GDCs.

4.4 Impurity reduction

Another important effect of the lithization is the reduction of impurities [71, 41, 62]. In RFX-mod carbon and oxygen are the main impurities [72]. To study the effect of lithization we have measured carbon influx (CII line at 6578 Å) and oxygen influx (OII line at 4415 Å). The atomic physics is from the ADAS database [63]. In figures 4.8 (a) and 4.8 (b) carbon and oxygen influxes are plotted versus the average density for high plasma current discharges performed on clean graphite, after boronization and after lithization. The influxes have been averaged on steps of $1 \times 10^{19} m^{-3}$ and error bars represent mean estimation error. At similar average density both boronization and lithization are very effective in reducing carbon and oxygen content, as found in other experiments; but lithization is slightly more effective in reducing carbon than boronization. The improved carbon screening by lithization could be surprising since the theoretical lithium thickness is much smaller than the boron one (10 nm of lithium against 100 nm of boron) and furthermore, as seen on section 4.2, lithium is mixed with carbon. A possible explanation can be related to the non-toroidal uniformity of boron coating in RFX-mod with probably some region of graphite wall not covered by boron at all [68].

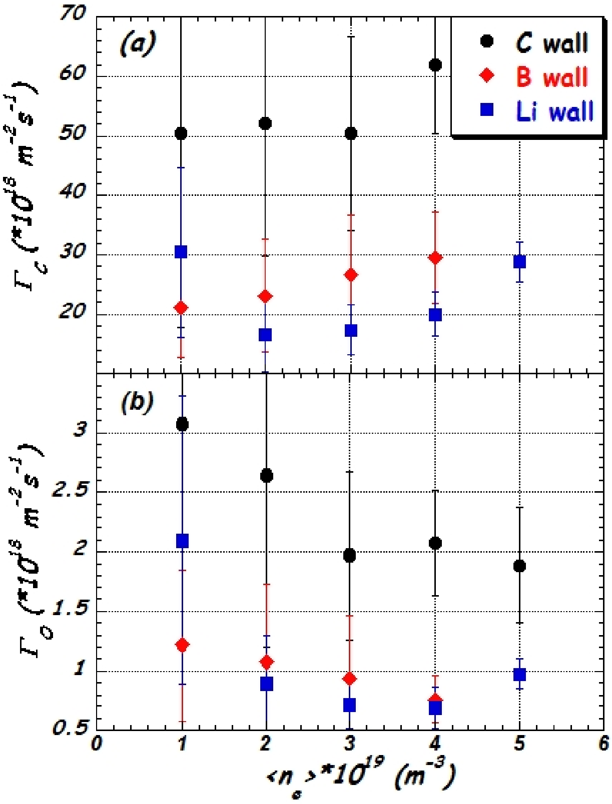

Figure 4.8: Impurity influxes versus average electron plasma density, with clean graphite (black circles), after lithization (blue squares) and after boronization (red diamond): a) carbon influx, b) oxygen influx.

4.5 Electron density and temperature profiles

One of the clearest results obtained with the lithium wall conditioning in tokamak devices is an increase of the density peaking factor [59, 61, 62, 73]

$$P_n = \frac{n(0)}{< n >}. \tag{4.1}$$

The same has been also partially observed after lithization on RFX-mod. The electron density radial profiles have been compared in discharges before and after the lithization. Due to the high variation of density profiles, mostly related to mean density and plasma current variations, the analysis has been done in two ways: comparing density radial profiles in pulses with the same mean electron density and plasma current and comparing the peaking factor as a function of the mean electron density and plasma current, before and after the wall conditioning.

Figure 4.9 shows the electron density profile measured by a multi-chord interferometer [50] on three discharges: before any wall conditioning, after lithization and after boronization. Density profile is peaked after lithization while it is hollow in the clean graphite case and flat in the boronized one.

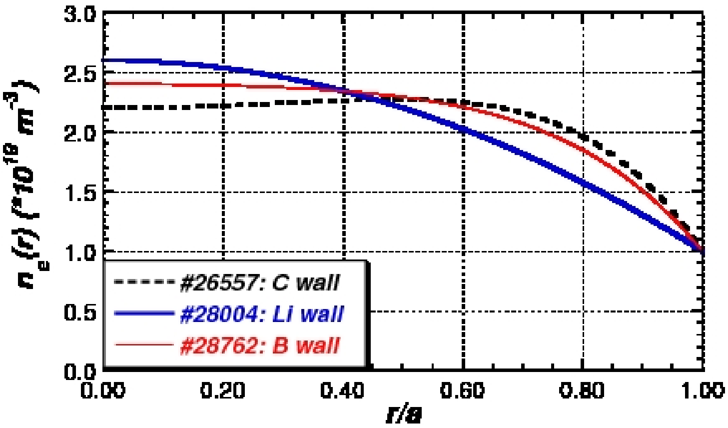

Figure 4.9: Electron density radial profile of a typical discharge with clean graphite (26557) after lithization (28004) and after boronization (28762). All discharges have an average electron density of about $2 \times 10^{19} m^{-3}$ and a plasma current of about 1.5 MA.

On a statistical basis, peaking factors P_n have been compared with values computed by a fitting function $Fit(P_n)$ of P_n measured on many clean graphite discharges. As $Fit(P_n)$ a power product of the mean electron density and plasma current has been chose. In figure 4.10 is plotted the ratio between the peaking factor P_n and the fitted value $Fit(P_n)$. The $P_n/Fit(P_n)$ ratios have been averaged on P_n and error bars represent mean estimation error. The plot shows that with lithizated graphite the peaking factor is typically higher than with clean graphite (with a full ensemble mean ratio$< \frac{P_n}{Fit(P_n)} >= 1.13$). Conversely boronized graphite with a full ensemble mean peaking ratio $< \frac{P_n}{Fit(P_n)} >= 1.03$ does not significantly modify density profile peaking.

Interferometric measurements provide only a smooth global indication of density profile variations, a more localized information at the edge is available from electron density and temperature measurements performed with the Thermal Helium Beam diagnostic [74] and, for density only, by reflectometer measurements. Figure 4.11 shows a lower edge density and a higher edge temperature after the lithium wall conditioning, in agreement with an increase of the density peaking factor. In contrast with the results of the previous peaking factor analysis, also the selected discharge after

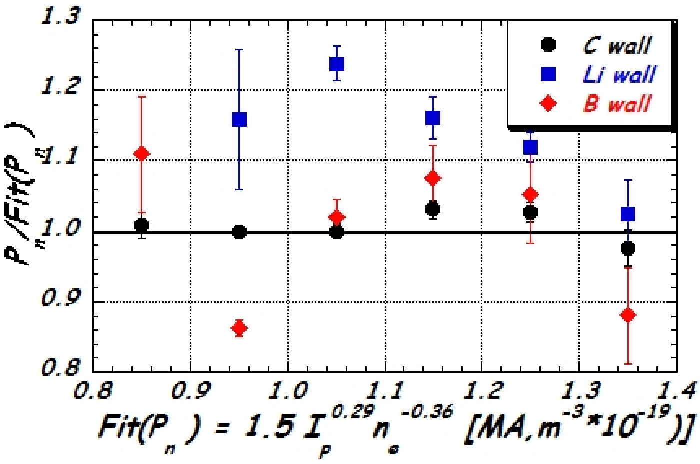

Figure 4.10: Comparison of the peaking factor in different wall conditions. On the x-axis the value of the peaking factor as fit of average plasma density and plasma current with a clean graphite first wall, on the y-axis the ratio between the measured peaking factor and the one from the fit. In case of lithizated wall (blue squares) the ratio is almost greater than one.

boronization shows a reduced edge density similar to that after lithization. In the lithium case the temperature increase more than compensates the plasma density decrease, providing an higher edge pressure compared to the discharge performed with clean graphite wall, whereas this is not the case after boronization.

Another confirmation of the modification of radial density profile after lithization is shown by the reflectometer. RFX-mod is equipped with a single band reflectometer [75] monitoring a cut-off layer that corresponds to a density of $10^{19}\ m^{-3}$. In figure 4.12 is plotted the position of the cut-off layer as a function of the mean electron density measured with the interferometer and averaged on discharges with similar electron density. Circles correspond to discharges with a first wall of clean graphite, squares to a lithizated first wall.

After lithization the same density layer is about at 1 cm smaller radius, in agreement with the previous observations of a more peaked profiles.

Both analysis show that, as in the other devices where lithization has been tested, the electron density radial profile after the Lithium wall conditioning becomes more peaked. This implies that the lithization strongly acts on the plasma behavior at the edge. This is highlighted also by the behavior of the electron temperature, which does not show any difference in the core before and after lithization, despite the observed difference on T_e at the edge.

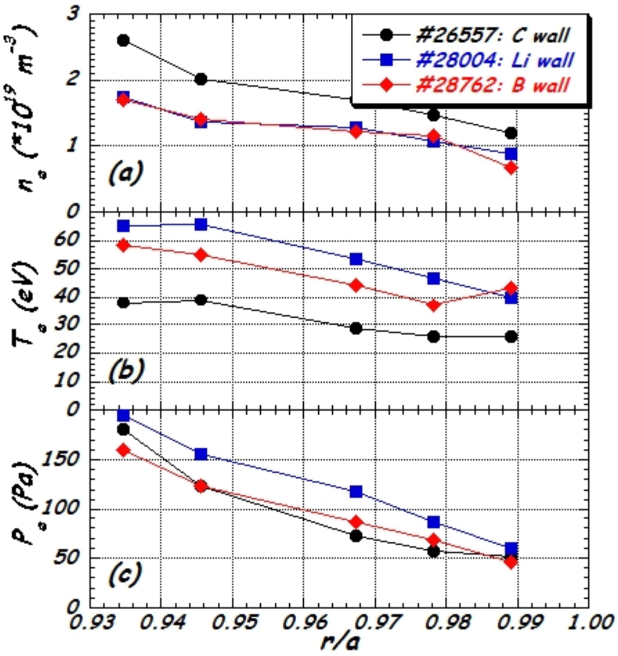

Figure 4.11: Density, temperature and pressure radial profile at the edge measured with the THB, for a discharge with clean graphite (26557), for a discharge after the lithization (28004) and for a discharge after boronization (28762).

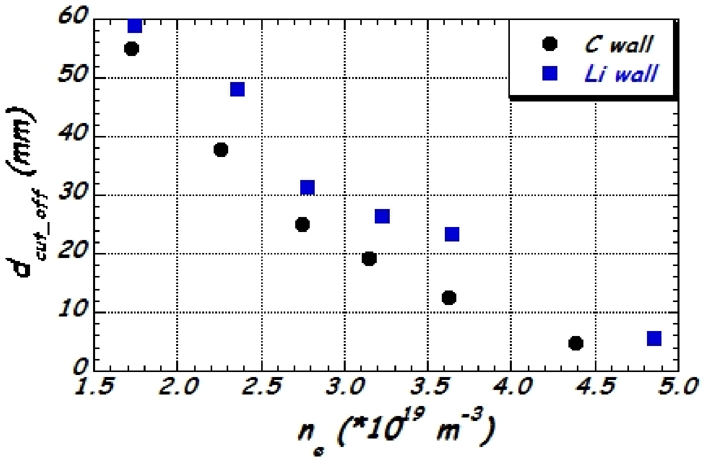

Figure 4.12: Average distance of the density layer of $10^{19} m^{-3}$ from the wall as a function of the average electron density. Circles with clean graphite, squares after the lithization.

4.6 Particle and energy confinement time

The effect of lithium coating provides a small increase of particle confinement time. This is seen first of all as a decrease of the H_α emission at the edge comparing discharges with the same average density with and without lithium wall conditioning.

Starting from this observation, a comparison of the particle confinement time on discharges with plasma current greater than 1.4 MA as a function of the average density at the flat top has been done. Figure 4.13 (a) shows an increase of the particle confinement time after the lithization with respect to the discharges on clean graphite and on boronized first wall.

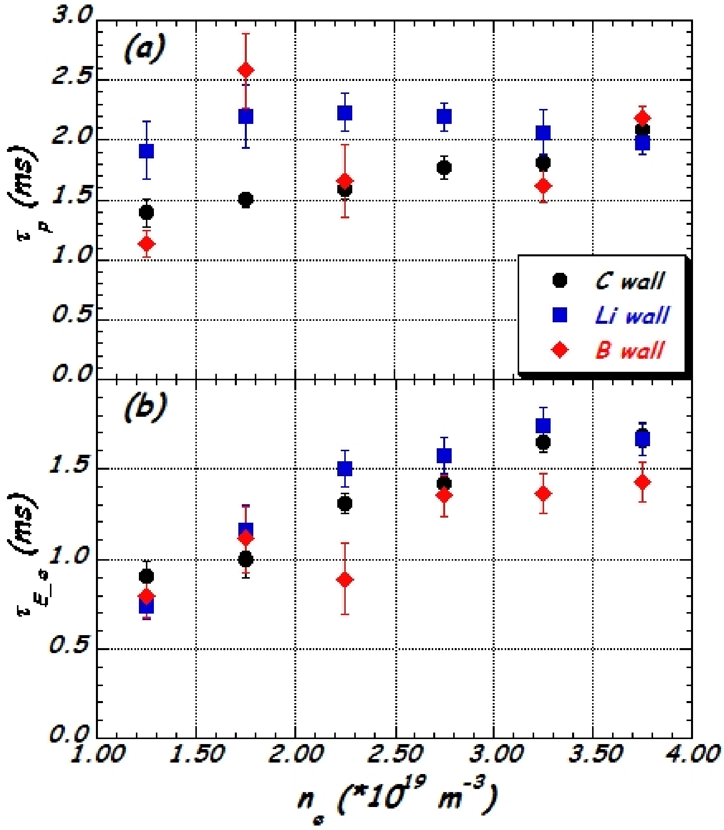

Figure 4.13: Average confinement times versus plasma density for pulses with a plasma current of about 1 MA for clean graphite (black circles) after lithization (blue squares) and after boronization (red diamonds). Error bars refer to mean evaluation error. (a) particle confinement time, (b) electron energy confinement time.

Differently from τ_P, electron energy confinement time, τ_{Ee}, does not show any improvement related to lithization or boronization, as can be seen in figure 4.13 (b). This could be a consequence of the fact that τ_P strongly depends on plasma edge transport, whereas τ_{Ee} is more linked to the plasma core. According to this view the different effect on τ_P and τ_{Ee} is an indication that wall conditioning affects mainly the plasma edge.

4.7 Edge transport

Lithium wall conditioning modifies the edge plasma parameters by directly affecting transport. A confirmation of the transport modification at the edge is provided by the different time and spatial distribution of edge density fluctuations. In RFX-mod the edge fluctuations are measured with the Gas Puff Imaging (GPI) diagnostic [76], which measures the light emitted from helium gas puffed into the plasma edge. The emission fluctuations are proportional to fluctuations of local electron density and temperature. Figure 4.14 shows the large difference on raw signals between discharges after lithization compared to discharges without wall conditioning or with boronization. Comparing the edge emission in the $0.2\,ms$ time-window during the discharge, it is clear seen a strong reduction of the shortest time scale fluctuations only with the lithizated wall.

The difference in fluctuations are statistically presented in figure 4.15 where the auto correlation time (τ_a) of the edge fluctuations and the packing fraction (f_p) which measures the time percentage of GPI signal is occupied by strong bursts [77] associated with coherent blobs of the plasma edge are plotted versus density normalized to n_G. The auto correlation shows that for all of the discharges with clean graphite the auto correlation time is less than $2\mu s$, instead for the discharges after lithization there is a spread in the auto correlation time, but it is greater than $2\mu s$ in the SHAx [78] operation regime ($n/n_G \lesssim 0.2$), with a tendency to decrease with the normalized density. Since the perpendicular propagation velocity of the edge fluctuations is the same for the two sets of discharges, this suggests the presence of larger blobs for lithizated wall compared to graphite and boronized ones.

The packing fraction has a similar behavior: for standard and boronized discharges the percentage of time series signal occupied by bursts is about 15%, while it is smaller for lithizated ones.

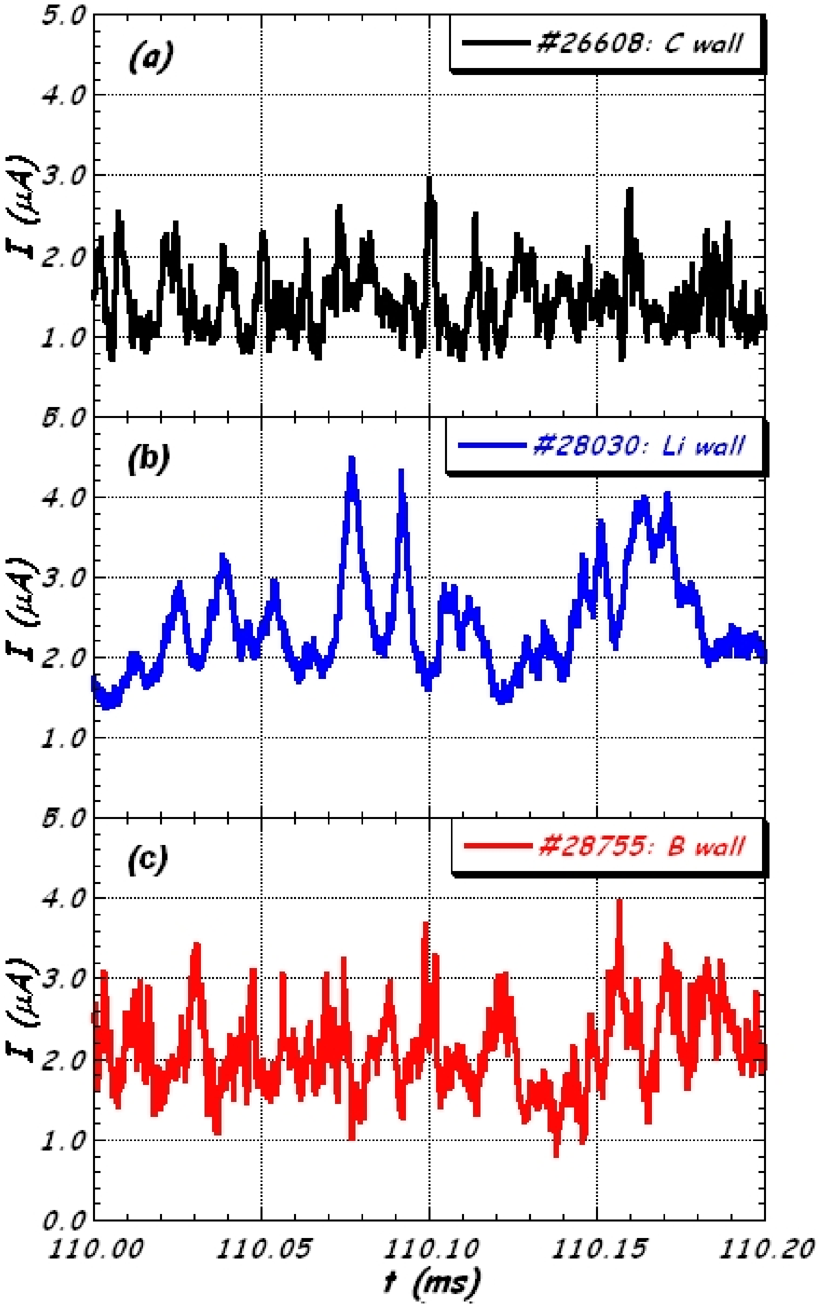

Figure 4.14: Raw signals from the GPI diagnostic: (a) a typical discharge with clean graphite, (b) with lithizated graphite, (c) with boronized graphite.

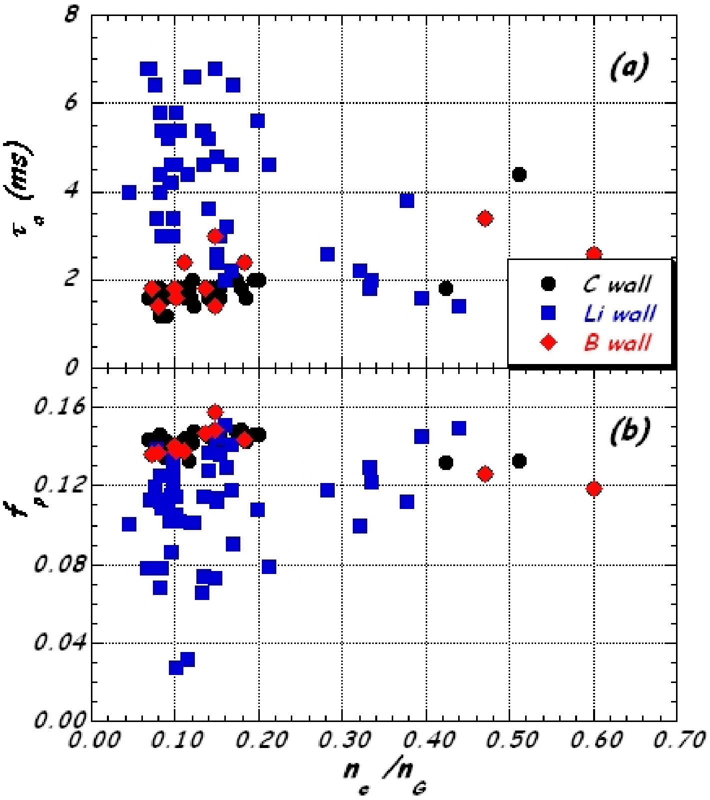

Figure 4.15: Auto correlation (a) and packing fraction (b) of the signals from the GPI as a function of the rate between the average density and the Greenwald density.

The different behavior of the edge coherent structures implies a different turbulent particle transport. It is possible to describe the particle out-flux due to edge bursts as:

$$\Gamma \propto \delta n f_p^2 \frac{\lambda_r}{L_\phi} \tilde{v}_\phi$$

where δn is the density fluctuation, λ_r the radial correlation length of the fluctuations, L_ϕ the toroidal amplitude of the blob and $\tilde{v}_\phi$ the fluctuation of toroidal velocity [79]. It is then found a lower flux due to blobs after the lithization as can be seen in figure 4.16. This suggests that lithization modifies the edge particle transport by a reduction of the level of intermittent events of boundary turbulence [79], related to a decreased ratio between the outflux and the influx of particles due to the edge blobs. Although the mechanism for such change is still under investigation, it is clear that lithization has changed plasma behavior at the edge.

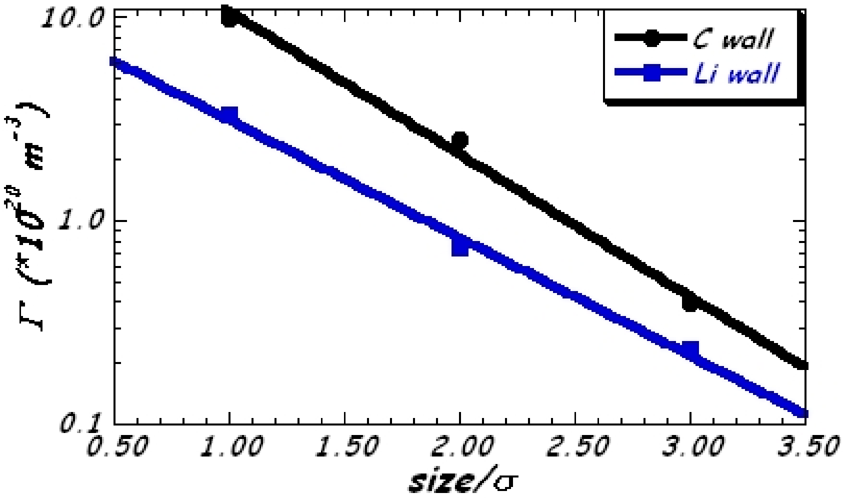

Figure 4.16: Particle outflux at the edge due to the edge bursts as a function of the event-amplitude threshold. Continuous black line indicates discharges with a clean graphite wall, dashed blue line with a lithizated first wall.

4.8 Conclusions

Several lithization experimental campaigns have been performed. Aim of these campaigns was the optimization of the technique, the lithium wall conditioning and the study of its effects. The solutions tested were focused mainly on the main plasma gas, H or He, the discharge duration, and the starting state of the wall, clean graphite or boronized one. The final result is that the best lithization is obtained injecting the greatest possible number of lithium pellets at a speed of 130 m/s on short He plasma discharges. This work proved therefore the possibility to perform for the first time the lithization on a RFP device.

Wall conditioning by means of lithium in RFX-mod proved to be an effective tool in controlling wall recycling. The technique provides or improves all the features of boronization wall conditioning: increases hydrogen wall absorbing capacity and reduces the impurity content. It is also able to improve the edge particle behavior providing a higher particle confinement time. The absorbing wall capacity allowed for the first time operating RFX-mod close to its 2 MA maximum target plasma current.

Though up to now the beneficial effect of lithium wall conditioning does not extend to the plasma core, the differences observed on density and temperature at the edge, open the perspective of improving also the global performance by optimizing both the lithization technique and the core fuel capability. Work will be done in the near future to improve the effectiveness of the lithization technique using different approaches: lithization over a better conditioned wall (for example removing all stored hydrogen by baking or intense He GDC); a thicker lithium deposition injecting a much higher number of pellet (by a centrifugal injector able to inject many pellet on each discharge) or by a Liquid Lithium Limiter (like on FTU).

Refueling Techniques

In this section will be presented the activity on RFX-mod fuelling optimization. As already mentioned RFX-mod first wall is entirely covered by graphite tiles and one of the problem of graphite is that in a few discharges the plasma facing side of tiles becomes completely saturated by hydrogen. After that the graphite acts as a hydrogen reservoir resulting in a hydrogen influx that depends only on the power load onto the wall. This prevents the possibility to perform series of discharges at the desired density, particularly at high plasma current ($I_p > 1.5\,MA$). The techniques explored up to now are mainly based on wall conditioning treatments, but none of them provided a solution stationary over many discharges. Even the lithization technique previously described, although it provides an improved density control over an higher number of discharges, it is not a stationary solution. Because up to now it has not been possible to improve significantly the wall behavior in terms of fuel retention capability, to improve density control capability is necessary to decrease the amount of hydrogen trapped on tiles, for the same sustained density.

To achieve a specified density in a typical RFX-mod discharge two techniques are used: gas puffing and frozen hydrogen pellet injection. A discharge where the two techniques were both used is #30060, whose electron density time evolution is shown in figure 5.1. In the plot in red it is shown when hydrogen gas is puffed inside the vessel and in blue when a frozen hydrogen pellet is injected. The increase of the electron density in correspondence of the two refueling techniques is clearly seen.

The section presents the activity performed on the cryogenic pellet injector and its usage during the experimental campaigns and then also on the comparison of the two refueling techniques. In section 5.1 there is an overview of the injector with its main features and a detailed descriptions of the component on which I have worked on to ensure a reliable and repeatable pellet injection. Section 5.2 is dedicated to a brief description of the gas puffing system and of the DESOrption diagnostic. The two techniques are then compared in section 5.3 in terms of plasma electron density and temperature response, and therefore in terms of discharge perturbation and of refuel efficiency.

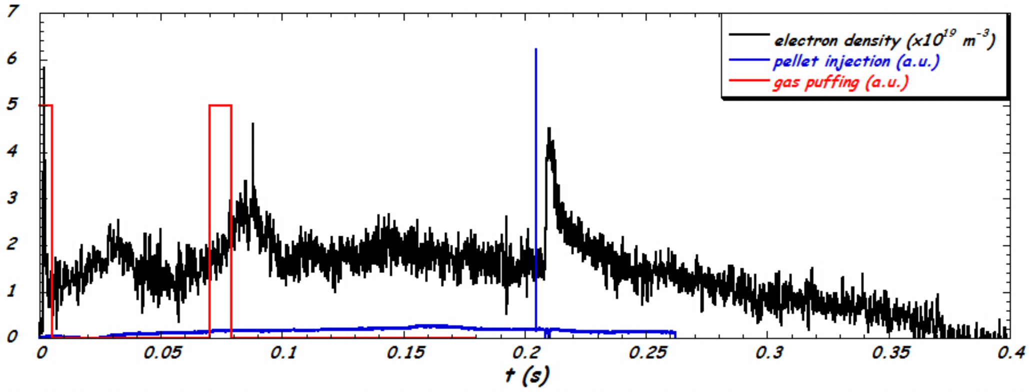

Figure 5.1: Correlation between the time evolution of the electron density (black line), the puffing (red line) and the pellet injection (blue line) in discharge #30060.

5.1 The cryogenic injector

Pellets are injected in RFX-mod by a multishot pellet injector built by *Risø National Laboratory* [80, 81]. The injector can inject up to 8 hydrogen pellets in each discharge.

Pellets are formed and accelerated in a unit, called *8-shot unit*, where eight pipe guns are placed symmetrically around a liquid helium flow cryostat. The pipe guns are independently fired with the same type of driver gas at pressures from 5 *bar* up to 60 *bar* by means of fast acting valves. Hydrogen pellets are of three different sizes, containing 1.5, 3 or 5 $\times$ 10^{20} atoms and can be fired with velocities up to 1.5 km/s. The driver gas pressure can be adjusted individually for each pipe gun. Pellets are injected into the vacuum vessel through a single guide tube system. The tube is placed on the top of an integrated vacuum tank consisting of two differential pumping chambers and a pellet gas reservoir. A schematic drawing of the injector with integrated tank, guide tube system and 8-shot unit is shown in figure 5.2.

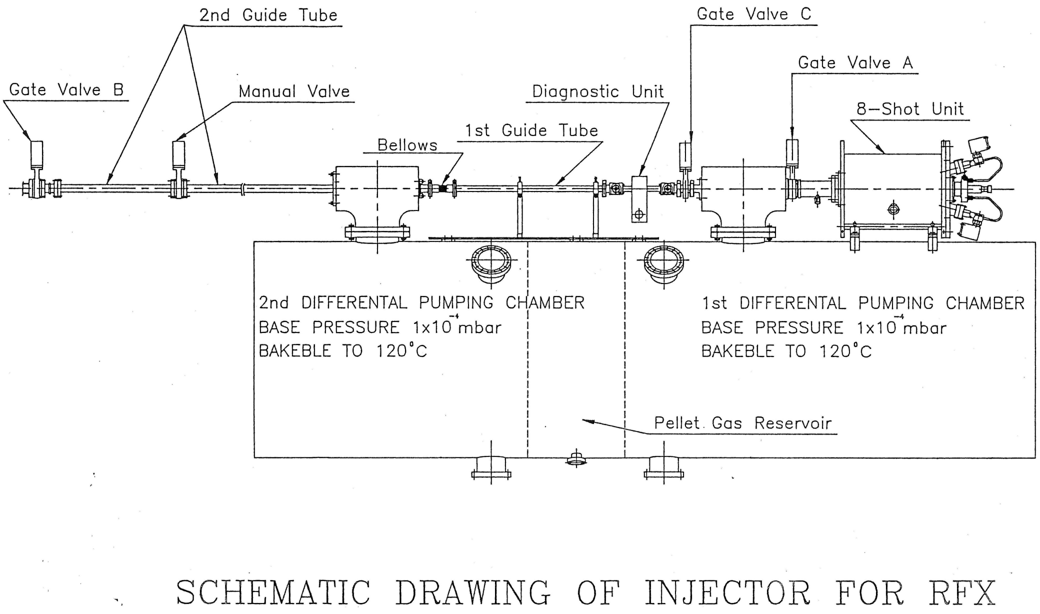

Figure 5.2: Schematic drawing of the cryogenic injector. At the bottom are highlighted the two pumping chambers with the pellet gas reservoir, where the gas used to create pellet is stored, in the middle. On the top, starting from the right, the 8-shot unit, where pellet are created and accelerated, the diagnostic unit composed of two optical detectors for velocity measurements and a microwave cavity for mass measurements, and the valves which connect the injector to the vacuum vessel.

5.1.1 The control system

Most parts of the injector can be operated from control panels placed outside the experimental room and also remote control is possible by means of signals from RFX-mod computer system by means of a RS232 serial interface. The control system of the cryogenic pellet injector is more complex than the one of the RTPI because it has to control not only the injection of the pellets, but also their formation and, moreover, it has to maintain the system at cryogenic temperature. The system is organized in states. There are seven main states and twentyfour minor states that are used to move from a main state to another. The main states are described in table 5.1.

Each state is a combination of valves state, pumping condition and temperatures. Due to the age of the injector (which was built in 1990), some components are not anymore fully functional to ensure a completely automatic operation of the injector. The most important maintenance have been devoted to ensure the freezing of the pellet and the operation of the

state	short description
NON OPERATIVE STATE	All parts of the system have been prepared for operation. The pumps are down and the system is at room temperature.
QUIESCENT STATE	The system is ready to become cryogenic. The pumping system is turned on, the gas used for pellet formation is stored in the *pellet gas reservoir*.
STANDBY STATE	The system is cold and ready for operation with pellet. It is achieved when the temperature inside the *8-shot unit* is below $5.8\,K$. To achieve this temperature it is used a system that fluxes liquid helium all around the unit where the pellets are formed.
STANDBY LOW STATE	Same as the standby state, apart for the 8-shot unit temperature that is maintained at about $20\,K$ in order to reduce the liquid helium consumption. To come back to the standby state it is sufficient to increase the helium flow.
READY TO FIRE STATE	The system is ready to fire pellets. The temperature is maintained at a value $\leq 8\,K$ and the high voltage of valves is turned on. The state is left after the fire signal from the RFXmod main system or after a timeout ≤ 5 minutes.
FIRE STATE	The duration of this state is of $5s$. In this state the fast valves are opened and the pellets are fired.
RECOVERY STATE	Barrels are evacuated of any residual gas and the system is brought back to the standby state.

Table 5.1: Description of the main states of the cryogenic pellet injector.

feedback system related to the temperature control in the 8-shot unit. To do that, the unit was opened, cleaned and fixed. Some pictures of the cleaning operation are shown in figure 5.3. In the next paragraphs there is a description of pellets creation and acceleration.

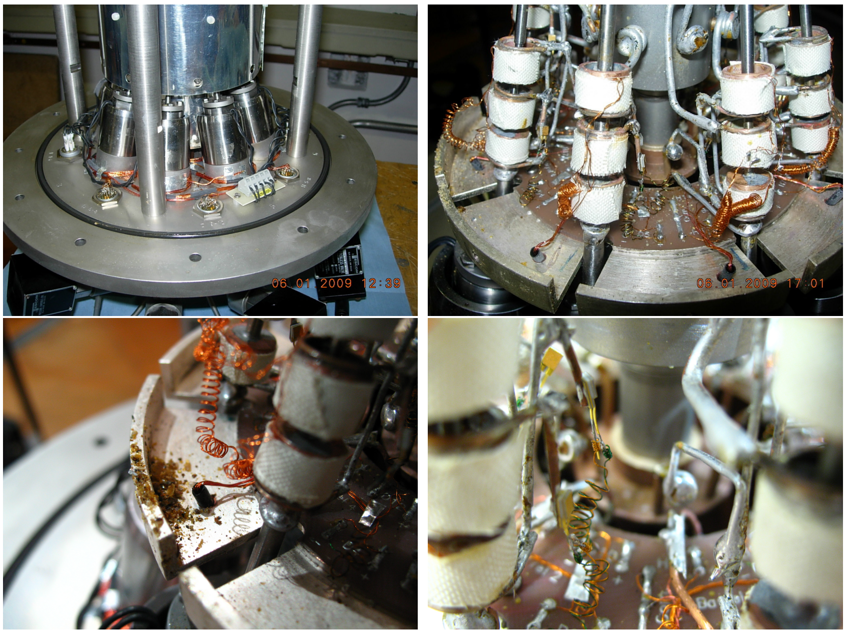

Figure 5.3: Pictures of the opened 8-shot unit before its maintenance. In clockwise direction from the top-left: the fast valves and some debris on the O-ring, the region of the pellets formation, a thermistor and some debris in the 8-shot unit.

5.1.2 Pellet formation

Pellets are created by condensation of hydrogen gas inside the freezing cell of a pipe gun shown in figure 5.4. The pipe gun consists of a fast valve yielding the driver gas pulse used for accelerating the pellet and a gun barrel where the pellet is formed and accelerated. There are eight pipe guns, thermally independent and that can be also fired independently. The pellet gas is let into the pipe gun through the gun barrel and it condenses to form a pellet in the freezing cell held at around $6 - 8\,K$.

The freezing cell is made of three copper segments attached to the gun barrel, cooled by means of a liquid helium flow cryostat. The central segment is the freezing cell, and it has the pourpose to be cold enough to allow condensation of the pellet gas. The two outer segments are connected

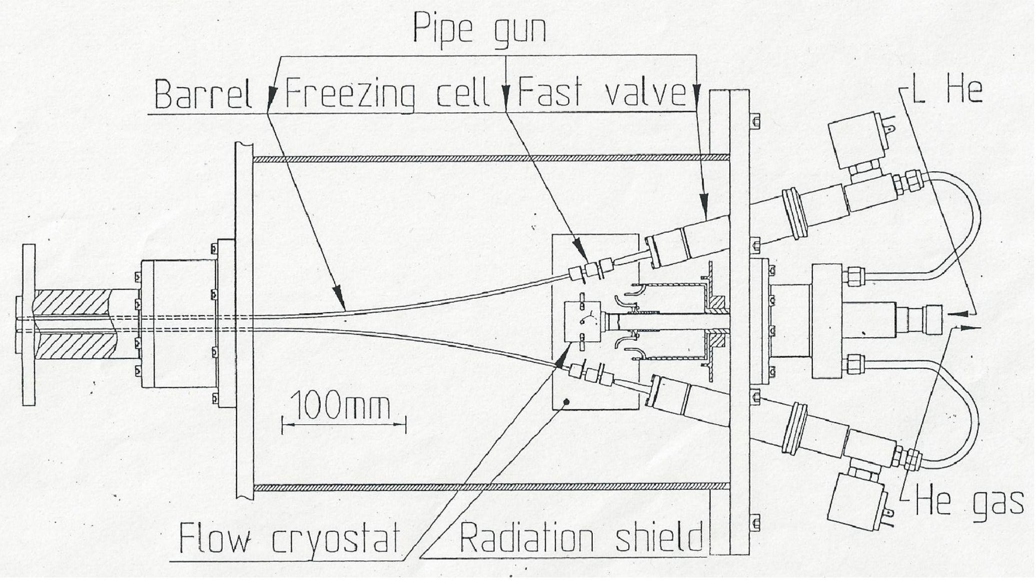

Figure 5.4: Schematic drawing of the 8 shot unit.

by a thermal bridge to have the same temperature and serve to two purposes: to reduce the thermal load on the central segment and to control the temperature gradients along the gun barrel. A copper tube is placed around each segment. At the end of each copper tube is soldered a copper wire for thermometer and thermal connection to the cryostat. Heaters are made of manganin wire twisted around each copper tube and connected in series.

The pellet gas, taken from the pellet gas reservoir, flows into a barrel and condense on the inner wall of the freezing cell where the temperature is low enough. The freezing cell has a constant wall temperature for a given length. At both ends of the freezing cell the temperature increases. When the pellet gas is let in from a pressure P_{pg} the gas will condense where the temperature is lower than the temperature giving a vapor pressure equal to P_{pg}. When a pellet is formed the gas flow will stop. After formation the pellet is stored until firing.

The pellets formed in this way are cylinders of some length and diameter placed inside a barrel. Because the length of the freezing cell is the same for the eight barrel, the size of the pellets depends on the barrel diameter. In the injector of RFX-mod there are 4 barrel corresponding to a pellet size of about 1.5×10^{20} particles, called *small pellets*, 2 barrels corresponding to a pellet size of about 3×10^{20} particles, called *medium pellets*, and 2 barrels corresponding to a pellet size of about 5×10^{20} particles, called *large pellets*.

5.1.3 Pellet injection

To inject pellets at high speed the pneumatic acceleration it is used [82]. An object that experience a pressure gradient get an acceleration. If the gradient is generated by a compressible gas, the object can be accelerated at speed also higher than the sonic speed of the driver gas.

Neglecting non ideal effects like the friction of the pellet with the barrel, heat exchange with driver gas and the viscosity, the velocity of the pellet $v(t)$ after a sudden application of a pressure P_0 is

$$v(t) = \frac{2C_0}{\gamma - 1} \cdot \left[1 - \left(1 + \frac{(\gamma + 1)\, A_p}{2MC_0} P_0 t \right)^{-\frac{(\gamma-1)}{(\gamma+1)}} \right] \tag{5.1}$$

where C_0 is the driver gas sonic speed, γ is the ratio between driver gas specific heats, M the pellet mass and A_p is the pellet section, that is the same of the barrel [83]. The pressure $P(t)$ behind the pellet decreases in time as

$$\frac{P(t)}{P_0} = \left[1 - \frac{\gamma - 1}{2} \frac{v(t)}{C_0} \right]^{2\gamma(\gamma-1)} . \tag{5.2}$$

From equation 5.1 and 5.2 it is possible to derive that the maximum possible pellet speed is:

$$v_{max} = \frac{2C_0}{\gamma - 1}. \tag{5.3}$$

In the case of an ideal gas sonic speed is $C_0 = \sqrt{\gamma RT/m}$, where R is the universal gas constant, T the temperature and m the molecular weight of the driver gas. It means that, at room temperature, in case of hydrogen ($\gamma = 7/5$) $v_{max} = 6.5\, km/s$, in case of helium ($\gamma = 5/3$) $v_{max} = 3\, km/s$. In practice the maximum allowable speed is lower because of the finite length of the barrel and of the non ideal situation. It will be explained at the end of paragraph 5.1.5. As for the RTPI the driver gas mainly used is helium, that allows to inject pellets at a speed of about $1\, km/s$. Moreover it is possible to use also other heavier gas to inject pellets at lower speed, for example with neon the pellet speed is about $600\, m/s$, while using hydrogen can be injected pellet at higher speed, up to $1.5\, km/s$.

In the RFX-mod cryogenic injector different driver gas pressures are allowed for each one of the eight pellets, depending on the desired velocity. Each fast valve opens when the pellet has to be injected creating a pressure gradient behind the pellet. Because the pellet is frozen on the barrel it acts as a plug. The system of heaters helps the departure of the pellet warming each barrel at a different desired temperature (usually about $20K$).

5.1.4 Pellet diagnostics

Because of the pellet wear and slow down during its movement through the barrel and its length uncertainty it is important that the pellet proprieties like mass and speed are measured during the free flight to the plasma. Thus the injector is provided with an integrated diagnostic unit system to measure them.

The diagnostic unit is integrated on the guide tube system of the injector. It is formed by a microwave cavity used for mass measurement and two light barrier used for speed measurements placed symmetrically on either side of the cavity. The two optical detectors are at a fixed distance of 20 *cm*. The maximum error on pellet speed measurements is 5%. The pellet mass is measured using the change in resonant frequency of a microwave cavity inserted in the pellet trajectory [84]. The resonant frequency depends upon the dielectric conditions in the resonating volume and it therefore changes as the pellet enters the volume. The change that occurs depends on the pellet mass and the instantaneous position of the pellet in the cavity.

In figure 5.5 it is shown an example of the measurement of speed and mass.

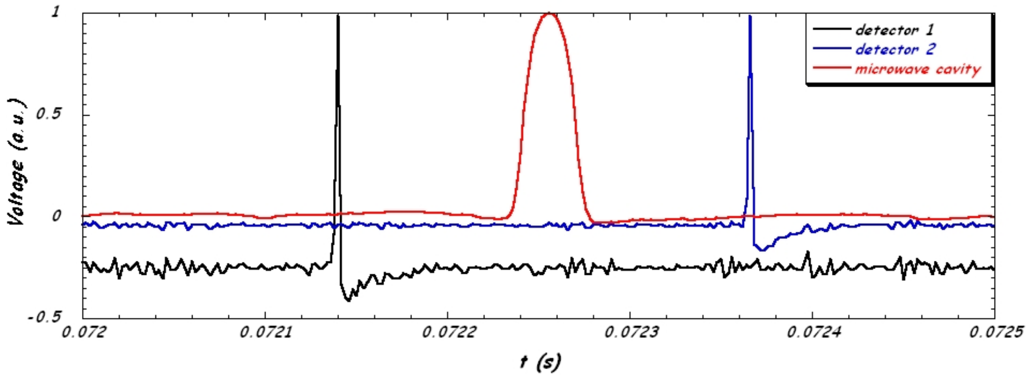

Figure 5.5: Example of speed and mass measurement. From the top, the detection of the pellet from the first optical detector, the detection from the second one and the volume variation of the microwave cavity.

5.1.5 Pellet injection speed characterization

As seen in section 3.5, the ablation rate of a pellet depends on the plasma electron temperature and density. It means that a big and fast pellet in a low current plasma will not be able to ablate completely inside the plasma column, going to hit the inner graphite tiles. There it will break, giving rise to a gas puffing from the inner side of the vessel. On the contrary, a small and slow pellet injected in an high current plasma will be completely ablated as soon as it enters the plasma, without depositing any particle into the plasma center. Hence the control of pellet mass and speed is crucial to optimize refueling by achieving core pellet ablation. The control parameters available to adjust the speed and mass of the injected pellet are the pressure of the driver gas, the barrel diameter and the barrel temperature. Hence a study of the pellet velocity as a function of the three control parameters has been made.

The injection tests have been done using neon as driver gas, together with the pellet speed by the two optical detectors has been computed also the firing delay as the time difference between the trigger time and the time in which the pellet is detected by the microwave cavity. Although the firing delay measured in this way depends also on the pellet velocity, the contribution due to the flight time is negligible since it is two order of magnitude lower than the time delay due to initial detachment from the barrel.

Scan over driver gas pressure and barrel temperature

As seen in section 5.1.2, the injector can launch up to eight different pellets, 4 little, 2 medium and 2 large ones. Unfortunately during the tests two of the four little pellets were not available because of a problem with the trigger board, fixed later.

A preliminary scan in driver gas pressure has been performed from $p_{dg} = 5\,bar$ up to $p_{dg} = 15\,bar$, with variable steps. For each step of driver gas pressure also a scan over the barrel temperature has been done, from $T_{barrel} = 18\,K$ up to $T_{barrel} = 24\,K$ with steps of $\Delta T_{barrel} = 2\,K$. These injection tests have shown that small pellets are difficult to optimize, their delay has a big spread and sometimes they are also not launched, mainly at low driver gas pressure. Medium pellets have a speed comprised $v_p = 550\,m/s$ and $v_p = 600\,m/s$. Large pellets are the most reliables, they can be also launched at the lowest driver gas pressure and their speed is about $v_p \simeq 500\,m/s$.

Following the preliminary series of tests focused on the understanding of the dependence of pellet mass and speed from the injector settings, a second series of tests have been done with the aim to ensure the repeatability of the previous results.

Since pellets do not always start at driver gas pressure lower than $10\,bar$, the test have been performed at $p_{dg} = 10\,bar$ and $p_{dg} = 15\,bar$ only, both at $T_{barrel} = 20\ K$ and $22\ K$. Results are reported in figure 5.6. Colours refer to different barrel temperatures, symbols indicate the pellet barrel. Error bars are the standard deviation of the measured values. The most evident result is a great data dispersion. Nevertheless as it was expected the velocity increases with driver gas pressure and the firing delay decreases, while there is not any dependence from the barrel temperature.

Based on the results of the previous scans, the last one has been performed at fixed barrel temperature, $T_{barrel} = 20\,K$, and measuring pellet velocity at various driver gas pressures, precisely at $p_{dg} = 5,\ 8,\ 10,\ 12\,bar$. Results are drawn in figure 5.7. The pellet fired on barrel two is not reliable, in the other cases there is not any appreciable dependence of pellet velocity from the barrel and therefore from pellet mass. It is also confirmed the dependence of the pellet speed from the driver gas pressure.

Another evidence is that the measured pellet velocity is about one half of the maximum achievable speed using neon as driver gas ($v_{max} = 1305\,m/s$). This difference is explained in equation 5.1. It can be written synthetically as

$$v(t) = v_{max} - \frac{v_{max}}{(1 + CP_0t)^{\frac{1}{4}}} \tag{5.4}$$

where C is a constant equal to $1.92\,bar^{-1}ms^{-1}$ considering for example a pellet fired by barrel number 1 ($\varnothing = 1.45\,mm$, $M = 0.5\,mg$) with neon as driver gas. On the top of figures 5.8 and 5.9 equation 5.4 is drawn in case of driver gas pressure equal to $10\,bar$ and $15\,bar$ respectively. At the bottom there is the time trace of the pellet position. Because the barrel length is about $300mm$, in the first case pellet reaches the end of the barrel after about $0.65\,ms$. At this time the pressure boost ends and the theoretical velocity achieved is about $600\,m/s$, only slightly higher than the measured one. The remaining difference can be ascribed to the pellet wear and slow down during its movement through the barrel. The same can be also seen in the case of the $15\,bar$ driver gas pressure.

Equation 5.4 shows also the dependence of the pellet velocity from the driver gas pressure. This dependence is drawn in figure 5.10 where the pellet speed is plotted as function of the driver gas pressure always for the barrel 1. It shows that the measured speed is constantly lower than the theoretical one of about $50\,m/s$, that is the velocity decrease to be ascribed to the various frictions. The same was noticed also for the other barrels.

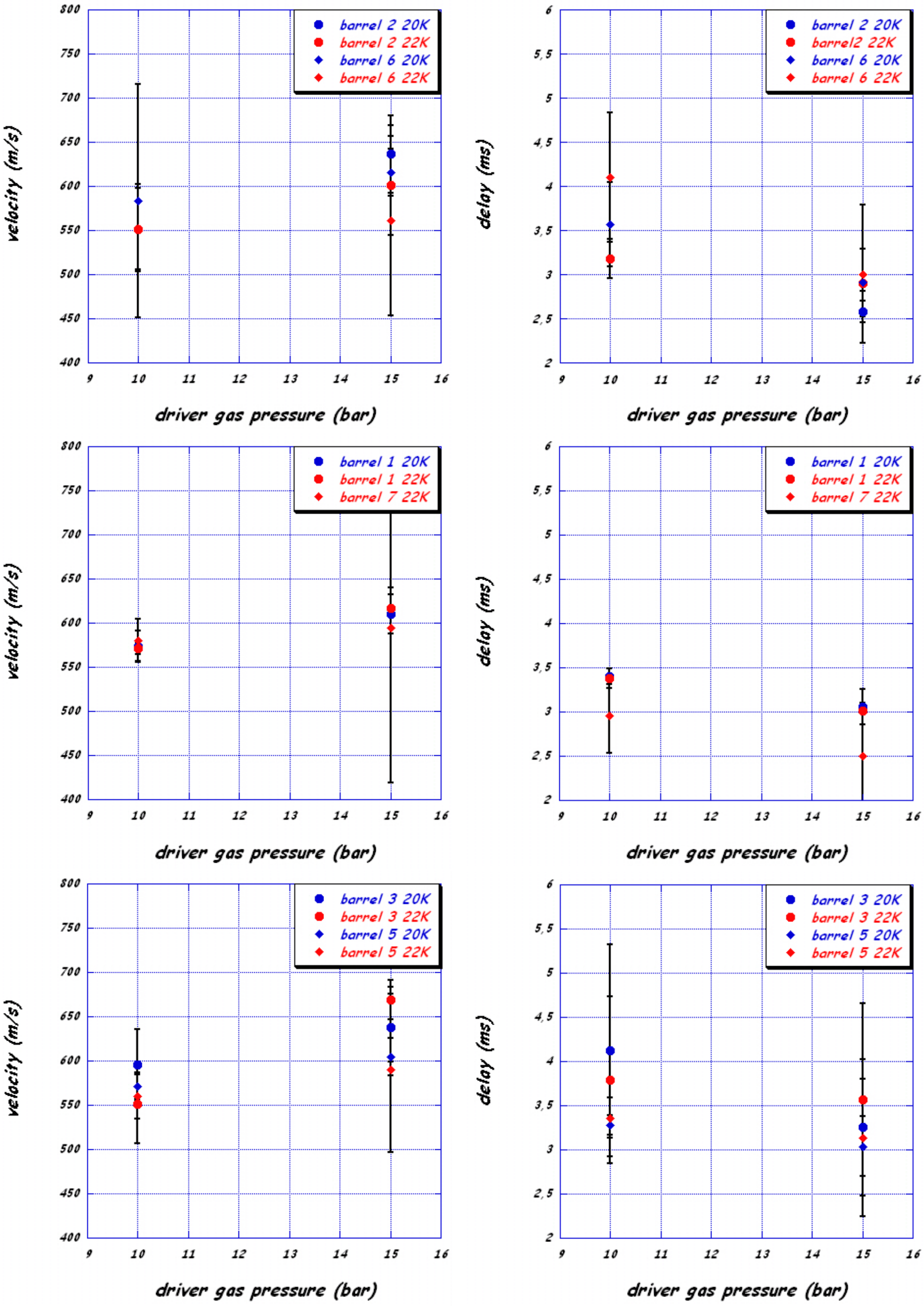

Figure 5.6: Pellet velocity and average fire delay, divided on reference barrel and temperature as function of the driver gas pressure.

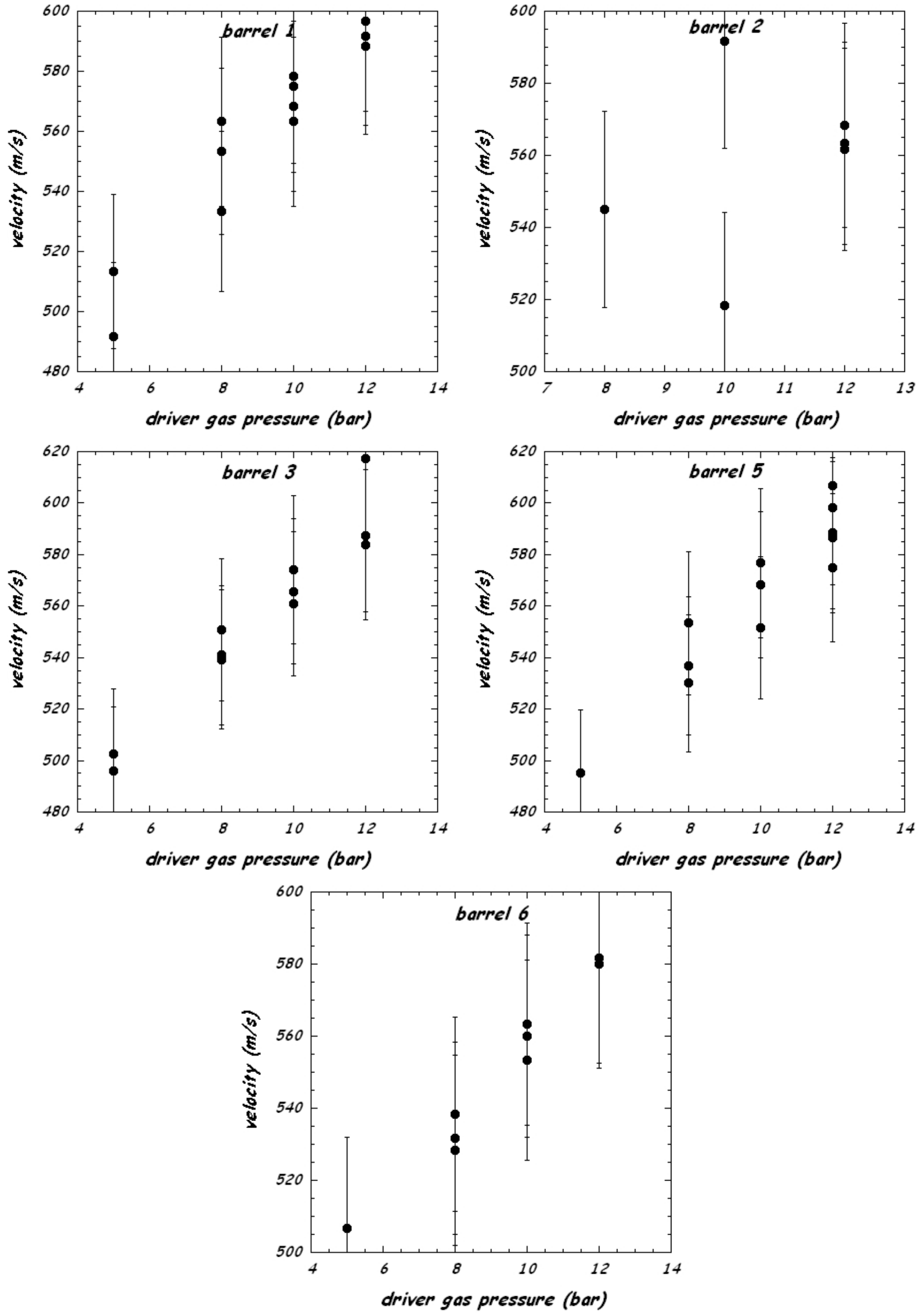

Figure 5.7: Pellet velocity as function of driver gas pressure, divided on reference barrel.

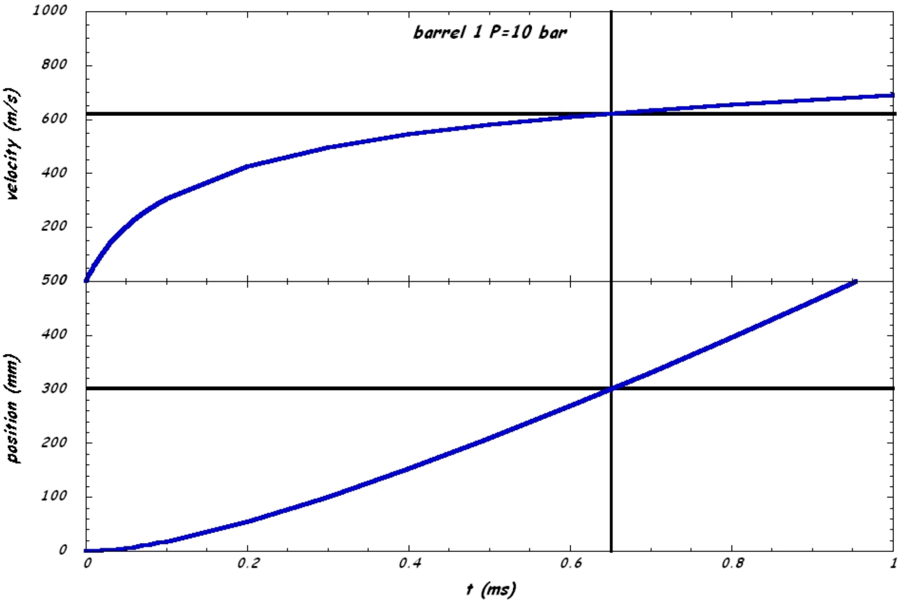

Figure 5.8: On the top equation 5.1 evaluated for neon as driver gas and pellet fired from barrel 1. The driver gas pressure is 10 *bar*. At the bottom its integration. The red lines correspond to the barrel length.

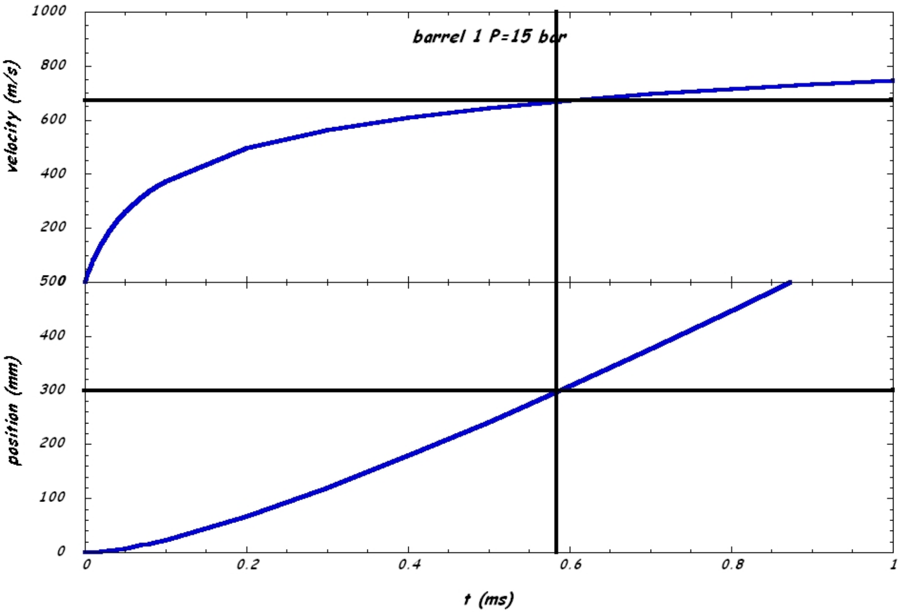

Figure 5.9: On the top equation 5.1 evaluated for neon as driver gas and pellet fired from barrel 1. The driver gas pressure is 15 *bar*. At the bottom its integration. The red lines correspond to the barrel length.

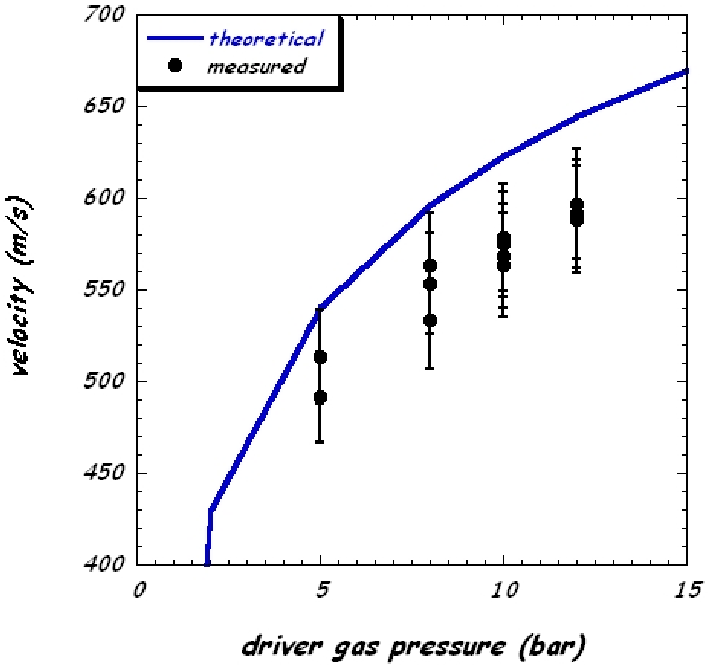

Figure 5.10: Comparison between the pellet velocity measured for pellet injected from barrel 1 and the velocity predicted by equation 5.1.

5.2 Gas puffing

The gas puffing fuelling technique consists into the injection of gas during the plasma discharges. On RFX-mod the gas injection system is arranged in four injection groups of gas valves [85]. Each group entails four Maxtek [86] piezoelectric valves, it is installed on the RFX-mod top portholes of the vacuum vessel. Groups are equally spaced in the toroidal direction at 90° from each other. The sixteen valves are arranged in two different groups, eight forms the so called *filling* group, whereas the remaining eight form the *puffing* group. The difference between the two groups is that they were designed to be fed by two different power supply: the filling limited to 100 V and the puffing to 170 V. The reason was that the filling valves should be used to fill the vacuum vessel at the desired pressure before the plasma pulse, while the puffing ones should be used for very short time periods with higher voltage during the plasma pulse to sustain the density. After a damage to the valves caused by the application of the maximum voltage continuously, the two valves system were modified and the maximum applied voltage was limited for both at 120 V.

With this gas injection system the amount of injected gas depends on the voltage applied to the valves, the duration of their aperture and the pressure of the gas. The two quantities that can be directly controlled are the voltage applied and the aperture time of the valves. A calibration table of the valves has been compiled measuring the dependence of the amount of molecules injected in RFX-mod in function of the aperture time at fixed voltage. Thus, using that calibration tables it is possible to pre-program the amount of gas injected inside the vessel.

It was observed that the valves, after a relatively long period of stand-by, are characterized by a lower gas flow compared to that one obtained during continuous operation [85]. Moreover the gas pressure depends on several elements, it is not always the same, so it is possible that the same voltage and aperture time of the valves does not correspond to the same amount of injected particles. Since in RFX-mod gas injection is done in a pre-programmed way both for the initial filling of the vacuum vessel and for the subsequent gas puffing during the discharge, it is possible calibrate by performing a dummy gas injection flux before the discharge applying the same voltage to the valves. To do that it has been installed on RFX-mod a diagnostic system called *DESO* [64], described in the following section, that measures the change in pressure in the vacuum vessel at each pulse.

5.2.1 Diagnostic of Desorption

The diagnostic system to study the desorption (DESO) is devoted to allow a precise fuelling and a better density control during operations. It works as follow: just before each RFX-mod discharge DESO executes a sequence of three dummy openings of the piezo valves to keep them in an operating state that assure a reproducibility within 10% on their flow. Then it executes the same opening of the valves scheduled for the nex discharge and computes, from the measure of the pressure, the time evolution of the flux of particles entering the vessel. After the end of the pulse DESO calculates the neutral gas extracted from the vacuum vessel after the plasma discharge. The ratio between the fuelled particles and those extracted is called *Desorption factor*, *Des*%. The Desorption factor can be used as an indicator of the state of the wall: a value below 100% corresponds to the capability of the wall to behave as a particle adsorber, and hence to a not saturated wall, whereas a 100% value corresponds to a saturated graphite that at the end of the discharge gives back all the fuelled particles.

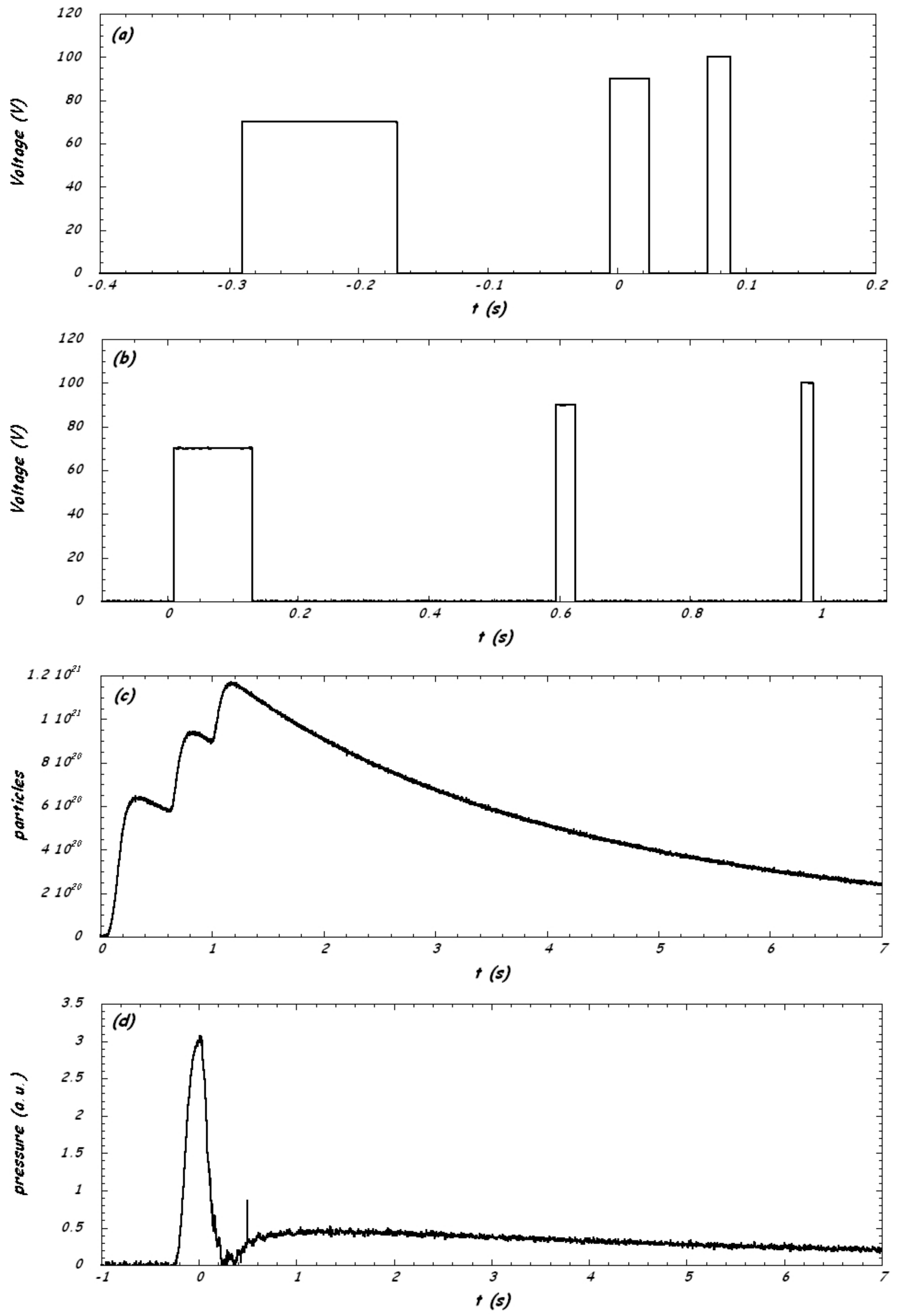

Figure 5.11: Example of DESO measurement in RFX-mod pulse #29990. In (a) there is the voltage applied to the valves during the discharge, in (b) the voltage applied to the piezo valves for the DESO measurement to reproduce the gas injection scheduled for the discharge, in (c) the time evolution of the molecules injected in the vessel calculated from the measure of the pressure variation and in (d) the vessel pressure during and after the discharge.

In figure 5.11 there is an example of the measurements done with DESO in the RFX-mod pulse #29990. In figure 5.11 (a) there is the voltage applied to the valves during the discharge, in figure 5.11 (b) the voltage applied to the piezo valves to reproduce the gas injection scheduled for the discharge for the DESO measurement. The time lag between the opening of the valves is larger for the test puffing, in order to allow the pumping system to evacuate part of the particles, avoiding in this way the saturation of the signal coming from pressure gauge.

Discharge #29990 is an example of those execute to compare the effectiveness o density control by pellet injection and gas puffing. In the discharge there was two standard gas injections: a puffing at $-0.3\ s$ as initial filling of the vacuum vessel for discharge breakdown and a puffing at $0\ s$ to provide particles during the discharge start-up phase. Then for pellet injection comparison there is a puffing from $0.07\ s$ to $0.088\ s$ at $100\ V$ to simulate the injection of a large pellet. In figure 5.11 (c) there is the time evolution of the number of molecules injected in the vessel during the opening of the piezo valves calculated from the pressure measurement. The three steps correspond to the three aperture of the valves. The jumps provide the amount of molecules injected on each opening. In this case the third jump is $\Delta H_2 = 2.6 \times 10^{20}$ molecules that correspond to the desired amount. In figure 5.11 (d) it is drawn the vessel pressure during and after the discharge, the first peak corresponds to filling gas injection while the smooth decreasing curve corresponds to the slow gas release from the wall; the nearly zero pressure measured just after the discharge shows the wall adsorption effectiveness.

5.3 Comparison of refueling techniques

The aim of the comparison between the two techniques is to find the better solution to perform the density control in RFX-mod with the minimum discharge perturbation and the minimum amount of particles embedded on graphite tiles.

To compare the two refueling techniques in terms of discharge perturbation and of refueling efficiency, several discharges have been executed fueling plasma by means of pellet injection and of an equivalent number of particles injected by gas puffing. The comparison have been done only for medium and big pellets, since the small ones have a too small amount of particles to be reproduced in a reliable way by gas puffing.

Discharges with gas puffing have been performed at four different values of valves voltage, $70V$, $90V$, $100V$ and $120V$, corresponding to a particle flux of $\Gamma = 0.9 \times 10^{22} s^{-1}$, $\Gamma = 2.2 \times 10^{22} s^{-1}$, $\Gamma = 3 \times 10^{22} s^{-1}$ and $\Gamma = 5.6 \times 10^{22} s^{-1}$ respectively. The opening time of the piezo valves was chosen to provide a number of puffed particles equal to the quantity of particles injected by the pellets. Plasma current was about $I_p \simeq 1.2\, MA$ on each pulse. In table 5.2 there are the features of the analyzed discharges.

shot	voltage (V)	opening time (ms)	starting time (ms)	atoms injected ($\times 10^{20} atoms$)	particle flux ($\times 10^{22}\, s^{-1}$)
30065	70	40	70	3.6	$\Gamma = 0.9$
29995	90	16	70	3.5	$\Gamma = 2.2$
29994	100	12	70	3.6	$\Gamma = 3$
30056	120	6	70	3.4	$\Gamma = 5.6$
30066	MEDIUM PELLET		150	3.1	
29998	70	56	70	5.1	$\Gamma = 0.9$
29992	90	21	70	4.6	$\Gamma = 2.2$
29990	100	18	70	5.3	$\Gamma = 3$
30060	120	9	70	5	$\Gamma = 5.6$
30052	LARGE PELLET		70	5.3	

Table 5.2: Database of the refueling experimental test.

5.3.1 Plasma response

The discharge perturbation is evaluated in a qualitative way in terms of time evolution of the average electron density, the average electron temperature and the electron density radial profile. This because on RFX-mod there is a relatively high irreproducibility from pulse to pulse, so usually the ensamble average values are used. In this case there is only a small amount of data available to perform a statistical analysis, therefore it has been chosen to use "typical" discharges. "Typical" meaning discharges that are situated in the most populated density and plasma current range.

In figure 5.12 and 5.13 are shown on the left the time evolution of the electron density measured by the central chord of the multi-chord interferometer [50] and on the right the highlighted regions expanded. In the figures on the right it is shown the average electron density and the gas puffing time is highlighted. Figure 5.12 is related to the injection of about $3.5 \times 10^{20}\, atoms$ and figure 5.13 to the injection of about $5 \times 10^{20}\, atoms$. In the figures are drawn the cases with a particle flux $\Gamma = 0.9 \times 10^{22} s^{-1}$, $\Gamma = 5.6 \times 10^{22} s^{-1}$ and the pellet case.

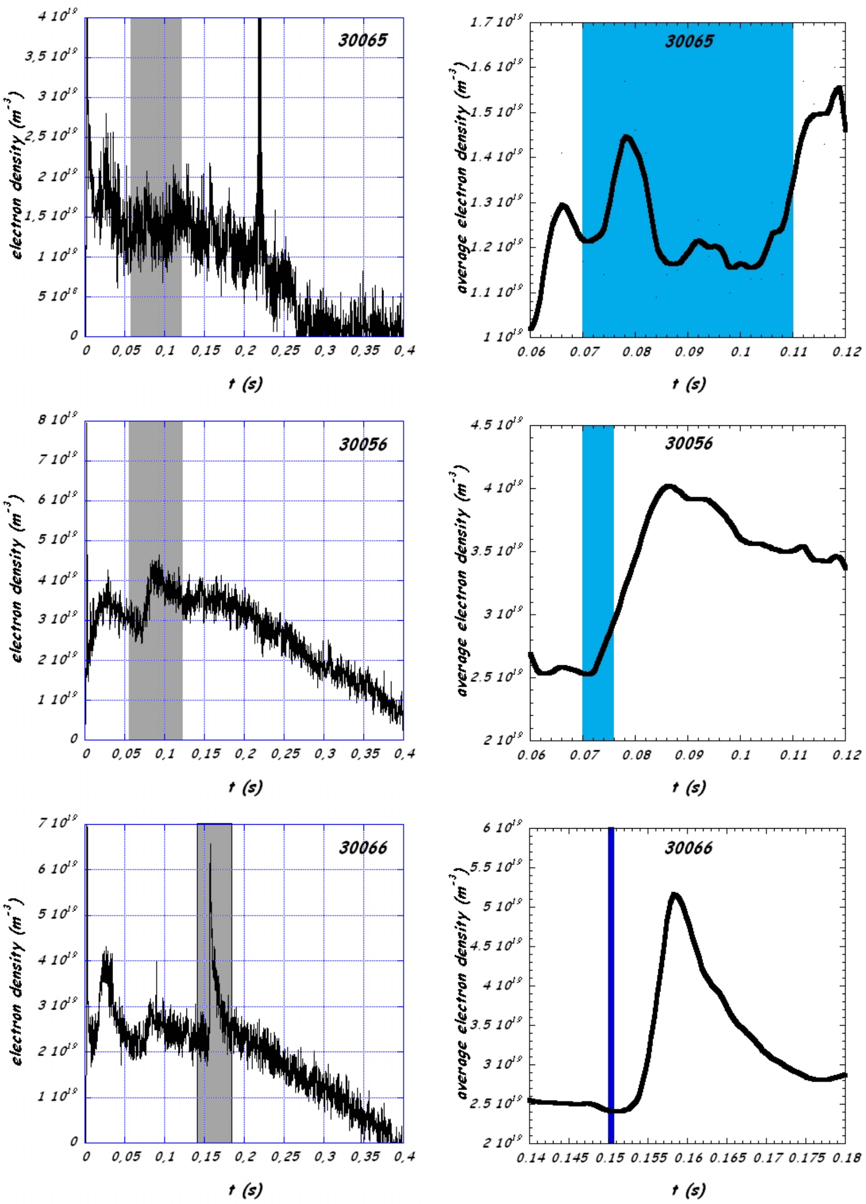

Figure 5.12: On the left the time evolution of the electron density measured by the chord number four of the multi-chord interferometer of RFX-mod. On the right the highlighted regions are expanded and the average electron density is plotted instead of the density measured by chord 4. The cyan region highlights the gas puffing duration or thepellet injection time. The amount of particles injected is about 3.5×10^{20} *atoms*.

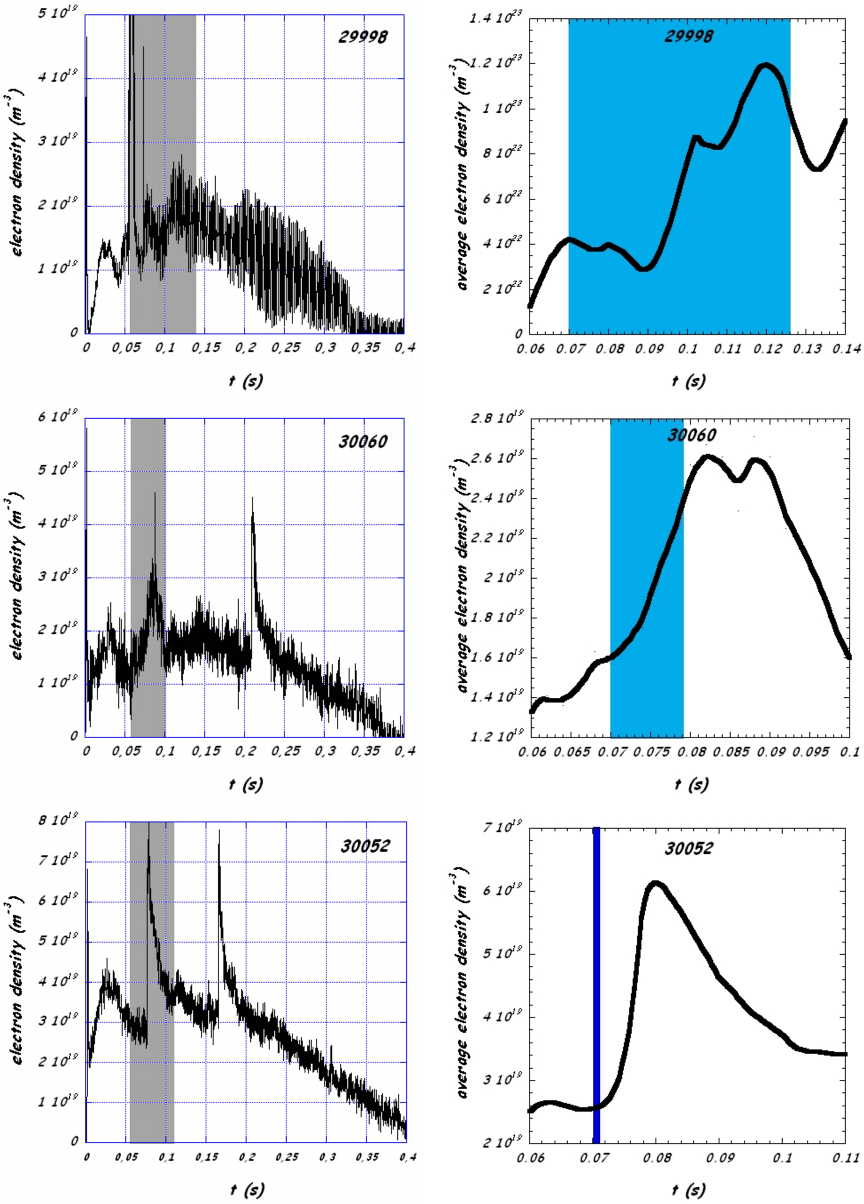

Figure 5.13: On the left the time evolution of the electron density measured by the chord number four of the multi-chord interferometer of RFX-mod. On the right the highlighted regions are expanded and the average electron density is plotted instead of the density measured by chord 4. The cyan region highlights the gas puffing duration or thepellet injection time. The amount of particles injected is about 5×10^{20} *atoms*.

The general behavior is that the average density increases after the refueling. The increase of the average electron density is much higher than density fluctuation in case of pellet injection and of high particle flux, while in the case of low particle flux the density increase is mixed with plasma density fluctuations, because of the long gas puffing time. Conversely, only pellet injection affects the average electron temperature.

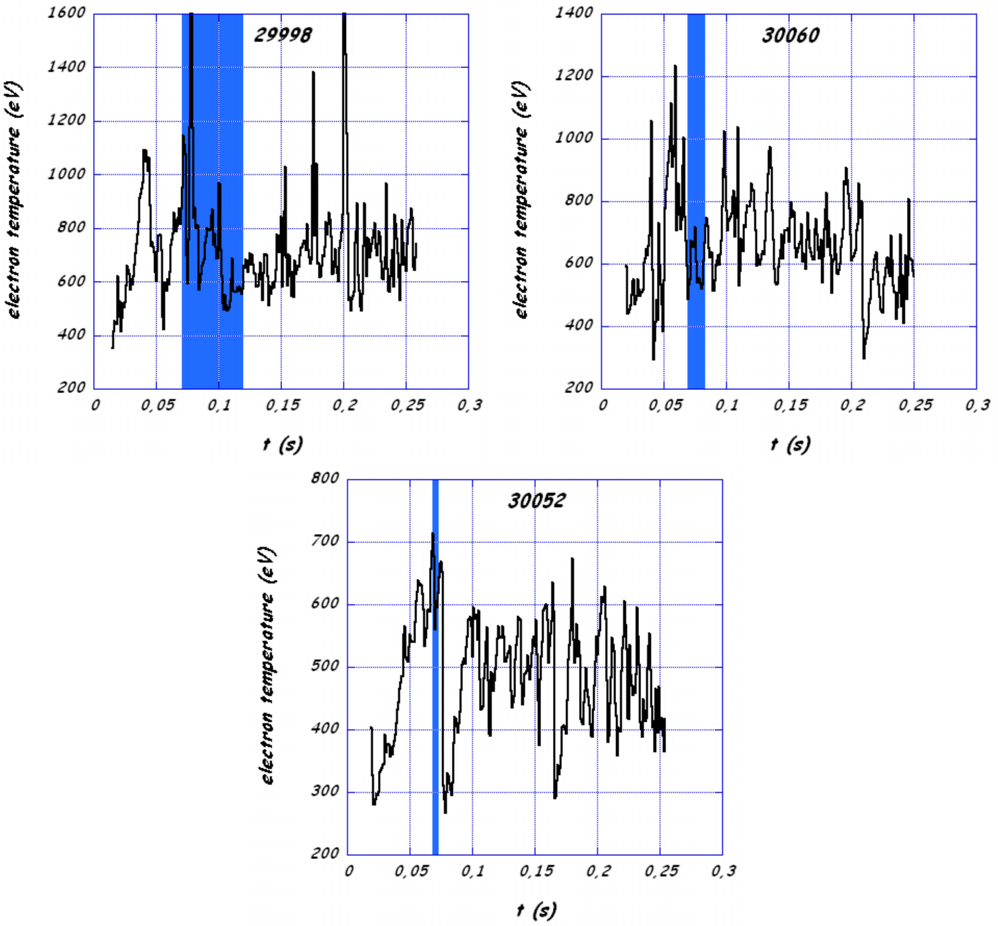

Figure 5.14: Temporal evolution of the global electron temperature measured with the double filter technique. The cyan region highlights the gas puffing duration or the pellet injection time. The amount of particles injected is about $5 \times 10^{20}\,atoms$.

The time evolution of the global electron temperature measured with the double filter technique [87] is shown in figure 5.14 with the injection of about $5\times10^{20} atoms$. The gas puffing time is highlighted in cyan. The first two plots are related to the gas puffing. The decrease of the temperature in discharge

#29998 is related to the plasma evolution since it happens during the gas puffing but also at a crash of the QSH state. In discharge #30052 instead the decrease of the electron temperature is much higher than fluctuations and then it remains lower than before the pellet injection.

Information on the position of the particles deposition can be extracted from the electron density contour plots of figure 5.15. The x-axis is the plasma radius, the y-axis is the time and the colour represents electron density value.

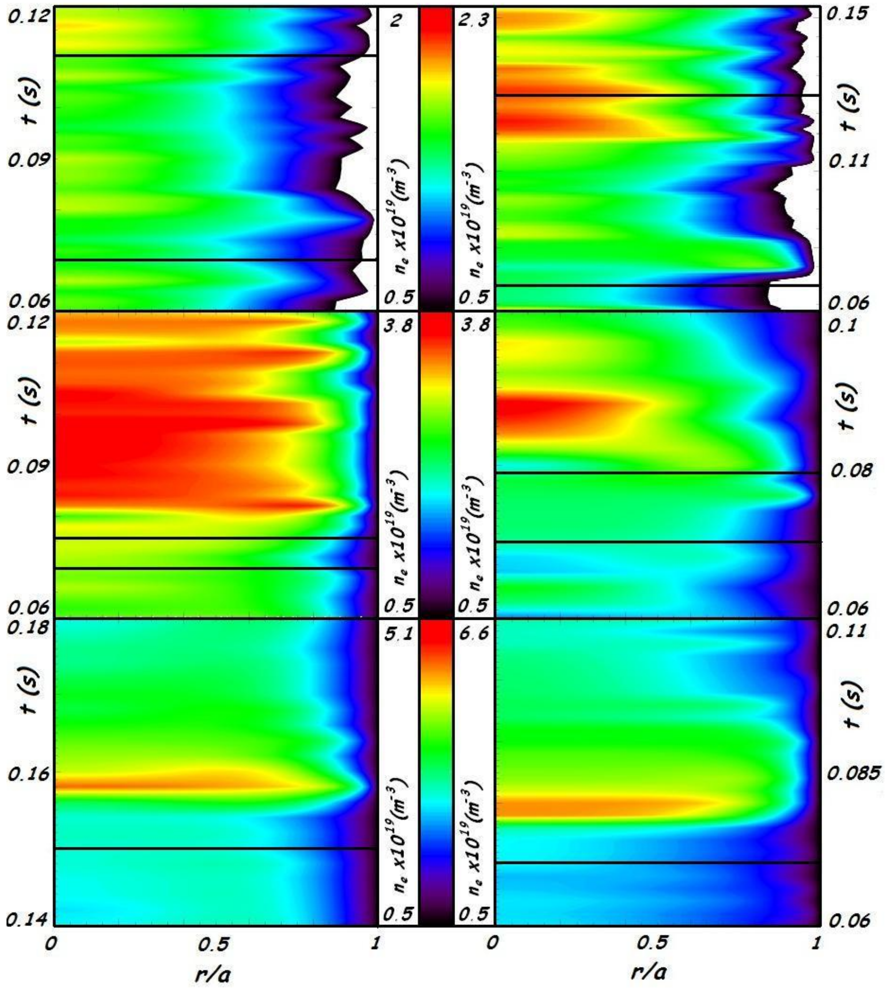

Figure 5.15: Electron density radial profile evolution. X-axis is plasma radius, y-axis time and colours the electron density. On the left, from the top, discharges #30065, #30056 and #30066, on the right #29998, #30060 and #30052.

The profile in the case of lower particles flux is not modified by the refueling, independently from the amount of total particles injected. Increasing the particles flux there is a density increase at the edge that moves to the core at a further step of the influx. It can be seen in the two plots in the middle of figure 5.15, the cases of highest flux. Here, a region of high density appears at the edge in correspondence of the gas puffing. This region of high density then moves to the center. Pellet injection deposes the particle directly in the plasma core in both the cases.

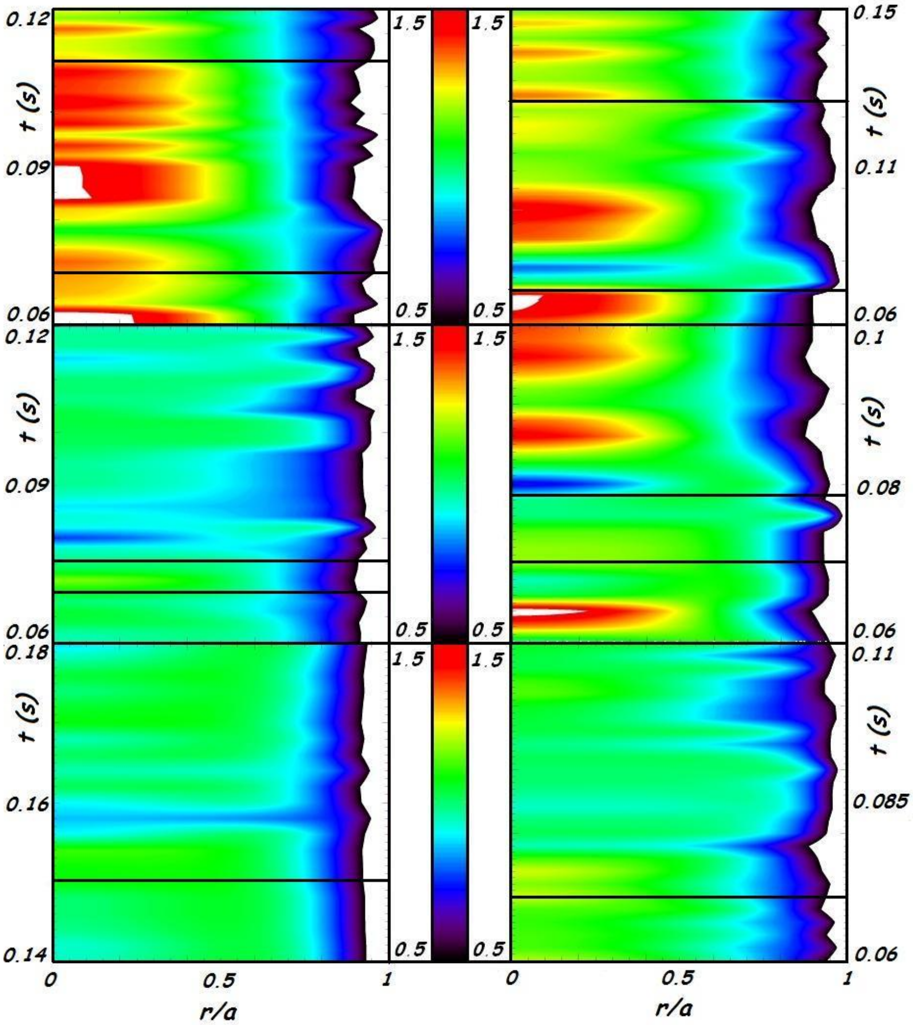

Figure 5.16: Electron density radial profile evolution normalized over the average electron density. X-axis is plasma radius, y-axis time and colours the ratio $\frac{n_e(r)}{<n_e>}$. On the left, from the top, discharges #30065, #30056 and #30066, on the right #29998, #30060 and #30052.

A confirm of the behavior described is seen in figure 5.16, where is drawn the time evolution of the electron density normalized over the average electron density. The profile shape is not modified by the puffing in the case of low flux and small amount of injected particles. In all the other three cases it is possible to notice that in correspondence of the gas puffing the profile becomes hollow (there is a blue region in the center) and then the profile comes back to the previous situation. This is explained by the fact that the gas entering the plasma is ionized at the edge and then stuck in the tiles. In this way there is an instantaneous increasing of the edge electron density and then the plasma follows its normal evolution but with an higher reservoir of particles from which to draw.

5.3.2 Refueling efficiency

The previous analysis provided an overview of the effects on plasma behavior. To evaluate the effective influence of the gas puffing and pellet injection it has been studied the efficiency parameter. To study the refueling efficiency it has been considered that the variation of the density on time ($\frac{dN}{dt}$) depends on the particles confinement time τ_p, the hydrogen influx from the wall Γ_{wall} and the flux due to the refueling $\Gamma_{puffing}$ according to the equation:

$$\frac{dN}{dt} = -\frac{N}{\tau_p} + \Gamma_{wall} + \alpha\Gamma_{puffing} \tag{5.5}$$

where N is the average density and α is the refueling efficiency, that gives the ratio of the injected particles that enter the plasma before being adsorbed by the wall.

To compute the equation 5.5 it is not possible to consider the density derivative because of the fluctuations, therefore the variation of the density on time is considered as the increase of density during the refueling divided by the refueling duration. The hydrogen influx from the wall, Γ_{wall}, comes from the measurements of the H_α emission at the edge, the flux due to the refueling from DESO measurements. In figure 5.17 it is plotted the efficiency α as function of the particles flux.

With the pellet injection the refueling efficiency is close to one, which means that all the particles injected are ionized and deposited in the plasma. The refueling by gas puffing has an average efficiency of about 0.4 apart for the case of pulse #30065 ($\Gamma = 0.9 \times 10^{22}\ s^{-1}; 3.5 \times 10^{20}\ atoms\ injected$), this means that less than one half of the particles injected contributes to the plasma density. To explain the efficiency of the discharge #30065 it has to be considered that there is an electron density increase that is one

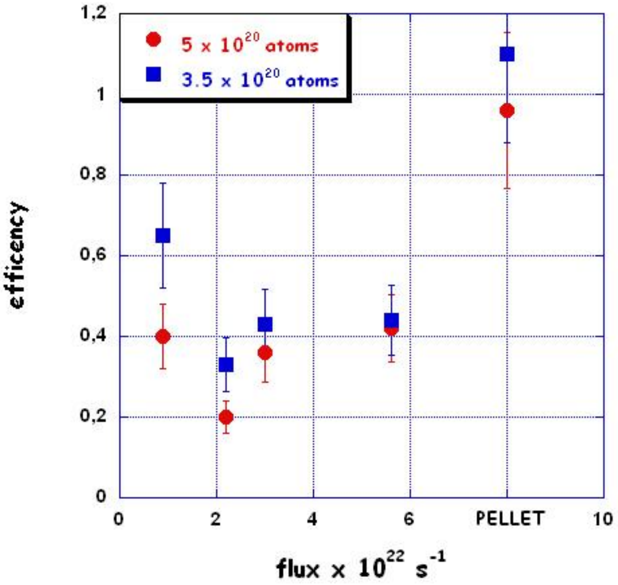

Figure 5.17: Efficiency as function of particles flux. The error bars consider a 20% of error in calibration of the H_α diagnostic.

order of magnitude less than all the other cases, and the time in which it happens is about 40 ms. During this time the plasma evolution leads to several phenomena that make the equation 5.5 to be too simple to describe the situation. The same has to be taken into account for the discharge #29998 ($\Gamma = 0.9 \times 10^{22}\, s^{-1}; 5 \times 10^{20}\, atoms\, injected$).

In equation 5.5 the particle influx coming from the wall can also be written as a recycling term:

$$\frac{dN}{dt} = -(1-R)\frac{N}{\tau_p} + \alpha\Gamma_{puffing} \tag{5.6}$$

Using the efficiency coefficient calculated before, the recycling coefficient as function of the particles flux is plotted in figure 5.18.

Recycling coefficient is typically between 0.7 and 1, but in the case with the higher particle influx the recycling coefficient drops to values of about 0.5. Also in the case of medium pellet injection the recycling coefficient is higher than the typical values. A recycling coefficient lower than one means an high adsorption of particles from the wall with respect to the desorption. It is in agreement with the observation of a peaked density profile in case of higher particle flux. A recycling coefficient lower than one, with an efficiency of about 0.4, means that lots of the particles injected by gas puffing are stored in the graphite without a beneficial effect on density control.

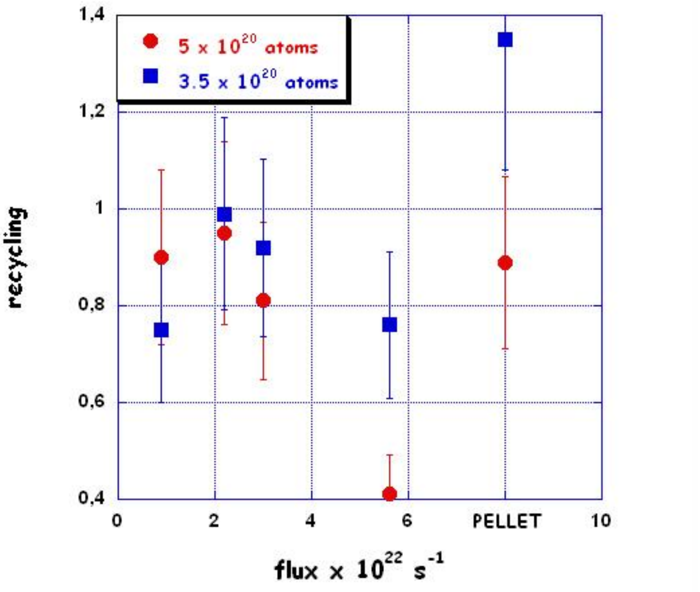

Figure 5.18: Recycling as function of the particles flux.

5.4 Conclusions

The aim of the experiments with different refueling techniques was to improve the density control over an higher number of discharges relative to that after a wall conditioning. To do that it has been compared gas puffing and hydrogen pellet injection refueling techniques in terms of both plasma response and efficiency. The pellet injection techniques has been found to be more efficient of the gas puffing techniques since all the particles injected are ionized and then contribute to the plasma density, instead with the gas puffing only less than the 50% of the injected particles once ionized are seen to increase of the average plasma density.

About the plasma response it has been noticed that it is not affected by a low particle influx when the amount of particles injected is not too high. When the particles flux is high enough the wall is no more able to provide a recycling factor of about 1. The pellet injection instead leads to an immediate modification of the radial electron density profile and after the particles diffusion time the profile comes back to the initial situation but at an higher average electron density. It was then observed that only pellet injection affects the average electron temperature.

Summarizing, the best refueling technique both from the efficiency and the perturbation point of view is the hydrogen pellet injection as it was expected. In the event that gas puffing was request to avoid the crash in temperature or to furnish a different amount of particles from the fixed one of pellets, the best choice is the one with the lowest influx. Indeed in this case there is not a big perturbation of plasma behavior and the efficiency is the same if not higher than the other particles influx.

Joint European Torus Edge Modeling

The **J**oint **E**uropean **T**orus (JET), is the largest Tokamak device with a poloidal divertor configuration. In this chapter will be presented the modeling of JET Scrape-Off Layer done with EDGE2D-EIRENE [88, 89]. The aims of this modeling are: the study of the dependence of power deposition on the outer target from the main plasma features, to test the range of convergence of the code and the study of the range of validity of the Two Point Model.

In section 6.1 will be presented the Two Point Model and its predictions and in section 6.2 will be presented several density scan to study what happens at the target plates with different density in the core. The scan are performed varying the deuterium gas injection both in terms of particles influx and of injecting position.

6.1 Two Point Model

One of the main aim of using a divertor is to achieve a large temperature drop along the length of the SOL, with a low plasma temperature at the target end, $T_t \lesssim 10\ eV$, to reduce the heat load on the solid materials, maintaining at the same time sufficient performance in the main plasma.

The simplest divertor model that can be used is a zero-dimensional one that links the conditions in the main plasma with those at the target [90]. This model, called *Two Point Model*, does not attempt to model the physical quantities as function of the parallel distance along the SOL, but it relates the conditions between two points, *upstream* and *target*. Considering a single-null poloidal divertor geometry, the upstream location u is the half-way point between the targets (see figure 6.1). Since calculated parallel gradients are usually small at locations far from the targets, the precise location chosen to represent the upstream region is not critical, therefore it is usually chosen as upstream region the equatorial plain instead of the half-way point between the targets.

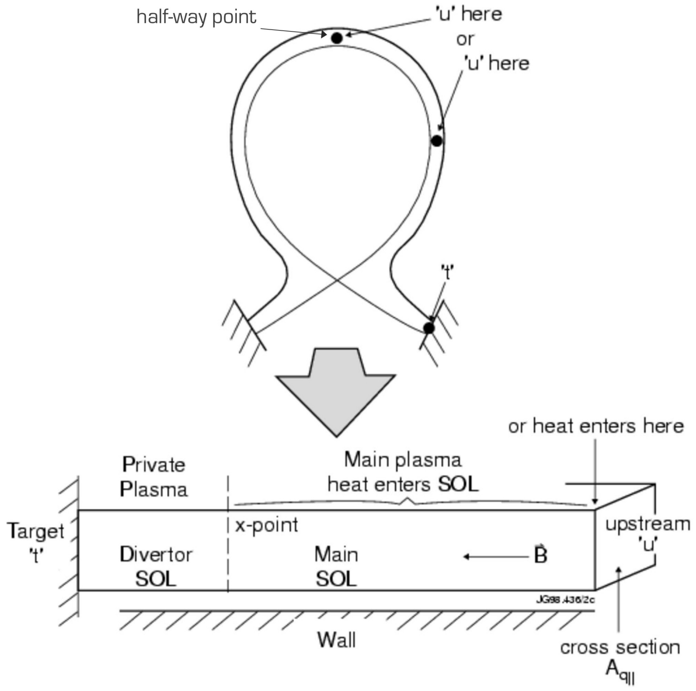

Figure 6.1: Position of the upstream point u and target point t in the single-null poloidal divertor geometry. At the bottom it is rappresented the divertor SOL straightened out for the simple modeling pourposes.

The main assumptions for the *two point model* are described below.

Particle balance It is assumed that neutrals recycling from the target are all ionized in a thin layer immediately in front of the target. Moreover, a neutral which resulted from a ion impacting the target while travelling along a magnetic field line, is assumed to be re-ionized on that same field line. Therefore in steady state each flux tube has its own particle balance, with the same particles just recycling over and over. It leads to a parallel plasma flow only in a very thin layer between the ionization point and the target. With these assumptions the particle balance is purely one dimensional and there is no volume recombination, being the target the only particle sink.

Pressure balance It is assumed that there is no friction between the plasma flow in the thin ionization region and the target. Thus through the entire length of each SOL flux tube $p_{static} + p_{dyn}$ is constant. Moreover it is assumed $T_i = T_e$, therefore the plasma static pressure is

$$p = nkT_e + nkT_i = 2nkT. \tag{6.1}$$

and the dynamic pressure is

$$p_{dyn} = mnv^2 . \tag{6.2}$$

The entire length of the flux tube from the upstream region to the start of the thin ionization region is characterized by a velocity $v = 0$ and at the target $v = c_s = (2kT_t/m_i)^{1/2}$ from the Bohm criterion [30] (see section 2.1). Therefore the pressure balance can be written as

$$2n_tT_t = n_uT_u \tag{6.3}$$

Power balance Since $v = 0$ over almost the entire length L of the flux tube, parallel heat convection is absent and the parallel power flux density $q_\parallel$ is carried by conduction. If it is assumed that $q_\parallel$ entered entirely at the upstream end it is removed at the target, it is possible to write for the temperature [90]:

$$T_u^{7/2} = T_t^{7/2} + \frac{7}{2}\frac{q_\parallel L}{k_{0e}} \tag{6.4}$$

where the electron parallel conductivity coefficient $k_{0e} \approx 2000$ in case of T expressed in $[eV]$, $q_\parallel$ in $[Wm^{-2}]$ and L in $[m]$. Moreover, in principle there is a temperature change across the ionization zone, but, as this is taken to be a very thin region, this is ignored and thus T_t can be considered equal to the temperature at the target sheath edge. Therefore also $q_\parallel$ can be considered equal to heat flux entering the sheath q_t:

$$q_\parallel = q_t = \gamma n_t k T_t c_{st} \tag{6.5}$$

with γ the sheath heat transmission coefficient.

Summarizing the assumptions: the 2 point model is described by the three equations 6.6 with three unknowns, n_t, T_t and T_u, controlled by the independent parameters n_u and $q_\parallel$. L, γ and k_{0e} are specified constants of the problem.

$$\begin{cases} 2n_tT_t = n_uT_u \\ T_u^{7/2} = T_t^{7/2} + \frac{7}{2}\frac{q_\parallel L}{k_{0e}} \\ q_\parallel = \gamma n_t k T_t c_{st} \end{cases} \tag{6.6}$$

6.2 Effect of a density scan on the SOL

The overall effect of increasing the upstream density is that the temperature at the target plates decreases, passing through the three different divertor regimes: the *sheath-limited*, the *conduction-limited* and the *detached* one. The three regimes are characterized respectively by low density-high temperature, high density-low temperature and low density-low temperature at the target plates. It follows from equation (6.5) that the power deposited on the target is strictly related to the density and the temperature on the target, so to reduce the power deposited on the target it is necessary to reduce at least one of the two.

In order to test if the code is able to reproduce the three divertor regimes, to find when the two point model can be used to predict the temperature on the target plates and to study the general effects on the SOL due to the increase of the core plasma density a density scan was performed. To perform the scan, the JET discharge #78647 has been chosen as reference case. The features of the case are:

- a typical JET geometry;
- a pure deuterium plasma with no impurities;
- a core power $P_{core} = 2.16\,MW$ equally divided by electrons and ions ($P_i^{CORE} = P_e^{CORE} = 1.08\,MW$);
- cross-field particle transport coefficient $D_\perp = 1\,m^2/s$ (at the separatrix position it is set at $D_\perp^{LCFS} = 0.5\,m^2/s$);
- cross-field thermal transport coefficients $\chi_e^{CORE} = \chi_i^{CORE} = 1\,m^2/s$ inside the separatrix and $\chi_e^{SOL} = \chi_i^{SOL} = 0.5\,m^2/s$ outside;
- pumping in the right corner of the outer target (in blue in figure 6.2), with a pumping albedo $AoP = 94\%$;
- a gas injection from the top (in red in figure 6.2);
- 4000 neutrals history followed by mean of the EIRENE Monte Carlo neutral code.

The density has been changed varying the deuterium influx, from $\Gamma_{D_2} = 2.5 \times 10^{20}\,s^{-1}$ up to $\Gamma_{D_2} = 8 \times 10^{21}\,s^{-1}$. The geometry of the case is shown in figure 6.2.

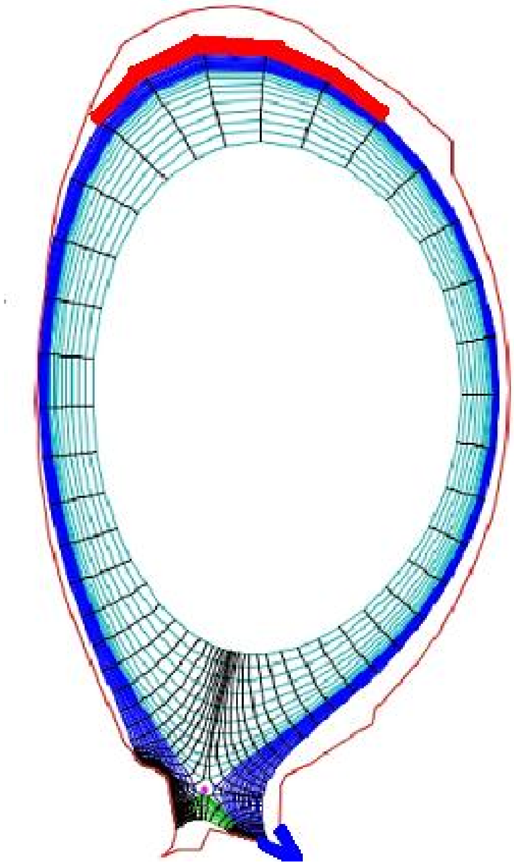

Figure 6.2: Grid of the reference case JET #78647. In red the deuterium puffing position, in blue the pumping region.

6.2.1 Convergence of the code

To ensure the validity of the obtained results the range of convergence of the code has been tested. The first observation is that the code achieves the so called *density limit*, i.e. it does not converge, when deuterium influx $\Gamma_{D_2} > 7 \times 10^{21}\, s^{-1}$. The quality of the convergence can be estimated from the fluctuation of the solution. In figure 6.3 the time evolution of the electron density at the outer target is plotted as function of the time steps. The green line corresponds to a deuterium influx of $\Gamma_{D_2} = 4.5 \times 10^{21}\ s^{-1}$, the black one to $\Gamma_{D_2} = 7 \times 10^{21}\ s^{-1}$. It is possible to notice that increasing the density the convergence of the solution get worse. A way to get a better convergence is to increase the statistic by considering a larger number of neutrals. This is confirmed by the red trace in figure 6.3 which is the time evolution of the electron density with $\Gamma_{D_2} = 7 \times 10^{21}\, s^{-1}$ but following 10000 neutrals. The drawback of an high number of neutrals is the large increase of the computational time.

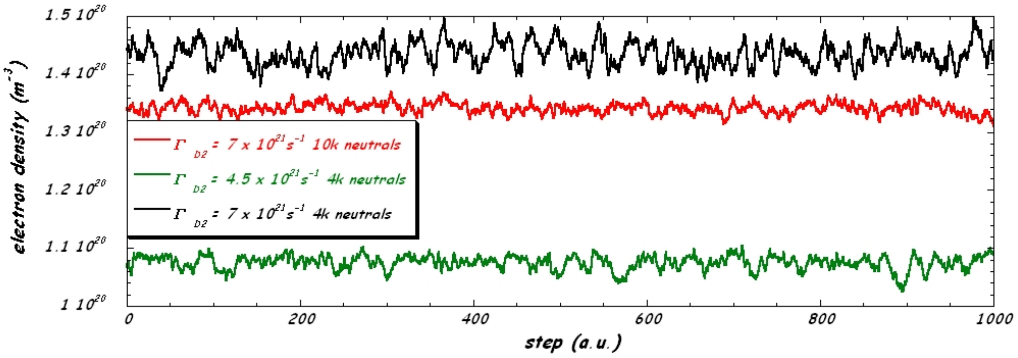

Figure 6.3: Time traces of the electron density on the outer target.The green line corresponds to a deuterium influx of $\Gamma_{D_2} = 4.5 \times 10^{21}\ s^{-1}$ with 4000 neutrals, the black one to $\Gamma_{D_2} = 7 \times 10^{21}\ s^{-1}$ with 4000 neutrals, the red trace to $\Gamma_{D_2} = 7 \times 10^{21}\ s^{-1}$ with 10000 neutrals.

The deuterium influx range where considering 4000 neutrals leads to a stable solution has been studied also performing a density scan with 6000 and 10000 neutrals. Since the convergence get worse only at high influx values and with the highest number of neutrals it is needed up to more than a week of computational time, the scans have been performed at different influx ranges and with different influx steps. A higher resolution was used where a different number of neutrals led to a different solution. The scan are summarized in table 6.1.

neutrals $\times 1000$	Γ_{D_2} min $\times 10^{21}\ s^{-1}$	Γ_{D_2} max $\times 10^{21}\ s^{-1}$	step $\times 10^{21}\ s^{-1}$
6	3	8	0.5
10	4	8	1
10	6	7	0.25
13	5.5	7	0.5
16	5.5	7	0.5

Table 6.1: Density scan performed considering more than 4000 neutrals.

The set of scans confirms that the code is not able to deal with $\Gamma_{D_2} > 7 \times 10^{21}\ s^{-1}$. The neutral scan moreover highlights that with a deuterium influx greater than $5 \times 10^{21}\ s^{-1}$ with 10000 neutrals the solutions is different from that obtained using less neutrals. To verify that the right solution is the one with the highest number of neutrals, other two scans have been done considering 13000 and 16000 neutrals. Their features are in table 6.1. The results of the neutral scan is plotted in figure 6.4, where the computed density in the upstream region is drawn versus the deuterium influx. The values chosen to represent the density are related to the first cell outside the LCFS. This convention will be used for all the plots of this chapter.

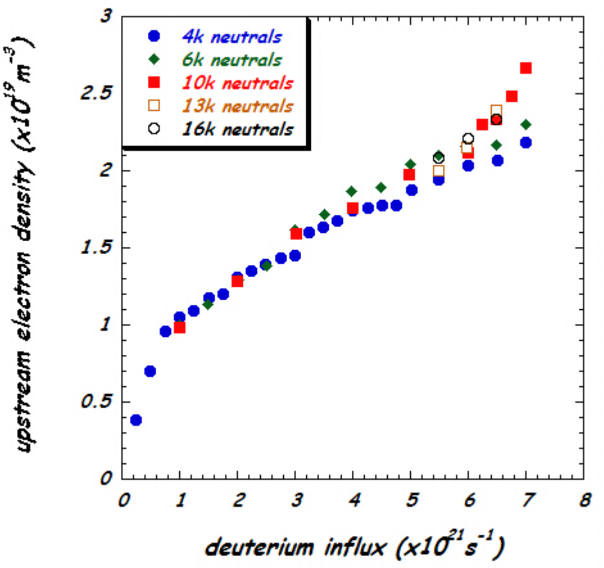

Figure 6.4: Electron density in the upstream region as function of the particles influx for different number of neutrals followed.

The density scan with several number of neutrals followed shows that with $\Gamma_{D_2} > 5 \times 10^{21}\, s^{-1}$ it is necessary to consider at least 10000 neutrals to have a solution with correct values of the several physical quantities. Since the aim of the study is the relation between the quantity in the outer target region and the density and temperature in the upstream region are of interest, it has been evaluated if also it is affected from the numbers of neutral considered.

In figures 6.5 and 6.6 the electron density and temperature at the outer target are plotted as function of the electron density in the upstream region. From these two plots it follows that the relation between the electron temperature at the target and the electron density in the upstream region is not affected by the number of neutrals considered. Some differences are shown in the relation between the electron density at the target and the electron density in the upstream region. For values of electron density $n_u \leq 2 \times 10^{19}\, m^{-3}$ there is not any appreciable difference in case of different number of neutrals followed. When the electron density in the upstream region exceeds this value the electron density at the target achieves a

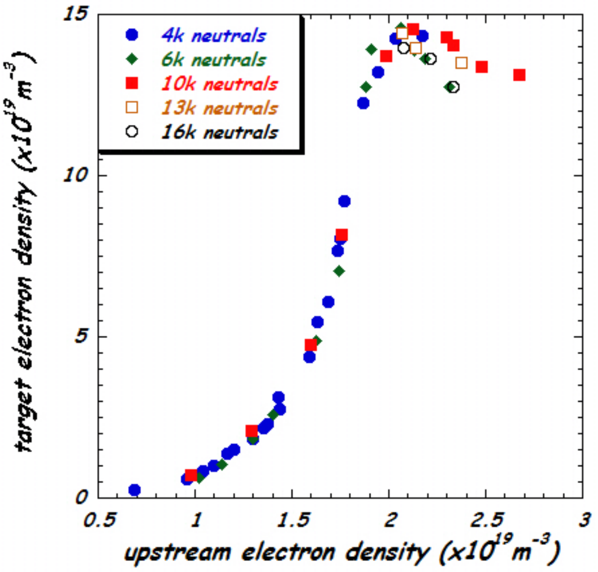

Figure 6.5: Electron density at the outer target as function of the electron density in the upstream region, for different numbers of neutrals followed.

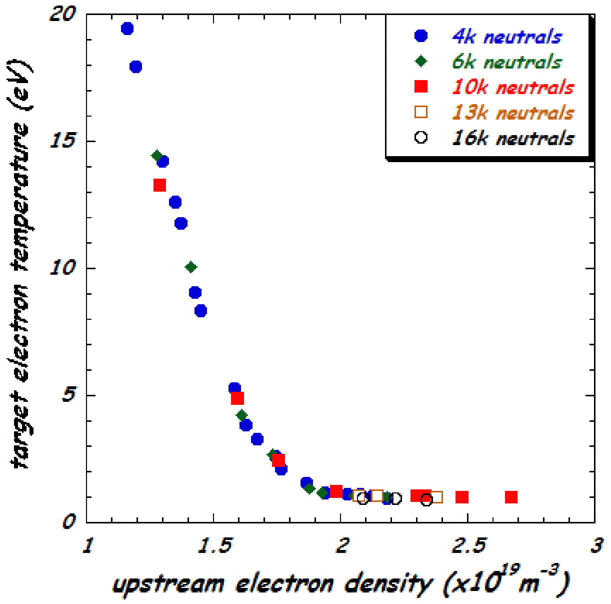

Figure 6.6: Electron temperature at the outer target as function of the electron density in the upstream region, for different numbers of neutrals followed.

maximum and then it starts to decrease. This behavior corresponds also to the decrease of the electron temperature at the target under $T_e = 1\,eV$. It is known from the theory and from the experiments that this situation happens when the plasma moves to the detached divertor regime, where the temperature at the target is under $1\,eV$ and the electron density at the divertor plates decreases because the ionization layer moves up to the X-point. Also increasing the number of followed neutrals there is a great indetermination in the electron density at the target when the density in the upstream region is greater than $2 \times 10^{19}\,m^{-3}$. It is possible to conclude that the code is not able to deal with the low target temperature-low target density scenario, that corresponds to the detached divertor regime.

Starting from the above results, for the aim of this study it is sufficient to perform the density scan following 4000 neutrals.

6.2.2 Comparison with the *two point model*

Starting from the equations of the basic two point model (6.6) it is possible to write all the quantities at the target as function of the control parameters, i.e. the upstream electron density n_u and the parallel power flux density $q_\parallel$ can be directly related with the two principal control knobs of a discharge: the main plasma average electron density and the input power respectively. Considering that $T_u^{7/2} \gg T_t^{7/2}$ [90] it is also possible to write the parallel power flux density as function of the electron temperature in the upstream region, so the equations of the two point model becomes:

$$\begin{cases} q_\parallel \approx T_u^{7/2} \dfrac{2k_{0e}}{7L} \\ n_t = \left(\dfrac{n_u T_u}{2} \gamma k \right)^2 \dfrac{k n_u {T_u}^2}{m_i q_\parallel} \\ T_t = \dfrac{n_u T_u}{2n_t}. \end{cases} \tag{6.7}$$

The simplest comparison between the two point model and the code simulations that can be done is on the density at the target as function of the density in the upstream region. This is shown in figure 6.7.

The solid line is the prediction of the two point model, the stars are the values computed by the simulations. The prediction of the model is correct only at very low upstream density. At medium density the dependence $n_t \propto n_u^3$ can be considered still valid, but at $n_u \geq 1.8 \times 10^{19}\,m^{-3}$ the model is not able to predict the detached regime. This is in agreement with the assumptions done for the model in paragraph 6.1.

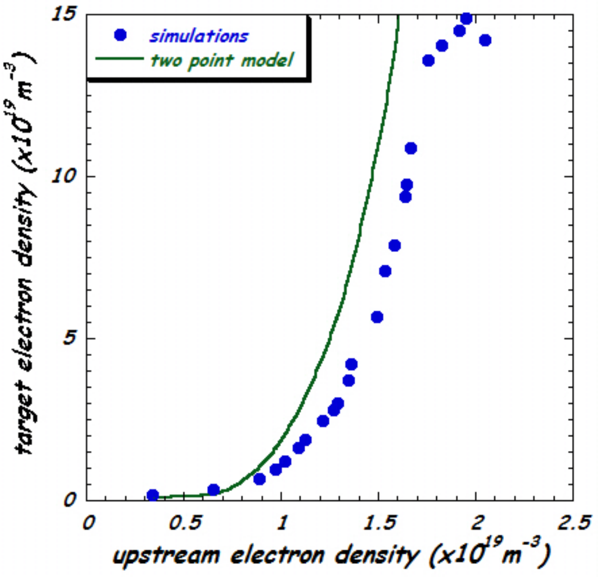

Figure 6.7: Electron density in the target region as function of the electron density in the upstream region. The crosses are simulation results, the solid line is the two point model prediction.

Parallel temperature gradient

Since one of the aims of the divertor is achieving a low power deposition on the target without losing the performance of the main plasma, it is necessary to have a parallel temperature gradient along the SOL. A parameter that highlight this gradient is the *temperature parallel gradient factor*, defined as

$$f_T \equiv \frac{T_u}{T_t}. \tag{6.8}$$

From the equation of the two point model it is simple to write it as a function of the *collision parameter* evaluated at the target plasma conditions $n_t L/T_t^2$. The relation between the two is:

$$\frac{n_t L}{T_t^2} = C_1(f_t^{7/2} - 1) \tag{6.9}$$

with the temperature expressed in $[eV]$ and

$$C_1 \equiv \frac{2}{7}\frac{k_0}{\gamma e c_{s0}}. \tag{6.10}$$

To compare the prediction for the temperature parallel gradient factor of the two point model and EDGE2D-EIRENE one, the parameter used are $\gamma =$

$\gamma_e + \gamma_i = 7$ and $c_{s_0} = 9788 ms^{-1}$. Results are plotted in figure 6.8, where stars are the computed data and the solid line is the prediction of the two point model. They are in agreement at low collisionality where the temperature gradient factor is less than 10, that corresponds to a low density at the target, but they do not agree at high parallel temperature gradient. The agreement is not good at high density, the temperature gradient predicted by the 2-D code is higher than the one predicted by the two point model, that means that the 0-D model predict an higher power deposited on the target than the real one. This is due to the assumption of a very thin ionization layer near the target.

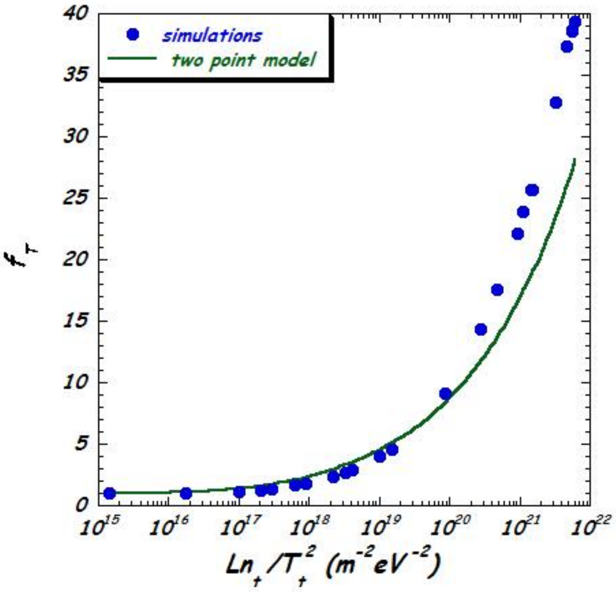

Figure 6.8: Relationship between T_u/T_t and the collision parameter evaluated for target plasma conditions. The solid line is the prediction of the two point model.

Since we also want to relate everything to the temperature and density in the upstream region, it is useful to express the temperature parallel gradient factor in terms of n_u and T_u, obtaining:

$$\frac{n_u L}{T_u^2} = C_2 f_T^{1/2} (1 - f_t^{-7/2}) \tag{6.11}$$

with

$$C_2 \equiv \frac{4}{7} \frac{k_0}{\gamma e c_{s0}}. \tag{6.12}$$

The left hand side of equation 6.11 is directly related to the *collisionality parameter* ν^*_{SOL} defined as

$$\nu^*_{SOL} \equiv 10^{-16} \frac{n_u L}{T_u^2} \tag{6.13}$$

The relation of f_T as function of ν^*_{SOL} is plotted in figure 6.9, where again the stars are the data coming from the simulation and the solid line is the prediction of the two point model.

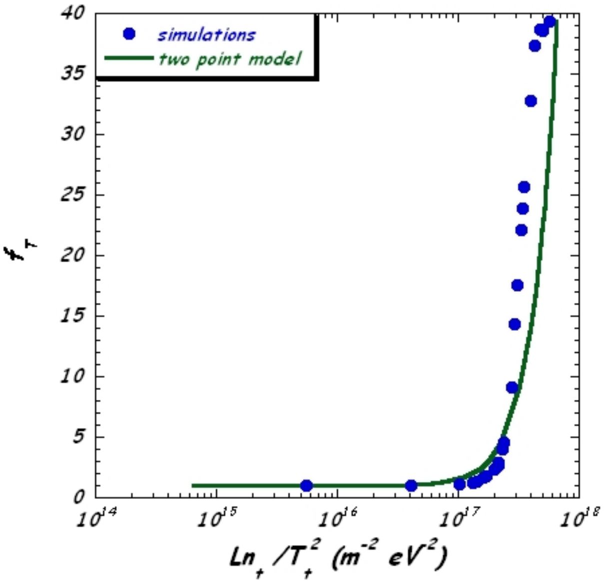

Figure 6.9: Relationship between T_u/T_t and the collision parameter evaluated for upstream plasma conditions. The solid line is the prediction of the two point model.

6.2.3 SOL collisionality to estimate different divertor regimes

Since the collisionality parameter is strictly related to the temperature parallel gradient factor, it can be also used to define the different divertor regimes that are simulated. The transition from the sheath-limited (constant T along flux tube) to the conduction-limited regime is somewhat arbitrary, but it can be taken to occur at

$$f_T \approx 1.5. \tag{6.14}$$

Considering also that because of power loss due to radiation and charge exchange, $q_t \approx q_{\|}/2$ [90], it is possible to write the collisionality criterion for the transition:

$$\nu^*_{SOL}|_{sheath\leftrightarrow cond} \approx 10 \tag{6.15}$$

that means

$$T_u|_{sheath\leftrightarrow cond} \approx 3.2 \times 10^{-9}\sqrt{n_u L}. \tag{6.16}$$

A similar consideration can be also done for the transition from the conduction-limited to the detached regime. Assuming simply that detachment sets in when T_t has been reduced to a few eV, at which point ion-neutral friction and volume recombination become important, and that $T_u = 100\,eV$ being rather insensitive to all control parameters at fixed P_{core}, the transition can be arbitrarily taken at $f_T \approx 100/1.5$. With this assumption the criterion for transition from the conduction-limited to the detached regime is:

$$\nu^*_{SOL}|_{cond\leftrightarrow det} \approx 85 \tag{6.17}$$

that means

$$T_u|_{cond\leftrightarrow det} \approx 1.1 \times 10^{-9}\sqrt{n_u L}. \tag{6.18}$$

The assumption of $T_u = 100\,eV$ is not strictly necessary if the equations (6.6) are used to write T_u as function of T_t and n_u, although the criterion is no longer in terms of ν^*_{SOL} only. Therefore, considering only that the transition sets in when $T_t = 1.5\,eV$ the criterion becomes:

$$T_u|_{cond\leftrightarrow det} \approx 1.7 \times 10^{-7}(n_u L)^{2/5}. \tag{6.19}$$

In figure 6.10 are plotted the points corresponding to the simulated discharges in the $(\sqrt{n_u L}, T_u)$ parameter space. The blue line corresponds to the transition from the sheath-limited to the conduction-limited regime, the yellow one corresponds to the transition from the conduction-limited to the detached regime using equation (6.18) and the green one is the same transition but using the prediction of equation (6.19). It is possible to notice that the density scan performed goes from a case of sheath limited regime (very low upstream density) to a case of detached regime.

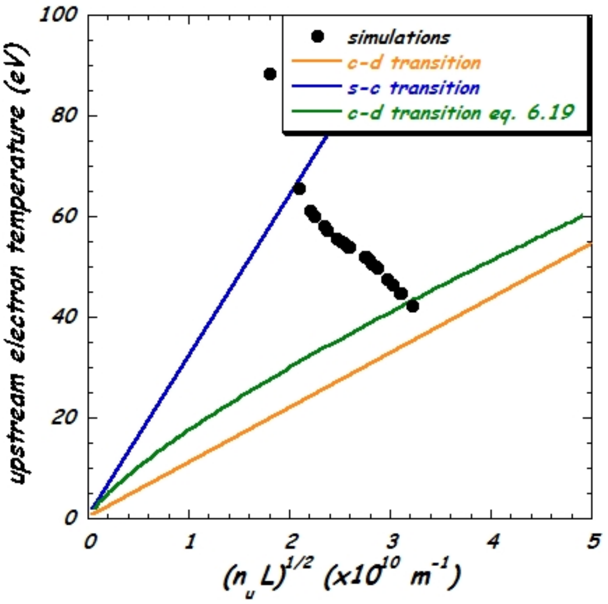

Figure 6.10: Values of upstream electron temperature as function of $\sqrt{n_u L}$. The blue and yellow solid lines are respectively the equation 6.16 and 6.18, while the green solid line is equation 6.19. The density scan performed sweep the three regimes with at least one case.

6.2.4 Deuterium gas puffing from other locations

In principle the relation between the deuterium influx, the upstream electron density and the target electron temperature could be also related to the gas puffing position. It is possible to think that an injection from the outer midplane instead of from the top could lead to an higher electron upstream density because of the lower radial thickness of the SOL, resulting into a lower power deposited on the target for the same deuterium influx. In the same way a gas injection from the private region could lead to an increase of the density near the target larger than the increase in the upstream region because of the proximity with that region. In this way the relation between the two densities is modified and moreover also the power deposited on the target is reduced at lower upstream density than injecting deuterium from the top. In order to confirm such hypothesis other density scan have been performed with the same features as the previous ones, but with the deuterium influx set in two different positions: the *outer midplane* (see figure 6.11) and the *private region* (see figure 6.12)

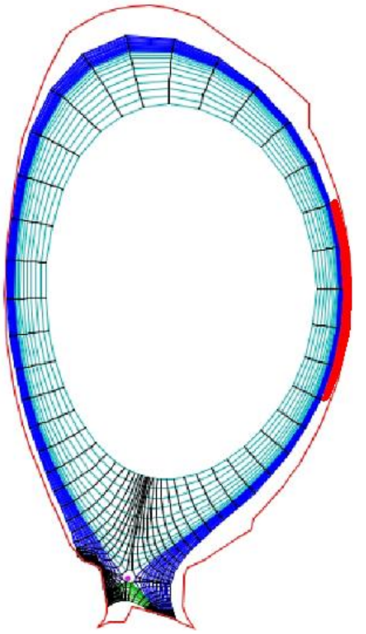

Figure 6.11: Grid of the reference case JET #78647 with gas injection from the outer midplane.

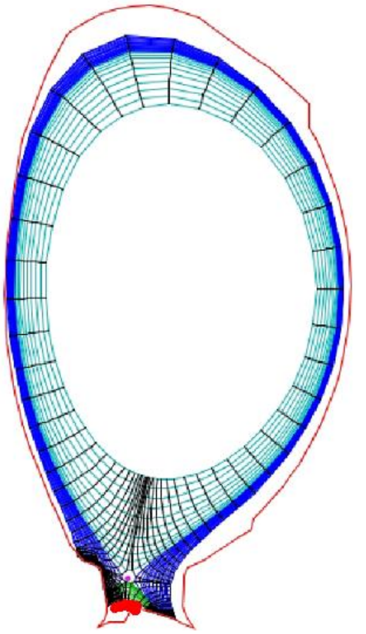

Figure 6.12: Grid of the reference case JET #78647 with gas puffing from the private region.

The first case analyzed is the gas puffing from the outer midplane. The scan has been performed from a deuterium influx of $\Gamma_{D_2} = 1 \times 10^{21}\, s^{-1}$ up to $\Gamma_{D_2} = 8 \times 10^{21}\, s^{-1}$ with steps of $\Gamma_{D_2} = 1 \times 10^{21}\, s^{-1}$. The other parameters are the same as the scan with deuterium puffing from the top.

To check if the upstream electron density is higher for the same deuterium influx, these two quantities have been plotted in figure 6.13. From the plot it is possible to notice first of all that the density limit is achieved also in the case of puffing from the outer midplane when $\Gamma_{D_2} > 7 \times 10^{21}\, s^{-1}$, and then that upstream electron density achieved in the two cases is the same for equal deuterium influx.

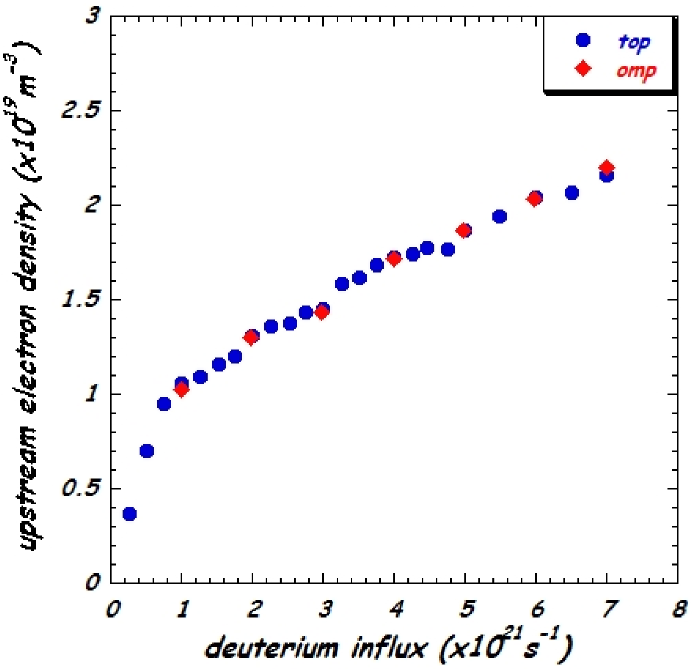

Figure 6.13: Upstream density achieved as function of the deuterium influx. Circles are related to the gas puffing from the top, diamonds from the outer midplane.

To confirm that there is no difference related to the gas injection position, also the relation between the target electron density and temperature and the upstream electron density has been studied. They are plotted in figures 6.14 and 6.15, where, as in the previous figure, the blue points are the point related to the deuterium injection from the top and the red diamonds are related to that from the outer midplane. It has therefore to be concluded that there are no differences in these two cases.

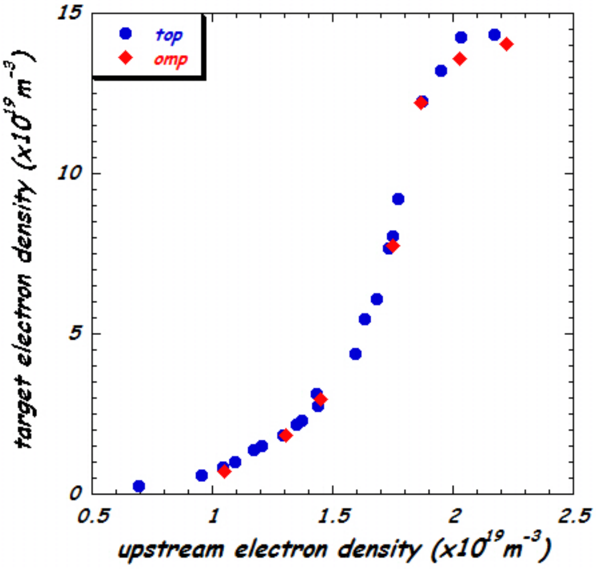

Figure 6.14: Comparison of the electron density at the target as function of the upstream density in case of puffing from the top (circles) and from the outer midplane (diamonds).

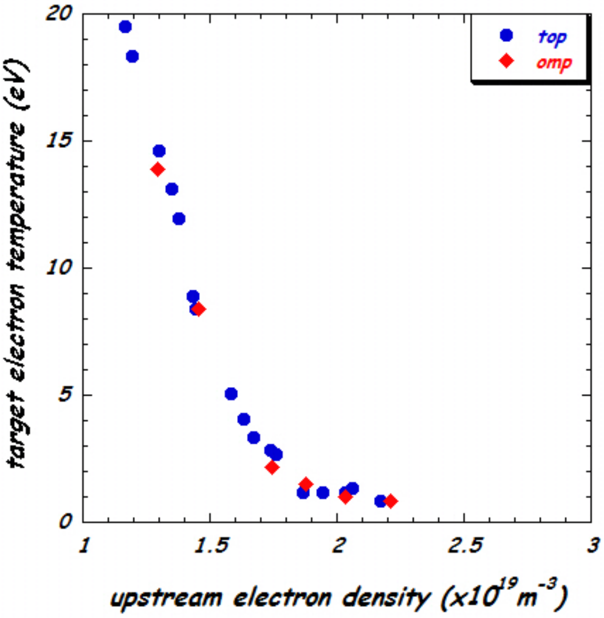

Figure 6.15: Comparison of the electron temperature at the target as function of the upstream density in case of puffing from the top (circles) and from the outer midplane (diamonds).

The case with the gas puffing from the private region seems more promising. Indeed plotting the upstream electron density as function of deuterium influx (see figure 6.16) it shows some differences at high influx.

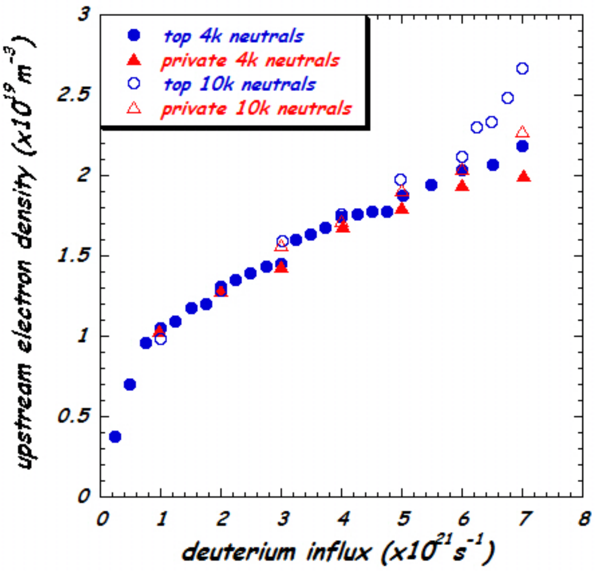

Figure 6.16: Upstream electron density achieved as function of the deuterium influx. Circles are related to the gas puffing from the top, triangles from the private region, simulated respectively following 4000 (fill) and 10000 (empty) neutrals.

Since for values of $\Gamma_{D_2} \geq 5 \times 10^{21}\, s^{-1}$ the electron density in the upstream for the gas injection from the private region (red fill triangles) are lower than those with puffing from the top (blue fill points), and taking in to account that using 4000 neutrals the value of density at high deuterium influx is not correct (see section 6.2.1), the same comparison has been done also with a density scan performed following 10000 neutrals. The scan with an higher number of neutrals highlights the difference of electron density in the upstream region, up to a 15% less in the case of gas injection from the private region for $\Gamma_{D_2} = 7 \times 10^{21}\, s^{-1}$.

Nevertheless the difference between electron density at the target in the two cases is strongly reduced. It can be seen in figure 6.17 that the electron density at the divertor plates is only $\sim$ 5% higher in case of puffing from the private region, and only at the highest deuterium puffing. Moreover looking at the electron temperature at the target as function of the upstream density (see figure 6.18) it is possible to notice that there is no difference between the two cases.

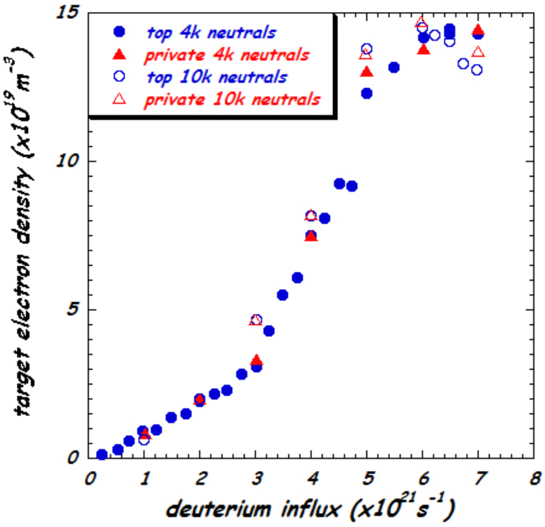

Figure 6.17: Target electron density achieved as function of the deuterium influx. Circles are related to the gas puffing from the top, triangles from the private region, simulated respectively following 4000 (fill) and 10000 (empty) neutrals.

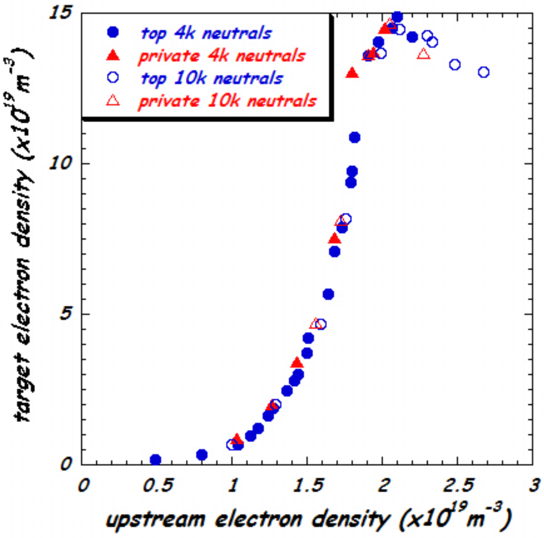

Figure 6.18: Comparison of the electron density at the target as function of the upstream density in case of gas puffing from the top (circles) and from the private region (triangles). Filled labels are related to simulations performed following 4000 neutrals, empty labels following 10000 neutrals.

Summarizing, the electron density in the SOL and consequently the power deposited on the outer target plate is only slightly dependent on the gas puffing position.

6.2.5 Density scan varying the pumping albedo

Another factor that can affect the relation between the upstream electron density and the target one is the albedo of pumping (AoP), where the albedo is defined as the reflectivity of the pumping region, that can be read also as the inverse of pumping speed. Since, as shown in figure 6.2, the pumping position is in the region of the outer target, a faster pumping speed could lead to a faster decrease of the electron density in the divertor region because of a faster removal of the neutrals, without modifying the upstream density, that leads to a slower decrease of the temperature and so of the power deposited on the divertor plates.

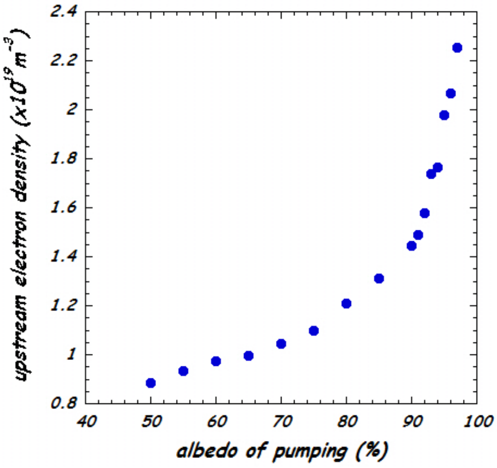

Figure 6.19: Upstream electron density as function of the albedo of pumping.

The influence of the pumping albedo on the relation between the quantity on the upstream and the target region has been studied by mean of a scan, from an $AoP = 50\%$ up to $AoP = 99\%$ with variable steps. The scan has been performed using a deuterium puffing of $\Gamma_{D_2} = 4 \times 10^{21}\ s^{-1}$ from the top and following 6000 neutrals. In this way a density scan has been obtained. The density limit has been achieved with $AoP = 98\%$. To be able to achieve $AoP = 99\%$ it is necessary to decrease the deuterium flux down to $\Gamma_{D_2} = 1 \times 10^{21}\ s^{-1}$. In figure 6.19 the upstream electron density as function of the albedo of pumping, in figures 6.20 and 6.21 the electron density and temperature on the target as function of the upstream electron density. The lowest upstream electron density corresponds to the lowest *AoP*, the highest to the highest one.

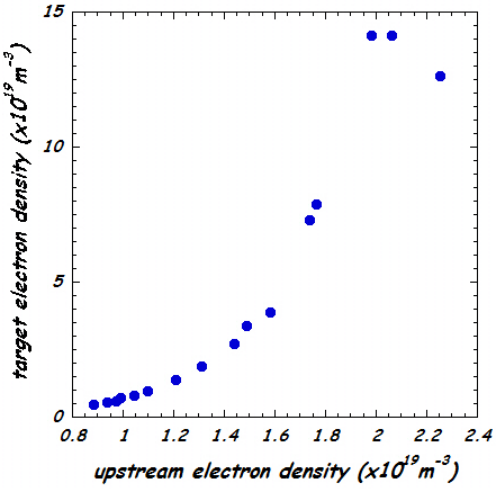

Figure 6.20: Electron density at the target as function of the upstream electron density.

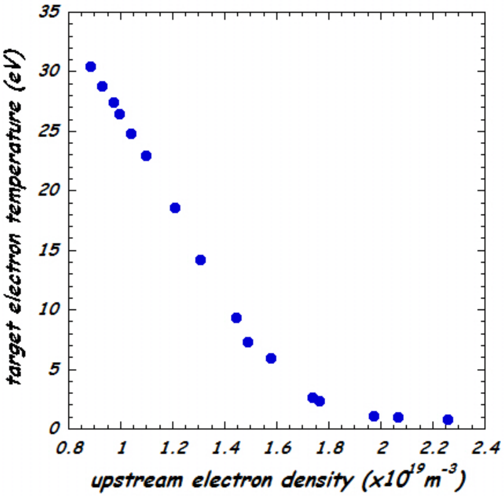

Figure 6.21: Electron temperature at the target as function of the upstream electron density.

Also in this case there is no difference from the previous density scan regarding the relation between the quantities in the upstream region with the ones at the target.

6.2.6 Distance of the ionization layer

As seen above, the overall effect of increasing the upstream density is that the temperature at the target plates decreases, going through the three different divertor regimes. This process can be seen in a qualitative way looking at the 2D plot in figure 6.22 of the electron density and temperature.

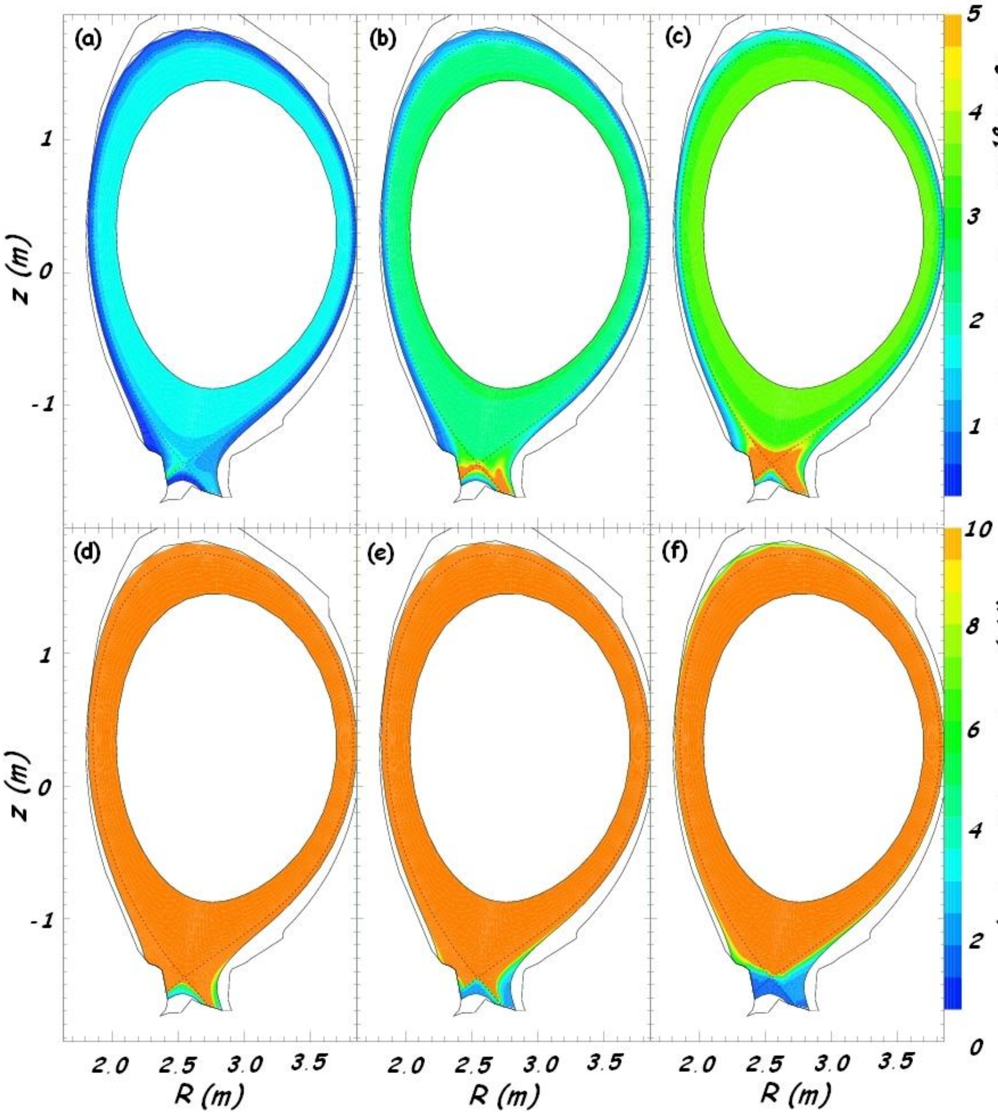

Figure 6.22: (a), (b), (c): electron density at the edge. The density varies from $n_e = 10^{16}\, m^{-3}$ in blue to $n_e = 5 \times 10^{19}\, m^{-3}$ in orange. (d), (e), (f): the respective electron temperature in the edge. Temperatures from $T_e = 0\, eV$ in blue to $T_e = 10\, eV$ in orange.

Figures (a), (b) and (c) are the electron density at the edge, while figures (d), (e) and (f) are the respective electron temperature in the edge. Figures (a) and (d) are related to $\Gamma_{D_2} = 1 \times 10^{21}\ s^{-1}$ from the top, following 10000 neutrals, (b) and (e) to $\Gamma_{D_2} = 4 \times 10^{21}\ s^{-1}$ and (c) and (f) to $\Gamma_{D_2} = 7 \times 10^{21}\, s^{-1}$, always with the same number of neutrals. The figure highlights that increasing the gas puffing, and consequently the average electron density, also the density at the target increases. Moreover it is possible to notice that at low density the temperature achieved at the target is greater than 10 eV. Increasing the average electron density the target area with a plasma at temperature $T_e \geq 10eV$ decreases to zero in the case of the highest deuterium influx. This is the so called *detached regime*. The temperature of 10 eV has been chosen because it is representative of the region where the deuterium is fully ionized.

To evaluate in a more quantitative way the plasma detachment one can consider the distance of the region at $T_e = 10\ eV$ (also called *ionization layer*) from the target along the separatrix. In figure 6.23 is plotted such distance normalized to the distance of the X-point from the divertor against the upstream electron density.

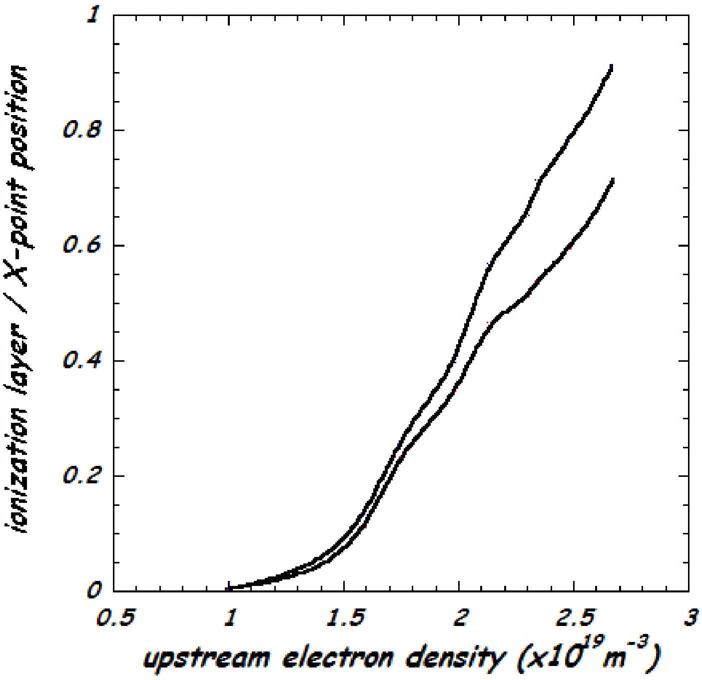

Figure 6.23: Range of the ionization layer position normalized to the distance of the X-point. It is the distance from the divertor plates along the separatrix for the outer target.

The plot shows that for the lowest upstream density the ionization layer is on the target (as shown already in figure 6.10), then increasing the density it starts to move inside. At an upstream density $n_u \geq 2 \times 10^{19}\, m^{-3}$ the distance is greater than the 50% of the distance of the X-point. This corresponds also to the density where the simulations made with EDGE2D show the achievement of the limit for the target electron density (see figure 6.5). The last point of the simulation, corresponding to $n_u \approx 2.7 \times 10^{19}\, m^{-3}$, also shows that the code achieve the density limit before the ionization layer moves inside the LCFS.

6.3 Conclusions

The main aims of the several simulations performed were: to test the range of convergence of the code; to study the range of validity of the Two Point Model; to study the dependence of power deposition on the outer target from the main plasma features.

About the convergence of the code it has been found that the code achieves the density limit, and therefore is not able to converge anymore, when the system is moving from the conduction divertor regime to the detached one, i.e. it is not able to reproduce the case of low temperature and low electron density at the target position.

The comparison between the two point model and the simulations performed with EDGE2D-EIRENE shows that the assumptions done for the simple model are valid only in the case of high temperature and low electron density at the target position. It means that the simple model can be used only in the sheath limited divertor regime and only in part in the conduction limited divertor regime. It is not able to predict the detached divertor regime.

It has been finally found that increasing the electron density by means of external deuterium puffing or reducing the pumping speed the temperature at the outer target decreases up to values less than $1\, eV$, and thus the power deposited on the target surfaces also decreases, independently from the gas puffing position and from the system used to increase the density.

The SOLPS Package

In this chapter will be presented the transport code B2 and the kinetic neutrals code EIRENE that have been studied and installed on the server of the *Consorzio RFX* to model the FTU limiter SOL configuration as described in the next section.

To study the edge transport in a Tokamak device with limiter configuration it has been chosen to use the version 4.0 of the SOLPS package, since it was already adapted for that configuration. The SOLPS package is a suite of codes which consists of: **B2**, a multi fluid plasma code originally written by Bas Braams [91, 92]; **EIRENE**, a Monte-Carlo kinetic neutrals code written by Detlev Reiter [93]; **b2plot**, a postprocessing code used for plotting results from simulation runs originally written by David Coster; **gridgen** and **gridadap** for grid generation; and various scripts for other pourposes.

In section 7.1 are presented the Braginskii equations, a set of fluid equations that provide a bi-dimensional model to describe transport processes in a plasma. The reduced set of these equations solved in B2 is given in section 7.2. In section 7.3 will be described how the codes deal with the neutrals. Section 7.4 is dedicated to the technical aspects I had to deal with to run the code.

7.1 2-D toroidal plasma edge description

Following the considerations of section 2.1, a description for the plasma edge has to include both transport perpendicular to the magnetic surfaces, which dominates inside the LCFS, and parallel transport to the material boundaries in the SOL. This means that for plasma edge modeling at least a two-dimensional description is required. Although particles move along the twisted magnetic field lines, a bi-dimensional model is based on the axisymmetrical geometry of the torus. This results in a two-dimensional edge model which describe the plasma parameters in a poloidal cross section of the torus. A complete derivation of an edge plasma fluid model in toroidal geometry can be found in [94, 92]. Here it will be shortly summarized.

The fluid approach is valid if the collisionality of a particle is large, meaning that its mean free path λ has to be small in comparison with a typical characteristic length of the device $L_{\shortparallel}$. Since electron and ion gases reach separate equilibrium in a time scale shorter than that required for the two gases to equilibrate among themselves, the approximation embedded in a fluid approach is:

$$L_{\shortparallel} \gg v_{th,i}\tau_i \tag{7.1}$$

and

$$L_{\shortparallel} \gg v_{th,e}\tau_e. \tag{7.2}$$

$L_{\shortparallel}$ is the scale length of variation of the macroscopic plasma parameters such as density, temperature and the magnitude of the magnetic field B. $v_{th,\alpha}$ is a measure for the thermal velocity of fluid species α with mass m_α and is defined as

$$v_{th,\alpha} = \sqrt{\frac{T_\alpha}{m_\alpha}}. \tag{7.3}$$

τ_i and τ_e are the basic collisional times and are defined as

$$\tau_i = 2.09 \times 10^{13} \frac{T_i^{3/2}}{n\lambda} \mu^{1/2}\ s \tag{7.4}$$

$$\tau_e = 3.44 \times 10^{11} \frac{T_e^{3/2}}{n\lambda}\ s. \tag{7.5}$$

with $\mu = m_i/m_p$ and λ is the Coulomb logarithm [95]. All the variables expressed in S.I. units except for the temperature expressed in eV.

A set of fluid equations for the plasma, known as *Braginskii equations*, were derived by Braginskii in *Transport processes in a plasma* [94]. Their classical tensor formulation is written below, in the case of a plasma composed by electrons and a single ion species with ion charge state Z_i and mass m_i. Furthermore the interactions with neutral particles are incorporated by means of neutral source terms and it is assumed the local quasineutrality ($n_e = Z_i n_i$). The equations to determine macroscopic plasma proprieties as density n_α, average particle velocity $\overrightarrow{V}_\alpha$, temperature T_α and electric field $\overrightarrow{E}$ are:

1. continuity equations for ions

$$\frac{\partial}{\partial t} n_i + \overrightarrow{\nabla} \cdot (n_i \overrightarrow{V}_i) = S_{n_i} \tag{7.6}$$

   and electrons

$$\frac{\partial}{\partial t} n_e + \overrightarrow{\nabla} \cdot (n_e \overrightarrow{V}_e) = S_{n_e} \tag{7.7}$$

2. total momentum equation

$$\frac{\partial}{\partial t}(m_i n_i \overrightarrow{V}_i) + \overrightarrow{\nabla} \cdot (m_i n_i \overrightarrow{V}_i \overrightarrow{V}_i) = -\overrightarrow{\nabla} p - \overrightarrow{\nabla} \overleftrightarrow{\Pi}_i + \overrightarrow{j} \times \overrightarrow{B} + \overrightarrow{S}_{m_i \overrightarrow{V}_i} \tag{7.8}$$

   that can be formally written also in the form

$$\begin{aligned} \frac{d}{ds}(\rho v^2 + p) \quad &= \quad S_{CX} \ + \ viscosity \ + \ convective\, momentum \\ &\qquad transport\, across\, flux\, surface \end{aligned} \tag{7.9}$$

   with $\rho = m_i n_i$.

3. energy equations for ions

$$\begin{aligned} &\frac{\partial}{\partial t}\left(\frac{3}{2} n_i T_i + \frac{m_i n_i}{2} \overrightarrow{V}_i^2\right) + \\ +\overrightarrow{\nabla} \cdot &\left[\left(\frac{5}{2} n_i T_i + \frac{m_i n_i}{2} \overrightarrow{V}_i^2\right) \overrightarrow{V}_i + \overleftrightarrow{\Pi}_i \cdot \overrightarrow{V}_i + \overrightarrow{q}_i\right] = \\ &= (e n_i Z_i \overrightarrow{E} - \overrightarrow{R}) \cdot \overrightarrow{V}_i - Q_{ei} + S_E^i \end{aligned} \tag{7.10}$$

   and electrons

$$\frac{\partial}{\partial t}\left(\frac{3}{2} n_e T_e\right) + \overrightarrow{\nabla} \cdot \left(\frac{5}{2} n_e T_e \overrightarrow{V}_e + \overrightarrow{q}_e\right) = -e n_e \overrightarrow{E} \cdot \overrightarrow{V}_e + \overrightarrow{R} \cdot \overrightarrow{V}_i + Q_{ei} + S_E^e \tag{7.11}$$

where the energy fluxes for ions is

$$\overrightarrow{q}_i = -\kappa_{\parallel}^i \nabla_{\parallel} T_i - \kappa_{\perp}^i \nabla_{\perp} T_i + \kappa_{\wedge}^i \frac{\overrightarrow{B}}{B} \times \overrightarrow{\nabla}_{\perp} T_i \tag{7.12}$$

for electrons (if $Z_i = 1$) is

$$\overrightarrow{q}_e = -\kappa_{\parallel}^e \nabla_{\parallel} T_e - \kappa_{\perp}^e \nabla_{\perp} T_e - \kappa_{\wedge}^e \frac{\overrightarrow{B}}{B} \times \overrightarrow{\nabla}_{\perp} T_e - 0.71 \frac{T_e}{e} \overrightarrow{j}_{\parallel} - \frac{3}{2} \frac{T_e}{e \omega_e \tau_e B} \overrightarrow{B} \times \overrightarrow{j}_{\perp} \tag{7.13}$$

the energy exchange term between electrons and ions is

$$Q_{ei} = \frac{3m_e}{m_i}\frac{n_e}{\tau_e}(T_i - T_e) \tag{7.14}$$

For single ion fluid species $\overrightarrow{R}$ is defined as

$$\overrightarrow{R} \equiv \overrightarrow{R}_e = -\overrightarrow{R}_i = en_e\left(\frac{\overrightarrow{j}_{\shortparallel}}{\sigma_{\shortparallel}} + \frac{\overrightarrow{j}_{\perp}}{\sigma_{\perp}}\right) - 0.71 n_e \overrightarrow{\nabla}_{\shortparallel} T_e - \frac{3}{2}\frac{en_e^2}{\sigma_\perp B^2}\overrightarrow{B} \times \overrightarrow{\nabla} T_e \tag{7.15}$$

and

$$\begin{array}{rcl}
S_{n_\alpha}, S_{m_\alpha \overrightarrow{V}_\alpha}, S_E^\alpha & = & \mathit{volume\ sources\ of\ particles,\ momentum\ and} \\
 & & \mathit{energy\ for\ particle\ species\ } \alpha \\
\overleftrightarrow{\Pi} & = & \mathit{viscosity\ tensor} \\
\sigma_{\shortparallel},\ \sigma_\perp & = & \mathit{classical\ electrical\ conductivities} \\
\kappa_{\shortparallel}^\alpha,\ \kappa_\perp^\alpha,\ \kappa_\wedge^\alpha & = & \mathit{classical\ thermal\ conductivities} \\
 & & \mathit{for\ particle\ species\ } \alpha \\
\omega_e & = & \mathit{electron\ gyrofrequency} \\
\tau_e & = & \mathit{basic\ collosional\ time\ for\ electrons}
\end{array}$$

Moreover the electron and ion pressure are

$$p_e = n_e T_e\,; \tag{7.16}$$

$$p_i = n_i T_i\,; \tag{7.17}$$

the total pressure

$$p = p_i + p_e\,; \tag{7.18}$$

and the electric current density

$$\overrightarrow{j} = e(Z_i n_i \overrightarrow{V}_i - n_e \overrightarrow{V}_e)\,. \tag{7.19}$$

The equations are expressed in the curvilinear orthogonal co-ordinate system. In this system the three characteristic directions of the plasma motion are directed parallel to the magnetic field $\overrightarrow{B}$ ($\|$), perpendicular to $\overrightarrow{B}$ in the magnetic flux surface ($\perp$), usually referred as diamagnetic direction, and "radial" or normal to the flux surface (r). Since to have a bi-dimensional description it is necessary to impose a toroidal symmetry, it can be easily imposed in a "toroidal-poloidal-radial" co-ordinate system. In this way the plasma is described in an orthogonal poloidal-radial

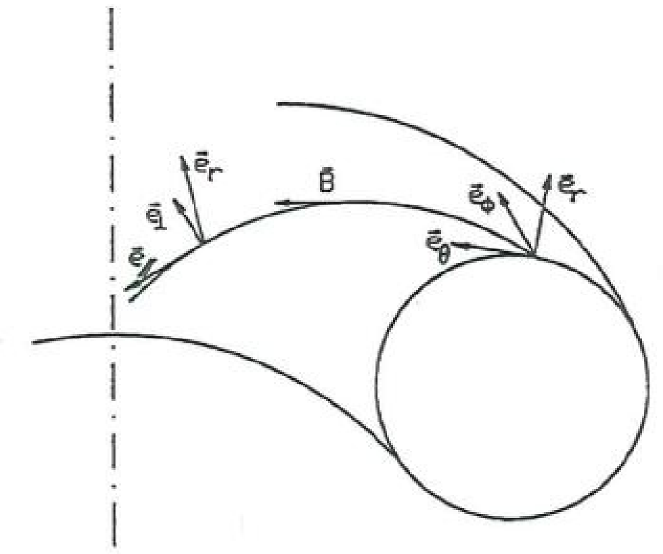

Figure 7.1: Two basic co-ordinate system for toroidal applications.

co-ordinate system (θ, r) with the toroidal co-ordinate ϕ ignorable. The two co-ordinate system are shown in figure 7.1

The transformation between the parallel-diamagnetic-radial system ($\overrightarrow{e}_{\shortparallel}$, $\overrightarrow{e}_\perp$, $\overrightarrow{e}_r$) to the toroidal-poloidal-radial one ($\overrightarrow{e}_\theta$, $\overrightarrow{e}_r$, $\overrightarrow{e}_\phi$) is given by

$$\begin{cases} \overrightarrow{e_\perp} = \dfrac{h_\perp \widetilde{B_\phi}}{h_\theta \widetilde{B}} \overrightarrow{e_\theta} - \dfrac{h_\perp \widetilde{B_\theta}}{h_\phi \widetilde{B}} \overrightarrow{e_\phi} \\ \overrightarrow{e_{\shortparallel}} \cdot \overrightarrow{e_\perp} = 0 \\ \overrightarrow{e_r} = \overrightarrow{e_r} \end{cases} \tag{7.20}$$

7.2 B2 transport code

The main part of SOLPS is the multifluid transport code B2. B2 is a two-dimensional code that combines the processes dominant inside the separatrix, like the radial transport, with the flow and thermal conduction along open field lines onto a material boundary. The code solves a reduced set of fluid equations simplified for improved numerical convergence starting from theoretical models based on the Braginskii equations written in section 7.1.

7.2.1 Magnetic configuration

B2 is set up to handle SOL of different Tokamak types and dimensions, describing the dominant edge plasma effects. It is appropriate for toroidally symmetric configurations such as toroidal-limiter and poloidal-divertor Tokamaks under conditions of sufficiently high collisionality. Finite-difference calculations are performed on a topologically rectangular mesh related to the physical geometry by specifying for each cell the discrete metric functions characterizing the transformation.

The physical region of interest for edge plasma modeling is the outer section of a poloidal cross-section, consisting of the SOL and an annulus of closed flux surfaces inside the separatrix. This physical region is mapped onto an x-y plane (see figure 7.3) with the poloidal projection of the magnetic field lines along the x co-ordinate, and the radial direction along the y co-ordinate. The choice of this orthogonal system ensures that all fluxes coming in and out of a volume element can be specified between the cell itself and those neighboring its faces, rather than involving other cells adjoining just its edges as well (see figure 7.2). Orthogonality therefore simplifies the discretized equations and reduces computing time.

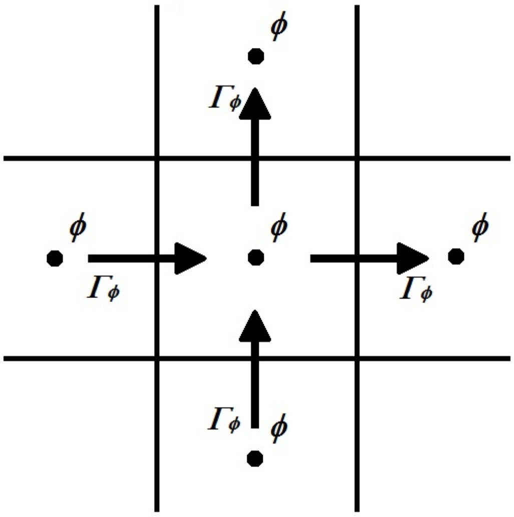

Figure 7.2: Fluxes in the orthogonal discretized grid.

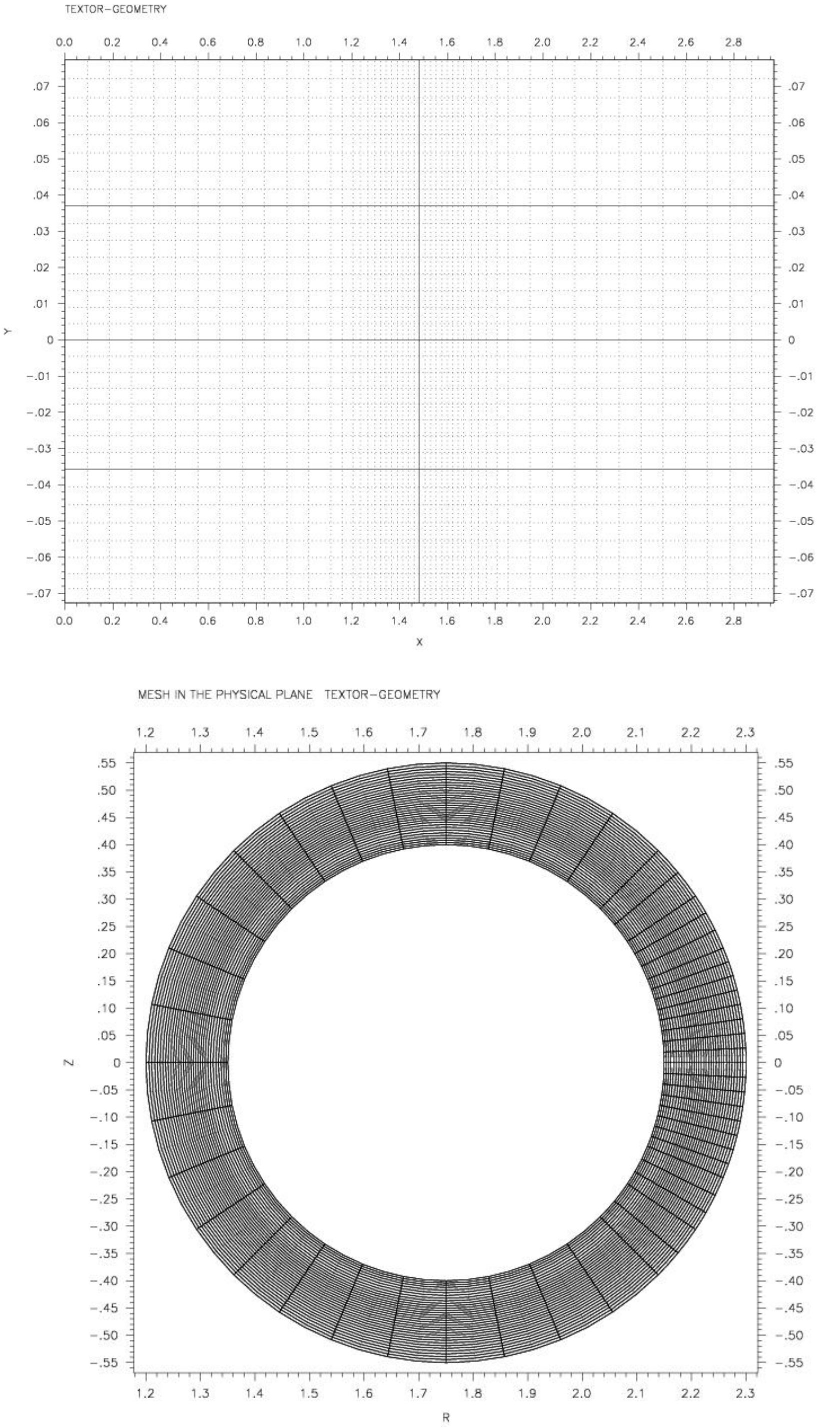

Figure 7.3: TEXTOR computational and physical mesh.

7.2.2 Fluid equations

It was anticipated that B2 solves a reduced set of the Braginskii fluid equations on a two-dimensional grid in the poloidal cross-section of a Tokamak. The set of equations entails: the ion continuity equations for all ion species; the parallel ion momentum balance equations for all ion species; two energy balance equations, one for the averaged ion energy over the ion species and one for the electron energy. Momentum and heat transport parallel to the magnetic field are determined by neoclassical theory, while the transport normal to the magnetic flux surfaces is represented by anomalous transport coefficients. Although the model contains time-dependent terms, it is designed primarily for steady-state solutions.

To reduce the number and complexity of the equations, B2 is based on five additional assumptions:

1. plasma is quasineutral ($n \equiv n_i = n_e/Z_i$) and the flow is ambipolar ($\overrightarrow{j} = 0$). Therefore no separate electron momentum equation is considered;

2. ion velocity in the diamagnetic direction is neglected. Thus one component of the ion momentum equation is neglected;

3. classical cross-field transport terms are complemented by anomalous transport in the radial direction. The radial momentum equation is replaced by a diffusive equation with constant particle diffusion coefficient D_n. Radial transport coefficient η_y and κ_y are introduced to model anomalous effects in viscosity stress and heat conductivity. These coefficients are related to constant diffusion coefficients for the viscosity D_η and the heat conductivity D_κ by $\eta_y = mnD_\eta$ and $\kappa_y = nD_\kappa$;

4. the viscosity tensor is simplified neglecting cross-field derivative terms;

5. terms due to curvature of $\overrightarrow{B}$ and gradients of $\overrightarrow{B}$ are only partially taken into account.

This leads to a simpler form of the equations and to a more robust numerical system.

In the following equations x and y corresponds to the poloidal and radial direction respectively, corresponding to θ and r in equations of section 7.1. The reference system is plotted in figure 7.4. Physical components of the fluid velocity in these two directions are u and v respectively. The transformation from the parallel to the poloidal reference system is that expressed in the

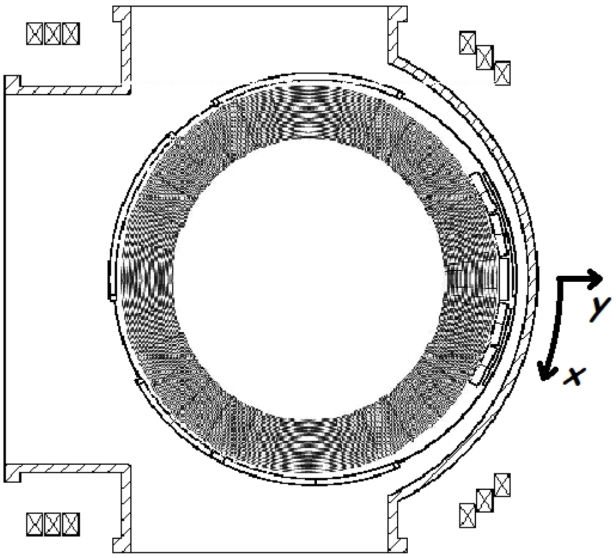

Figure 7.4: Coordinate system of the equations in the B2 code. x is the poloidal coordinate and y is the radial coordinate orthogonal to the flux surfaces.

equation 7.20. The resulting metric coefficients are $h_x = 1/\|\nabla x\|$, $h_y = 1/\|\nabla y\|$, $h_z = 2\pi R$ with R the local major radius and the Jacobian of the metric matrix is $\sqrt{g} = h_x h_y h_z$ [96]. The equations governing the evolution of ion density n, parallel and radial flow velocity components $u_{\shortparallel}$ and v and electron and ion temperatures T_e and T_i are the following set:

1. Continuity of species a $(1 \leq a \leq N)$:

$$\frac{\partial n_\alpha}{\partial t} + \frac{1}{\sqrt{g}}\frac{\partial}{\partial x}\left[\frac{\sqrt{g}}{h_x} n_a (u_a + v_{p,a})\right] + \frac{1}{\sqrt{g}}\frac{\partial}{\partial y}\left[\frac{\sqrt{g}}{h_y} n_a v_a\right] = S_n^a \tag{7.21}$$

2. Momentum balance of species a $(1 \leq a \leq N)$:

$$\begin{aligned} &\frac{\partial}{\partial t}(\rho_a u_{\shortparallel a}) + \frac{1}{\sqrt{g}}\frac{\partial}{\partial x}\left[\frac{\sqrt{g}}{h_x}\rho_a (u_a + v_{p,a}) u_{\shortparallel a} - \frac{\sqrt{g}}{h_x^2}\eta_x^a \frac{\partial u_{\shortparallel a}}{\partial x}\right] + \\ &\qquad + \frac{1}{\sqrt{g}}\frac{\partial}{\partial x}\left[\frac{\sqrt{g}}{h_y}\rho_a v_a u_{\shortparallel a} - \frac{\sqrt{g}}{h_y^2}\eta_y^a \frac{\partial u_{\shortparallel a}}{\partial y}\right] = \\ &= \frac{B_\theta}{B}\frac{1}{h_x}\left[-\frac{\partial p_a}{\partial x} - \frac{Z_a n_a}{n_e}\frac{\partial p_e}{\partial x} + c_e\left(\frac{Z_a}{Z_{eff}} - 1\right) Z_a n_a \frac{\partial T_e}{\partial x} + \right. \\ &\qquad \left. + c_i\left(\frac{Z_a}{Z_{eff}} - 1\right) Z_a n_a \frac{\partial T_i}{\partial x}\right] + \sum_{b=1}^{N} F_{ab} + S_{mu\shortparallel}^a \end{aligned} \tag{7.22}$$

3. Diffusion of species a $(1 \le a \le N)$:

$$v_a = -\frac{1}{h_y}\frac{D_n^a}{n_a}\frac{\partial n_a}{\partial y} - \frac{1}{h_y}\frac{D_p^a}{n_a}\frac{\partial p_a}{\partial y} \tag{7.23}$$

$$v_{p,a} = -\frac{1}{h_x}\frac{D_n^a}{n_a}\frac{\partial n_a}{\partial x} - \frac{1}{h_x}\frac{D_p^a}{n_a}\frac{\partial p_a}{\partial x} \tag{7.24}$$

4. Electron energy balance:

$$\begin{aligned}
&\frac{\partial}{\partial t}\left(\frac{3}{2}n_eT_e\right) + \frac{1}{\sqrt{g}}\frac{\partial}{\partial x}\left(\frac{\sqrt{g}}{h_x}\frac{5}{2}n_eu_eT_e - \frac{\sqrt{g}}{h_x^2}\kappa_x^e\frac{\partial T_e}{\partial x}\right) + \\
&+\frac{1}{\sqrt{g}}\frac{\partial}{\partial y}\left(\frac{\sqrt{g}}{h_y}\frac{5}{2}n_eu_eT_e - \frac{\sqrt{g}}{h_y^2}\kappa_y^e\frac{\partial T_e}{\partial y}\right) = \\
&= \frac{u_e}{h_x}\frac{\partial p_e}{\partial x} + \frac{v_e}{h_y}\frac{\partial p_e}{\partial y} - k(T_e - T_i) + S_E^e
\end{aligned} \tag{7.25}$$

5. Ion energy balance:

$$\begin{aligned}
&\frac{\partial}{\partial t}\left(\frac{3}{2}n_iT_i + \sum_a \frac{1}{2}\rho_a u_{\shortparallel a}^2\right) + \\
&+\frac{1}{\sqrt{g}}\frac{\partial}{\partial x}\left[\frac{\sqrt{g}}{h_x}\left(\sum_a \frac{5}{2}n_a(u_a + v_{p,a})T_i + \sum_a \frac{1}{2}\rho_a(u_a + v_{p,a})u_{\shortparallel a}^2\right) + \right. \\
&\left. +\frac{\sqrt{g}}{h_x^2}\left(\kappa_x^i\frac{\partial T_i}{\partial x} + \sum_a \frac{1}{2}\eta_x^a\frac{\partial u_{\shortparallel a}^2}{\partial x}\right)\right] + \\
&+\frac{1}{\sqrt{g}}\frac{\partial}{\partial y}\left[\frac{\sqrt{g}}{h_y}\left(\sum_a \frac{5}{2}n_av_aT_i + \sum_a \frac{1}{2}\rho_av_au_{\shortparallel a}^2\right) - \right. \\
&\left. -\frac{\sqrt{g}}{h_y^2}\left(\kappa_y^i\frac{\partial T_i}{\partial y} + \sum_a \frac{1}{2}\eta_y^a\frac{\partial u_{\shortparallel a}^2}{\partial y}\right)\right] = \\
&= -\frac{u_e}{h_x}\frac{\partial p_e}{\partial x} - \frac{v_e}{h_y}\frac{\partial p_e}{\partial y} + k(T_e - T_i) + S_E^i
\end{aligned} \tag{7.26}$$

with

$$n_i = \sum_a n_a; \quad n_e = \sum_a Z_an_a; \quad \rho_a = m_an_a;$$

$$p_a = n_aT_i; \quad p_e = n_eT_e; \quad u_e = \frac{\sum_a Z_an_a(u_a + v_{p,a})}{n_e};$$

$$v_e = \frac{\sum_a Z_an_av_a}{n_e}; \quad Z_{eff} = \frac{\sum_a Z_a^2n_a}{\sum_a Z_an_a}; \quad u_{\shortparallel} = \frac{B}{B_\theta}u$$

and

$$\begin{aligned}
S_n, S_{mu_{\parallel}}, S_E^e, S_E^i &= volume\ sources\ of\ ions,\ parallel\ momentum, \\
&\quad electron\ and\ ion\ energy\ respectively \\
\eta_x^i, \eta_y^i &= poloidal\ and\ radial\ ion\ viscosity\ coefficients \\
\kappa_x^{e,i}, \kappa_y^{e,i} &= thermal\ conductivities
\end{aligned}$$

7.3 Neutral particle model

While all transport coefficients are determined as analytic functions of local parameters, interaction between recycled neutral particles and the plasma do not depend only on the local parameters. More information is required to obtain the source terms $S_n, S_{mu_{\parallel}}, S_E^e, S_E^i$. The default neutral particle model implemented in B2 gives a highly simplified description. It assumes that a prescribed fraction of the ion particle flow impinging on the limiter and the wall is recycled with a fixed energy of $5\,eV$. These neutrals move along the poloidal coordinate away from the target with a velocity $v_{n,\theta} = \sqrt{\frac{10\,eV}{m_i}}$. The neutral atoms interact with the plasma only via ionization defined by the rate coefficient:

$$S_{ion} = \langle \sigma_{ion} v \rangle = 3 \times 10^{-14} \frac{\left(\frac{T_e}{10\,eV}\right)^2}{3 + \left(\frac{T_e}{10\,eV}\right)^2}\ m^3 s^{-1} \tag{7.27}$$

Therefore, particle sources are determined by the expression

$$S_n = n_0 n_e S_{ion} \tag{7.28}$$

with the neutral density computed as:

$$n_0 = \frac{\Gamma_0 \tau_0}{V}\ , \tag{7.29}$$

where Γ_0 is the integrated neutral particle flux through the surface of a grid cell and τ_0 is the average time a particle is expected to stay in the grid volume V.

With each ionization event is associated an electron energy loss of $25\,eV$ and an ion energy gain of $5\ eV$. The parallel momentum sources from ionization process are ignored because of the small pitch angle of field lines. The expression for momentum, ion and electron energy sources are therefore:

$$S_{mu_{\parallel}} = 0 \tag{7.30}$$

$$S_E^i = 5\,eV\ S_n \tag{7.31}$$

$$S_E^e = -25\,eV\ S_n\ . \tag{7.32}$$

7.3.1 EIRENE, a Monte-Carlo neutral code

The neutral particle model implemented in B2 does not include some processes such as the charge exchange between neutral particles and ions, although they can be dominant for some combinations of configurations and plasma conditions. To solve this problem in SOLPS it is possible to couple the B2 code with the neutral gas transport code EIRENE. EIRENE is a multi-species code solving simultaneously a system of time dependent or stationary linear kinetic transport equations. It is coupled to external databases for atomic and molecular data and for surface reflection data, and it calls user supplied routines for exchange of data with other fluid-transport codes, such as B2 in this case.

To describe the neutral particles behavior, the quantity of interest is the *one particle distribution function* $f \equiv f(\mathbf{r}, \mathbf{v}, i, t) \equiv f(x)$ where the state x in the phase space of a single particle ($\mu - space$) is characterized by a position vector $\mathbf{r}$, a velocity vector $\mathbf{v}$, a species index i and the time t. It evolves according to the 3D Boltzmann transport equations

$$\frac{\partial f(x)}{\partial t} + \overrightarrow{v} \nabla f(x) = C(f(x)) \qquad (7.33)$$

where C is the collision term. Since the characteristic time constants for neutral transport phenomena are very short (μs) compared to those for plasma transport (ms), it is possible to simplify the equations neglecting the explicit time dependence. A computational simplification is to neglect the neutral-neutral interactions, rendering the equation for $f(x)$ linear. For stationary problems the scalar transport flux Φ, where

$$\Phi(x) \equiv |\mathbf{v}| \cdot f(\mathbf{r}, \mathbf{v}, i), \qquad (7.34)$$

is used instead of $f(x)$. It is used in the (pre-) collision density form Ψ

$$\Psi(x) = \sum_t (x) \cdot \Phi(x), \qquad (7.35)$$

where the macroscopic cross section $\sum_t(x)$ is the total inverse local mean free path. The transport equation can be most conveniently written for the collision density as

$$\Psi(x) = S(x) + \int dx' \Psi(x') \cdot K(x' \to x). \qquad (7.36)$$

Here x' and x are the states at two successive collisions and the integral $\int dx'$ is an integral over all initial coordinates. The code provides a statistical solution to this equation. A description of the Monte Carlo solution of the equation is given by D. Reiter in *The EIRENE code, version:Jan. 92 Users manual* [97].

7.4 Technical aspects to run the codes

Differently from EDGE2D-EIRENE where the features of the simulations can be defined by means of a graphical interface, in SOLPS everything has to be qualified by means of text input files. Since the goal is to have a tool to simulate FTU SOL, it was necessary to learn how to deal with these input files and other technical aspects. To do that I run a test case of a circular shape Tokamak with a limiter configuration, since it is the simplest case.

To run the code first of all it is necessary to create the computational grid related with the geometry and magnetic configuration of the experimental plasma to simulate. It has to be made by quadrilaterals with two of the sides aligned along flux surfaces. The grid is generated by means of the gridgen script. For the test case the grid has the TEXTOR geometry ($R_0 = 1.75\,m$, $a = 0.45\,m$), the **T**okamak **EX**periment for **T**echnology **O**riented **R**esearch in the field of plasma wall interaction, a circular shape device with a toroidal limiter situated at the *Jülich Forschungszentrum*. This geometry has been chosen because TEXTOR was already been simulated by means of the SOLPS package and moreover the geometry is similar to the FTU one. The main features of the magnetic configuration chosen are: toroidal field along the axis $B_t(0) = 2.25\,T$, plasma current $I_p = 0.35\,MA$, and Shafranov shift $\Delta_s = 1 \times 10^{-6}\,m$.

Once that the main geometrical and magnetic features are prescribed, the technical features of the grid have to be selected. They are the minimum radius and the maximum radius that fix the radial region considered for the simulation and the number of main cells in the poloidal and in the radial direction. In the test case they are $r_{in} = 0.4\,m$, $r_{out} = 0.55\,m$ and 32 divisions in both the directions. The cells in the region of the limiter are also divided into an higher number of cells to better simulate the region of the limiter-plasma interaction. In figure 7.5 the grid is plotted in the physical plane. The cyan region is the limiter. The higher cells density around the limiter is well distinguishable.

Another important thing to be defined when building the grid is the so called *cut position*. It is the position where the grid is opened to warp it from the physical plane to the computational grid the code interfaces with. In this case it is set at 180° to have symmetry in the grid. The cut position is the red line in figure 7.5. In figure 7.6 the computational grid corresponding to the magnetic configuration described above is plotted. The *x-axis* in the computational grid corresponds to the poloidal direction in the physical plane and the *y-axis* corresponds to the radial direction consistent with the fluid equations of section 7.2.2.

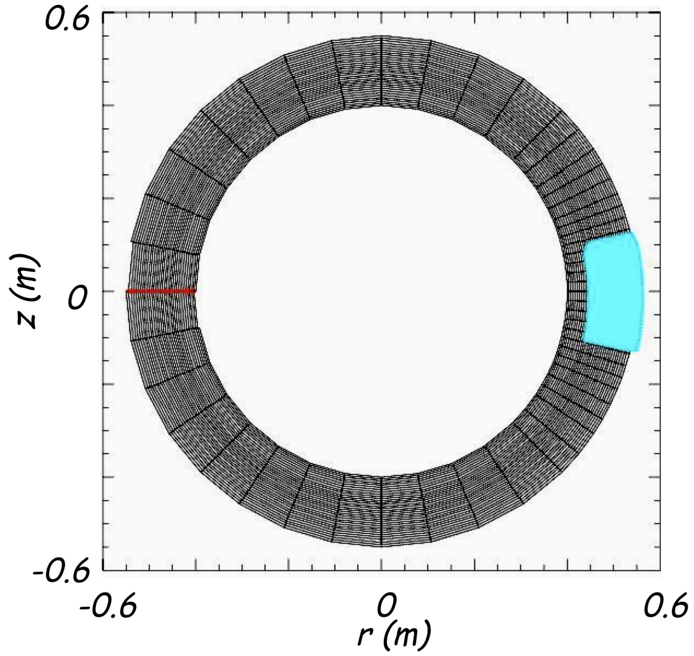

Figure 7.5: TEXTOR grid in the physical plane used to perform the test simulations with B2.

The orientation of the computational grid is described with the cardinal point. The side faced with the plasma in radial direction is called **S**outh, the one faced with the wall is called **N**orth and so on.

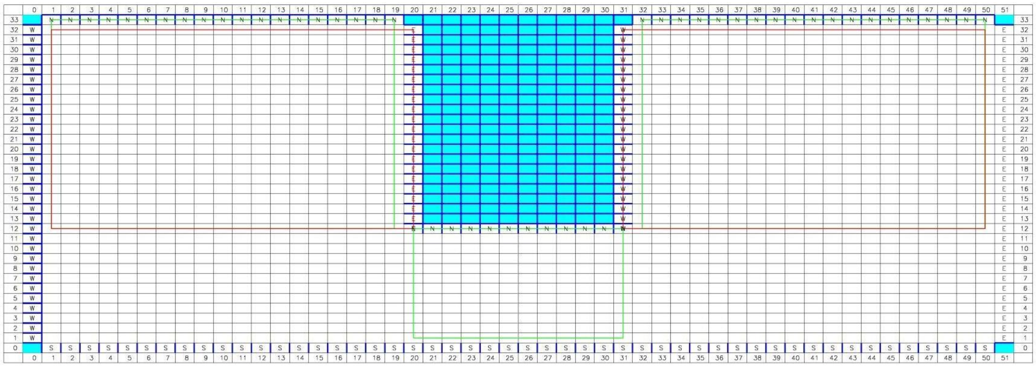

Figure 7.6: TEXTOR computational grid used to perform the test simulations with B2.

After setting the grid to run B2, it is necessary to define the boundary conditions and the transport parameters. In order to do that a so-called *input file* has to be written. It consists of six main blocks briefly described below.

1. **The cuts block**. It defines the position of the solid surfaces in the grid and the side of the cells that are involved with the boundary conditions. Moreover it defines a fixed density and temperature for the solid surfaces that do not interfere with the boundary conditions.

2. **The boundary conditions block**. In this block the density and the temperature along the boundary of the grid are fixed. Since the boundary conditions are related with with the simplify set of Braginskii equations [92, 94] solved by B2, it is not strictly necessary to fix the values of density and temperature, but it can be also defined an influx of particles and power respectively, or even a gradient. In this block also the periodic conditions on the cut position are defined, i.e. the values on the east side of the computational grid have to be equal to them on the west side.

3. **The transport parameters block**. Here are defined the values of the radial diffusion coefficient and of parallel and radial thermal coefficients, both for ions and electrons.

4. **Neutral block**. This block has two different functions depending if B2 is running standalone or coupled with EIRENE. If it is running standalone the neutral block defines the regions that act as neutral sources and the region that act as sink. If B2 is coupled with EIRENE the neutral block is used to link the B2 computational grid to the EIRENE one.

5. **Impurities block**. Here the number of fluids that has to be managed is set. Each fluid corresponds to a ionization state of the species considered.

6. **Computational block**. In this block the parameters of the numerical procedure are defined, such as the number of steps the code has to do and their duration.

Once that the mesh and the physical parameters are defined it is possible to run B2 for the number of steps prescribed. The quality of the solution is given by the analysis of the convergence of the code. It is done looking at the residual of the equations. A good convergence can be asserted if the normalized residuals achieve a constant low value ($\simeq 10^{-5}\ s^{-1}$).

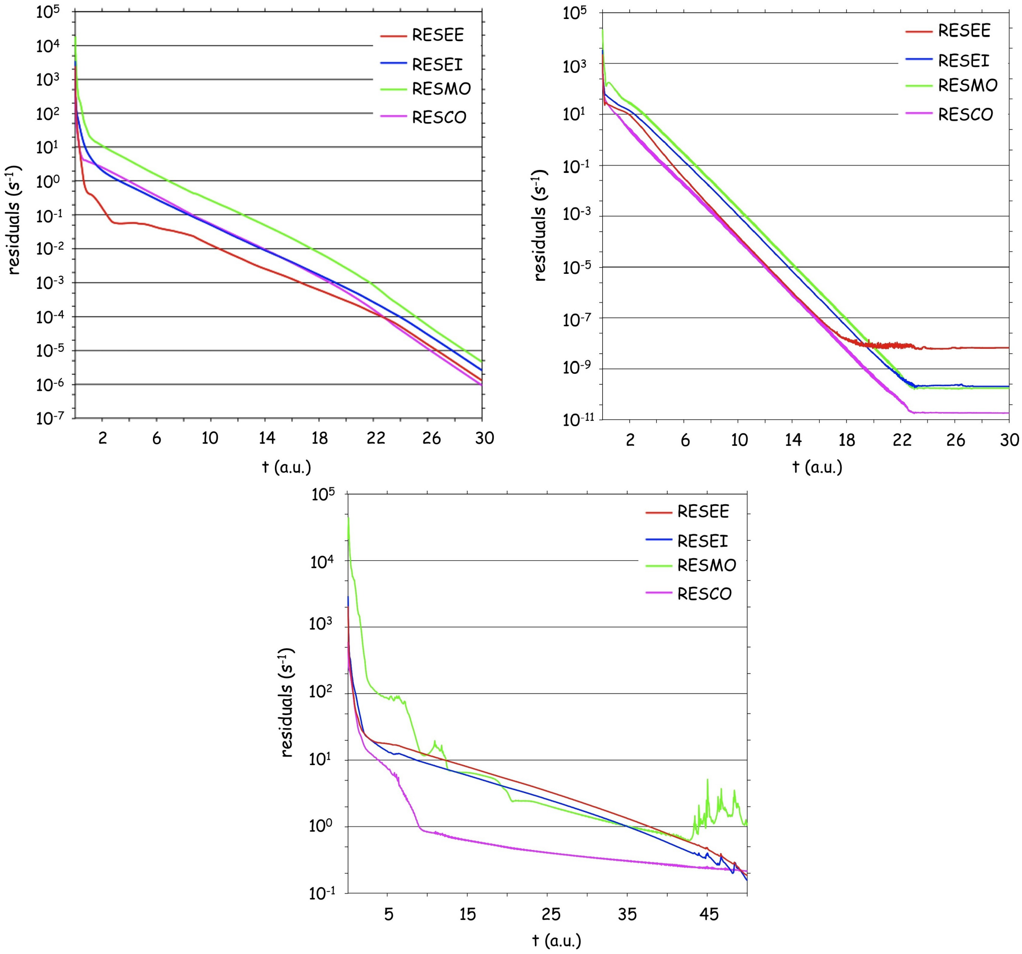

Figure 7.7: Time traces of residuals for the electron energy (red), ion energy (blue), momentum (green) and continuity (purple) equations of B2. In the first picture a case not yet converged because residuals are still decreasing at the end of the simulation, in the second picture a converged case and in the third a non converging case.

In figure 7.7 are reported three different cases: a not yet converged case; a converged case and a non converging case. In red and blue are drawn time evolution of the residuals for the energy equation for electrons and ions respectively, in green for the momentum equation and in purple for the continuity equation. In the first case the solution can be considered valid since the value of the normalized residuals is less than $10^{-5}\ s^{-1}$ also if it is not converged yet, while the third case cannot be considered valid because the residuals show a very small decreasing rate (that of momentum equation does not decrease at all) and moreover the value of residual is around $1\ s^{-1}$.

To couple B2 with the EIRENE Monte-Carlo kinetic neutrals code it is needed to provide EIRENE with some parameters. These parameters are: the mesh and the cells that have particular proprieties such as reflectivity or absorption; the reactions to consider and how they interact with the particles followed; the interaction of the surfaces with the incident particles; numerical aspects about computation and outputs. A further description of the input file is given in the *"The EIRENE Code User Manual including: B2-EIRENE interface"* by D. Reiter [93].

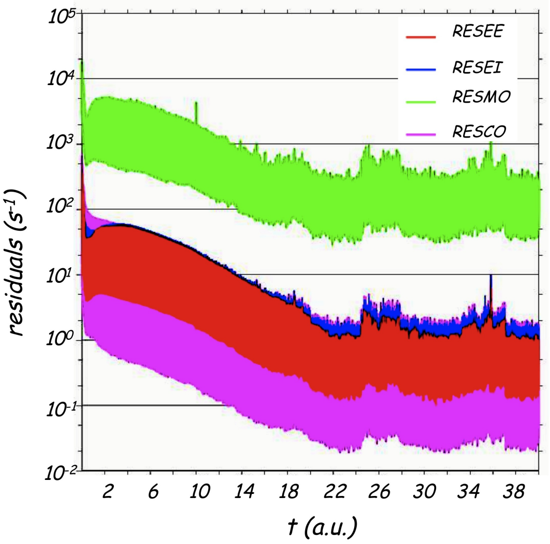

Figure 7.8: Time traces of residuals for the electron energy (red), ion energy (blue), momentum (green) and continuity (purple) equations in case of B2 coupled with EIRENE.

Since the coupling of B2 with EIRENE introduces a statistical noise, to check the convergence of the solution by looking at the residuals is not anymore possible. An example of residual evolution in case of the two codes coupled is given in figure 7.8

To test the validity of the results it is therefore necessary to check the convergence of the solutions for different quantities. In figure 7.9 the values of several quantities are plotted at different grid positions as a function of the numerical steps. Although the residuals do not converge to a low value, the solution converges to stable values, that means the code converged to a valid solution.

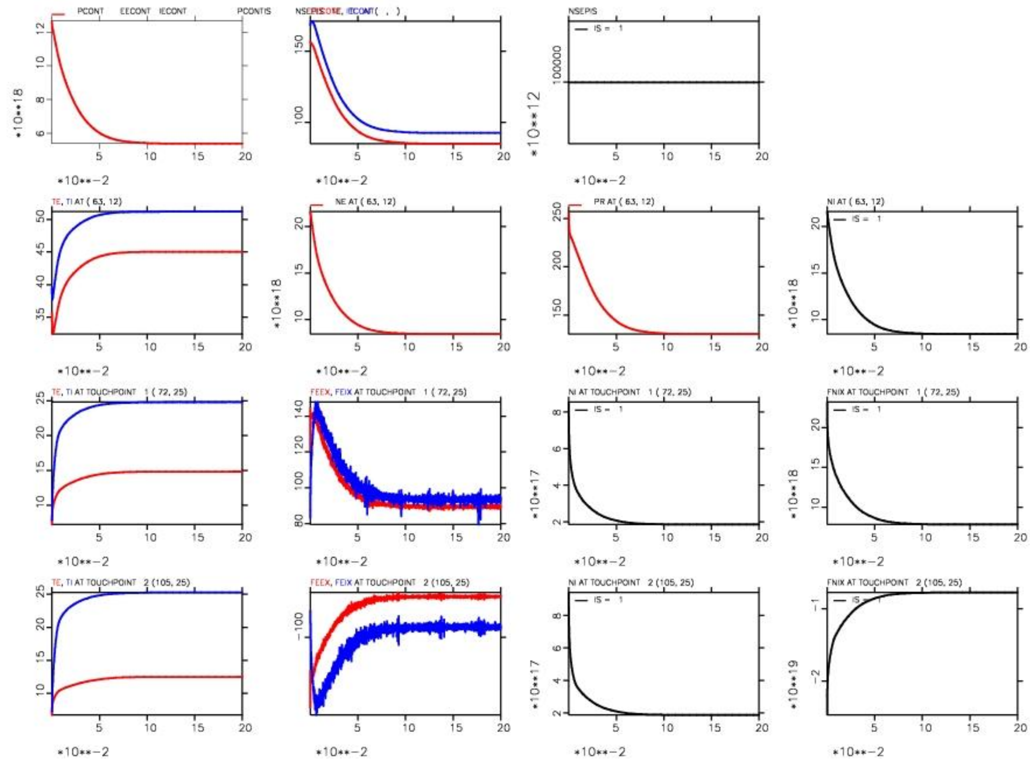

Figure 7.9: Time traces of several quantities in different grid positions.

Frascati Tokamak Upgrade Edge Modeling

The **F**rascati **T**okamak **U**pgrade (FTU) is a Tokamak device with toroidal limiter geometry where wall conditioning experiment have been performed. Since the end of 2005 a liquid lithium limiter (LLL) has been installed in order to study the effects of lithium as a plasma facing material [61, 98]. The main effects observed are the reduction of radiation losses, plasma contamination and main gas recycling. Moreover also an higher core density peaking and an higher electron temperature in the SOL have been observed. To better understand these results a simulation of the edge plasma physics of FTU by means of the 2D edge transport code TECXY [99] had been already done, proving to be very useful to understand the observed phenomena [100]. Starting from these results, there is a need to perform the study of the edge transport also with other codes, such as the SOLPS package presented in chapter 7.

Aim of this work is to model FTU discharges by means of SOLPS in order to have the tools that will be then used to study the effect of lithization on the impurities transport in the SOL, on the power load on the limiter surfaces and its contribution to the impurities content in the main plasma. In this chapter it will be presented the work carried out along this way. In section 8.1 is presented the modeling with SOLPS of the simple TEXTOR limiter SOL configuration presented in section 7.4, in order to understand the code sensitivity to the different available control knobs. In section 8.2 is reported the first approach with simulation of FTU data in case of non-lithizated discharges.

8.1 Simple limiter configuration modeling

To study the code sensitivity to the various code controlling parameters several scans of them have been performed. It was said in section 7.3 that the transport code can deal with the neutrals by itself or can be coupled with EIRENE. Since the goal of the test was to understand the sensitivity of the transport code to different parameters rather than the validity of the results and a Monte Carlo code needs a lot of computational time to converge, the first scans have been done running B2 standalone. A significant scan performed is presented below. Once that the goal was achieved, it was studied also the improvement coming out from the use of EIRENE to describe neutrals behavior.

8.1.1 B2 standalone, pure deuterium

The scans done running B2 standalone show how the transport code reacts modifying the boundary conditions rather than the transport coefficients or the numerical parameters. An important scan in particular for the simulation of FTU discharges presented in section 8.2 is that of the radial transport coefficients. In fact it is possible to think that the density and temperature in the plasma core and at the wall are known from diagnostics data, while the choice of the radial coefficients gives their radial profile. The scan has been performed considering a particle influx from the core $\Gamma_{D+} = 5 \times 10^{21}\, m^2 s^{-1}$ and a power incoming from the core $P_{in} = 1\, MW$ equally divided by electrons and ions. At the wall the electron density is $n_e^{wall} = 1 \times 10^{17}\, m^{-3}$ and the temperature is $T_i = T_e = 5\, eV$. The scan is done modifying the radial transport coefficient from $D_\perp = 0.2\, m^2 s^{-1}$ to $D_\perp = 5\, m^2 s^{-1}$. Figures 8.1, 8.2, 8.3, 8.4, 8.5 and 8.6 show the results of the scan looking at the edge radial profile in the upstream region, near the target and poloidally along the LCFS respectively.

Since the boundary condition on the density at the core is a particles influx instead of a fixed value, the simulations show that increasing the transport coefficient the average value of the density at the edge decreases for perpendicular transport coefficient $D_\perp \leq 5\, m^2 s^{-1}$. Neglecting the case with the highest $D_\perp$ value, the effect of a different $D_\perp$ affects only slightly the shape of the two radial profiles plotted in the SOL, both for the density and for the temperature, while it affects the values of these two quantities in the thin layer inside the LCFS. Moreover also poloidally the profile shape is not strongly affected: increasing $D_\perp$ decreases only the average value.

It is interesting to note that decreasing the radial transport coefficient, the code needs more steps to converge.

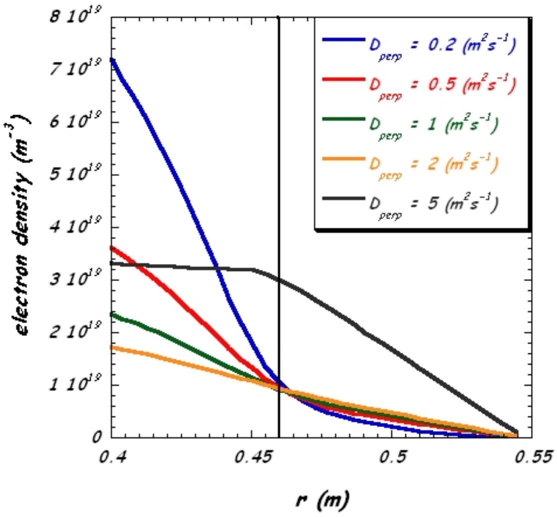

Figure 8.1: Radial electron density profiles for different radial transport coefficient at the stagnation point. The vertical line is the LCFS radial position.

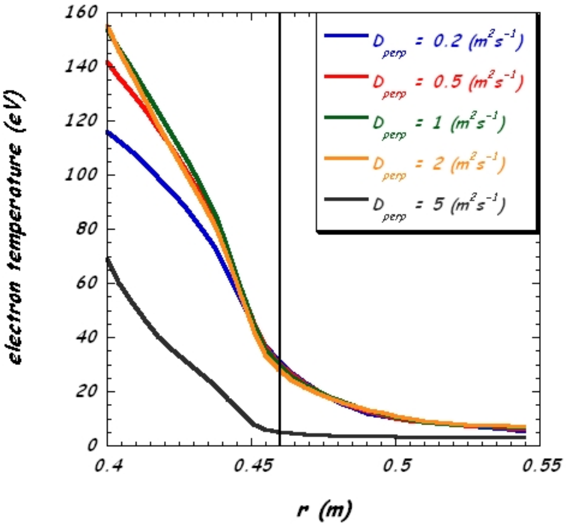

Figure 8.2: Radial electron temperature profiles for different radial transport coefficient at the stagnation point. The vertical line is the LCFS radial position.

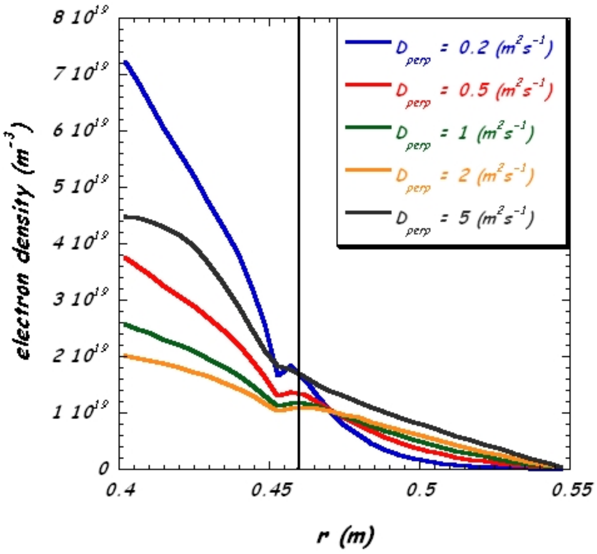

Figure 8.3: Radial electron density profiles for different radial transport coefficient at the target position. The vertical line is the LCFS radial position.

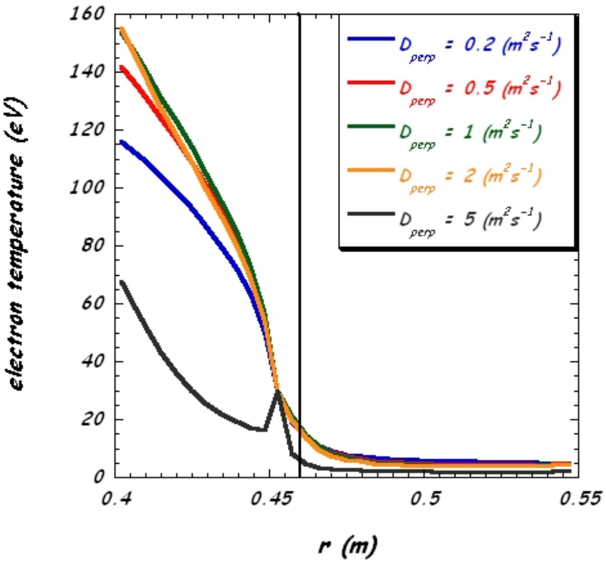

Figure 8.4: Radial electron temperature profiles for different radial transport coefficients at the target position. The vertical line is the LCFS radial position.

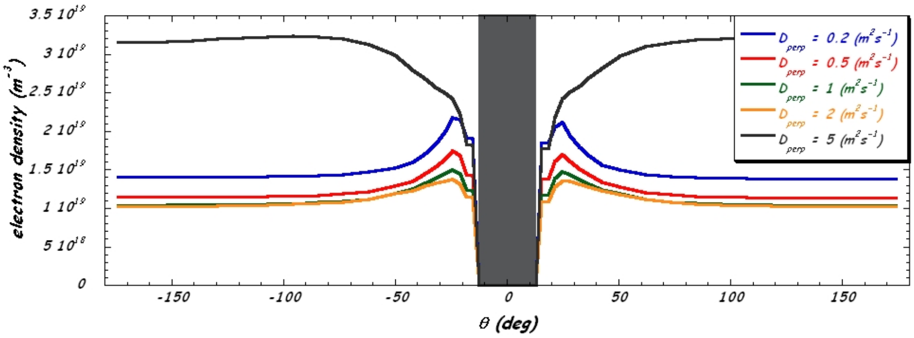

Figure 8.5: Poloidal electron density profiles for different radial transport coefficients at the LCFS. The shadow area is the limiter position.

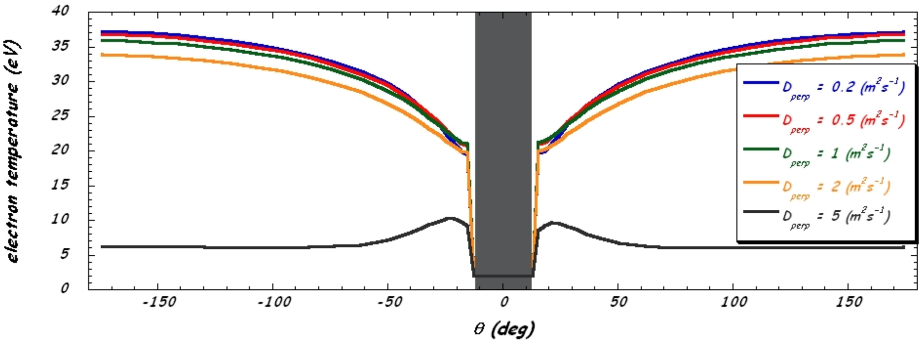

Figure 8.6: Poloidal electron temperature profiles for different radial transport coefficients at the LCFS. The shadow area is the limiter position.

8.1.2 B2-EIRENE, pure deuterium

Another important effect on the simulations is given by the use of EIRENE to describe the neutrals behavior. Using EIRENE for neutral distribution several problems emerge, both technical and physical. The test simulations done introducing the neutral code were therefore focused on the understanding of the parameters that lead to convergence of the solutions and on the comparison with the results obtained with B2 standalone.

In figure 8.7, 8.8, 8.9, 8.10 and 8.11 it is reported the comparison between a simulation with B2 standalone and the same simulation done coupling it with EIRENE. The plasma parameters considered are $D_\perp = 1\, m^2 s^{-1}$, $\chi_\perp^{i,e} = 1\, m^2 s^{-1}$ and $\chi_\parallel^{i,e} = 1\, m^2 s^{-1}$. In this case it is considered a fix density and temperature also at the core boundary. The main plasma electron density is $n_e^{core} = 5 \times 10^{19}\, m^{-3}$ and the temperature is $T_e^{CORE} = T_i^{CORE} = 100\, eV$. At the wall it is assumed a density $n_e^{wall} = 5 \times 10^{18}\, m^{-3}$ and a temperature $T_e^{wall} = T_i^{wall} = 6\, eV$. At the top of the limiter the fixed boundary conditions are $n_e^{lim} = 6 \times 10^{18}\, m^{-3}$ and a temperature $T_e^{lim} = T_i^{lim} = 30\, eV$.

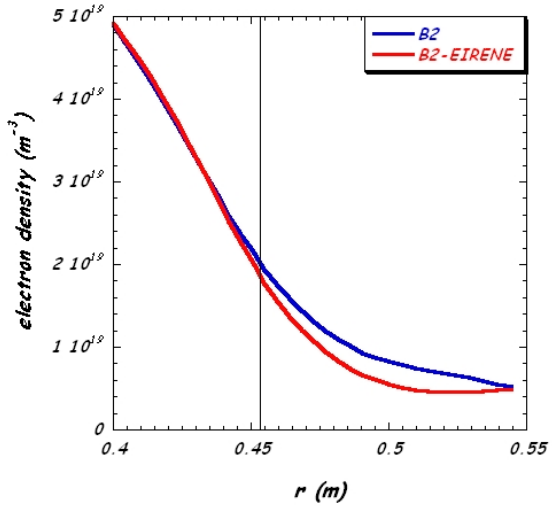

Figure 8.7: Comparison of the radial electron density profiles between B2 standalone (blue) and coupled with EIRENE (red) at the stagnation point.

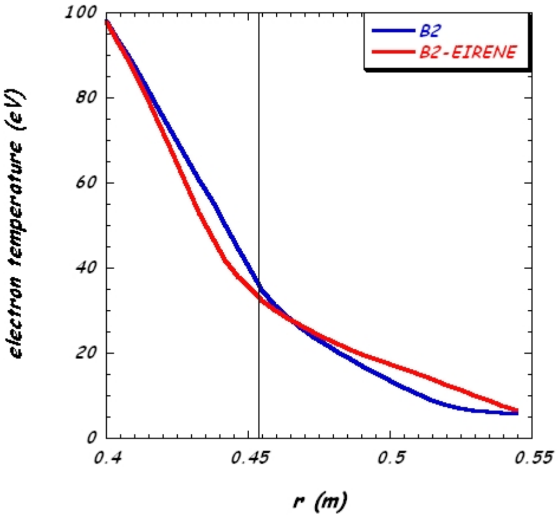

Figure 8.8: Comparison of the radial electron temperature profiles between B2 standalone (blue) and coupled with EIRENE (red) at the stagnation point.

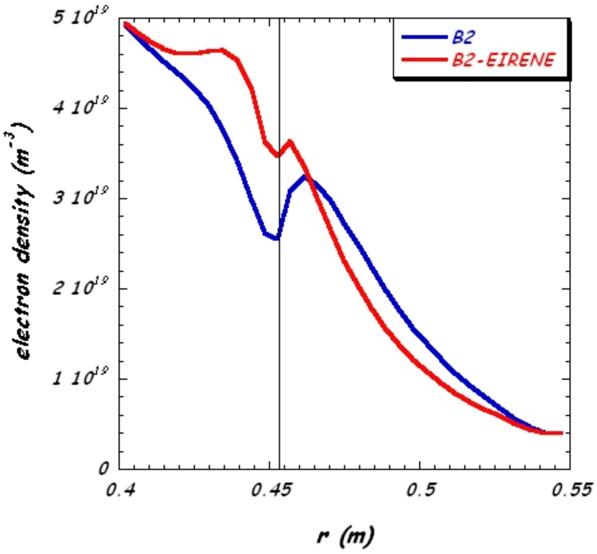

Figure 8.9: Comparison of the radial electron density profiles between B2 standalone (blue) and coupled with EIRENE (red) at the target position.

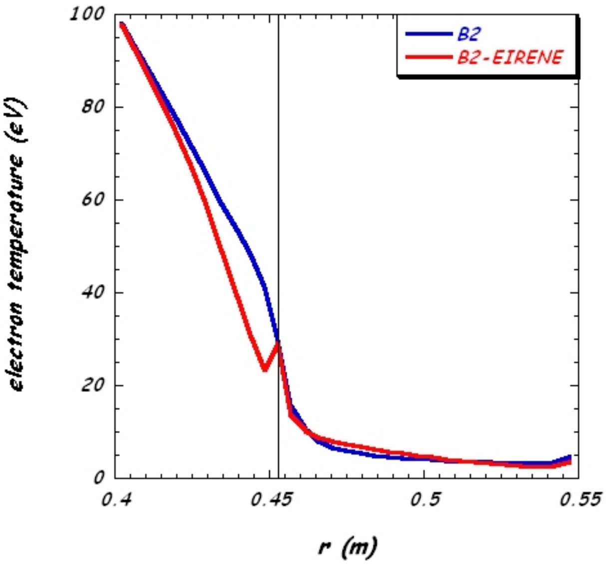

Figure 8.10: Comparison of the radial electron temperature profiles between B2 standalone (blue) and coupled with EIRENE (red) at the target position.

Figures 8.7, 8.8, 8.9 and 8.10 show that the main differences due to the presence of the neutral code are near the limiter, where there is a greater neutral influx due to the plasma-limiter interaction, while they are negligible at the stagnation point. The electron density and temperature radial profiles at the target also show an higher electron density near the top of the limiter that leads to a decrease of the temperature just at the target position in case of neutrals driven by the Monte Carlo code. Another remarkable result of this simple simulation is related to the shape of the profiles. Due to the choice of fixed density and temperature at the core boundary instead of particles and power fluxes, the shapes are less smooth, resulting in unphysical results.

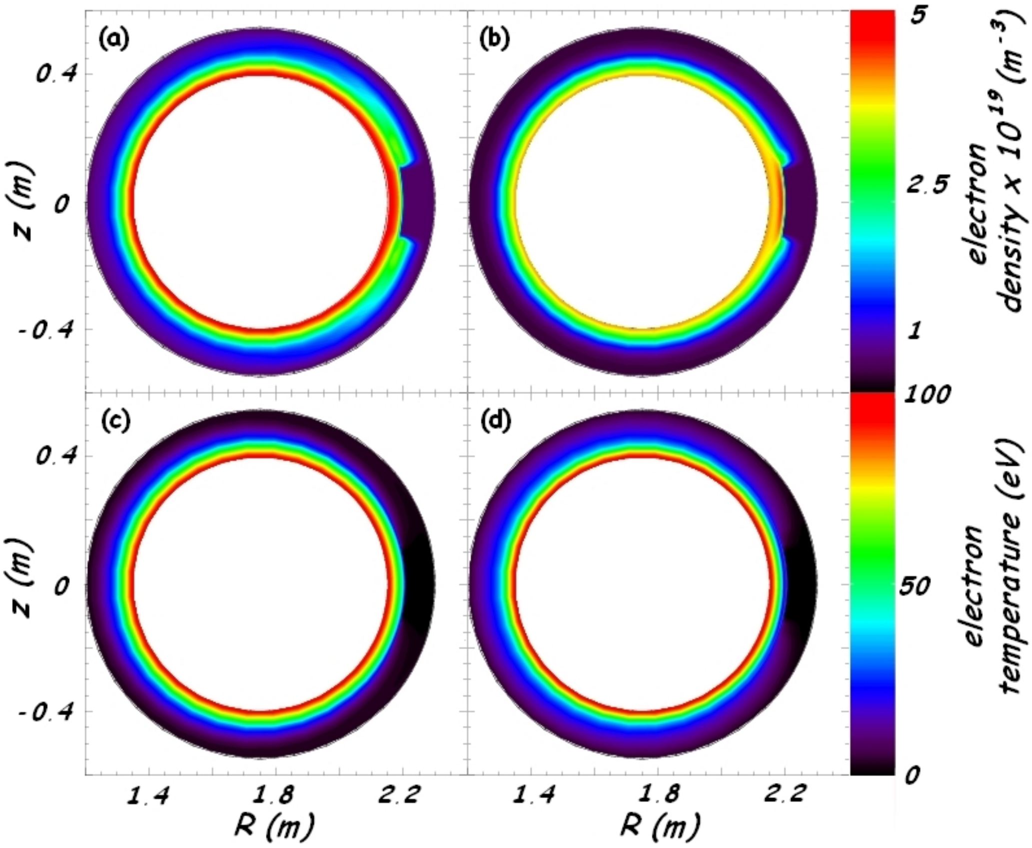

Figure 8.11: Electron density ((a),(b)) and temperature ((c),(d)) in case of B2 standalone ((a),(c)) and coupled with EIRENE ((b),(d)). The colours go from $5 \times 10^{18}\, m^{-3}$ to $5 \times 10^{19}\, m^{-3}$ for the density, and from $0\, eV$ to $100\, eV$ for the temperature.

Figure 8.11 shows the electron density and temperature in the whole poloidal cross section for the two cases. The increase of the electron density occurs more smoothly in case of B2 coupled with EIRENE, leading to a faster increase of the electron temperature around the poloidal cross section in the region away from the target. There is a steep increase of the electron density profile well localized in front of the limiter. It contributes to maintain a lower electron temperature just there with respect to the case simulated with B2 standalone.

8.2 FTU modeling with SOLPS

8.2.1 Simulation of experimental current scan

A grid describing the FTU shape has been build by means of the gridgen and gridadap scripts (see figure 8.12) then some simulations were performed in order to find plasma parameters able to reproduce the electron density and temperature profiles measured by means of Langmuir probes [100]. To do that, three reference discharges with different plasma current have been chosen, from 0.5 to 0.9 MA. The discharges chosen are the FTU pulse #25489, #23999 and #25501.

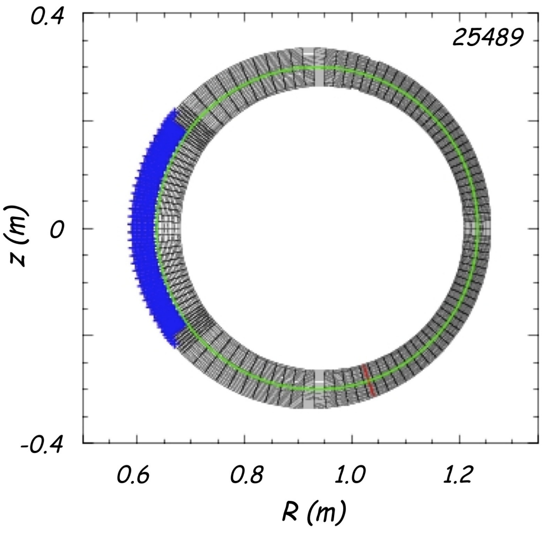

Figure 8.12: Grid of the discharge #25489 of FTU. In blue is highlighted the toroidal limiter, in green the LCFS and in red the Langmuir probes poloidal position.

The simulations are performed with pure deuterium plasma. The perpendicular diffusion coefficient has been assumed $D_\perp = 1\, m^2 s^{-1}$ for all the cases. Also the electronic and ionic radial thermal coefficients have been taken equal to $\kappa_\perp^{e,i} = 1\, m^2 s^{-1}$. The electron and ion temperatures in the core have been imposed $T_e^{core} = T_i^{core} = T^{core} = 100\, eV$. The particles influx from the core is $\Gamma_{D+} = 2 \times 10^{21}\, m^{-2} s^{-1}$ for the discharges #23999 and #25501 and $\Gamma_{D+} = 1 \times 10^{21}\, m^{-2} s^{-1}$ for the case #25489. The density at the wall is imposed to be $n_e^{wall} = 1 \times 10^{17}\, m^{-3}$ and the electron and ion temperature at the wall is $T_e^{wall} = T_i^{wall} = T^{wall} = 15\, eV$. The results of the simulation compared with Langmuir probes measurements are shown in figure 8.13 (electron density radial profile) and 8.14 (electron temperature radial profile).

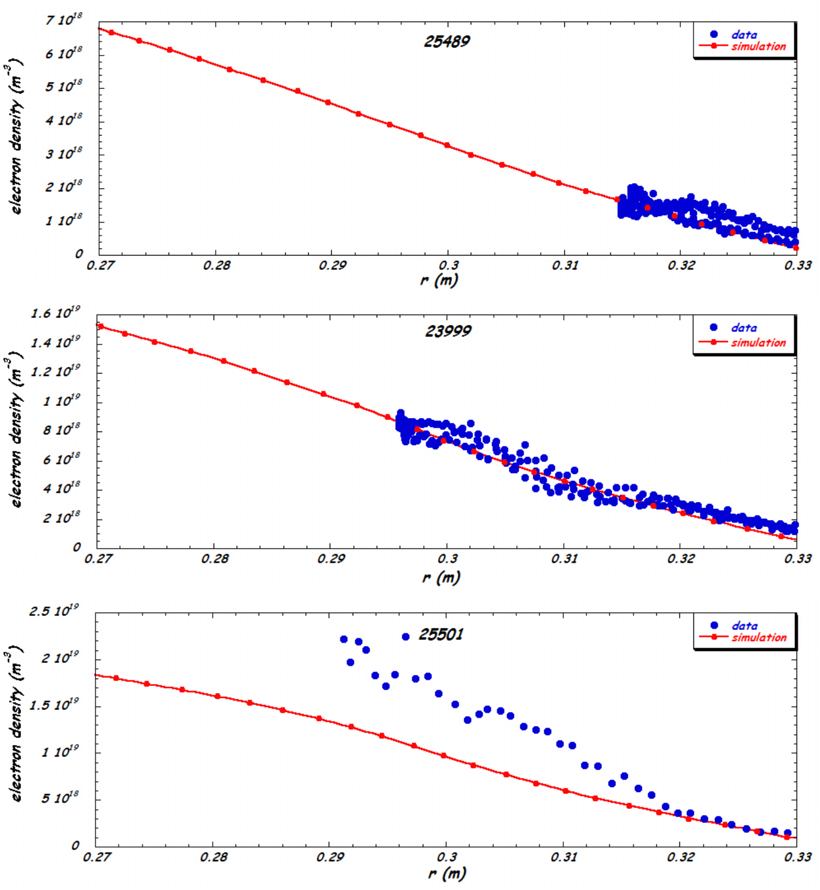

Figure 8.13: Langmuir probes measurement of the electron density radial profile for three different discharges and their reconstruction with SOLPS with $D_\perp = 1\, m^2 s^{-1}$.

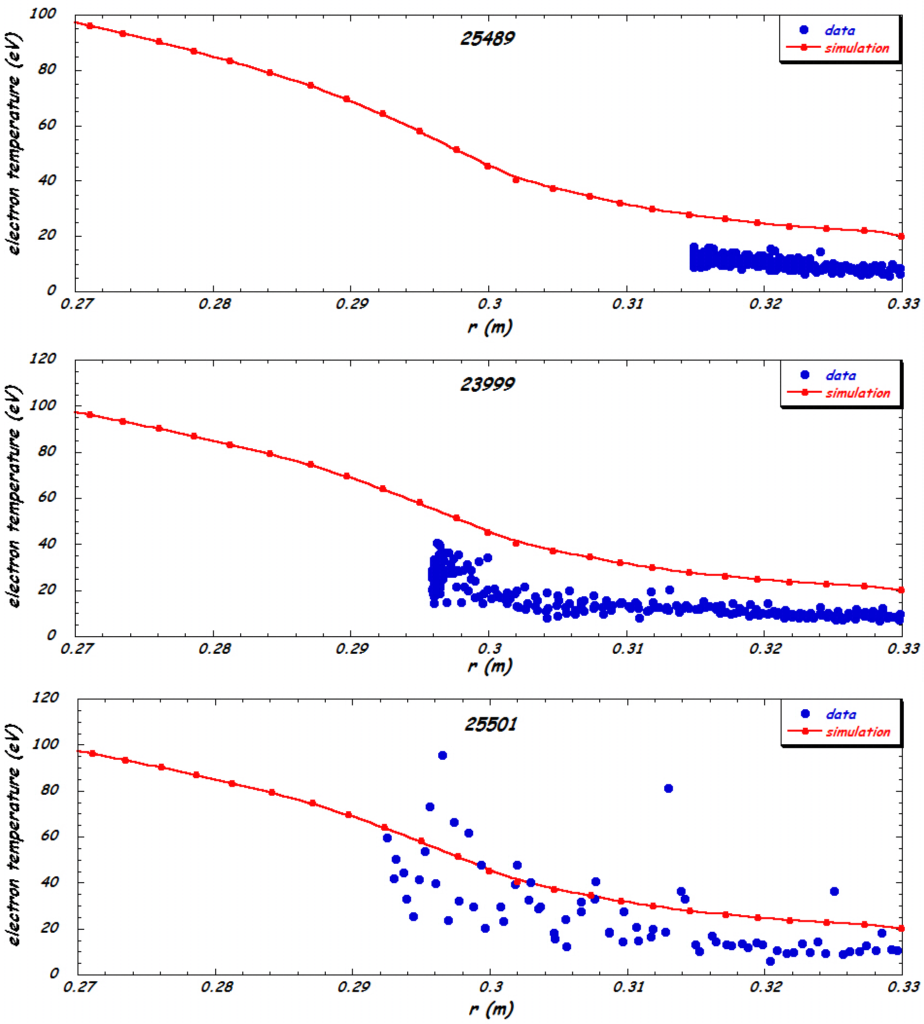

Figure 8.14: Langmuir probes measurement of the electron temperature radial profile for three different discharges and their reconstruction with SOLPS with $D_\perp = 1\, m^2 s^{-1}$.

The density radial profile is well reproduced in the two cases of lower plasma current (#25489 and #23999), while the shape of the radial profile for the case #25501 is different from the measurements. Looking at the electron temperature, the shape of the simulated profiles is similar to the measurements, but the values are always higher, except in the case #25501 where data from the probes are very noisy and also the simulated density is wrong. The different values of the electron temperature can be explained by the lack of impurities in the simulation, that act as energy sink.

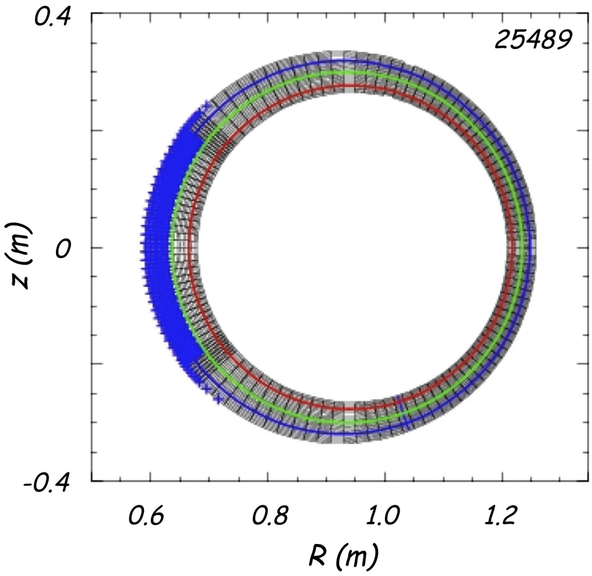

Figure 8.15: Poloidal rings position on the physical plane considered for the analysis.

It was seen in chapter 6 that the existence of a parallel temperature gradient leads to different divertor regimes and it is an indicator of the power deposited on the target. Thus it is of interest to look at the poloidal profile of electron density and temperature. They are drawn in figure 8.16 and 8.17 respectively. In figure 8.15 is drawn the poloidal ring the profiles are referred to. They show that increasing the plasma current also the density in the edge increases, even though the particle influx from the core is the same, at least for the cases #23999 and #25501. A consequence of the density increase is that also the density in front of the limiter along the separatrix increases, from a value lower than the one away from the limiter to an higher one. Moreover it leads to a density increase also in the SOL region. As it is expected, increasing the density, the temperature along the SOL decreases.

The different value of the electron temperature in the three cases does not lead to different shapes of the poloidal profile. It is costant along the SOL and inside the LCFS. The only poloidal profile where there is a temperature gradient is along the LCFS. This is also confirmed by the radial profile of the electron parallel power flux density at the target position. Being it related with the parallel temperature gradient, the maximum of the power flux is at the separatrix, and it decreases quickly moving from it. Moreover the maximum increases also if the electron temperature decreases, following the increase of the plasma current. The parallel power flux density profiles are plotted in figure 8.18.

Figure 8.17 also highlights that there is a problem in the boundary conditions of the code. Although at the cut position it was required that the quantities on the left were equal to the one on the right (periodic conditions), a jump on the values is evident in its position.

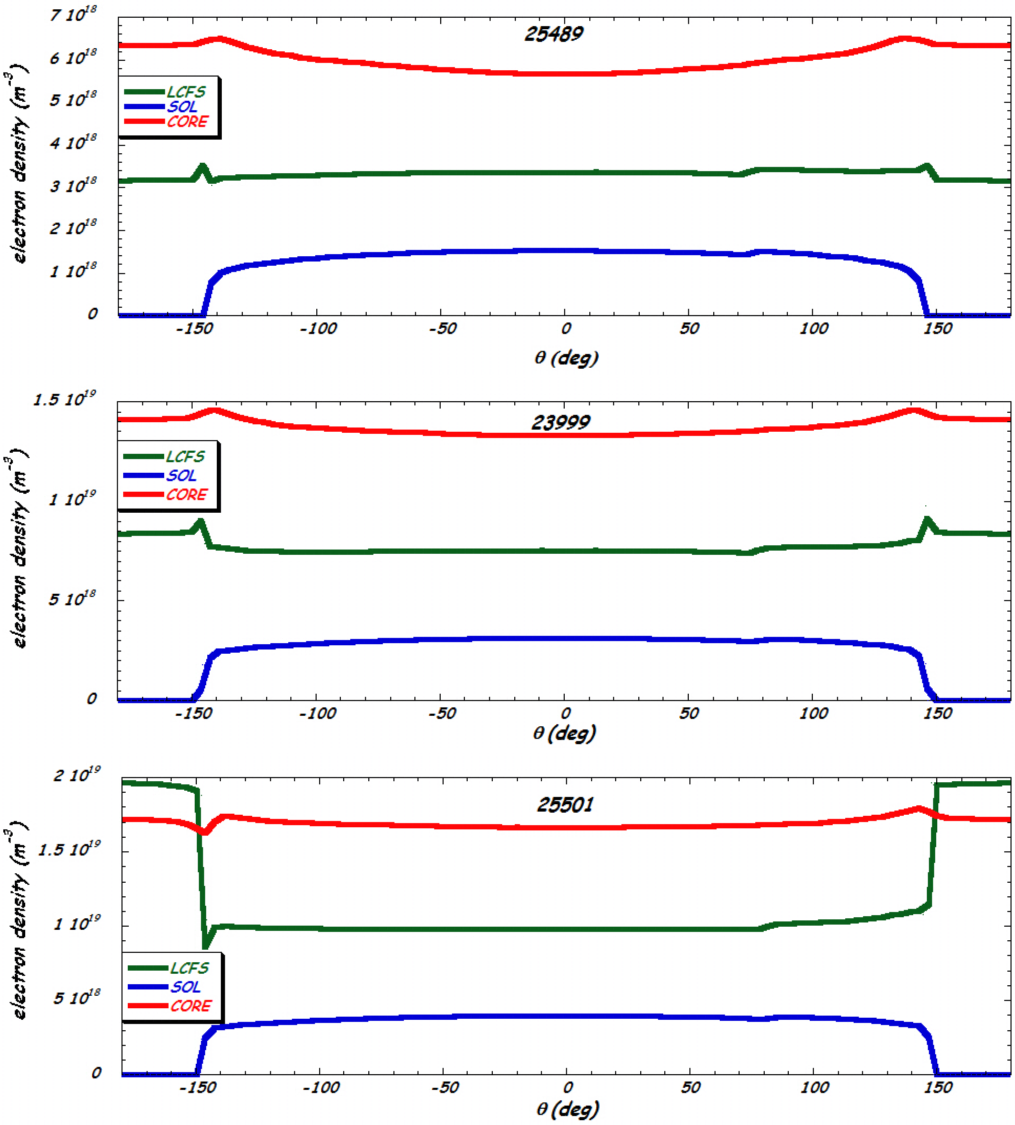

Figure 8.16: Reconstruction of the electron density poloidal profile for three different discharges in three different positions.

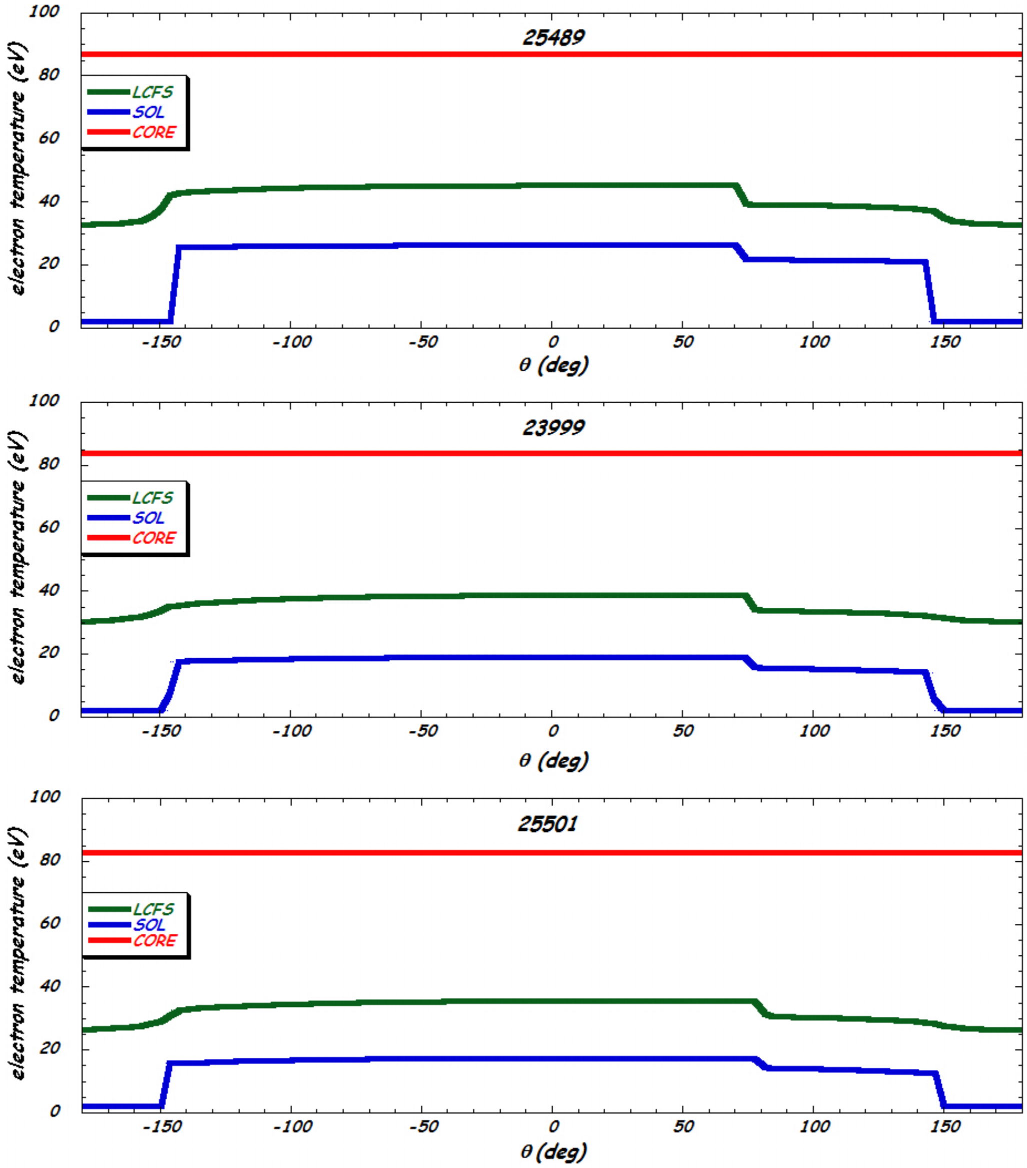

Figure 8.17: Reconstruction of the electron temperature poloidal profile for three different discharges in three different positions.

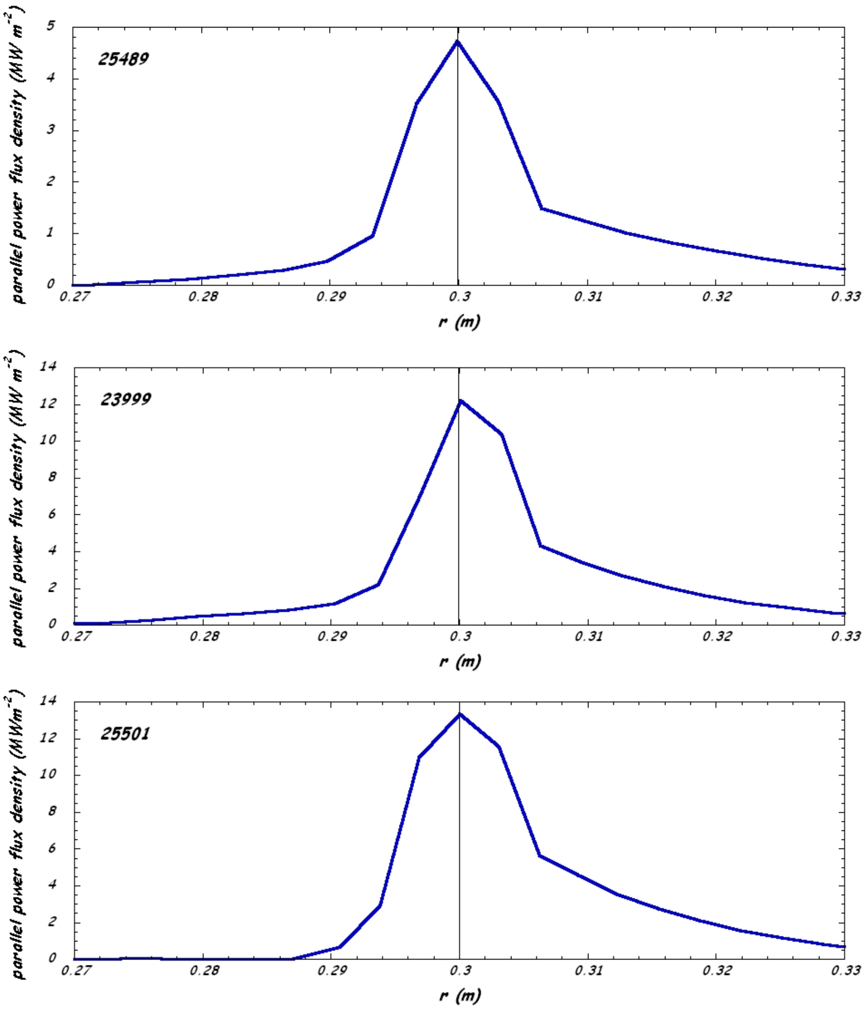

Figure 8.18: Parallel power flux density radial profile carried by electrons at the target for the three different discharges.

8.2.2 Other solutions to fit experimental data

Since the the shape of the radial profile for the case #25501 is different from the measured one, two ways have been tested to reproduce it: a change in the perpendicular diffusion coefficient or the inclusion into the simulations of the poloidal limiter.

In figures 8.19, 8.20 it is shown the effect on the electron density and temperature profiles of the scan over the perpendicular diffusion coefficient. In blue $D_\perp = 0.5\,m^2s^{-1}$, in green $D_\perp = 1\,m^2s^{-1}$ and in red $D_\perp = 2\,m^2s^{-1}$.

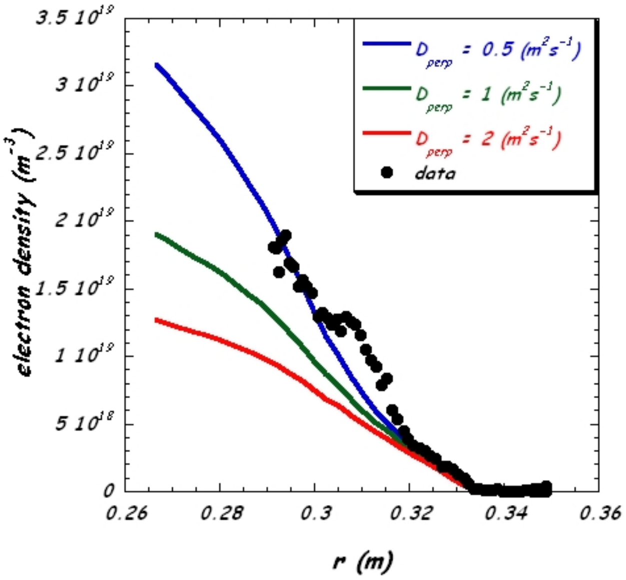

Figure 8.19: Effect of the perpendicular diffusion coefficient scan on the electron density radial profiles and their comparison with the Langmuir probes measurements for the case #25501.

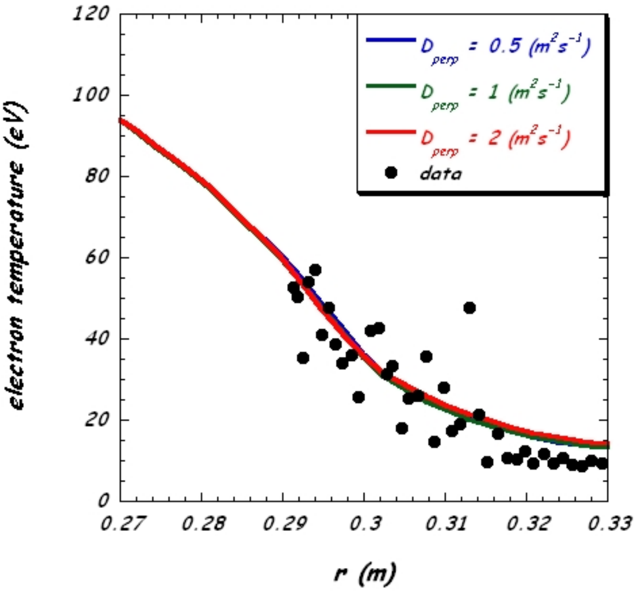

Figure 8.20: Effect of the perpendicular diffusion coefficient scan on the electron temperature radial profiles and their comparison with the Langmuir probes measurements for the case #25501.

The boundary conditions are the same in the three cases. The shape of the electron density profile with $D_\perp = 1\,m^2 s^{-1}$ and $D_\perp = 2\,m^2 s^{-1}$ is the same, the only difference is that the average value of the density with an higher perpendicular diffusion coefficient is lower. In case of $D_\perp = 0.5\,m^2 s^{-1}$ the average density in the edge is higher, and also the shape is different, achieving higher values inside the separatrix but without any improvement in the SOL with respect to the agreement with the experimental data. About the electron temperature, there are no differences in the three cases. This is expected because the thermal coefficients are still the same.

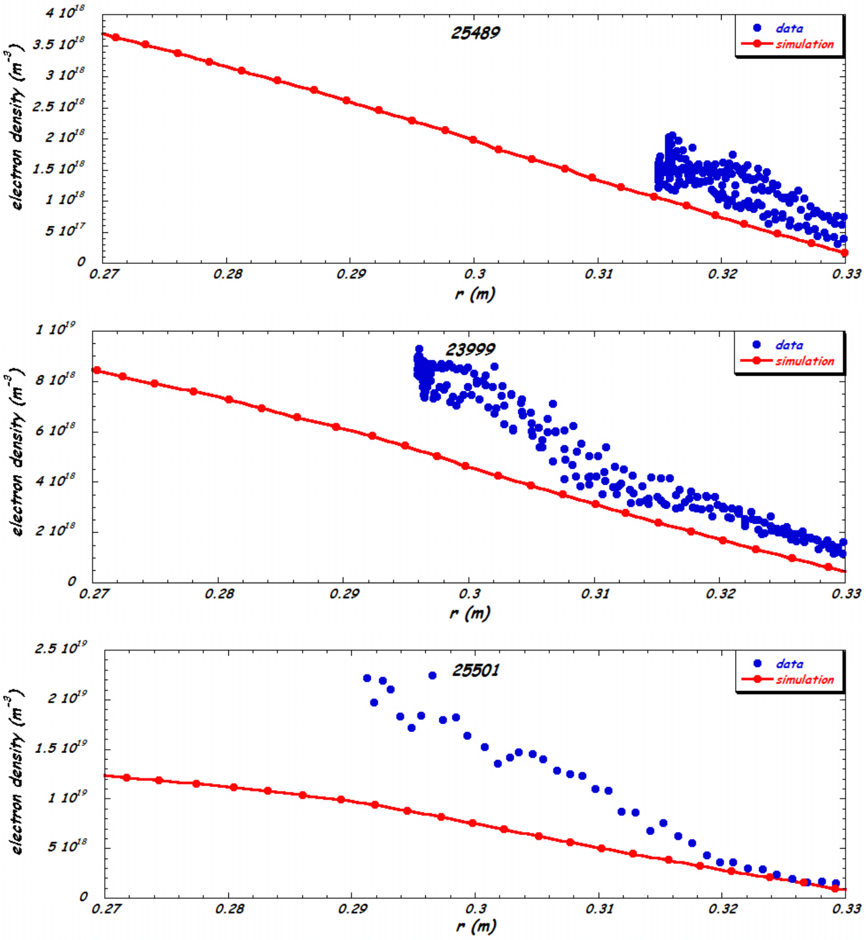

Figure 8.21: Langmuir probes measurement of the electron density radial profile for three different discharges and their reconstruction with SOLPS with $D_\perp = 2\,m^2 s^{-1}$.

In figure 8.21 it is shown the effect of $D_\perp = 2\, m^2 s^{-1}$ in the three discharges. It is seen that the agreement with the data get worst with respect to the case with $D_\perp = 1\, m^2 s^{-1}$. The result is the expected one since it is in agreement with the performed $D_\perp$ scan presented in section 8.1.

In the FTU machine there is also a poloidal limiter. It is therefore possible to explain the different profile shape in the pulse #25501 by its presence. This was not considered in the previous simulation because it is not toroidally symmetric. To insert the poloidal limiter in the simulation, a new grid is needed. It is shown in figure 8.22, where in blue are marked the two limiters, in green the LCFS and in red the Langmuir probes position.

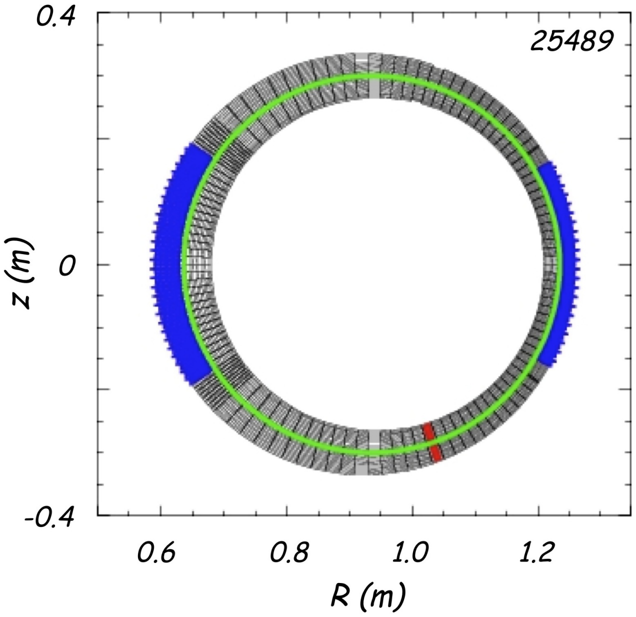

Figure 8.22: Grid of the discharge #25489 of FTU considering also the poloidal limiter. In blue are highlighted the two limiters, in green the LCFS and in red the Langmuir probes poloidal position.

Figures 8.23 and 8.24 show the electron temperature and density radial profiles in this configuration. The effects of the presence of the poloidal limiter in the simulation are mainly two: one on the shape of the radial density profiles and one on the temperature average value. About the density, in the case #25501 the agreement with the data is better than without the limiter, while in the case #23999 it is worst. Regarding the case #25489 it is not possible to compare the two simulations because the data range (from $31.5 cm$ up to $33 cm$) is too small. About the temperature radial profiles, they are in agreement with the measurements. As observed in the previous section, to obtain a right value of the temperature it was needed an energy sink. In this case, since the poloidal limiter is considered also toroidal because of the bi-dimensionality of the code, the target take the roles previously attributed to the impurities in decreasing the temperature.

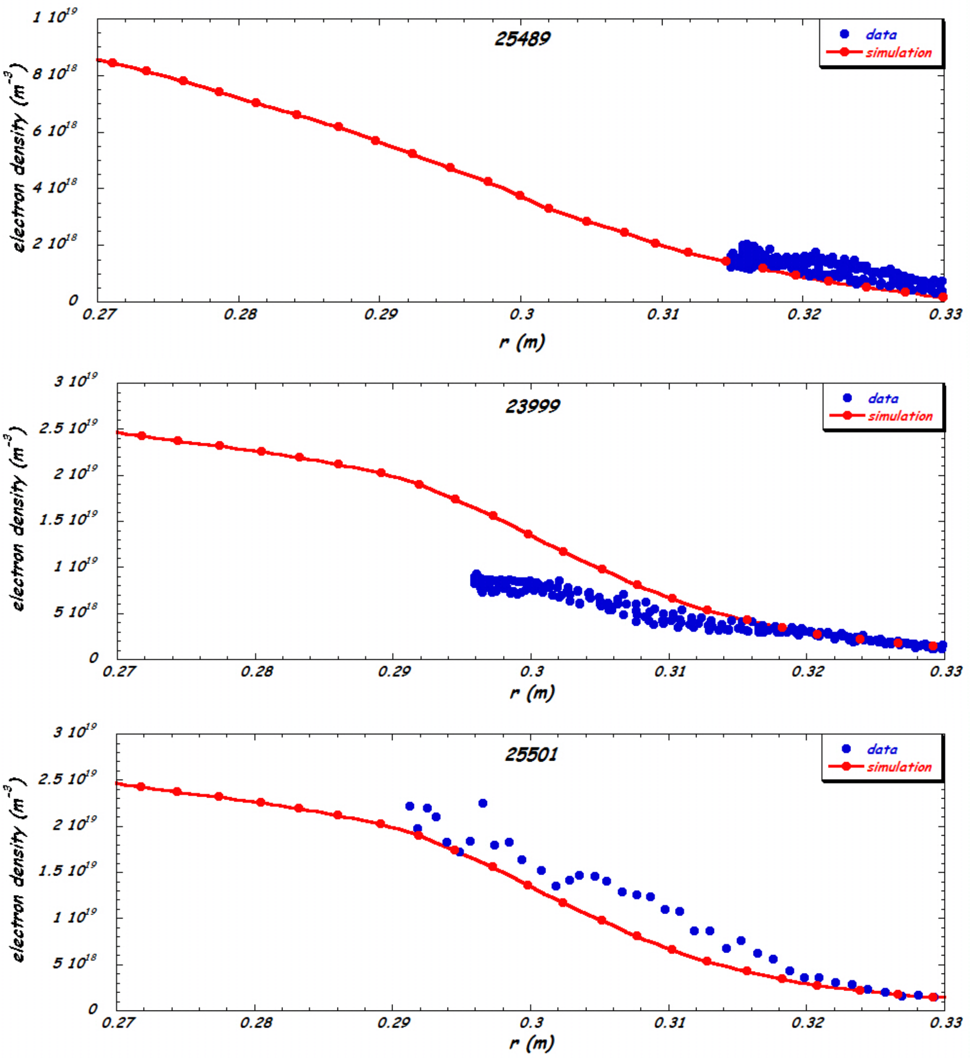

Figure 8.23: Langmuir probes measurement of the electron density radial profiles for the three different discharges and their reconstruction with SOLPS with $D_\perp = 1\, m^2 s^{-1}$ and considering also the poloidal limiter.

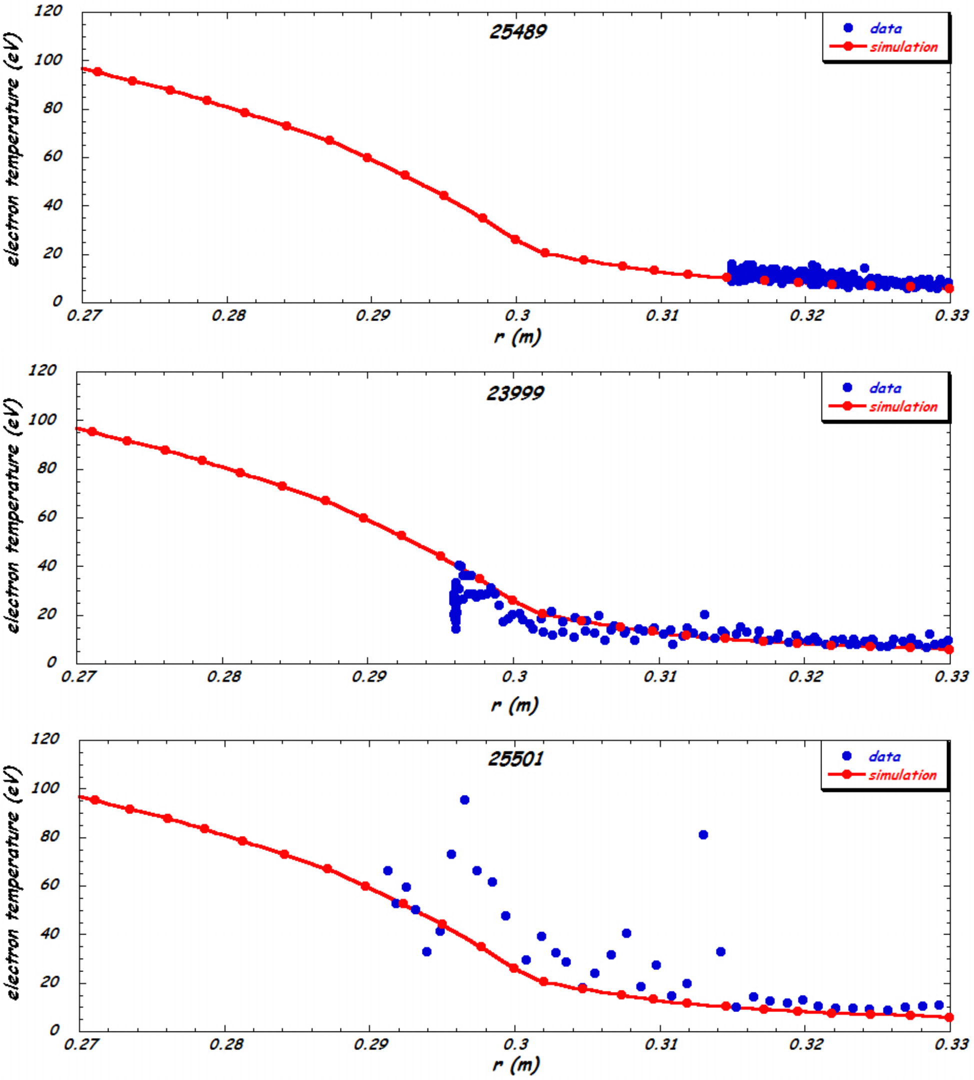

Figure 8.24: Langmuir probes measurement of the electron temperature radial profiles for the three different discharges and their reconstruction with SOLPS with $D_{\perp} = 1\, m^2 s^{-1}$ and considering also the poloidal limiter.

8.3 Conclusions and future work

Summarizing, the work carried out up to now was focused on the implementation of SOLPS as a tool to simulate the SOL of FTU. To increase the knowledge of the tool, several simulations have been done on a test-case based on TEXTOR, a limiter experiment already modelled by means of SOLPS. The test simulations were performed using B2 standalone and coupling it with EIRENE.

Once a sufficient know-how had been achieved, it was possible to prepare a mesh for FTU and to start the search for plasma parameters able to reproduce the experimental data. The simulations performed using pure deuterium plasma show that considering only the toroidal limiter it is needed to introduce also impurities to correctly reproduce the energy transport in the SOL, while in the cases of low electron density the particle transport is well reproduced. To reproduce correctly also the case at higher electron density two solutions have been explored: a scan over the perpendicular transport coefficient and the introduction in the simulation of the poloidal limiter as if it was a toroidal one. The first solution does not bring to any improvement, instead the second one significantly modifies all of the plasma quantities. This will have to be considered also when the LLL will be inserted in the simulations.

The next steps to study the effect of lithization on the impurities transport in the SOL are:

- introduction of Molybdenum as impurity for the non-lithizated case to reproduce correctly also the energy transport in the SOL
- description of the LLL as a lithium puffing from the wall in the position of the LLL to study the variation of plasma behavior in presence of lithium.
- simulations considering the limiter made of lithium and without the lithium puffing to investigate the different behavior of plasma distinguish what is due to the presence of lithium in the plasma and what to the presence of deposited lithium on the limiter.
- description of the LLL as a solid object inside the plasma, in this case it will be possible to study the power load on it.

General Conclusions and Future Developements

The aim of the research on the magnetically confined plasma is to achieve the possibility to produce energy by means of thermonuclear fusion. One of the main issues to be faced is the interaction of the hot plasma with the material components of the future nuclear fusion reactor, since the interaction can alterate the plasma introducing impurities and the wall material by means of particle bombardment. This means that there is a connection between the processes occurring at the wall and those of the main plasma.

In this thesis have been presented several aspects of the relation between plasma edge and the material facing components. In particular it has been paid attention to:

- the density control performing the lithization of the graphite tiles on RFX-mod;
- the density control comparing two different plasma refueling techniques on RFX-mod;
- the plasma edge transport proprieties on Tokamak with poloidal divertor configurations modeling JET by means of EDGE2D-EIRENE;
- the plasma edge transport proprieties on Tokamak with toroidal limiter configuration modeling FTU by means of SOLPS.

In order to control the recycling of the hydrogen retained on the RFX-mod first wall graphite tiles, and therefore to control the plasma density, two types of experiments were performed: studies on wall conditioning by means of lithium; a comparison of two different refueling techniques.

Lithization was done by means of injections of lithium pellets. To do that I followed the commissioning of the Room Temperature Pellet Injector, of the diagnostics related to it and the development of the ablation reconstruction by means of an ablation code. Once that the whole system was ready, several lithization campaigns were performed to optimize the technique and to study its effects on the plasma. Lithization proved to be an effective tool in controlling wall recycling, allowing for the first time to operate RFX-mod close to its 2 MA maximum target plasma current. Although the beneficial effect of lithium wall conditioning did not extended to the plasma core, the differences observed on density and temperature at the edge open the perspective of improving also the global performance by optimizing both the lithization technique and the core fuel capability.

The work started during this thesis can therefore be continued in the near future improving the effectiveness of the lithization technique by a thicker lithium deposition. In order to achieve this goal, a centrifugal injector able to inject many pellets on each discharge has been loaned from NSTX [101] and will be optimized and adapted for RFX-mod.

The lithization provides density control over a limited number of discharges. To increase this number it is necessary to control also the number of particles embedded on the graphite tiles of the RFX-mod first wall. This can be done using the most efficient refueling techniques, those where most of the injected particles contribute to the density increase. Two techniques have been compared: the gas puffing and the hydrogen pellet injection. The latter proved to be the most effective and also the less plasma perturbing one.

On Tokamak experiments two techniques to overcame the difficulties coming from the plasma-wall interaction are commonly used: moving away from the main plasma the wall interaction region by means of a divertor configuration; performing wall conditioning in a limiter configuration. In order to study the plasma edge transport proprieties I began the modeling of the two most common configurations in Tokamak devices, one for each solution: poloidal divertor and toroidal limiter. The divertor configuration considered was the one of JET, the conditioned limiter configuration considered was the one of FTU.

The simulations on JET were performed with EDGE2D-EIRENE code and achieved several goals: the test of the range of convergence of the code; the study of the range of validity of the two point model; and the study of the dependence of power deposition on the outer target from the main plasma features. These simulations proved that the code is able to reproduce the sheath limited and the conduction limited divertor regime, while it does not converge in case of low density and low temperature at the target position. It is therefore not able to predict the detached divertor regime. Their comparison with the two point model shows that the 0-dimensional model can be used only in the sheath limited divertor regime and partially in the conduction limited divertor regime. It has been moreover found that increasing the electron density by means of external deuterium puffing or reducing the pumping speed the temperature at the outer target decreases up to values less than 1 eV, and thus the power deposited on the target surfaces also decreases, independently from the gas puffing position and from the system used to increase the density.

The work performed during this thesis will continue applying these results in simulation of JET discharges, comparing the results with the experimental data. Modeling of the JET SOL is now particularly useful since the plasma facing components of JET first wall has been recently changed to provide an ITER-like wall.

To perform the simulation of the FTU SOL the SOLPS package has been used. Differently from the case of the EDGE2D-EIRENE code which was already configured for JET SOL simulations, a version of SOLPS adapted for the toroidal limiter configuration was available only for TEXTOR. To adapt it also for FTU SOL it was important first of all to study the code itself and the technical aspects to deal with it. Once that a sufficient know-how of the code was achieved, also by performing several test simulations, it was possible to proceed with the simulations of FTU SOL. The first simulations performed using pure deuterium plasma show the importance to consider also impurities for the energy transport and the possible difficulties to simulate the LLL, since it is not toroidally symmetric.

The work carried out during the thesis was part of a larger project with the ultimate goal that is to understand the effects of the lithization on the edge transport. It was important to prepare the tools and then to start along this roadmap. The next steps to carry out are: 1) the introduction of Molybdenum as impurity for the non-lithizated case; 2) the description of the LLL as a lithium puffing from the wall in the position of the LLL; 3) simulations considering the limiter made of lithium and without the lithium puffing; 4) implement the description of the LLL as a solid object inside the plasma.

Summarizing, during these three years an important contribution on density control and plasma edge transport studies was given, both on RFP and on Tokamak devices. Moreover it gives to me the possibility to have a background on several aspects of the edge plasma physics, both by an experimental and by a theoretical point of view.

Bibliography

[1] Shultis J.K. and Faw R.E. *Fundamentals of nuclear science and engineering.* CRC Press, 2002.

[2] Lawson J.D. Some criteria for a power producing thermonuclear reactor. *Proceedings of the physical society. Section B*, 1:6–10, 1957.

[3] Goldstone R.J. and Rutherford P.H. *Introduction to plasma physics.* Institute of Physics, 1995.

[4] Chouduri A.R. *The Physics of Fluids and Plasmas: an introduction for Astrophysicists.* Cambridge University Press, 1998.

[5] Yagi Y. and Sekine S. and Sakakita H. and Koguchi H. and Hayase K. and Hirano Y. and Hirota I. and Kiyama S. and Maejima Y. and Sato Y. and Shimada T. and Sugisaki K.

[6] United Nations. *Proc. Second United Nations International Conference on the Pecaful Uses of Atomic Energy*, Geneva, 1958.

[7] Boozer A.H. What is a stellarator? *Phys. Plasmas*, 5:1647, 1998.

[8] Wesson J. *Tokamaks.* Clarendon Press, 2004.

[9] Ortolani S. and Schnack D.D. *Magnetohydrodynamics of Plasma Relaxation.* World Scientific, 1993.

[10] http://www.ipp.mpg.de/ippcms/eng/for/projekte/w7x/index.html.

[11] Artsimovich L.A. *Nuclear Fusion*, pages 12–215, 1972.

[12] Taylor J.B. Relaxation of Toroidal Plasma and Generation of Reverse Magnetic Fields. *Physical Review Letters*, 33, 1974.

[13] Baker W., Dal Bello S., Marcuzzi D., Sonato P., and Zaccaria P. Design of a new toroidal shell and support structure for RFX. *Fus. Eng. Des.*, 63-64:461–466, 2002.

[14] Sonato P., Chitarin G., Zaccaria P., Gnesotto F., Ortolani S., Buffa A., Bagatin M., Baker W.R., Dal Bello S., Fiorentin P., Grando L., Marchiori G., Marcuzzi D., Masiello A., Peruzzo S., Pomaro N., and Serianni G. Machine modification for active MHD control in RFX. *Fus. Eng. Des.*, 66-68:161–168, 2003.

[15] Rostagni G. Rfx: an expected step in rfp research. *Fusion Engineering and Design*, 25(4):301–313, 1995.

[16] Fellin L., Kusstatscher P., and Rostagni G. Overall plant design, layout and commissioning. *Fusion Engineering and Design*, 25(4):315–333, 1995.

[17] http://www.fusione.enea.it/.

[18] De Marco F., Pieroni L., Santini F., , and Segre S.E. *Nuclear Fusion*, 26:1193, 1986.

[19] Alladio F. and FT Group. *Nuclear Fusion*, 25:1069, 1985.

[20] Rebut P.H., Bivkerton R.J., and Keen B.E. *Nuclear Fusion*, 25:1011, 1985.

[21] http://www.iter.org/newsline/62/143.

[22] Romanelli F., Laxåback M., Durodié F., Horton L., Lehnen M., Murari A., Rimini F., Sips G., and Zastrow K.D. The role of jet for the preparation of the iter exploitation. *Fusion Engineering and Design*, 86:459 – 464, 2011.

[23] Paméla J., Romanelli F., Watkins M.L., Lioure A., Matthews G., Philipps V., Jones T., Murari A., Géraud A., Crisanti F., and Kamendje R. The jet programme in support of iter. *Fusion Engineering and Design*, 82:590 – 602, 2007.

[24] Paméla J., Matthews G.F., Philipps V., and Kamendje R. An iter-like wall for jet. *Journal of Nuclear Materials*, 363-365:1–11, 2007.

[25] Philipps V., Mertens P., Matthews G.F., and Maier H. Overview of the jet iter-like wall project. *Fusion Engineering and Design*, 85:1581 – 1586, 2010.

[26] http://www.iter.org/.

[27] Winter J. *Plasma Physics and Controlled Fusion*, 38:1503–1542, 1996.

[28] Pitcher C.S. and Stangeby P.C. *Plasma Physics and Controlled Fusion*, 39:779–930, 1997.

[29] Loarte A. *Plasma Physics and Controlled Fusion*, 43:R183–R224, 2001.

[30] Bohm D. *The Characteristics of Electrical Discharges in Magnetic Fields*. McGraw-Hill, 1949.

[31] Thomas E.W., Janev R.K., and Smith J. *Nuclear Instruments and Methods in Physics Research*, B69:427, 1992.

[32] Haasz A.A. and Vietzke. *Physical process of the Interaction of Fusion Plasma with Solids*. Academic Press, 1996.

[33] Philipps V. Plasma wall interaction and its control by wall conditioning. *Transactions of Fusion Science and Technology*, 45, 2004.

[34] Jackson G.L., Winter J., Taylor T.S., Burrell K.H., DeBoo J.C., Greenfield C.M., Groebner R.J., Hodapp T., Holtrop K., Lazarus E.A., Lao L.L., Lippmann S.I., Osborne T.H., Petrie T.W., Phillips J., James R., Schissel D.P., Strait E.J., Turnbull A.D., and West W.P. *Phys. Rev. Lett.*, 67:3098–3101, 1991.

[35] Winter J., Esser H.G., Könen L., Philipps V., Reimer H., Seggern J.V., Schlüter J., Vietzke E., Waelbroeck F., Wienhold P., Banno T., Ringer D., and Vepřek S. *J. Nucl. Mater.*, 162-164:713–723, 1989.

[36] Tabarés F.L., Tafalla D., Balbín R., Bra nas B., Estrada T., García-Cortés I., Medina F., and Ochando M.A. *J. Nucl. Mater.*, 313-316:839–844, 2003.

[37] Renner H., Boscary J., Erckmann V., Greuner H., Grote H., Sapper J., Speth E., Wesner F., Wanner M., and W7-X Team. *Nucl. Fusion*, 40:1083, 2000.

[38] Sonato P., Antoni V., Baker W.R., Bertoncello R., Buffa A., Carraro L., Costa S., Della Mea G., Marrelli L., Murari A., Puiatti M.E., Rigato V., Scarin P., Tramontin L., Valisa M., and Zandolin S. *J. Nucl. Mater.*, 227:259–265, 1996.

[39] Garzotti L., Innocente P., Martini S., Reggiori S.A., and Daminelli G.B. Noncryogenic pellet injector for diagnostic purposes on the RFX reversed field pinch. *Review of Scientific Instruments*, 70(1), January 1999.

[40] http://www.zworld.com/.

[41] Khlopenkov K.V., Yu Sergeev V., Sudo S., Kondo K., Sano F., Zushi H., Okada H., Nagasaki K., Kuteev B.V., and Obiki T. *Fus. Eng. Des.*, 34-35:337–341, 1997.

[42] Barnes G.W., Gernhardt R.C., and Mansfield D. *SOFE '95 - 16th IEEE/NPSS Symposium on Fusion Engineering 'Seeking a New Energy Era'*, 1:517–519, 1995.

[43] http://www.alfa-chemcat.com/it/GP100w.pgm?DSSTK=010767.

[44] Innocente P., Boscolo B., Martini S., and Garzotti L. Three-dimensional time-resolved H pellet trajectory reconstruction in RFX by position sensitive detector H_α diagostic. *Review of Scientific Instruments*, 70(1):943–946, January 1999.

[45] Milora S.L., Houlberg W.A., Lengyel L.L., and Mertens V. Pellet fuelling. *Nuclear Fusion*, 35(6), 1995.

[46] Milora S.L. and Foster C.A. ORNL Neutral Gas Shielding model for pellet-plasma interactions. *Transactions on Plasma Science*, 1977.

[47] Pégourieé B. Review: Pellet injection experiments and modelling. *Plasma Physics and controlled Fusion*, 49:R87–R160, 2007.

[48] Parks P.B., Leffler J.S., and Fisher R.K. *Nucl. Fusion*, 28:477, 1988.

[49] Parks P.B. *Model of an Ablating Solid Hydrogen Pellet in a Plasma.* Garland Pub, 1979.

[50] Innocente P. and Martini S. *Rev. Sci. Instrum.*, 63:4996, 1992.

[51] Martin P., Murari A., Buffa A., Marrelli L., Baker W., Gadani G., Hemming O., Manduchi G., Parini . andA Taliercio C., Hoffman A., Stasek G., and Wirth R. *Review of Scientific Instruments*, 68:1256, 1997.

[52] Bonomo F., Alfier A., Gobbin M., Auriemma F., Franz P., Marrelli L., Pasqualotto R., Spizzo G., and Terranova D. *Nuclear Fusion*, 49:45011, 2009.

[53] Dexter R.N., Kerst D.W., Lovell T.W., Prager S.C., and Sprott J.C. *Fus. Tech.*, 19:131–139, 1991.

[54] Brunsell P.R., Bergsåker H., Cecconello M., Drake J.R., Gravestijn R.M., Hedqvist A., and Malmberg J.A. *Plasma Phys. Control. Fusion*, 43:1457, 2001.

[55] Martines E., Lorenzini R., Momo B., Munaretto S., Innocente P., and Spolaore M. *Nuclear Fusion*, 50:035014, 2010.

[56] Valisa M., Bolzonella T., Carraro L., Casarotto E., Costa S., Garzotti L., Innocente P., Martini S., Pasqualotto R., Puiatti M.E., Pugno R., and Scarin P. *J. of Nucl. Mater.*, 241-243:988–992, 1997.

[57] Tramontin L., Antoni V., Bagatin M., Boscarino D., Cattaruzza E., Rigato V., and Zandolin S. *J. Nucl. Mater.*, 266-269:709–713, 1999.

[58] Valisa M., Bolzonella T., Buratti P., Carraro L., Cavazzana R., Dal Bello S., Martin P., Pasqualotto R., Sarff J.S., Spolaore M., Zanca P., Zanotto L., Agostini M., Alfier A., Antoni V., Apolloni L., Auriemma F., Barana O., Baruzzo M., Bettini P., Bonfiglio D., Bonomo F., Brombin M., Buffa A., Canton A., Cappello S., Cavinato M., Chitarin G., De Lorenzi A., De Masi G., DEscande D.F., Fassina A., Franz P., Gaio E., Gazza E., Giudicotti L., Gnesotto F., Gobbin M., Grando L., Guazzotto L., Guo S., Igochine V., Innocente P., Lorenzini R., Luchetta A., Manduchi G., Marchiori G., Marcuzzi D., Marrelli L., Martini S., Martines E., McCollam K., Milani F., Moresco M., Novello L., Ortolani S., Paccagnella R., Peruzzo S., Piovan R., Piron L., Pizzimenti A., Piovesan P., Pomaro N., Predebon I., Puiatti M.E., Rostagni G., Sattin F., Scarin P., Serianni G., Sonato P., Spada E., Soppelsa A., Spagnolo S., Spizzo G., Taliercio C., Terranova D., Toigo V., Vianello N., Yadikin D., Zaccaria P., Zaniol B., Zilli E., and Zuin M. *Plasma Phys. Control. Fusion*, 50:124031, 2008.

[59] Mansfield D.K., Hill K.W., Strachan J.D., Bell M.G., Scott S.d., Budny R., Marmar E.S., Snipes J.A., Terry J.L., Batha S., Bell R.E., Bitter M., Bush C.E., Chang Z., Darrow D.S., Ernst D., Fredrickson E., Grek B., Herrmann H.W., Janos A., Jassby D.L., Jobes F.C., Johnson D.W., Johnson L.C., Levinton F.M., Mikkelsen D.R., Mueller D., Owens D.K., Park H., Ramsey A.T., Roquemore A.L., Skinner C.H., Stevenson T., Stratton B.C., Synakowski E., Taylor G., von Halle A., von Goeler S., Wong K.L., and Zweben S.J. *Phys. Plasmas*, 3:1892–1897, 1996.

[60] Mirnov S.V., Azizov E.A., Evtikhin V.A., Lazarev V.B., Lyublinski I.E., Vertkov A.V., and Yu Prokhorov D. *Plasma Phys. Control. Fusion*, 48:821–837, 2006.

[61] Apicella M.L., Mazzitelli G., Pericoli Ridolfini V., Lazarev V., Alekseyev A., Vertkov A., and Zagórski R. *J. Nucl. Mater.*, 363-365:1346–1351, 2007.

[62] Sánchez J., Tabarés F.L., Tafalla D., Ferreira J.A., García-Cortés I., Hidalgo C., Medina F., Ochando M.A., and Pedrosa M.A. *J. Nucl. Mater.*, 390-391:852–857, 2009.

[63] Summers H.P. and O'Mullane M.G. *AIP Conf. Proc. - 7TH International Conference on Atomic and Molecolar Data and their Applications - ICAMDATA-2010*, 1344:179–187, 2011. doi:10.1063/1.3585817.

[64] European Physical Society. *35th EPS European Conference on Plasma Physics*, volume 32D, 2008. D-1.002.

[65] Kugel H.W., Bell M.G., Bell R., Bush C., Gates D., Gray T., Kaita R., Leblanc B., Maingi R., Majeski R., Mansfield D., Mueller D., Paul S., Raman R., Roquemore A.L., Sabbagh S., Skinner C.H., Soukhanovskii V., Stevenson T., and Zakharov L. *J. Nucl. Mater.*, 363-365:791–796, 2007.

[66] Allain J.P., Rokusek D.L., Harilal S.S., Nieto-Perez M., Skinner C.H., Kugel H.W., Heim B., Kaita R., and Majeski R. *J Nucl. Mater*, 390-391:942–946, 2009.

[67] Taylor C.N., Heim B., and Allain J.P. *J. Appl. Phys.*, 109:053306, 2011.

[68] Barison S., Canton A., Dal Bello S., Fiameni S., Innocente P., Alfier A., Munaretto S., , and Rossetto F. *J. Nucl. Mater.*, 2011. doi:10.1016/j.jnucmat.2010.12.311.

[69] Itou N., Toyoda H., Morita K., , and Sugai H. *J. Nucl. Mater.*, 290-293:281–285, 2001.

[70] Carraro L., Bettella D., Innocente P., Puiatti M.E., Sattin F., Scarin . andP Valisa M., and Zaniol B. *ECA*, 25A:1545–1548, 2001.

[71] Kato S., Watanabe M., Toyoda H., and Sugai H. *J. Nucl. Mater*, 266-269:406–411, 1999.

[72] Carraro L., Costa S., Puiatti M.E., Sattin F., Scarin P., and Valisa M. *Plasma Phys. Control. Fusion*, 47:731, 2000.

[73] Bell M.G., Kugel H.W., Kaita R., Zakharov L.E., Schneider H., LeBlanc B.P., Mansfield D.K., Bell R.E., Maingi R., Ding S., Kaye S.M., Paul S.F., Gerhardt S.P., Canik J.M., Hosea J.C., and Taylor G. *Plasma Phys. Control. Fusion*, 51:124054, 2009.

[74] Agostini M., Scarin P., Cavazzana R., Fassina A., Alfier A., and Cervaro V. *Rev. Sci. Instrum.*, 81:10D715, 2010.

[75] De Masi G., Cavazzana R., Fassina A., Martines E., Momo B., and Moresco M. *Nucl. Fusion*, 51:53016, 2011.

[76] Cavazzana R., Scarin P., Serianni G., Agostini M., Degli Agostini F., Cervaro V., Lotto L., Yagi Y., Sakakita H., Koguchi H., and Hirano Y. *Rev. Sci. Instrum.*, 75:4152, 2004.

[77] Spolaore M., Antoni V., Spada E., Bergsåker H., Cavazzana R., Drake J.R., Martines E., Regnoli G., Serianni G., and Vianello N. *Phys. Rev. Lett.*, 93:215003, 2004.

[78] Lorenzini R., Martines E., Piovesan P., Terranova D., Zanca P., Zuin M., Alfier A., Bonfiglio D., Bonomo F., Canton A., Cappello S., Carraro L., Cavazzana R., Escande D.F., Fassina A., Franz P., Gobbin M., Innocente P., Marrelli L., Pasqualotto R., Puiatti M.E., Spolaore M., Valisa M., Vianello N., and Martin P. *Nature Physics*, 5:570, 2009.

[79] Scarin P., Vianello N., Agostini M., Spizzo G., Spolaore M., Zuin M., Cappello S., Carraro L., Cavazzana R., De Masi G., Martines E., Moresco M., Munaretto S., Puiatti M.E., and Valisa M. *Nucl. Fusion*, 51:073002, 2011.

[80] Backer W. and al. *Proc.* 16^{th} *IEEE/NPSS Symp. on Fusion Engineering.* Urbana-Champaign, 1994.

[81] Sørensen H. *The pellet injector for RFX*, February 1995.

[82] Milora S.L. and Foster C.A. Pneumatic hydrogen pellet injection system for the ISX tokamak. *Review of Scientific Instruments*, pages 482–487, January 1979. Oak Ridge National Laboratory.

[83] Landau L.D. and Lifshitz E.M. *Fluid Mechanics.* Reading. Addison-Wesley, MA, 1959.

[84] Sorensen H., Hansen J.E., Michelsen P., Sass B., Weisberg K-V., Knudsen O., and Michelsen E. A microwavw cavity fo measurement

of the mass of hydrogen pellets. *Review of Scientific Instruments*, 61(11):3464–3466, July 1990.

[85] Masiello A., Dal Bello S., Fincato M., and Rossetto F. *Fusion Engineering and Design*, 82:2282–2287, 2007.

[86] Maxtek piezoelectric gas leak valve MV-112, Operation and service manual, http://www.maxtekinc.com.

[87] Martin P., Murari A., and Marrelli L. Electron temperature measurements with high time resolution in RFX. *Plasma Physics and controlled Fusion*, 38(7):1023, 1996.

[88] Taroni A., Corrigan G., Radford G., Simonini R., Spence J., and Weber S. *Contrib. Plasma Physics*, 32:438, 1992.

[89] *EDGE2D/EIRENE code interface report, June 30, 2006, Wiesen S.*

[90] Stangeby P.C. *The plasma boundary of magnetic fusion devices.* Institute of Physics Publishing, 2000.

[91] Braams B.J. *Computational Studies in Tokamak Equilibrium and Transport.* PhD thesis, Rijksuniversitet Utrecht, 1986.

[92] Baelmans M. *Code improvements and applications of a two-dimensional edge plasma model for toroidal fusion devices.* PhD thesis, Katholieke Universiteit Leuven, 1993.

[93] Reiter D. *The EIRENE Code User Manual including: B2-EIRENE interface, version:11/2009.*

[94] Braginskii S.I. *Reviews of Plasma Physics*, 1:205, 1965.

[95] Naval Research Laboratory. *NRL Plasma Formulary.* Washington DC, USA, 2009.

[96] Schneider R., Bonnin X., Borras K., Coster D.P., Kastelewicz H., Reiter D., Rozhansky V.A., and Braams B.J. *Contrib. Plasma Phys.*, 46:3–191, 2006.

[97] Reiter D. *The EIRENE code, version:Jan. 92 Users manual.*

[98] Mazzitelli G., Apicella M.L., Pericoli Ridolfini V., Apruzzese G., De Angelis R., Frigione D., Giovannozzi E., Gabellieri L., Granucci G., Mazzotta C., Marinucci M., Romano A., Tudisco O., Alekseyev A.,

Ljublinski I., Vertkov A., and ECRH Team. *Fusion Engineering and Design*, 85:896–901, 2010.

[99] Zagórski R., Apicella M.L., Mazzitelli G., Pericoli Ridolfini V., and the FTU team. *Czech. Journal of Physics Suppl. B*, 56:B182–B188, 2006.

[100] Pericoli Ridolfini V., Apicella M.L., Mazzitelli G., Tudisco O., Zagórski R., and the FTU team. *Plasma Physics and Controlled Fusion*, 49:S123–S135, 2007.

[101] http://nstx.pppl.gov/.